Engineering Gold Nanorods for Photothermal Application

Tahani Albogami
Department of Physics and Astronomy
University of Leeds

A thesis submitted for the degree of

Doctor of Philosophy

28th November 2022

Intellectual Property

The candidate confirms that the work submitted is her own and the appropriate credit has been given where reference has been made to the work of others.

Acknowledgement

I would like to express my special thanks to my supervisor Dr. Kevin Critchley for his guidance, advice and kindness that carried me throughout my degree. I am grateful for his time and useful feedback. Without his continuous support, this thesis would not be possible. I would also like to thank my co-supervisors Prof. Stephen Evans and Dr. Zhan Yuin Ong for their advice and helpful suggestions.

I would like to acknowledge and thank Dr. James Mclaughlan, Dr. Zabeada Aslam, Dr. Lucien Roach and Dr. Thomas Maisey for their contributions in this work. I take this opportunity to appreciate all the support coming from the entire Molecular and Nanoscale Physics group at University of Leeds. I would like to acknowledge and thank the Ministry of Education in Saudi Arabia for providing me with a scholarship and the financial support.

Finally, my deepest appreciation for my mum, I am forever grateful for her endless love and support. I would also like to thank my whole family, my grandmother, my brother Rashed and sisters Rashidah and Abeer for their support throughout my degree.

Abstract

At the moment, cancer therapies involve harmful side effects on patients. Therefore, it is necessary to create safer cancer treatment strategies that can significantly enhance treatment experience. Using near-infrared-absorbent gold nanorods (AuNRs), which have the ideal optical and thermal properties to be used in methods like photothermal therapy, is one way to accomplish this goal. However, the challenges associated to using AuNRs such as the CTAB toxicity, instability under pulsed laser irradiation need to be met. This thesis aims to develop AuNRs in order to make them biocompatible, thermally stable, well-controlled, reproducible and efficient in NIR absorption for effective photothermal applications.

In this thesis, this is discussed in three main areas: Firstly, the reduction of the toxicity of CTAB bilayer of bare CTAB@AuNRs through a direct coating method with the inorganic silica shell. Followed by different techniques to confirm the silica coating, such as UV-Vis spectroscopy, Zeta potential, TEM, and EDX elemental mapping. The In-situ TEM heating study showed that the silica shells enhanced the thermal stability of AuNRs, with maintaining their rod shape and protected them from turning into nanospheres even up to 1200 °C. Secondly, the surface of the silica coated-AuNRs were functionalised with DPPC + DSPE-PEG2000 phospholipids to enhance their colloidal stability and biocompability *in vitro* tests in human colorectal cancer cell lines such as SW620 and HT29. Thirdly, the influence of the silica coating on AuNRs reshaping behaviour under nanosecond pulsed laser irradiation as a function of irradiation time, fluence, and porosity degree was explored and analysed by UV-Vis spectroscopy and Transmission electron microscopic (TEM). In this thesis, it was found that when the AuNR@mSiO_2 is off resonance of the nanosecond pulsed laser, the thermal reshaping is more controllable for AuNR@mSiO_2. The slight blue shift helped to form sealed cavities. After pulsed laser irradiation, the gap size of AuNRs@mSiO_2 was found to be controlled by tunning the LSPR band positions to the wavelength of pulsed laser either (on resonance) or (off resonance). Finally, I introduce a new route for fabrication an advantageous dual AuNR@Cavity@mSiO_2 of well-controlled and reproducible cavity and high efficiency for photothermal therapy in the near-infrared biological window (700-800 nm) with high porosity for potential drug uploading without influencing the absorption spectra.

Abbreviations

AuNR	Gold nanorod
BSA	Bovine serum albumin
CMC	Critical micelle concentration
CTAB	Cetyltrimethylammonium bromide
CTCF	Corrected total cell fluorescence
DMEM	Dulbecco's modified eagle medium
DSPE-PEG_{2000}	1,2-distearoyl-sn-glycero-3-phosphoethanolamine-N-[methoxy(polyethylene glycol)-2000]
DPPC	1,2-dimyristoyl-sn-glycero-3-phosphocholine
EDX	Energy-Dispersive X-ray spectroscopy
FWHM	Full width at half maximum
HSA	Human serum albumin
IC_{50}	Half-maximal inhibitory concentration
LSPR	Longitudinal surface plasmon resonance
LC-MSNs	Lipids coated mesoporous silica coated nanoparticles
MSOT	Multispectral optoacoustic tomography
NaOL	Sodium oleate
PBS	Phosphate-buffered saline
PPTT	Plasmonic photothermal therapy
PTA	Photothermal agent
PA	Photoacoustic
SiO_2@AuNR	Silica coated gold nanorod
SiO_2	Silicon dioxide
SPR	Surface Plasmon Resonance
TEM	Transmission Electron Microscopy
TEOS	Tetraethoxysilane
TSPR	Transverse surface plasmon resonance
Thiol-PEG	Thiolated polyethylene glycol

TABLE OF CONTENTS

List of Figures

List of Tables

Attribution of Work

I wish to express my gratitude for the following people for their contributions in performing some experimental work in this thesis.

Chapter 3

All work of the Energy Dispersive X-Ray Spectroscopy in Chapter 3 and other chapters and In Situ Transmission Electron Microscopy were performed by Dr Zabeada Aslam from School of Chemical and Process Engineering. The Multi-spectral optoacoustic tomography (MSOT) was performed by Dr James Mclaughlan. All other experimental work and all analysis were performed by myself.

Chapter 4

The fluorescence microscopy images in Chapter 4 were collected by Dr Thomas Maisey from Leeds Institute of Medical Research at the University of Leeds. The *in vitro* cytotoxicity assays were performed by myself with help of Dr Thomas Maisey. All analysis and other experimental work were performed by myself.

Chapter 5

The pulsed laser irradiation in Chapter 5 was performed by Dr James Mclaughlan from School of Electronic & Electrical Engineering. The simulation work was performed by Dr Lucien Roach. All analysis and other experimental work were performed by myself.

1. Introduction and Theoretical Background

1.1. Introduction

Globally, there were over 19 million new cases of cancer and over 10 million cancer deaths reported in 2020 [1]. Almost one in six deaths are caused by cancer, making it one of the top causes of death globally (Figure 1.1) [1, 2]. The most prevalent types of cancer cases (Figure 1.1) are breast (2.26 million), lung (2.21 million), and colon (1.93 million) [2].

The treatment of cancer has improved in recent decades with new therapies and more effective early diagnostic techniques, such as screening programmes. Detecting cancer early improves the prognosis and influences the treatment pathway. However, many cancer therapies have undesirable side effects [3, 4]. The most common cancer treatments are chemotherapy, surgery, immunotherapy, and radiation. Each of these therapies has serious drawbacks [4]. Chemotherapy causes non-specific harm to healthy cells during targeting the malignant cells, as a result of the toxicity of the drugs and the lack of ability to localise the drug to cancer tissue [5]. Moreover, the malignant cells become resistant to chemotherapy medications over time [5]. On the other hand, surgery can be an effective technique if the cancer is localised to tissue that can be removed without preventing essential organs from functioning. However, its consequent damage to the patients' tissues and increase cancer cell dissemination remain unavoidable [6]. The immunotherapy mainly works by empowering patient's immune system to destroy cancer cells. However, the immune system can be negatively impacted and the healthy tissues of organs are affected and destroyed [7, 8]. Immunotherapy is ineffective for patients with compromised immune system. There have been efforts to improve the efficiency and minimize the safety risks of all these current treatment methods. In the last two decades, the non-invasive photothermal therapy treatment (PTT) treatment has attracted massive attention. PTT is a method uses photothermal agents (PTAs), which convert light into heat that can destroy cancer cells of specific areas of tissue using different types of electromagnetic energy sources, such as visible light, infrared, and near infrared [9]. In medicine PTT is considered to be a method that is included in the non-invasive branch of therapies.

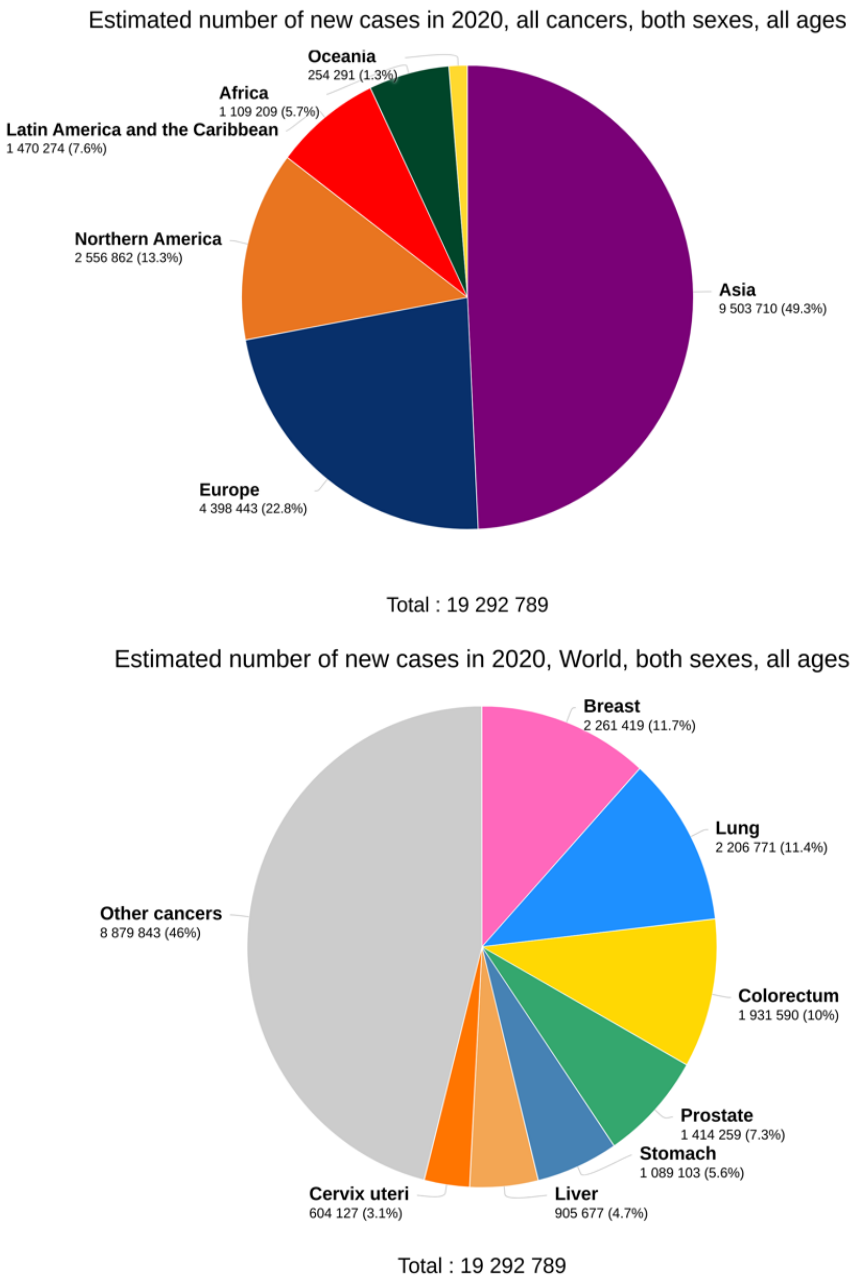

Figure 1.1. Estimated cancer cases reported globally in 2020.

Estimated cases were reported globally in 2020 (Top chart). Estimated cases were reported 2020 regarding to cancer types (Bottom chart). (Adapted from the World Health Organization (WHO) Ref [2]).

There are variety of photothermal agents (PTAs) have been investigated, including noble metals nanoparticles (NPs) [10, 11] (e.g. Au and Ag of different shapes, structures, and compositions) and carbon-based nanomaterials such as carbon nanotubes [12] and graphene oxide [13]. To choose the ideal PTAs, properties such as high absorption cross sections in the biological window wavelength range (to be discussed shortly), low toxicity, and thermal stability are required [14]. Near infrared (NIR)-absorbing Au nanomaterials are considered as

one of the most promising type of PTA. AuNPs of different shapes and structures such as gold nanorods (AuNRs), nanoshells, nanocages, and nanostars have high absorption cross-sections in the NIR [15, 16].

For PTT, use of NIR light allows for deeper human tissue penetration [17]. It was reported that NIR light at 810 and 980 nm has exhibited good efficiency to penetrate deeply into skin up to 3 cm of scalp, skull, and brain tissue when the power ranges from 10 to 15 W [18]. In particular, AuNRs have demonstrated exceptional optical tunability at visible (Vis) and near-infrared wavelengths (NIR) region by adjusting their aspect ratio (AR) and high molar extinction coefficients [17, 19-21]. Depending on the AR of AuNR, the longitudinal extinction coefficients were found to range from 1.6×10^8 to 1.4×10^9 M^{-1} cm^{-1} [22]. Using NIR light, AuNRs have been shown to generate local heat to remotely and non-invasively kill cancer cells, with low impact to the surrounding healthy tissue, in small animal models [23, 24]. Nevertheless, before this strategy can be clinically used, there are still many challenges that need to be resolved. This Chapter mainly focuses into more detail on AuNRs advantages for PTT over other types of gold nanoparticles, their structures, optical properties and biomedical applications.

Chapter 2 presents the synthesis, methods, experimental techniques, and material used in this thesis, including the theories of equipment used.

This thesis presents three chapters of results. The first results chapter, Chapter 3, will discuss the preparation, characterization, optical properties, colloidal and thermal stability of AuNRs before and after silica coating. Additionally, a detailed study of the stability of the silica shell in photoacoustic imaging under high-energy nanosecond pulsed laser will be discussed.

In the second results chapter, Chapter 4, I describe the surface modification of silica coated-AuNRs with lipids and studying their biocompatibility, cytotoxicity and cellular uptake by human colorectal cell lines SW620 and HT29.

In the third results chapter, Chapter 5, I will introduce a novel method for the fabrication of AuNR@Cavity@SiO_2 nanomaterials that could be fabricated by nanosecond laser pulse

illumination. This chapter focuses on the effect of the silica coating on AuNRs thermal reshaping behaviour as a function of irradiation time, fluence, and porosity degrees.

In the remaining sections of this chapter, I will present the project's theoretical underpinnings of AuNRs and their optical and thermal properties. Additionally, surface modification on AuNRs and the potential photothermal reshaping under laser irradiation will be discussed. Furthermore, discussing the cytotoxicity, cellular uptake of AuNRs and their interactions with these cells, and the photoacoustic imaging.

1.2. Gold Nanorods (AuNRs) Synthesis Methods

In 1995, the rod-shaped AuNPs of typical sizes around 10-100 nm were reported by Esumi et *al* [25]. They prepared AuNRs under irradiation of ultraviolet [26] light in presence of a micellar solution of hexadecyltrimethylammonium chloride. Throughout the past decade, remarkable advancements have been achieved in the fabrication of AuNRs with high yield, good quality, and excellent uniformity. The most well-known AuNRs synthesis is the seed-mediated growth method which was developed by Wiesner and Wokaun [27]. Further improvements had been made to increase the shape-yield of rods, until El-Sayed et al. [28] and Murphy et al. [29] introduced their method of using cetyltrimethylammonium bromide (CTAB) and silver nitrate to controllably grow the anisotropic nanocrystals. This technique produce single crystals with a smooth shape, high yield, and a comparatively easy method. However, this strategy has a number of shortcomings such as the resultant AuNRs had limited ARs of 2 to 5 [30] and the low reproducibility due to the limited period of time of seeds stability [31]. Many developments have been published on this general method to produce high aspect ratio AuNRs. Recently, one-pot synthesis of AuNRs has attracted much attention [32-34]. This method is termed as ‘seedless synthesis’ which replaced using a separate seed solution by adding sodium borohydride directly to the growth solution of AuNRs [26, 35, 36]. Jana and co-workers initially synthesized AuNRs by using seedless procedure [35], they encountered a difficulty of exciting impurities of spheres. Therefore, El-Sayed and co-workers improved this procedure by adjusting both the $NaBH_4$ and pH of the solution to produce AuNRs of high monodispersity [34].

Our group [37] has reported an improved AuNRs seedless synthesis by adjusting both sodium oleate (NaOL) and CTAB concentrations in a one-pot binary surfactant protocol, which enable a direct manipulation of the soft-template in a facile and controllable procedure. The seedless binary surfactant protocol was used in all the presented work in this thesis. The CTAB and NaOL were combined to create the AuNRs. The weak reducing agents used in the growth solution were ascorbic acid and silver nitrate. The sodium oleate has the capability of reducing Au^{3+} to Au^{1+} after adding the $HAuCl_4$ solution due to its unsaturated double-bond [38, 39].

1.3. Growth mechanism of Gold nanorods

1.3.1. Crystal Structure

Penta-twinned AuNRs may form via a more simple mechanism of selective surface passivation in the single-crystal, due to the penta-twinned seed particles' intrinsic shape. As shown in Figure 1.2 [40], the nanorods possess five {111} surfaces on each of its two ends and five {100} or {110} side facets, forming an idealised three-dimensional prism shape, all the five identical crystal units are connected by {111} surface facets make up decahedral seeds [41]. The AuNR formation is mainly dependant on a surfactant that has the ability to selectively passivate a certain side facets giving a fundamental justification for favouring growth longitudinally along one direction rather than the other [42]. CTAB is frequently employed for

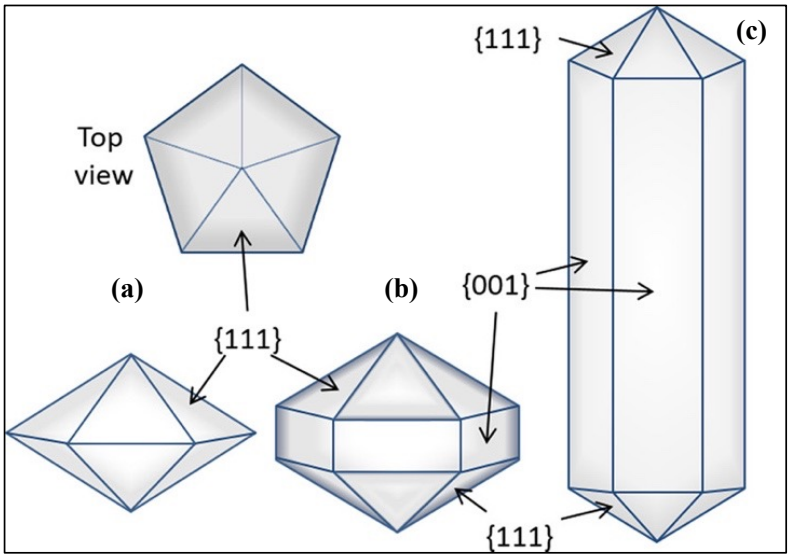

Figure 1.2. Schematic illustration of penta-twinned nanorod formation. (a) Truncated decahedral seed of five {111} surfaces on each of its two ends and five {100}. (b) Penta-twinned decahedral. (c) The formed penta-twinned nanorod. (Adapted from Ref [40]).

the control of the anisotropic growth of AuNRs [43]. In the following subsection, the structure, function, and properties of CTAB in anisotropic growth of AuNRs are presented.

1.3.2. Cetyltrimethylammonium bromide (CTAB)

The surfactant, CTAB, is made up of 16 carbons, and the ammonium head group. Its chemical structure is shown in Figure 1.3. It is used widely as a nanoparticle coating agent due to its hydrophobic tail and hydrophilic positively charges allowing nanoparticles to be synthesized and dispersed in aqueous medium [44-46].

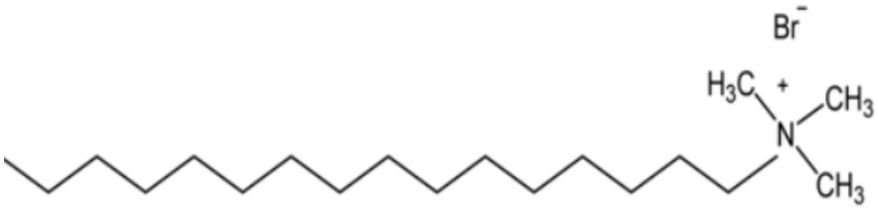

Figure 1.3. Chemical structure of Cetyltrimethylammonium bromide CTAB.

It has been reported by Murphy's group that packing density of CTAB is selectively higher on the {110} and {100} surfaces than on the {111} surfaces at the ends of the rods, yielding a more condensed layer [47], as illustrated in Figure 1.4 [47]. The interfaces between the gold-CTAB and the CTAB-water layers are depicted in Figure 1.4, which is a snapshot of a simulation box including the gold (111) surface, the CTAB layer, and the water layer. A deformed cylindrical micelle structure is formed on the gold surface by the CTAB headgroups as they adhere to it favourably [47]. The CTAB headgroups are arranged in the cylindrical micelle's core, while the CTAB tails are arranged in the micelle's outer layer. The CTAB nitrogen layer of the micelle is where the bromide ions (yellow) are most frequently located [47]. On both the gold (100) surface and the gold (110) surface, the surfactant layer is seen to have a comparable shape as shown in (Figure 1.4b&c). The cetyltrimethylammonium bromide cation (CTA+) bilayer is adsorbed on both sides of the gold surface and bromide ions (yellow) are present in water in the initial configuration for the (111) gold surface. In the diffuse layer, the Br- ion density is lower because to the greater Br- adsorption percentage that is associated with the higher CTA+ density on the (110) and (100) surfaces. On the gold (111) surface, as opposed to

the (110) and (100), it was reported that a higher cross-sectional area of the water ion channel is available for the diffusion of $AuCl_2$ [47].

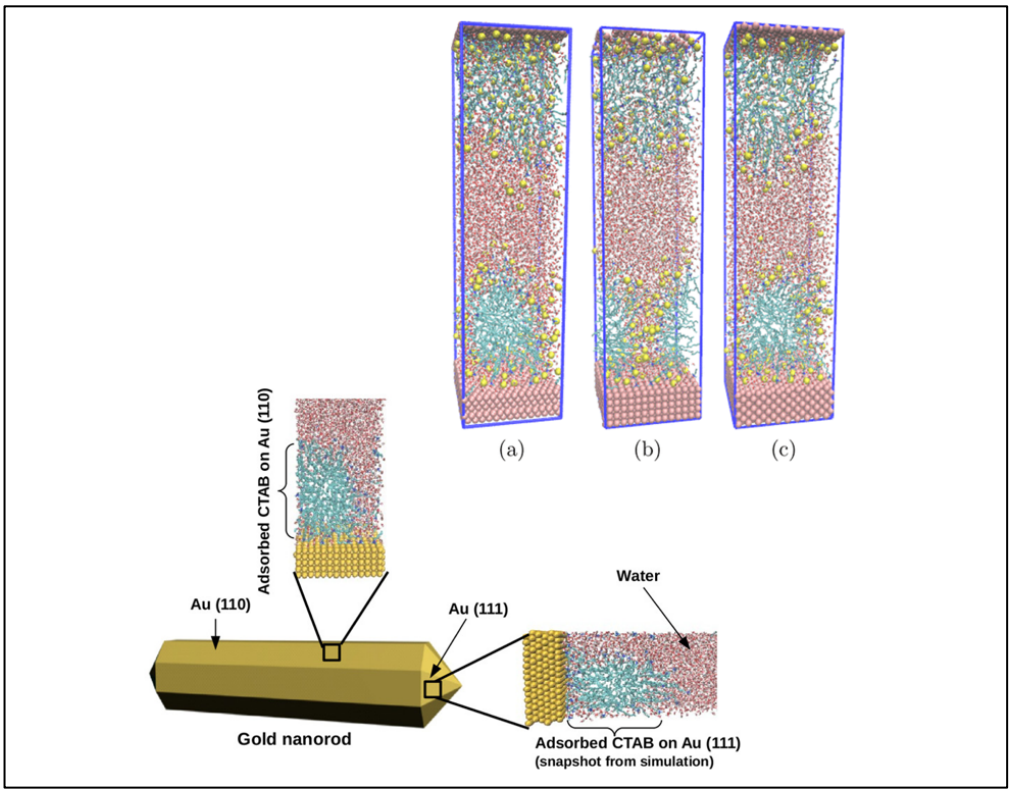

Figure 1.4. Anisotropic growth of gold nanorod (AuNR) from a Molecular Dynamics Simulation.

(a) {111} (b) {110} (c) {100}. Showing CTAB is selectively higher on the {110} and {100} surfaces than on the {111} surfaces are at the ends of the rods, yielding a more condensed layer. (Adapted from Ref [47]).

The following describes the reaction via which the ion-pair complex between the CTAB monomer and $HAuCl_4$ is formed.

$$HAuCl_4 \rightarrow AuCl_4^- + H^+ \quad (1)$$

$$CH_3(CH_2)_{15}(CH_3)_3\,N^+Br^- \Leftrightarrow CH_3(CH_2)_{15}(CH_3)_3\,N^+ + Br^- \quad (2)$$

$$CH_3(CH_2)_{15}(CH_3)_3\,N^+ + AuCl_4^- \quad (3)$$

$$\rightarrow \quad CH_3(CH_2)_{15}(CH_3)_3\,N\text{-}AuCl_4$$

When $HAuCl_4$ is dissolved, deprotonation occurs, with the $AuCl_4^-$ (square planer geometry) and H^+ ions separated in the aqueous solution [48], as represented in Eq.1. The surfactants, at low concentrations, generally act as an electrolyte and suppress the electrospray ionization.

Eq. 2. represents the ionization of CTAB and the resultant ionized CTA^+ and Br^-. During AuNRs synthesis, the $AuCl_4^-$ and CTA^+ form a compound of ion pairs ($CTA–AuCl_4^-$) as shown in the Eq. 3. When the ascorbic acid added to the reaction, $AuCl_4$–CTA complex is exposed to reduction into Au^0 (nucleation and growth) [49].

The rod-shaped CTAB-micelles of an estimated bilayer thickness of ~3.2 nm act as soft templates for the fabrication of AuNRs [42]. It was reported that if the concentration of CTAB in the growth solution is lower than the critical micelle concentration which is (CMC = 0.0009 mol/L in water), the rods tend to cluster. Therefore, the concentration of CTAB has shown a significant role in the growth, monodispersity, aspect ratio, colloidal stability, and purity of the synthesised of AuNRs [50].

It was reported that by employing binary surfactant mixtures by adding NaOL that act as a second surfactant alongside CTAB results in highly pure and monodisperse AuNRs [51]. According to literature, the AuNR surface was found to be sensitive to pH. The amount of CTAB on the surface of AuNRs was found to be less as pH value of the growth solution rises, causing in producing different shapes [51]. Additionally, a high salt content and the inclusion of organic solvents have all been reported to reduce stability to an unsatisfactory level, which restricts the use of GNRs in other applications [52, 53]. Furthermore, it has been observed that CTAB molecules are harmful to human cells [54]. However, free CTAB was found to be more toxic than the CTAB bound to the AuNR [55]. The CMC of CTAB is substantially higher than the indicated threshold for cytotoxicity (IC_{50} 1 mM) [56, 57].

CTAB in known to interact with the phospholipid cell membrane causing defects and holes which results in cell death [58, 59]. Using centrifugation to remove the majority of the free CTAB from the AuNR sample is a possible solution, but it may completely remove both the free CTAB and the CTAB linked to the GNRs, which then would cause considerable aggregation [47]. Therefore, the surface modification is significantly needed to make these CTAB-capped-AuNRs non-toxic to be used in biological applications. The most used strategies for surface modification of CTAB-capped-AuNRs are surface covering and ligand exchange [47].

1.4. Surface modification of the CTAB-capped AuNR

A variety of surface modifications have been employed to lower the concentration of CTAB to levels that are no longer cytotoxic without seriously affecting dispersion stability, such as replacing the CTAB layers with more biocompatible ligands, the commonly used ones are thiolated polyethylene glycol (PEG) [60], 1,2-dimyristoyl-sn-glycero-3-phosphocholine (DMPC) phospholipid molecules [61], and thiolated polyamidoamine (PAMAM) [62]. However, another mechanism to reduce CTAB cytotoxicity is using an additional biocompatible coating such as bovine serum albumin (BSA) or human serum albumin (HSA) to completely coat the AuNR surface [59]. In addition, Ma and co-workers published a modified Stöber method for synthesising biocompatible silica-coated AuNRs [63, 64]. This section's main emphasis will be on the functionalization of AuNRs using lipid and silica coatings to passivate the poisonous bilayer CTAB and increase biocompatibility of AuNRs in PTT experiments.

1.4.1. Silica Coating of Gold Nanorod (AuNR@SiO_2)

Silica coating of AuNRs has attracted extensive attention among other surface modification mechanisms due to exhibiting high colloidal and thermal stability [65-67]. Moreover, it has been reported that coating AuNR by SiO_2 shell of tunable porosity increases the rods' surface area, improves biocompatibility, and maintaining the optical characteristics of the gold core [68]. There are a range of synthetic techniques of silica coating to encapsulate AuNRs. The commonly utilized techniques for silica coating on CTAB capped-AuNR are illustrated in Figure 1.5: (1) Replace the CTAB bilayer by a functional primer, (2) coating the CTAB bilayer by a primer, (3) direct coating for the CTAB bilayer [68].

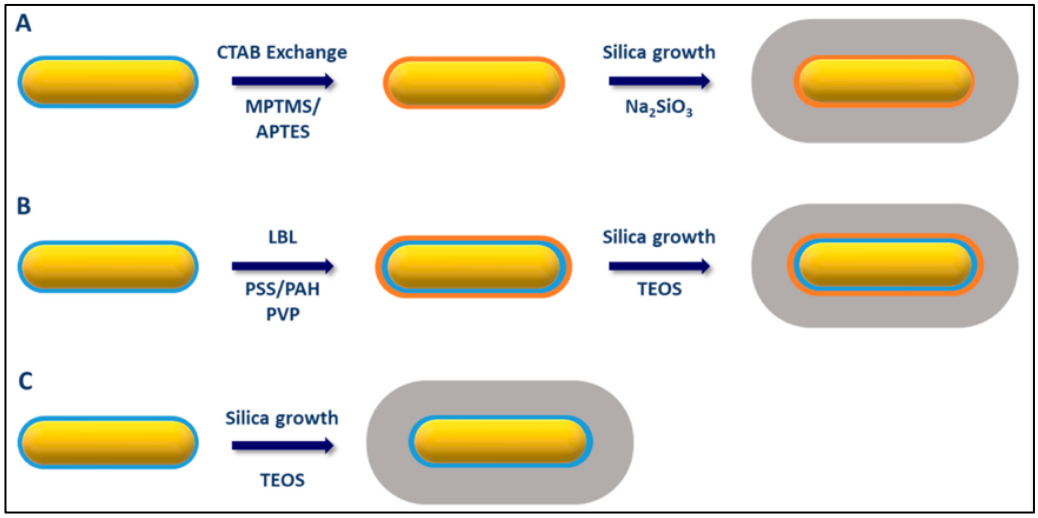

Figure 1.5. Schematic illustration of the commonly utilised silica coating techniques for AuNRs. (a) Replace the CTAB bilayer by a functional primer, (b) Coating the CTAB bilayer by a primer, and (c) Direct coating for the CTAB bilayer. (Adapted from Ref [68]).

Replacing the CTAB bilayer by a functional primer aims to stabilize the role of CTAB on the surface of AuNR with primer, (3-aminopropyl)trimethoxysilane (APTMS), to enhance the surface's affinity for silica coating, this was developed by Liz-Marzàn et al. when they introduced the approach in 2003 [69], using a layer of polyvinyl pyrrolidone (PVP) to coat colloidal nanoparticles with SiO_2 shell. In this mechanism, the surface charge of CTAB bilayer is reduced by a negatively charged and positively charged of polystyrene sulfonate (PSS) and polyallylamine chloride (PAH), respectively, followed by the Stöber process of SiO_2 shell growth by base-catalyzed hydrolysis and condensation of tetraethoxysilane (TEOS). The direct coating of SiO_2 for the CTAB bilayer is discussed in the following subsection, this strategy was used throughout this thesis.

1.4.1.1. Direct Coating of AuNR with a Mesoporous Silica Shell

The silica direct coating of AuNR was firstly introduced by Gorelikov et al., followed by several studies have successfully performed direct coating of AuNR with silica [70-72]. Stöber process, which was first discovered in 1968 by Werner Stöber [73]. The detailed synthesis protocol is described in (Chapter 2 section 2.2.2). Briefly, the procedure is very straightforward, a solution of the CTAB@AuNRs redispersed in water is mixed with injections of the primary precursor of TEOS which is used as the source of silica in alcohol (methanol, ethanol) [68]. The formation of SiO_2 shell on the surface of CTAB@AuNR is attributed to the

charge compensation that occurred between the negatively charged siloxy (≡SiO^-) (basic catalytic activity) and the positively charged cetyltrimethylammonium (CTA^+) of the CTAB surfactant [74, 75], as illustrated in Figure 1.6, [76]. The growth solution is left to grow the SiO_2 shell for several hours to days under stirring. It has been observed that AuNR concentration, TEOS concentration, excess CTAB concentration, alcohol concentration, pH, and growth times are parameters that have a strong impact on the shape and the thickness of the SiO_2 shell [77]. In addition, the pH of the solution is typically adjusted to be 10 –11 to control the hydrolysis and adsorption of siloxy (≡SiO^-) on the ammonium group of CTAB on AuNR surface [77].

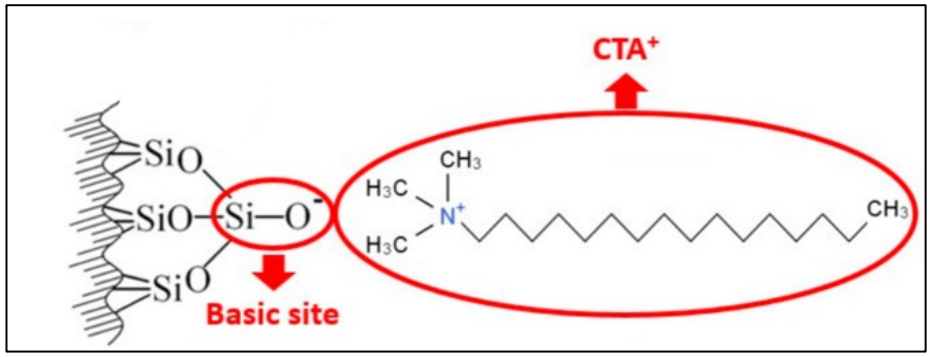

Figure 1.6. Schematic illustration of the charge compensation between SiO_2 and CTA^+. Showing the basic siloxy site. (Adapted from Ref (76)).

The very early attempts of the direct coating of silica on AuNR exhibited some challenges, such as producing the uncoated AuNR due to the formation of free silica nanoparticles in the solution, this is due to the excess CTAB present in the AuNR solution before adding the silica precursor (TEOS). Gorelikov was able to successfully resolve this problem by simply applying centrifugation to the AuNR solution before starting the silica coating protocol. However, an extensive washing that causes a complete removal of CTAB cause aggregation of AuNR, because CTAB molecules support the AuNR solution by offering an electrostatic repulsion due to their positively charged headgroups [72]. The Gorelikov et al. protocol states that the CTAB concentration during the silica direct coating of AuNR should be around 1.5 mM, which is quite higher than CMC in water [68]. Therefore, the interaction between the remaining CTAB and the negatively charged silicate species in the growth solution results in the formation of an irregularly shaped porous SiO_2 shell.

The relation between the SiO_2 shell thickness and the amount of added TEOS has been studied by several researchers [78-81]. They observed that SiO_2 shell thickness can be controlled by adjusting the amount of TEOS, the more added TEOS leads to a thicker SiO_2 shell [68], as shown in Figure 1.7. In addition, it has been reported that the spectral location of the LSPR bands is noticeably redshifts as the SiO_2 shell thickness is increased. This is attributed to the sensitivity of the LSPR to any changes of the local refractive index [82].

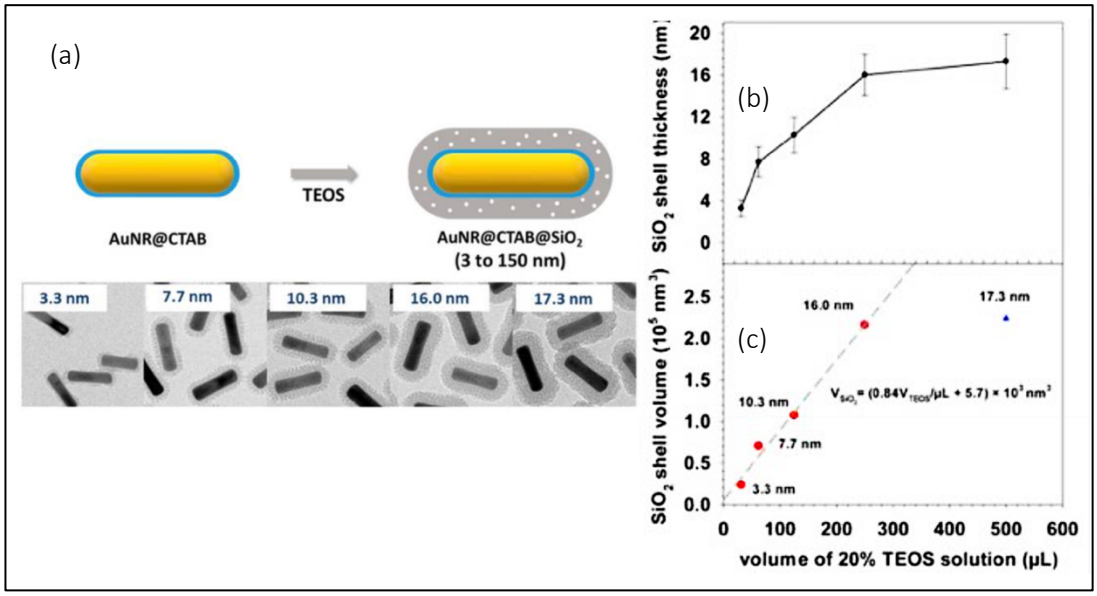

Figure 1.7. The dependence of silica coating thickness on the amount of TEOS added to the growth solution.

(a) TEM images show the average thickness of the SiO_2 shell upon adding different amount of TEOS. (b) Average thickness of SiO_2 shell vs. volume of added TEOS. (c) Average volume of SiO_2 shell vs. volume of added TEOS. The red dots indicate the conversion of TEOS added to complete SiO_2 shell, (blue triangle indicate incomplete conversion of TEOS) the bar scale displays to 50 nm. (Adapted from Ref [68]).

Despite all the previously mentioned advantages of using silica functionalised nanoparticles in biomedical applications; the charge-stabilized of the inorganic silica surfaces show a serious limitation on their biocompatibility due to the presence of the Coulomb repulsion between hydroxyl groups [83]. It has been reported that nanoparticles which are coated with organic molecules such as phospholipid-based micelles or liposomes are significantly biocompatible comparing to the inorganic molecules [84].

1.4.2. Phospholipid-Functionalized Silica Coated- Gold Nanorods

Phospholipid bilayer is the base of structure of the cells membrane. A typical bilayers structure consists of one or two fatty acid chains which form the hydrophobic tail and a hydrophilic head group [85], as illustrated in Figure 1.8, [86]. In the buffer solution, the fatty acyl chains will be packed together away from water due to the hydrophobic action, whereas the hydrophilic head groups will naturally expose themselves to the environment [87].

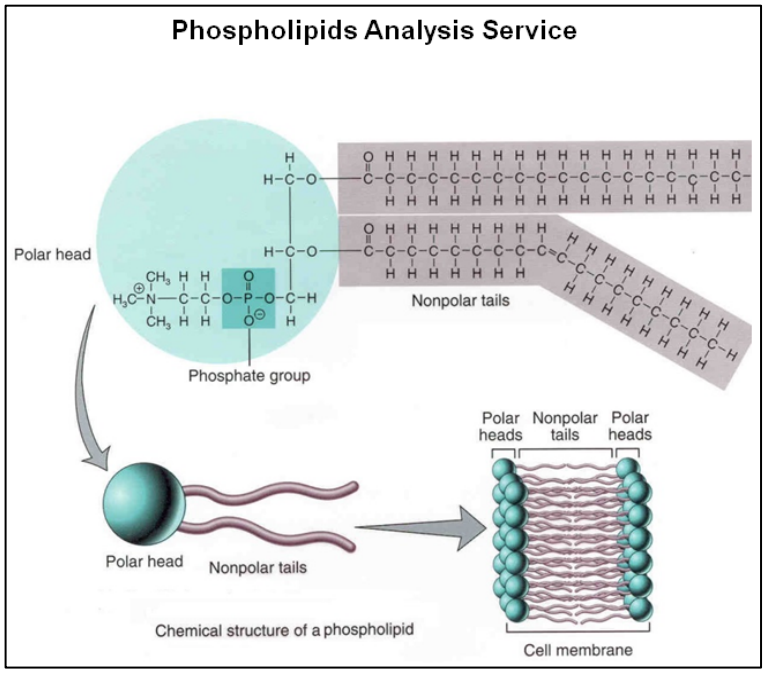

Figure 1.8. Phospholipid lipid structure and arrangement in cell membranes. (Adapted from Ref [86]).

The liposome vesicle size ranges between 30 nm and many micrometres [88]. It has an external lipophilic lipid bilayer and an inner hydrophilic core. When a liposome comes into interaction with a hydrophilic surface like SiO_2, the vesicular shape can convert into a planar bilayer that mimics a membrane, with releasing the water molecules that were enclosed in the inner hydrophilic core [89, 90]. The schematic illustration in Figure 1.9. [90] shows the liposome vesicle rupture and spread to form supported lipid bilayer to cover the SiO_2 surface.

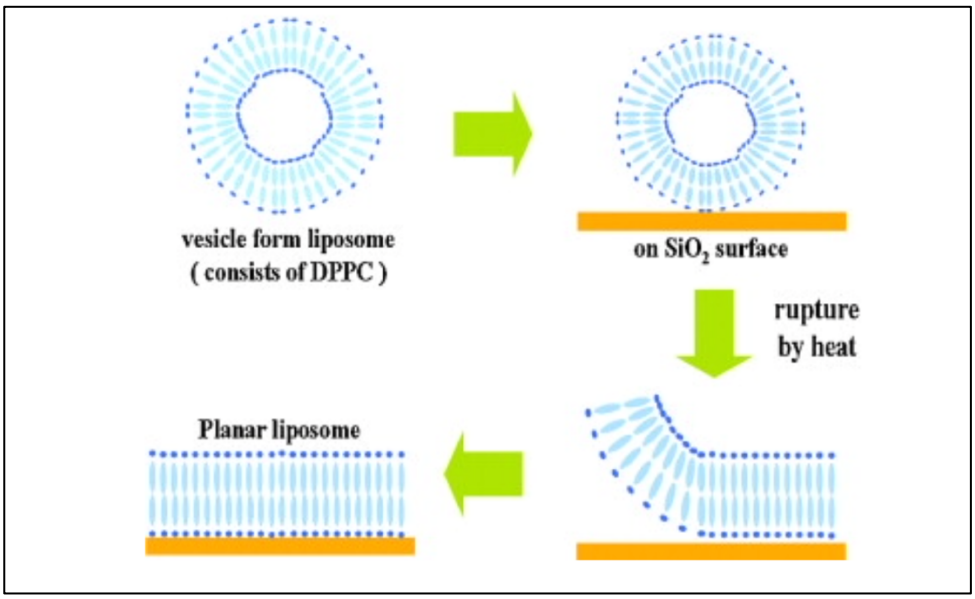

Figure 1.9 Schematic illustration of the liposome vesicle interaction with a hydrophilic surface SiO_2.

The liposome vesicle rupture and spread to form supported lipid bilayer to cover the SiO_2 surface. (Adapted from Ref [90]).

The electrostatic force is the fundamental factor influencing the interaction between the negatively charged silica nanoparticles and the positively charged lipid head groups of DPPC lipids [91] as shown in the schematic illustration in Figure 1.10. [92]. It has been reported that unsaturated lipids may impact the colloidal stability of lipids coated mesoporous silica coated nanoparticles LC-MSNs over time [93]. Therefore, the saturated lipids become an essential component for the lipids bilayer structure for coating NPs due to its saturated acyl chain. In addition, a PEGylated DSPE is preferred to be employed in the lipids bilayer formation to improve biocompatibility by increasing their time circulation and minimize protein adsorption to the surface of the LC-MSN [93-96].

Phospholipid bilayers have been fully investigated to induce AuNR interactions and increase their affinity with cells due to their biocompatible layers [97, 98]. The hydrophilic silica surfaces have been coated with PEGylated phospholipids that was physically adsorbed rather than covalently bonded [99]. It has been reported that the cells uptake of NPs after coating with lipids is highly higher than the uncoated ones [100]. Researchers have studied using lipids coated-silica NPs for drug and protein delivery applications due their high biocompatibility and efficiency for tissue-specific targeting [93, 94, 101, 102].

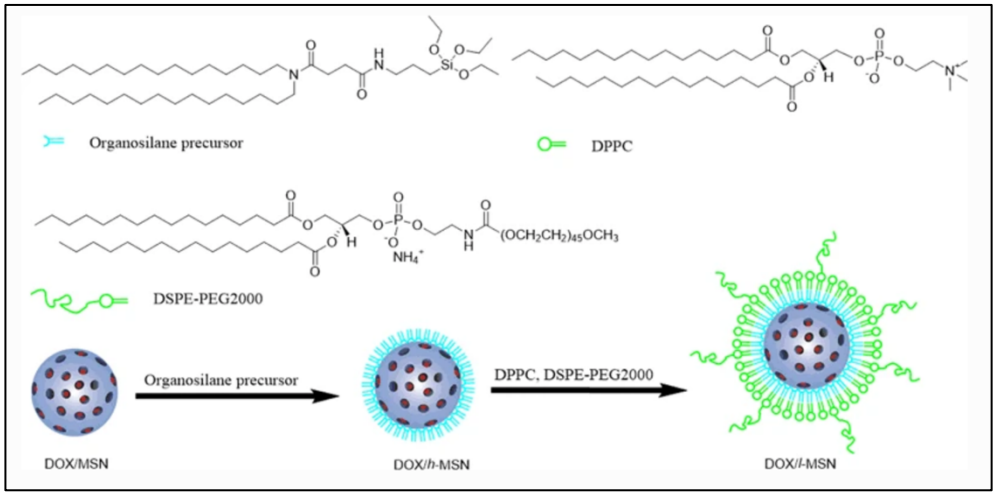

Figure 1.10. Scheme illustration for layer-by-layer construction of lipid bilayer on mesoporous silica nanoparticles (l-MSNs).

(Adapted from Ref [92]).

1.5. Optical Properties of Gold Nanorods (AuNRs)

1.5.1. Localized Surface Plasmon Resonance (LSPR)

Surface Plasmon Resonance (SPR) is a phenomenon that occurs when the incident light possess oscillating electric field that matches the electrons' collective oscillation of conduction band of the metal surface [103, 104]. These charge density oscillations that are known as localized surface plasmons (LSPs) [105, 106], (See Figure 1.11, [68]).

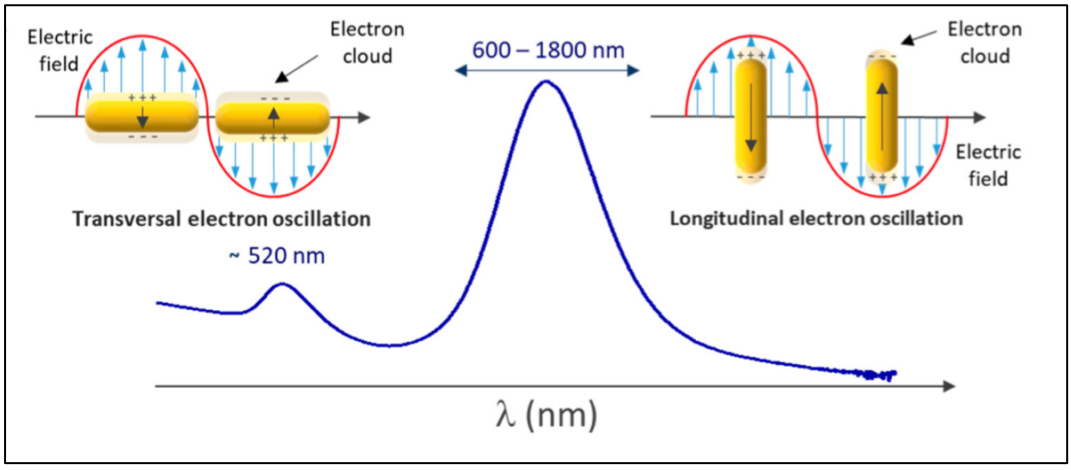

Figure 1.11 Schematic representation of electrons oscillation and the resulted surface plasmon resonance bands.

Showing two SP bands of AuNR, Transverse Surface Plasmon Resonance (TSPR) band and Longitudinal Surface Plasmon Resonance band (LSPR) band at ~ 520 and 600-1800 nm, respectively. (Adapted from Ref [68]).

When the free electrons on the metal surface of NPs interact with electric field of incident light, this induces the charge separation of free electrons from the ionic metal core [107]. Consequently, the unbound electrons are driven to move in the opposite direction by the Coulomb repulsion, which acts as a restoring force causing the collective oscillation of electrons [107]. This is what causes the particles to strongly absorb and scatter light [108].

The SP absorption bands' intensity and absorption maxima are indicative of the material composition such as gold, silver, or platinum [109]. Furthermore, they are sensitive to parameters such as the size, structure, and refractive index of surrounding medium [109]. The LSPR wavelength of these NPs can be easily tuned across the visible, near-infrared, and infrared spectrum by adjusting these parameters [110, 111]. Among all different material NPs, gold nanorods (AuNRs) show unique optical characteristics that rely on their anisotropic shape. Especially, they have two separate plasmon bands, one linked to the longitudinal electron oscillations called Longitudinal Surface Plasmon Resonance band (LSPR) and the other is linked to the transverse electron oscillations called Transverse Surface Plasmon Resonance band (TSPR) as shown in Figure 1.11. The transverse mode locates at about 520-525 nm. While for the tunable longitudinal mode locates above 600 nm and dependant on the aspect ratio of the AuNRs as shown in Figure 1.12a, [110]. The longer the ARs of AuNRs, the more redshifts of LSPR peak will be observed in UV-vis-NIR absorption spectra. Moreover, the solution colour can be used as an indicator for AR of the synthesised AuNRs, it has been noted that the aqueous solutions of AuNRs of various aspect ratios will display a range of different colours as presented in Figure 1.12b. Typically, NPs scatter and absorb particular visible light wavelengths, giving them a particular colour [112]. Therefore, these properties make AuNRs are ideal for biological applications such as sensing [113], imaging [114], and therapy [115].

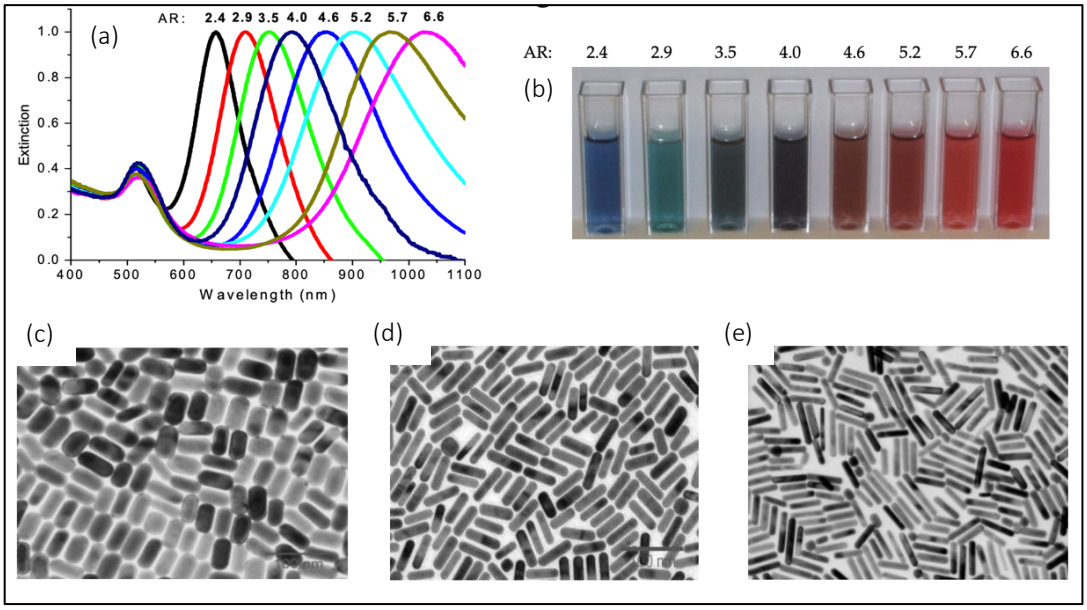

Figure 1.12 Gold nanorods characterizations of different aspect ratio.

(a) UV-vis-NIR absorption spectra of AuNRs showing the linear correlation between the longitudinal LSPR peaks (redshift) and the AR of AuNRs. (b) The AuNRs aqueous solutions of various aspect ratios display a range of different colours. (c-e) TEM images of AuNRs of different AR of 2.9 , 4.0, 4.6, respectively. (Adapted from Ref [110]).

The following formula is Mie-Gans theory which can be used to characterize how metallic AuNRs behave optically [116]. The extinction cross-section C_{ext} for AuNR can be determined from the following equation :

$$C_{\text{ext}} = \frac{2\,\pi\, VN\, \varepsilon_m^{3/2}}{3\lambda} \sum_j \frac{(1/p_j^{\,2})\varepsilon_i}{\left(\varepsilon_r + \left(\frac{1-p_j}{p_j}\right)\varepsilon_m\right)^2 + \varepsilon_i^2} \qquad (4)$$

Where v is the particle's volume, N represents the number of spheres per unit volume, ε_m is the dielectric constant of the surroundings, ε_r is real part and ε_i is imaginary part of the NPs' dielectric functions. The elongated particles' depolarization factor can be defined as follows:

$$p_{length} = \frac{1+e^2}{e^2}\left[\frac{1}{2e}\ln\left(\frac{1+e}{1-e}\right) - 1\right] \qquad (5)$$

$$p_{width} = \frac{1-p_{length}}{2} \qquad (6)$$

Where, *e* is defined as the ellipticity, which is determined by:

$$e^2 = 1 - \left(\frac{length}{width}\right)^{-2} \qquad (7)$$

For the longitudinal plasmon resonance, the condition is $\varepsilon_r = -((1 - Pj)/Pj)\varepsilon_m$, where Pj = P_{length}. Substituting Pj = P_{width} give the condition for transverse plasmon resonance. Even a tiny change in the aspect ratio of the nanorod will cause Eq. (4) to dramatically change for any small change in the nanorod's aspect ratio. Furthermore, the LSPR wavelength will shift as a result of modifications to the local environment surrounding the nanoparticles. The LSPR wavelength shift Δλ obtained as a result to the change in RI can be describe by the relationship shown below [117, 118]

$$\Delta\lambda = m\,\Delta n\left[1 - \exp\left(\frac{-2d}{l_d}\right)\right] \qquad (8)$$

Where Δn is the refractive index change (in RIU), m is the refractive index response of the bulk of the nanoparticles (in nm/RIU), d is the thickness of the adsorbed layer (in nm) and l_d is the average electromagnetic field decay length (in nm).

For reference, Eq. 4 can be approximated for spherical particles that are smaller than 20 nm to,

$$C_{ext} = \frac{24\pi^2 R^3 \varepsilon_m^{3/2}}{\lambda}\frac{\varepsilon_i}{(\varepsilon_r + 2\varepsilon_m)^2 + \varepsilon_i^2} \qquad (9),$$

where R is the radius of the NP. Under this condition the resonance will occur when $\varepsilon_r = -2\varepsilon_m$.

1.5.2 Localized Surface Plasmon Resonance (LSPR)

To generate heat for the thermal ablation of tumor tissues, photosensitizing agents are irradiated by pulsed laser irradiation at NIR [119]. However, there are some properties that the proposed photothermal agents should have such as large absorption cross sections, non-toxicity, and a tuneable surface for further functionalization [120]. Because the NPs are

delivered deep into the tissue, it is necessary to select a wavelength of radiation that will not be rapidly absorbed by the water and haemoglobin present there, as well as one with sufficient energy to reach the AuNRs [121]. By altering the physical dimensions of the AuNRs the absorption through the LSPR band, can be tuned to the NIR and therefore efficiently be absorbed the applied laser light [110]. The photothermal conversion efficiency (PCE), η, of NPs can be determined using the following expression [122]:

$$\eta = \frac{hS\,(Tmax - Tamb) - Qdis}{I\,(1-10^{-A})} \qquad (10)$$

Where h is the coefficient of heat transfer, s is the container's surface area, T_{max} and T_{amb} is the maximum equilibrium and the ambient temperature of the surrounding medium, respectively. The laser-induced heat input by the container is denoted by Q_{dis}. *I* and A are the laser power and the absorbance of the NPs, respectively [123]. Q_{dis} can be calculated by:

$$Q_{dis} = m\,C\,\Delta\,T/t \qquad (11)$$

Where, Q is the heat energy (Joules), m= the mass of the object/substance being heated (g), C = heat capacity of water (J g−1 K−1), ΔT = increased temperature (K), and t = laser exposure time (s).

Kim et al. has found that the AuNRs have high PCE of 50% or higher comparing to other AuNPs such as Au nanoshells, and Au nanocages [124], relying on the AR of AuNRs and wavelength of the laser irradiation [125, 126].

1.5.2.1 Heat Generation by Gold Nanorods AuNRs

In the 1950s, colloidal gold NPs has been recognized to be highly compatible with live animals after *in vivo* studies [127]. However, the idea of employing such nanoparticles as photothermal agents is relatively new. The principle of photothermal treatment is consistently photoexcite the conduction electrons in nanoparticles to trigger surface plasmon vibrations. Following the formation of surface plasmons, nonradiative relaxation takes place as a

consequence of electron-phonon (e-ph) and phonon-phonon (e-e) coupling, thereby producing localised heat that can be released into the surroundings [128-130], as illustrated in Figure 1.13.[131]. Depending on the level of excitation, the time constants for electron-electron and conduction electrons have been calculated to be between 0.3 and 0.4 and 1.6 and 3.3 ps, respectively [132, 133]. Moreover, AuNPs ranging in size from 9 to 48 nm were found to have approximately comparable electron-phonon coupling time constants [134]. However, when particles are smaller than 10 nm, the e-ph coupling time drops from 1 ps to 0.6 ps [135]. The generated heat has been extensively studied due to their promising effect as plasmonic photothermal agents for cancer treatment. [136-138].

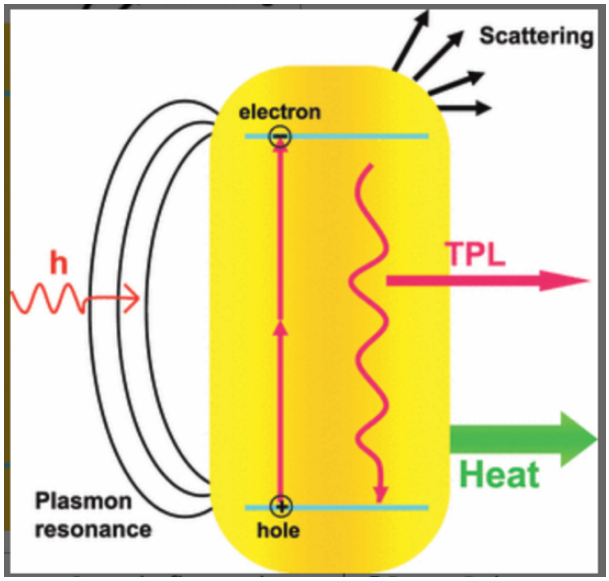

Figure 1.13 Schematic illustration of Gold nanorod photophysical phenomena.

A longitudinal plasmon resonance mode is excited by near-infrared radiation, usually causing absorption but also causing some resonant light scattering. Two-photon absorption causes an electronic transition from the d- band to the sp- band, producing an electron-hole pair; consequently, the separated are recombined producing heat and two-photon luminescence (TPL) emission. (Adapted from Ref [131]).

In 2003, Lin and co-workers firstly introduced using antibody-conjugated spherical gold nanoparticles as photothermal contrast agents when irradiated by nanosecond pulsed visible laser [139]. Near-infrared (NIR) radiation has been found to be capable of high penetration up to 10 cm in soft tissues (NIR spectral range is from 650–900 nm) [140]. With this in mind, the AuNRs have strong and tunable LSPR band that can be shifted to NIR transmission window by changing their ARs [141]. The absorption cross section and the absorption efficiency, which control the heat transduction, are the most crucial plasmonic features to consider when

evaluating the various nanoparticle shapes in terms of their applicability in PPTT [142]. Therefore, with regard to NIR photothermal heat conversion, AuNRs display the most optimal NIR absorption cross section [23] and exhibit high efficiency [24]. According to research on different AuNR sizes, it has been found that as the particle size of AuNRs reduces, the absorbance and scattering ratio rises (AR= absorption/scattering), enabling better photothermal heat conversion and potentially improving PPTT efficiency. Additionally, the electric field at the surface of the AuNR has been reported as a further plasmonic characteristic related to photothermal heat conversion. The strength of this field tends to increase with absorbance rather than scattering or extinction [143]. Smaller AuNRs would therefore produce a stronger field, which would then lead to increased photothermal heat conversion and improved PPTT efficiency. The energy of the incident light is absorbed rapidly in few ps, which faster than heat diffusion processes that release as heat in hundreds of ps to the surrounding media [144]. High photon density can cause the AuNR to absorb photons repeatedly at a pace that exceeds the rate at which heat diffuses, which can cause superheating and an extremely fast jump in local temperature [145].

1.5.2.2 Temperature Distribution of PPTT for in Vitro and in Vivo Studies

The concentration of NPs, the density of the laser beam, and the duration of the PPTT exposure all affect the temperature distribution. Therefore, regulation and distribution of temperature in malignant tissues are crucial for the successful treatment of cancer [110]. To optimize the PPTT, investigations of the temperature distribution of photothermal nanoparticles under laser irradiation have been conducted in a variety of theoretical and simulated studies [110].

Based on a computational model, Huang et al. determined the laser intensity and nanoparticle concentration needed to create a certain temperature that would result in cell apoptosis [146]. The heat generation from laser-induced heating of the nanoparticles and heat loss by conduction into the environment was considered in their model. According to their estimations, they found that gold nanoparticles with an optical density (OD) of 0.159 and a laser power of 150 mW would generate a temperature increase of 73–77 °C [110]. In addition, Von Maltzahn et al. [24] employed finite element modelling to estimate the temperature distribution of PEGylated AuNRs in tumor cells along with the temperature on the tumour

surface and at different depths within the tumour. The results confirmed experimental findings by demonstrating a rise in tumour surface temperature to 70 °C. Additionally, they estimated that 5 minutes after laser irradiation of 2 W/cm^2 the overall tumour region would be heated to over 60 °C.

1.5.2.3 Thermal Stability of AuNRs@SiO_2

AuNRs structure could expose to thermal reshaping and transfer into spheres during pulsed femtosecond (fs) and nanosecond (ns) lasers irradiation [147, 148]. The stability of AuNRs exposed to femto- to nanosecond laser pulses has been the subject of theoretical studies on the thermal stability of AuNRs [149-151], as well as several other works [152-156]. The findings are crucial for the AuNRs' future applications in which they are exposed to high temperatures without losing their optical capabilities. By using UV-Vis absorption spectroscopy and TEM technology, the thermal stability of the AuNRs in an aqueous solution was studied. At high temperatures, it was observed that the AuNRs' LSPR absorption band gradually shifted to a lower wavelengths, indicating a reduction in aspect ratio [157]. The increase in diameter and decrease in length, which were connected to Ostwald ripening in the solution, could be utilized to explain the drop in aspect ratio, subsequently has an impact on their optical characteristics [158-160]. Short AuNRs were observed by Murphy and co-workers and El-Sayed and co-workers to convert into spheres after only 15 min of solution boiling [161, 162]. It was observed that AuNRs would show instability even when they are heated at temperatures below the bulk melting point (1064 °C), even as low as 100 °C [152, 162]. The smaller AuNRs' tips would prefer to dissolve first due to their being more reactive than the larger AuNRs' bodies, and when this occurs at high temperatures, the resulting clusters would preferentially deposit on the larger AuNRs. Therefore, the average length would decrease, the average diameter would increase, resulting in a broad size distribution a result of this process [163]. The thermal reshaping can be prevented up to ~690 °C by coating the AuNR with silica shell, a titanium-oxide matrix [164], carbon [165], or other material. AuNRs@SiO_2 were found to be more stable under high-energy nanosecond laser irradiation, due to the silica shell efficiency to sustain its shape to prevent surface atoms from diffusing [165-168].

1.5.2.4 Heat Transfer Dynamics from Gold Nanorods to the Environment

It is well recognised that when examining the heat transfer on the relevant time scales, the thermal interface conductance, or the temperature change at the particle-environment interface, is crucial. When the AuNR is irradiated by ultrafast laser pulse, the photon energy is absorbed by the free electrons causing an increasing in its kinetic energy [169]. These extremely energetic electrons are attenuated through electron-electron scattering on the scale of 10–50 fs. Within these time scales, electrons and phonons do not interchange energy, and electron energy levels remain high [169]. The electron-phonon scattering causes the temperature of the particles (lattice) to start rising. Depending on the initial rise in electron temperature, a thermal equilibrium between the electrons and lattice is obtained in between 10 and 50 ps [169]. Therefore, the phonon-phonon coupling process starts to dissipate energy between the particle and its surrounding medium as the particle temperature rises [169]. Depending upon the particle diameter and laser pulse intensity, a thermal equilibrium is reached within 100 ps to 1 ns, which allows the temperature increase at the particle-aqueous solution interface [169].

However, to make AuNRs thermally effective for photothermal applications, understanding the heat transfer dynamics of these AuNRs with surrounding environment will assist to improve their performance. Heat diffusion from the local solvent to the bulk as well as the quantity and rate of heat transfer from the NPs to the nearby solvent are considered as a significant factors which play a role in the localization of heat and the temperature increase of the region around the NPs [170]. In the following section, the discussion will be restricted to the heat transfer dynamics between AuNR to the surrounding environment such as water, CTAB, and SiO_2.

Understanding the thermal processes of nanorod heating in respect to potential PTT application can be achieved by modelling laser heating of AuNR in water media. This has been made by Ekici, O., et al.[171], they created a model to simulate the heating process of a single gold nanorod of length and diameter of 48 nm, 14 nm, respectively. The simulated AuNR is surrounded by water and exposed to laser pulses with a duration of 250 fs of peak plasmonic frequency of 760 nm. A strong enhancement of the electromagnetic fields in the near-field of the AuNR was observed after laser irradiation. Figure 1.14a [171], shows the temperature

distribution at 70 ps of AuNR pulsed laser irradiation of 250 fs pulse and an average fluence of 4.70 J/m^2. At the middle of irradiated AuNR, the temperature of the water exceeds nearly 580 K at 70 ps. On the other hand, the temperature of AuNR decreases from its max of 1270 K at 30 ps following the laser pulse to 1079 K. As we move away from the interface, the temperature of the water decreases quickly to around 300 K. Studying the heat diffusion of AuNR to the surrounding medium at different times after laser exposure is necessary to assist in improvement their performance [171]. Therefore, Figure 1.14b demonstrates the temperature profiles as a function of distance r over three different time post the pulsed laser irradiation. About 50 ps following the laser pulse, the temperature at the interface significantly increases to about 1200 K.

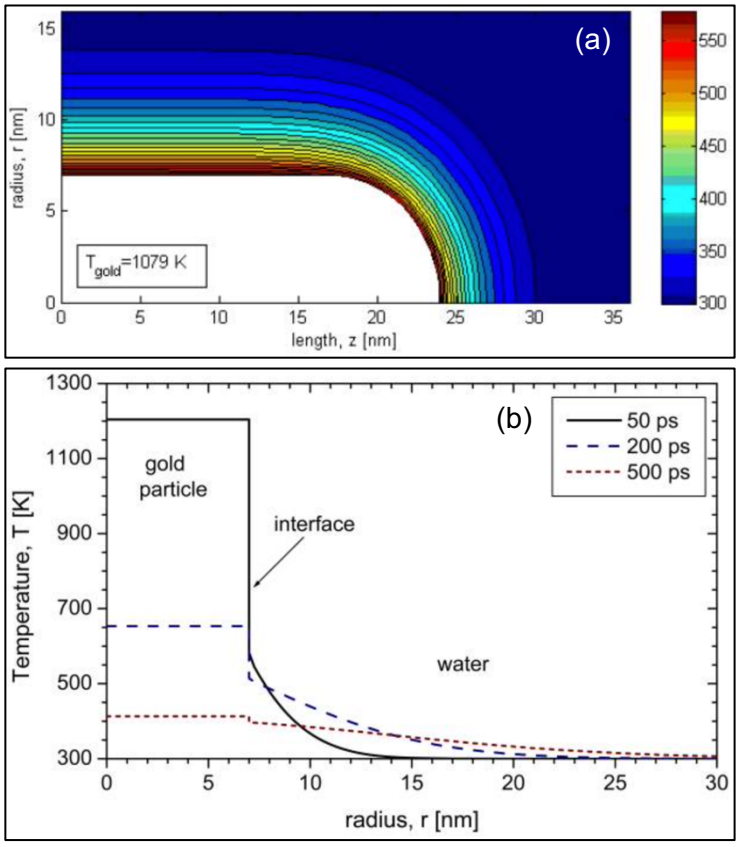

Figure 1.14 Heat distribution of a single AuNR.

(a) Heat distribution of a single AuNR of length 48 nm and diameter of 14 nm in water. The heat distribution was simulated at 70 ps after irradiation by a laser pulse of 250 fs with an average fluence of 4.70 J/m^2. (b) Temperature profiles at different times (50, 200, and 500 ps) after pulse laser irradiation as a function of distance in the mid-length of the single AuNR, the z=0 plane. (Adapted from Ref [171]).

With increasing the time to 500 ps after the laser pulse, the temperature dramatically decreases to around 400 K. These investigations are important to determine what the duration time of laser pulse and the pulse repetition needed for effective PTT [171].

The following equations provide description of the transient temperature response of the conduction electrons in the AuNR when absorb the laser pulse energy, when the AuNR is in a water medium [172]:

$$Ce\ \frac{dTe}{dt} = g\ (Tl - Te) + \frac{E\ abs}{Vp.t\ pluse} \qquad (12)$$

$$Cl\ \frac{dTl}{dt} = g\ (Te - Tl) - \frac{Qw}{Vp} \quad if \quad (Tl < Tm) \qquad (13)$$

Where the heat capacities of electrons and the bulk gold lattice are donated by C_e and C_l are, respectively. The particle's electron and lattice temperatures are T_e and T_l, respectively. The amount of laser energy that the particle has absorbed is E_{abs}. The particle's volume is denoted by V_p *and* t_{pulse} is the laser pulse width. g is the coupling factor used to calculate the rate at which heat is transferred from electrons to the lattice and Q_w is the rate at which a particle loses heat to its environment.

According to the following expression, the amount of laser energy a particle may absorb relies on the laser fluence F_{pulse} and the nanorod's absorption cross-sectional area A_{abs}:

$$E_{abs} = A_{abs} \cdot F_{pulse}. \qquad (14)$$

When calculating the rate of heat loss from a particle to its environment in Eq. (12), the conductance at the interface between the particle and the surrounding has to be considered:

$$Q_w = A_{surface} \cdot G \cdot (Tl - T_{w,s}) \qquad (15)$$

Where $A_{surface}$ is the particle's surface area, G is the thermal conductance at the interface between the particle and the fluid, and $T_{w,s}$ is the temperature of the water at the surface of the particle.

1.5.2.4.1 Heat Transfer Dynamics of AuNRs in Organic CTAB and Inorganic SiO_2

According to El-Sayed and co-workers, the environment of AuNPs affects how quickly heat dissipates [173, 174]. In the solvents with higher thermal conductivities, the AuNPs will provide faster heat dissipation times [174]. The organic bilayer CTAB is commonly utilized to manage the size and shape of plasmonic AuNRs during fabrication and to preserve their colloidal stability from aggregation after synthesis (as discussed earlier in section 1.3.2). However, it is important to investigate how transition occurs through such bilayers because they might act as thermal insulators. According to a publication, the CTAB bilayer of CTAB-capped-AuNRs has a 350 ps heat transmission time constant [169]. With increasing laser excitation power, this time constant increases and finally produces bubbles as a result of local solvent superheating [169]. The speed of heat diffusion into the bulk water as well as heat transfer through the surfactant/water interfaces have a significant impact on the heat transfer rate [130]. Additionally, it has been reported that the surface area-to-volume ratio has a significant impact on heat transfer rate, it is claimed that particles with a larger surface - to - volume ratio will transfer heat more quickly [169]. Moreover, longer heat transfer durations is expected from the bilayer of long carbon chain CTAB ligands of CTAB-capped-AuNRs compared to the short citrate ligands of citrate capped-AuNRs [175]. Because of the presence of the hydrophobic nature of CTAB, it has been shown a relatively low thermal interfacial conductance than hydrophilic ones, the fully fabricated bilayer has a lower thermal conductance [176]. However, other surface functionalization could impact the thermal interfacial conductance differently between AuNR and the surrounding environment [177]. It has been reported that PEG behave considerably better at heat dissipation than the CTAB surfactant, due to the covalent bonds between Au and PEG and the interactions of van der Waals between the penetrated water and AuNR and, which do not exist at the CTAB-capped-AuNR [177]. According to a publication, the CTAB bilayer's thermal conductivity was found to be a concentration dependant, it was found to be stabilized at 0.24 W m^{-1} K^{-1} for materials with CTAB concentrations under its CMC and drops to 0.18 W m^{-1} K^{-1} for samples with CTAB concentrations beyond 1 mM [178].

Different materials involved in the system of AuNRs such as (water, CTAB, silica., etc) provide different thermal resistance and impact the heat transfer dynamics of AuNRs [169]. SiO_2 is used to coat the CTAB bilayer on AuNRs to improve their biocompatibility and maintaining the optical characteristics [68]. However, it has been observed that this SiO_2 shell changes the dynamics of heat transfer in AuNRs [169]. The silica coated AuNR was found to be slower heat transfer than those of the surfactant-capped AuNRs, this attributes to the silica effect on the heat transfer dynamics [169]. Note that dried mesoporous silica has a thermal conductivity of 0.2–0.3 W/mK [179], which is equivalent to the CTAB bilayer's thermal conductivity of 0.2 W/mK in CTAB-capped-AuNRs but a little less than that of water's thermal conductivity of 0.6 W/mK [178]. Taking all of this into account, the water-filled mesoporous silica's will affect total thermal conductivity with a range from 0.3 to 0.6 W/mK [169].

The silica shell thickness has a crucial impact on the rate of heat dissipation of AuNRs [178]. As shown in Table 1.1 [180], the fused thin SiO_2 shell (thickness ~ 5 nm, in water) was found to dissipate heat faster than the fused thicker shell, it has an average heat dissipation times ~ 55 ±3 ps. While the thicker SiO_2 shell (thickness ~ 10 nm, in water) dissipate heat in ~ 83 ±3 ps [180]. This indicates that the silica shell limits the amount of water surrounding the GNR, results in reducing the heat transfer efficiency.

Table 1.1 The average heat dissipation times for three different samples, bare Au , Au@SiO_2 (shell thickness ~5 nm) , and Au@SiO_2 (shell thickness ~10 nm) , All samples dispersed in water. The data was obtained from transient bleach data. (Adapted from Ref (182)).

Sample	Shell thickness	Solvent	τ (ps)
Au	–	Water	90±3
Au–SiO_2	~5 nm	Water	55±3
Au–SiO_2[a]	10 nm	Water	83±3

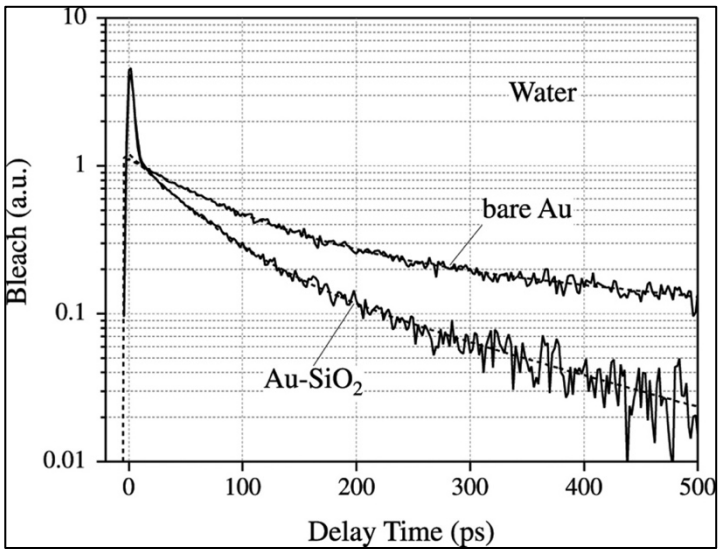

Figure 1.15 Transient bleach data obtained from time-resolved spectroscopy. Shows the heat dissipation times of bare Au, Au@SiO_2, both are dispersed in water. (Adapted from Ref (182)).

As shown in Figure 1.15. the transient bleach data for AuNPs in water, for both uncoated and coated with a SiO_2 shell (5 nm in thickness) illustrates that the Au-SiO_2 dissipate heat more quickly than the citrate stabilised NPs [180].

1.5.2.5 Thermal Reshaping of AuNRs

Through electron-phonon relaxation processes, the plasmon's energy is transferred into the nanocrystal lattice, causing an increase in the temperature of the nanorods and triggering reshaping [181]. It has been demonstrated that the AuNRs reshaping occurs at much lower temperatures than bulk melting point of the metal [152, 154, 162] and significantly dependent on AR [182]. This is because of the high surface-to-volume ratio, which raises the particles' surface free energy [183]. Gold nanoparticles have a melting point that is lower than that of bulk gold (i.e. < 1064 °C) [184]. Studies have reported that the thermal stability of AuNRs drastically degrades with increasing aspect ratio and that, for larger aspect ratios, reshaping can take place significantly below the bulk melting temperature [182]. The ionisation of the surface, charge repulsion, and change of NRs into spheres which the most thermodynamically stable shape, are all nonlinear phenomena caused by the high power femtosecond laser [185]. In addition, the nanosecond laser also induces nonlinear processes, the sample is mostly affected by cumulative thermal effects, which cause the NPs to melt and then fragment [185].

However, the duration of the processes that follow absorption determines how differently NRs behave when exposed to fs and ns laser pulses [186].

Nanoparticle reshaping could happen within 30 ps if the lattice's temperature is increased to levels beyond its melting point [147]. However, the stored energy is then released into the surrounding environment (solvent) over a time scale of the order of 100 ps by phonon-phonon interactions [187]. In comparison to a fs pulse with an equivalent pulse energy, a ns pulse has a much lower total particle temperature because its length exceeds the cooling period [185]. The accumulated energy on AuNR by a laser pulse was reported to be primarily determined by AuNR aspect ratio that plays a role in determining the absorption cross section at the laser wavelength, and the alignment of the nanorod with relative to the laser polarisation at a LSPR matching the laser wavelength [181]. Due to the fact that the nanorods are randomly oriented in solution during irradiation and various aspect ratios of AuNRs, it is challenging to estimate the precise amount of energy absorbed during a single shot [181]. González-Rubio, Guillermo, et al. have performed molecular dynamics (MD) simulations on AuNRs at various energies, up to about 0.5 eV/atom with aspect ratios of 3.25, 3.53, and 3.87, to better explain their thermal reshaping [181]. When AuNR in water medium is irradiated by a femto-second pulsed laser, its temperature is raised to a certain level in a remarkably brief period of time below 10 ps (up to 1900 K for 0.5 eV/atom), with t ~ 60 ps of time constant for heat transfer from Au NRs to surrounding medium [188]. Whereas, CTAB molecules behave as a thermal barrier for water at concentrations around its CMC, significantly slowed down heat dissipation (t ~ 350 ps)[169]. The electron-phonon and phonon-phonon coupling occur at the nanorod surface are related to the heating and cooling time scales, respectively, which enable the temperature increase almost independently of its thermal surroundings. However, the surroundings had a significant impact on how much heat was dissipated into the surrounding medium [169]. Therefore, it can be said that the overall energy deposited on the nanoparticle and the rate at which heat is dissipated into water are two linked characteristics that affect how quickly nanorods are modified.

Figure. 1.16c, [181]. shows the impact of the total energy deposited during the deformation process. Low energies (below 0.3 eV/atom) resulted in relatively little deformation [181]. However, even one pulse at higher energy resulted in significant deformation, causing the rod-like morphology to be lost and transformed into spheres[181], this when the energies

are high enough (above 0.45 eV/atom), considering that the melting point of gold might be exceeded for energies above 0.3 eV/atom [181]. AuNPs shapes "ϕ-shaped" was identified during the photo-annealing process of converting rods into spheres, as shown in (Figure 1.15d-e). This novel ϕ-shaped AuNRs structure were observed by Link et al. [147, 148] and Chang et al. [154] as the first stage of a AuNR shape reshaping during fs and ns pulses.

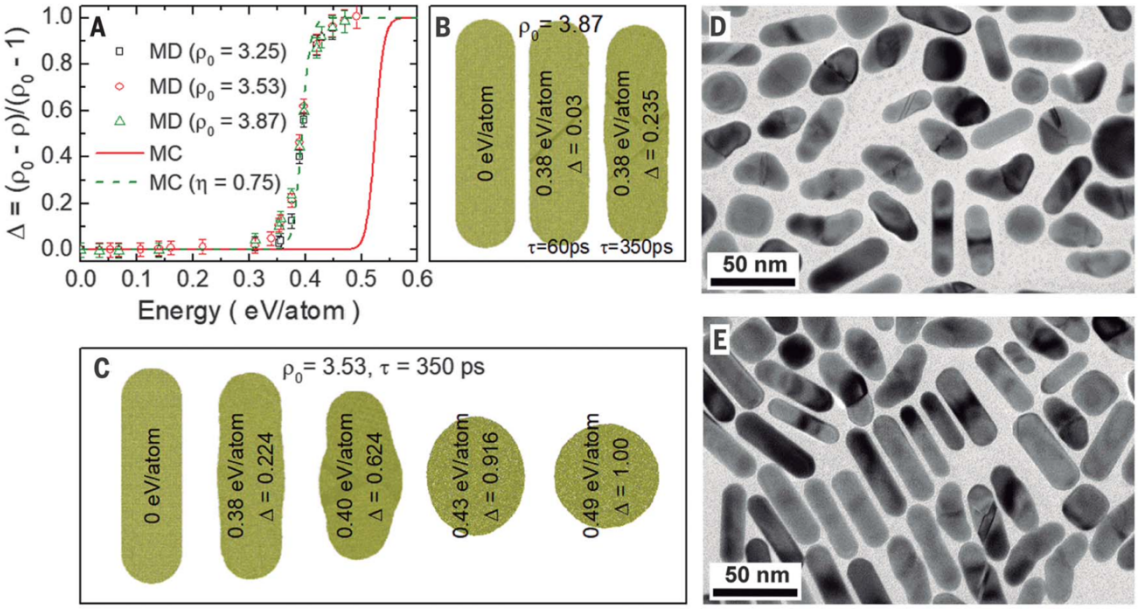

Figure 1.16 MD simulations describe the reshaping of AuNR after pulsed laser irradiation.
(A) Normalized changes of the AR as a product of the energy of laser pulse irradiation (red line refers to MC simulations data) and the energy that is transferred to the lattice (symbols, obtained from MD simulations). To normalize the aspect ratio variation, $\Delta = (\rho_0 - \rho)/(\rho_0 - 1)$, was independent of ρ_0. (B) The effect of surrounding medium on heat dissipation and AuNR shape and aspect ratio (AR of control AuNR ~3.87), (heat transfer time water and CTAB at the CMC t ~ 60 and t ~ 350), respectively. (C) The effect of amount of energy absorbed on aspect ratio change, (AR of control AuNR ~3.53 and the heat transfer time t ~ 350. (D) TEM image of AuNRs@CTAB at the CMC after irradiation femto-second laser pulse of 5.1 J/m^2 (up to 0.6 eV/atom in the electronic system) for 1 hour. (E) TEM image of AuNRs@CTAB at 5 mM after irradiation with 3.2 J/m^2 for 1 h (up to 0.38 eV/atom in the electronic system). (Adapted from Ref [181]).

The temperature of the NPs Tl increases until it reaches the temperature at which gold melts, after that it remains stable throughout the phase-change [171]. Once the melting temperature has been reached, any more energy would assist in the phase-change [171]. This following expression explain this :

$$\Delta E = \int_{\Delta t} (Vp \cdot g(Te - Tl) - Q.w) \cdot dt \quad if \quad (Tl = Tm) \qquad (16)$$

Where Vp is Volume of the particle (nm3), g is the electron-lattice coupling factor (W/m^{3}K), T_e is the electron temperature and Tl is the lattice temperatures of the particle. Q_w is the rate of heat loss from particle to its surroundings, and Tm is the melting temperature (K).

The heat of fusion of gold H_{fus} determines the amount of energy needed for full melting once the particle exceeds the melting point, the ΔH_{fus} can be determined as illustrated in the following expression:

$$E_{phase-change} = \rho_{gold} \cdot V_p \cdot \Delta H_{fus}. \qquad (17)$$

Where ρ_{gold} is density (kg/m^3), V_p is Volume (nm^3), and ΔH_{fus}. Is enthalpy of fusion (kJ/kg). When the two values from the above equations (15 and 16) are equals ($\Delta E = E_{phase-change}$), the particle has completely melted, and at this time, the temperature of the particle begins to increase once more above its melting point [171].

1.6. AuNRs efficiency in NIR-Biological Windows (BW)

The fluorescent probes which are clinically used are based on organic molecules. To excite these organic probes, high energy light (ultraviolet (UV) or blue) is typically used to generate the emission of visible (VIS) light [189]. However, the use of UV light in such imaging technique raises serious issues such as the reduction in the image contrast due to the background interference autofluorescence of the biological tissue under UV excitation, photobleaching of the organic molecules, and phototoxicity of UV light which can cause reverse damage to cells [189, 190]. Additionally, UV and VIS light cannot be used to image deep tissues because of their restricted ability to penetrate and then spread out of living samples. Moreover, the in-tissue absorption is significantly influenced by liquid water which has many vibrational overtone bands primarily focused at 970, 1450, and 1800 nm (see Figure 1.17b) [191]. To achieve maximum and deeper radiation penetration through tissue, minimum autofluorescence, and very low water in these NIR bands is needed [192-195]. Thus, the laser wavelength used in photothermal treatment is preferred to be in the NIR region.

The first biological window (BW) which is from 650 to 950 nm, and the second BW which is from 1000 to 1300 nm, are the two areas where NIR radiation is compatible with tissue [196], as shown in (Figure 1.17a). The characteristics of AuNPs can be adjusted to operate at the second biological window [189].

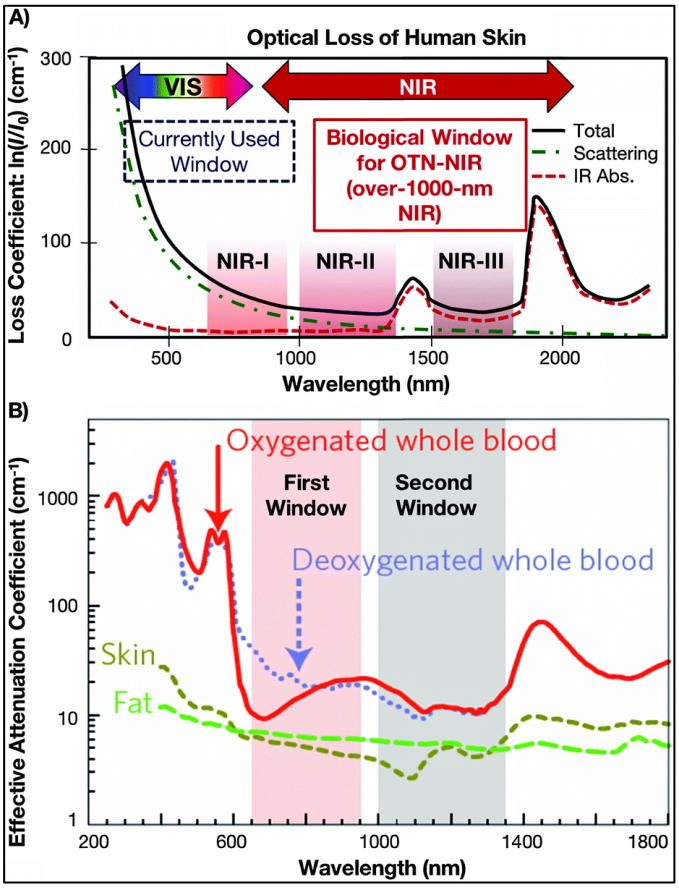

Figure 1.17 Human skin's absorption spectrum of the effective attenuation coefficient (on a log scale) versus wavelength.

(A) displaying the first, second, and third BWs (NIR-I, NIR-II, and NIR-III). (B) A closer look at the first two optical windows found in some biological fluids and tissues., demonstrating the quantitative relevance of variety of biological components (oxygenated blood, deoxygenated blood, skin, and fatty tissue) when attempting to obtain deep sub-skin imaging. (Adapted from Ref (193)).

AuNRs, nanoshells, and nanocages are plasmonic nanoparticles have promising efficiency in localised heating when they are exposed to radiation at the surface plasmon resonance (SPR) frequency that causes the conversion of light into heat energy [197, 198]. Gold-based strongly absorbing nanoparticles have demonstrated significant promise for imaging of cells and tissues utilising methods like photoacoustic tomography and multiphoton plasmon resonance microscopy [199, 200]. When the NIR optical resonance of the nanoparticles within

the biological water window is used, this allows high tissue transmissivity for actual *in vivo* imaging and therapeutic applications [142].

The NIR region (700-1,300 nm) is favourable for gold nanoparticles to have a deeper penetration depth in tumour therapy and imaging due to the poor absorption of water and haemoglobin [201]. The optical resonance of the nanorods can be controlled over the near-infrared spectrum by adjusting their effective size or aspect ratio [142]. Therefore , when they are exposed to low-energy laser radiation, they show the largest optical cross-section and absorption efficiency over all other gold nanostructures, leading to favourable photothermal characteristics [50].

1.7. Plasmonic Photothermal Therapy (PPTT) of Gold nanorods AuNRs

1.7.1 Localized Surface Plasmon Resonance (LSPR)

Endocytosis is a technique that entails a cell swallowing nanoparticles through the engulfment of a part of the plasma membrane, followed by the production of vesicles containing the nanoparticles within the cell [202, 203]. Researchers have reported that AuNPs typically localize intracellularly in the perinuclear region of endosomes and lysosomes [204-206]. Endocytosis is classified into the three categories, actin-dependent phagocytosis, micropinocytosis which is receptor-independent, and receptor-mediated endocytosis [203]. Radiation's ionisation action, which damages DNA and other biological components by reacting with water molecules, has the potential to kill tumour cells by directly destroying cellular DNA [207]. The toxicity of AuNRs must be considered prior to radiation application to cells. AuNRs' toxicity must be minimized through the removal or replacement of CTAB, this has been discussed earlier in Section.1.4. The AuNRs' ability to accumulate in tumour sites will rise significantly if they are coupled with targeted ligands like particular antibodies and peptides. This will boost the effectiveness of radiation therapy. The Nanoparticles' physical and biological characteristics, including as size, surface charge, hydrophobicity, protein corona, and ligand density, all affect how well they are taken up by cells [208]. It has been reported that the accumulation of AuNRs *in vivo* can cause massive long-term toxicity. Thus, preparing biocompatible AuNRs of the appropriate size need to be considered to prevent or minimise the potential accumulation of AuNRs following radiation therapy [209]. The effects

of AuNRs' surface modifications, size, and charge on cellular endocytosis, exocytosis, localization, and cellular toxicity have been the subject of several research recently [206, 210, 211]. They discovered that the aspect ratio significantly impacted each cell's intake of material [212]. Their long-term retention at a high dosage in target cells is crucial for achieving damaging effects from heat absorption. However, they should have little effect on healthy cells [213]. If photothermal therapies are used, the nonspecific uptake of nanorods may cause interference during site-directed imaging or may cause concurrent harm to healthy cells and tissues [57]. The cellular uptake of AuNRs is greatly influenced by their size and shape. Untargeted rod-shaped AuNRs are less successful at entering cells than untargeted gold nanospheres [208, 210]. It is claimed that sizes between 20 and 50 nm are ideal for cellular absorption [55, 214, 215]. However, the small AuNRs of higher surface area relative to mass were observed to exhibit high toxicity due the high interaction with healthy cells, small GNRs also had a higher surface area relative to mass. Therefore, it was found that short NRs modified with targeting ligands, phospholipids [216], and inorganic coating [217] displayed higher cellular uptake by cells more. Short AuNRs can be immediately taken up by cells without rotation, but long DNA-coated nanorods align before cellular uptake to the cell membrane approximately parallelly and subsequently rotate by around 90° to penetrate the cell [218], as illustrated in Figure 1.18. [218].

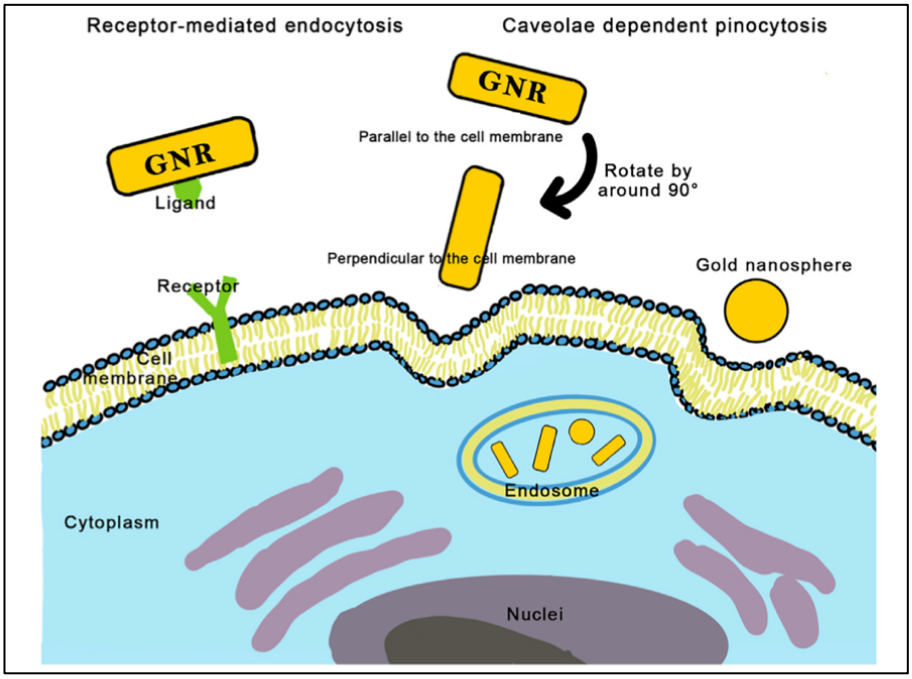

Figure 1.18 The cellular mechanisms uptake for AuNRs.

(i) caveolae-dependent pinocytosis. (ii) receptor-mediated endocytosis. Short AuNRs and small NPs could only be immediately engulfed by cells without any rotation, whereas long AuNRs must first align almost parallel to the cell membrane by 90 degrees to enter the cell. (Adapted from Ref [218]).

Additionally, it has been found that the surface charge of AuNRs has significant impact on the cellular uptake. The cationic AuNRs attach to the cell membrane and taken up more effectively by cells than anionic charged AuNRs, this is due to the positively charged surface making contact with the negatively charged cell membrane via electrostatic forces [210, 219].

1.7.2 Photothermal Ablation of Cancer Cells Using Plasmonic Photothermal Therapy (PPTT)

AuNRs have the most suitable NIR absorption cross section when evaluating the various nanoparticle architectures for their use in PPTT [23] due to their extremely effective NIR photothermal heat conversion [24]. Following cellular uptake of AuNRs, PTT is used to raise the local temperature and cause a series of cellular changes that result in the cell death [218]. It results in the creation of a heated electron gas, which rapidly cools by energy transfer with the NP lattice within around 1 ps. Following by a quick energy transfer that only lasts around 100 ps, the NP lattice in turn heats up the surroundings [128]. High temperatures will cause irreversible cell damage due to denaturation of proteins and breakdown of cell membrane [128].

AuNR with a successful PPTT is most often used in sizes that are 40 nm and 10 nm in length and width respectively, with a LSPR about 800 nm [121]. In addition, the right laser dosimetry and particle accumulation are essential for a particle-assisted photothermal therapy to be effective. The healthy tissue surrounding the cancer will be overheated and damaged by a laser exposure that is too high. Complete ablation might not be achieved if the laser dose is too low, and the tumour might come back [220]. Therefore, using a low-energy and safe near-infrared laser is highly demanded, the AuNRs attached to antibodies can be employed as a selective and effective photothermal agent for cancer cell treatment [221]. Due to the increased concentration of nanorods that are specifically linked to the tumour tissue, it is anticipated that the tumour tissue will be destroyed selectively at laser energies that will not affect the neighbouring healthy cells [221]. According to A. El Sayed et al, the cancer cell treated with AuNPs and exposed to 2 minutes to a femtosecond laser of different powers showed cell death at a laser power which is 20 times lower than the energy used for the control cells (untreated) with threshold energy of 1.1 mW (120 mJ) [222].

PTT primarily causes cell death through the routes of necrosis and apoptosis [223]. The plasma membrane may be damaged during necrosis by the heat produced by PPTT (if it is over 50 °C), allowing cellular components to seep out and damage neighbouring healthy tissues by inducing inflammation and metastasis [224]. However, apoptosis is a pathway for programmed cell death that causes the death of cancer cells reduces inflammatory activity and is thought to be a "cleaner" method of cell death [225, 226]. Therefore, it would be preferable in therapeutic circumstances to modulate PPTT to cause apoptosis [227, 228]. According to several reports, differing intracellular locations or forms of nanoparticles may control when cells enter necrosis or apoptosis [229].

1.8. Gold Nanorods AuNRs in Optoacoustic Imaging

Another benefit of AuNRs is their complete multifunctionality, which allows them to combine many desirable capabilities into a molecular-sized package [230]. Due to their NIR plasmon resonance, which has the ability to convert electromagnetic energy into heat for photothermal therapy, AuNR is specifically attracting a lot of attention as contrast agents and molecular probes for photoacoustic imaging [231, 232]. During photothermal therapy, photoacoustic imaging can be used to both monitor the delivery of MNPs to the targeted region in tissue and to display temperature maps [231].

Photoacoustic imaging is a non-invasive imaging technology with high resolution and strong contrast with a suitable depth range [233]. According to studies, it can visualise into tissues to depths (> 1 cm) more than other imaging techniques which have lower penetration limitations such as multi-photon microscopy or optical coherence tomography of (0.4-1 mm and 2 mm) depths, respectively [234]. As shown in the illustration in Figure 1.19. [235], when the pulses are irradiated to the area where the contrast agents are presence, the contrast agents absorb energy of the pulses, following by an increase in temperature. Then, the PA imaging start to identify and detect the ultrasonic waves produced by thermoelastic tissue and generate PA images.

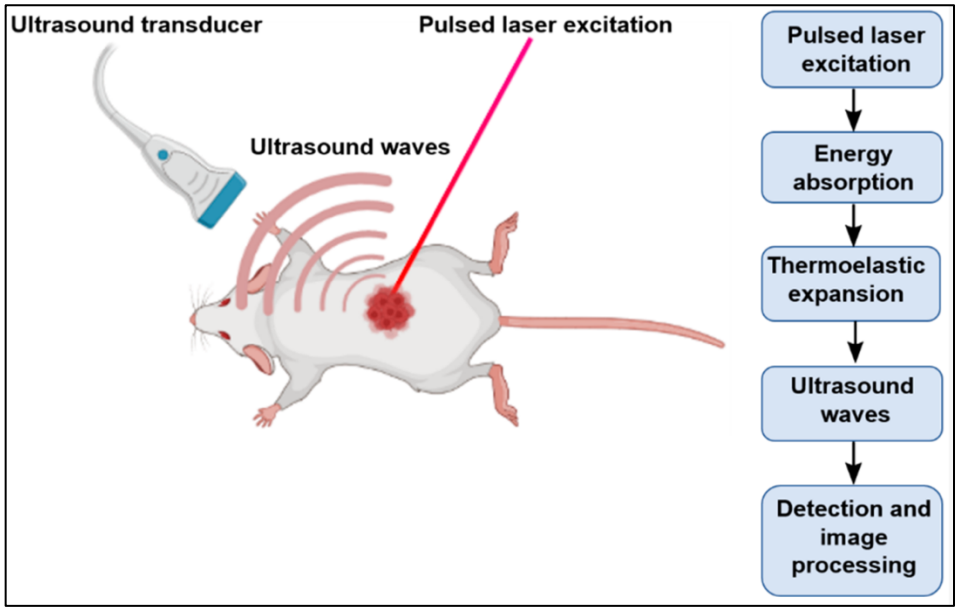

Figure 1.19 Schematic illustration of PA mechanism.
(Adapted from Ref [235]).

The amplitude of the generated ultrasonic waves are dependent on both the laser fluence used in the PA imaging and optical absorption characteristics of the tissue. It is necessary for the tissue to have weak scattering of ultrasonic waves as relative to scattering light to obtain a high resolution [236].

The efficiency of light energy conversion into a PA pressure wave during thermal expansion in an optical absorber is the key factor in determining the intensity of the consequent optical contrast [237]. Therefore, it is essential for effective PA imaging to use photoabsorbers that can efficiently absorb and convert light energy into acoustic energy. High NIR-absorbance of AuNRs shows a good performance as a strong contrast agent in photoacoustic imaging [233]. Hence, the PA conversion efficiency is significantly influenced by the size of AuNRs [238]. The main factor that can affect the optical absorption efficacy and consequently the generation of PA signals is the thermal stability of AuNRs under pulsed laser illumination [163, 239]. Then, as the peak SPR band starts to blue-shift, their ability to absorb the incident laser light will drastically decrease [182, 239].

In summary, the current challenges associated to using AuNRs such as the CTAB toxicity, instability and photothermal reshaping of AuNR under pulsed laser irradiation prevent them from being successful as a photothermal agent. Therefore, AuNR needs to be able to absorb

lasers strongly in the biological window (i.e., the so-called first biological window with wavelengths ranging from 700 nm to 950 nm (NIR-I)), colloidally stable, photothermal stability and efficiency at converting photon energy to heat in treatment, and no toxicity. In this thesis, AuNR is developed in order to make them biocompatible, thermally stable, well-controlled, reproducible and efficient in NIR absorption for effective photothermal applications.

1.9. Aims and Objectives

The main aim of this research is to engineer and modify a novel AuNR that is able to satisfy the conditions required for the ideal plasmonic photothermal agents for the clinical photothermal therapy of cancer treatment. This required considerable modification of current synthesis techniques as well as understanding the photothermal reshaping of AuNR. Specific objectives of the research were as follows:

1. To conduct a literature review of previous work to identify the gaps and challenges in the research.
2. To synthesise AuNR with well-defined shapes of absorption spectra that can be tuned over NIR region, via binary–surfactant seedless synthesis;
3. To investigate the effect of SiO_2 surface coating on the optical properties of AuNR using UV-vis spectroscopy;
4. To investigate the effect of SiO_2 surface coating on the thermal stability of during in-situ TEM heating;
5. To investigate the AuNRs efficiency and stability in photoacoustics imaging;
6. To investigate the effect of phospholipid coating on the colloidal stability of AuNR@SiO_2 in PBS buffer using UV-vis spectroscopy;
7. To investigate the effect of lipids functionalisation on the cellular uptake of AuNR@SiO_2 in human colorectal cell lines using fluorescence microscopy images.
8. To investigate the effect of silica coating on AuNR in cells viability of human colorectal cell lines compared to uncoated AuNRs;
9. To investigate the effect of phospholipid coating on AuNR@SiO_2 in cells viability of human colorectal cell lines compared to AuNRs@SiO_2;
10. To investigate the effect of silica coating on AuNRs reshaping behaviour as a function of irradiation time, fluence, and porosity degree under nanosecond pulsed laser irradiation using UV-vis spectroscopy and TEM;

11. To investigate the effect of silica coating on electric-field enhancement and photothermal response of AuNR@mSiO_2 using COMSOL Modelling.

2. Methods and Materials

This Chapter provides a description of all methods used in this Thesis including all chemicals, materials, tools and equipment used. It is divided into two main sections; the first section presents the synthesis protocols of gold nanorods (AuNRs), silica coated-gold nanorods (AuNRs@SiO_2), lipid-coated AuNRs@SiO_2, Atto488 lipids coated-AuNRs/SiO_2, *in vitro* cytotoxicity assays using SW620 and HT29 cell lines. Additionally, the synthesis AuNRs@mSiO_2 of different degrees of porosities and determining the silica shell porosity. The second section focuses on the methods for material characterisation that were employed such as ultraviolet and visible (UV-Vis) spectroscopy, fluorescence spectroscopy, Zeta potential analysis, Dynamic Light Scattering (DLS), Transmission Electron Microscopy (TEM), In situ heating transmission electron microscopy, Energy-Dispersive X-ray spectroscopy (EDX), Multi-spectral Optoacoustic Tomography (MSOT), and pulsed laser irradiation for both AuNRs and AuNRs@mSiO_2. The samples preparation, each technique's theory and the data analysis methods are presented in detail.

2.1. The Synthesis of Nanomaterials

2.1.1 The Synthesis of AuNRs

Seedless synthesis of AuNRs was developed in our research group by Roach *et al*.[37]. This methodology is the basis to the preparation of AuNRs in this Thesis and enabled the aspect ratio of the AuNRs to be varied from 2.7 to 3.5. The aspect ratio controls wavelength maxima of the longitudinal surface plasmon resonance (LSPR) band. The following steps were used to synthesize 10 mL of AuNR colloidal solution. In each synthesis, the reaction vessel was a 20 ml borosilicate glass vial. Prior to synthesis, all glassware was cleaned using aqua regia solution. A 100 ml mixture consists of nitric acid and hydrochloric acid in a volume ratio of 1:3 was prepared. **The Aqua regia solution is highly corrosive liquid and may cause explosion, skin burns, or eye/respiratory tract irritation if not cautiously handled.** The vials were filled with the aqua regia and left in a fume cupboard for 30 min, before carefully disposing of the aqua regia and rinsing the vessel with copious amounts of Milli-Q water. The cleaned vials were placed in a drying oven at 80°C until dry (typically 24 h). Once dried, the vials were cooled to 30°C by using dry heater and maintained at this temperature throughout the synthesis. The synthesis method is summarized in Figure 2.1.

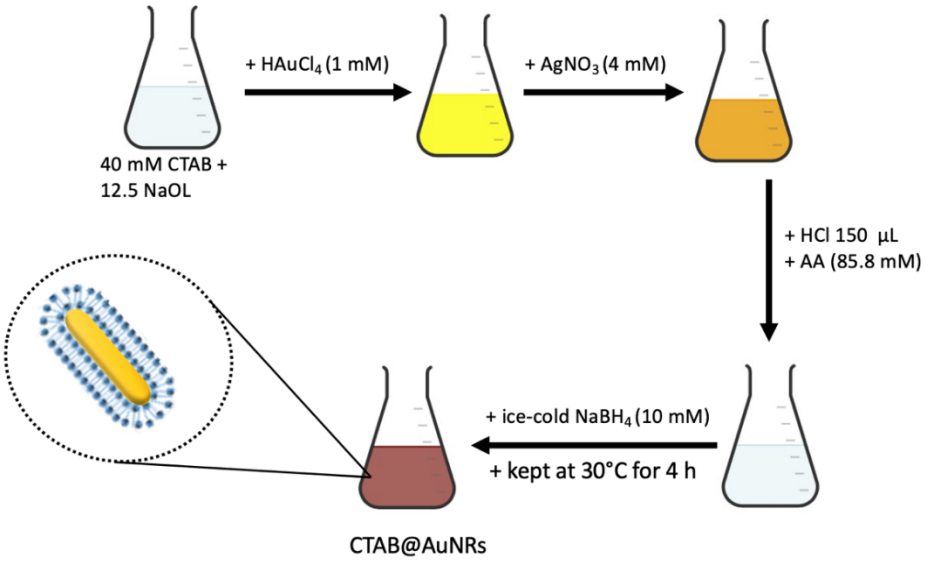

Figure 2.1. Schematic illustration of seedless-mediated growth approach for gold nanorods preparation.

Table 2.1 The stock solutions were used in AuNRs synthesis. The stock solutions were diluted as requested.

Compound		Concentration (mM)	Volume
(A)	CTAB	200	50
(B)	NaOL	200	50
(C)	$HAuCl_4$	40	50
(D)	$AgNO_3$	4	10
(E)	Ascorbic acid	85.8	10
(F)	$NaBH_4$	10	10

To prepare 10 mL of AuNRs, the stock solutions were prepared as summarized in Table. 2.1. Solutions A and B were prepared in advance in a 50 ml falcon tube by heating to 70°C until the solutes were completely dissolved. The solutions A and B were added at a predetermined ratio. The ratio of A:B controls LSPR wavelength and the aspect ratio as shown in Figure 2.2. To obtain a LSPR peak at 750- 850 nm (an aspect ratio of 2.7-3.5), 4 ml of CTAB (diluted to be 40 mM), 1.25ml of NaOL (diluted to be 12.5 mM) and 4.75 ml of Milli-Q water. This was followed by the addition of 10 ml of gold (III) chloride trihydrate (1 mM) from the stock aqueous solution of 40 mM, added to the borosilicate glass vial. Then 480 µl of silver nitrate $AgNO_3$ (4 mM), (covered and stored in the fridge before using) was added, followed by 100 µl

hydrochloric acid HCl (11.8 M). 150 µl ascorbic acid (AA) (85.8 mM) was added (mixed kept in the fridge before using). The addition of AA causes the reduction Au^{3+} to Au^{+} which can be observed as disappearance of the orange colour as depicted in Figure 2.1.

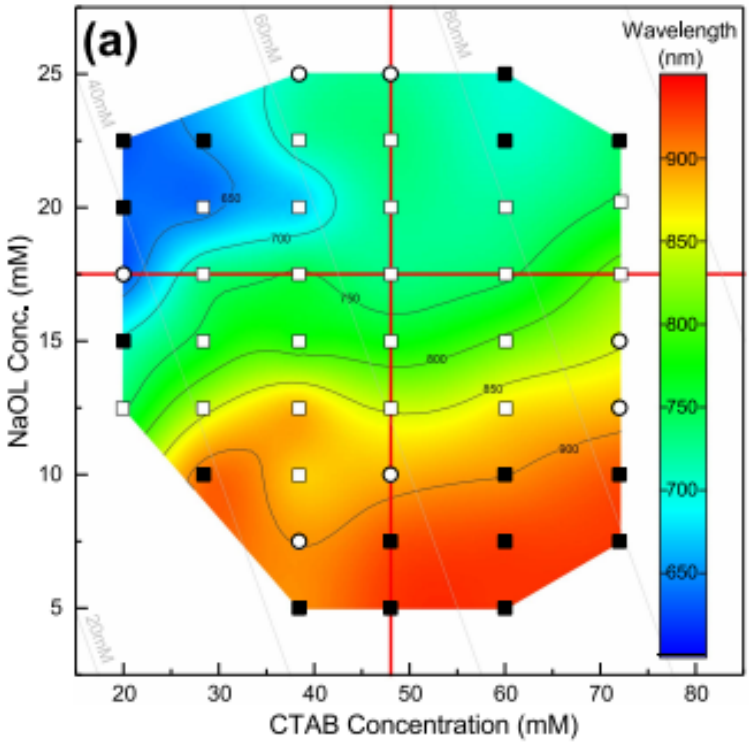

Figure 2.2 The relationship of concentrations of CTAB and NaOL on LSPR peak position. (With all other constituents were held constant). □ indicates the shape yield of AuNRs is higher than 98%,○ is higher than 90%, and ■ indicates the low shape yield. The colour scale on the right shows the wavelength. (Adapted from Ref [37]).

Following this, 15 µl of freshly prepared sodium borohydride (10 mM of ice-cold $NaBH_4$) was rapidly injected using a pipette to the solution. The borosilicate glass vials were kept at 30 °C for 4 h. The solution colour changed to reddish brown. The resultant solution containing AuNRs was transferred into centrifuge falcon tubes and centrifuged at 17000g for 30 min to pellet the resultant AuNRs. The supernatant containing the surfactant was discarded from the tube carefully using a pipette. The precipitate was resuspended in 10 ml Milli-Q and stored in the dark at room temperature. This method can be scaled up as required (up 100 ml has been tested).

2.1.2 Synthesis of Silica Coated AuNRs

Silica coating on AuNRs was carried out using a modified version reported by Ashrafi et al.[240] and is summarised in Figure 2.3. As shown in the preparation protocol shown in Figure 2.3, firstly, 10 ml of the cleaned AuNRs (prepared by the method in Section 2.1.1) were centrifuged 500g for 3 min to remove any aggregated particles. 20 µL of 0.1 M NaOH solution was added upon stirring to adjust the pH to 10. The solution was left for 30 min under gentle stirring. Followed by adding three 30 µL injections of 20 % by volume of tetraethyl orthosilicate (TEOS) dissolved methanol, were added at 30 minutes intervals per 1 ml of AuNRs. The reactions were left stirring for three days at temperature of 26~28 °C. The silica coated AuNRs were washed twice by centrifugation cycles (at 8000g, 10 min) and resuspended in 10 ml Milli-Q water and stored in the dark at room temperature.

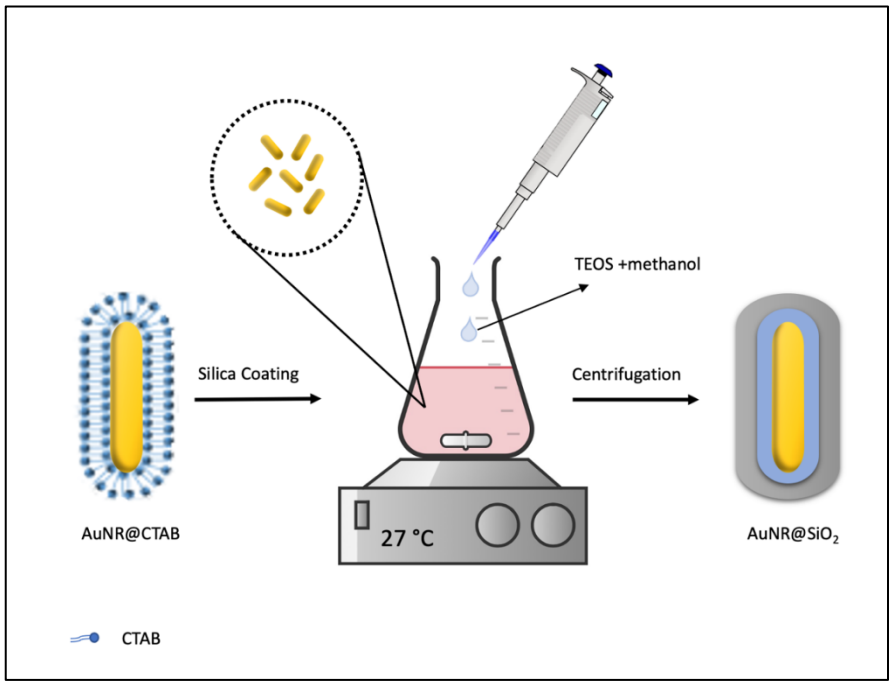

Figure 2.3 Schematic illustration of silica shell growth method for gold nanorods.

2.1.3 Increasing the Porosity of AuNR@SiO_2

Synthesis AuNR@SiO_2 with higher porosity degrees was carried out by adapting a reported method [241]. To grow a silica shell on CTAB@AuNRs with higher porosity degree, CTAB of two concentrations 5 $X10^{-3}$ M and 10 $X10^{-3}$ M were added to the AuNRs solution during silica shell growth. The CTAB of both concentrations were dissolved Milli-Q water. They were left in

falcon tubes in a 70 °C drying oven to completely dissolve CTAB for overnight. On the following day, they were added to the AuNR@SiO_2 solutions during the normal silica coating growth method explained earlier in this Chapter in Section 2.1.2. Once the silica coating completed, the AuNRs@$mSiO_2$ were washed to remove the excess CTAB in the solution. To determine the porosity degrees of the silica shells by changing the refractive indexes of their surrounding medium, the CTAB were extracted from the silica pores by refluxing as addressed in the following section.

2.1.3.1 CTAB Extraction

The CTAB was extracted from AuNRs@$mSiO_2$ by using the standard refluxing method [242]. The main purpose to use refluxing method is to allow the mixture to boil and condense, then transfer the condensed liquid back to the main flask. The reflux setup used in this work is shown in Figure 2.4. A three-neck flask with a round bottom was used in the setup and it was half-full of the mixture to give enough space during boiling. The three-neck flask was placed properly on the heating mantle that fit the flask and in good contact with the flask. One of the necks was closed using a glass stopper and the other with rubber stopper to allow insertion of a thermometer. The Allihn condenser was connected upright on the flask. Then, the condenser was connected to the water faucet through the water inlet (at the bottom) and water ran through the condenser column. A hose was connected to the upper arm (water outlet) to drain to the sink. The top side of the condenser in connected to the nitrogen that is connected to a bubbler system and then passing through the cold side of the condenser. The bubbler bottle used in this setup is filled with silicone oil for visually monitoring the pressure inside the setup. A stirring bar was placed in the mixture, the temperature and stirring were controlled as needed.

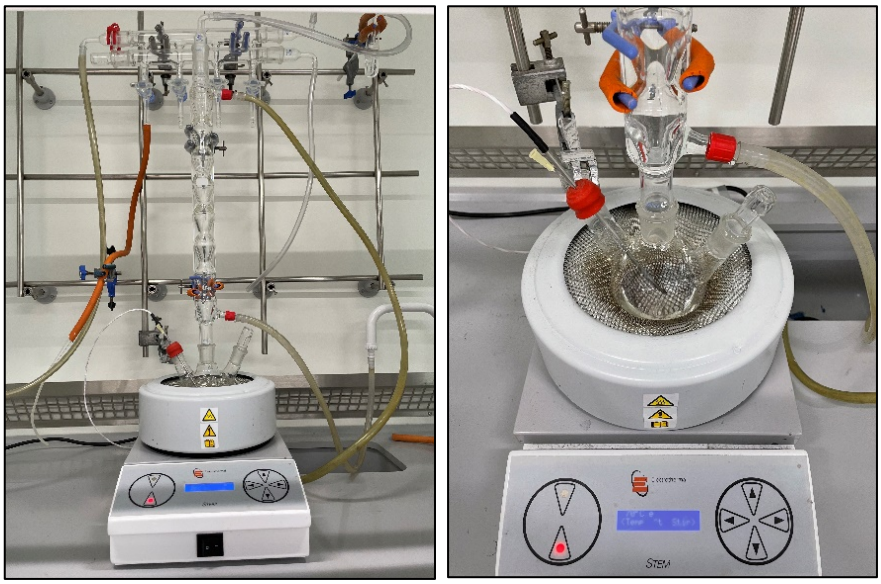

Figure 2.4 The pictures of the reflux setup used in CTAB extraction from AuNRs@mSiO$_2$.

The picture on the left side shows the reflux setup consisting of mantle heating with stirring and temperature control, a three-neck flask with a round bottom, an Allihn condenser. The picture on the right side shows a close view of the flask with a stirring bar.

The synthesized AuNR@SiO$_2$ were centrifuged (5 ml). Then, they were dispersed in a mixture of ethanol and hydrochloric acid solution 50 ml and 1 ml (36%), respectively. The solution of AuNR@SiO$_2$ in ethanol HCl solution were refluxed at 70 °C for 2 h in a fume hood. Once it is cooled, the AuNR@SiO$_2$ were washed with Milli-Q water and ethanol several times using centrifugation and they were dispersed in Milli-Q water.

2.1.4 Determine the degree of porosity of silica shells of AuNR@mSiO$_2$

After the successful CTAB extraction from silica pores, the AuNR@mSiO$_2$ of different degree of porosity were centrifuged to form pellets. Then they were dispersed in various concentrations of a mixture of glycerine/water of range of 20-70% v/v as presented in Table 2.2. Therefore, they were left for 30 min under stirring at room temperature. The UV-Vis absorption spectra were taken for each sample with no additional cleaning to determine the LSPR peaks position AuNR@mSiO$_2$ in different refractive index medium.

Table 2.2 Then they were dispersed in various concentrations of a mixture of glycerine/water of range of 20-70% v/v.

Sample	Glycerine (%)	Water (%)
1	0	100
2	20	80
3	30	70
4	40	60
5	50	50
6	60	40
7	70	30

2.1.5 Synthesis of Lipids Coated AuNRs@SiO_2

The lipid coating was carried out using modified method of Cui, X et al.,[243]. Two different lipids were used, 1,2-distearoyl-sn-glycero-3-phosphoethanolamine-N-[methoxy(polyethylene glycol)-2000] DSPE-PEG_{2000} (0.25 mg) and 1,2-dipalmitoyl-sn-glycero-3-phosphocholine DPPC (4.75 mg) of 5% and 95% respectively. The mixture of the two lipids were mixed in chloroform (2 mL) in a glass vial. The lipid films were prepared by flushing the glass vial with nitrogen gas for 30 min and allowed to dry overnight in a vacuum. Then, the lipid film was hydrated in Milli-Q water in the same volume, followed by vortex and sonication to dissolve it properly. Then, it was sonicated using tip sonicator for 30 min. The lipid was added to AuNRs@SiO_2 pellets of (5 ml of a concentration of 10 µg/ml) and was sonicated to resuspend it properly. For one hour, the sample was sonicated at room temperature. The sample was centrifuged at 10,000g for 10 min before being resuspended in 5 ml of pH 7.4 phosphate-buffered saline (PBS). The lipid film hydration method used in this work is illustrated in schematic illustration in Figure 2.5.

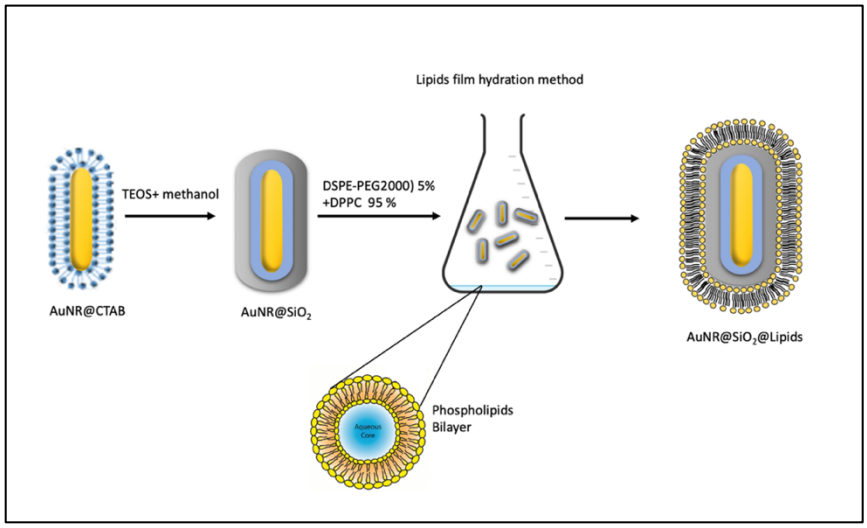

Figure 2.5 Schematic illustration of synthesis of lipids coated- AuNRs@SiO_2 using lipid film hydration method protocol.

2.1.6 Synthesis of Atto 488 Lipids-Coated AuNRs@SiO_2

The lipids were prepared by adding DSPE-PEG_{2000} (0.25 mg) and DPPC (4.745 mg) of 5% and 94.9% respectively. The fluorescent lipids Atto488 of 0.1 % of (0.005 mg) they were prepared via the hydration of a lipid film. The mixture of the three lipids was mixed in chloroform in a glass vial. The lipid films were prepared by flushing the glass vial with nitrogen gas for 30 min and allowed to dry overnight in a vacuum. Then, the lipid film was hydrated in Milli-Q water in the same volume, then vortex and sonicated to dissolve it properly. Then, it was sonicated using tip sonicator for 30 min. The lipids were added to AuNRs@SiO_2 pellets, then the mixture was sonicated to fully resuspend it. For one hour, the sample was sonicated at room temperature. The sample was centrifuged at 10,000g for 10 min and resuspended in Milli-Q water. The schematic illustration shown in Figure 2.6. illustrates the lipid film hydration method used to prepare Atto488 Lipids-Coated AuNRs@SiO_2.

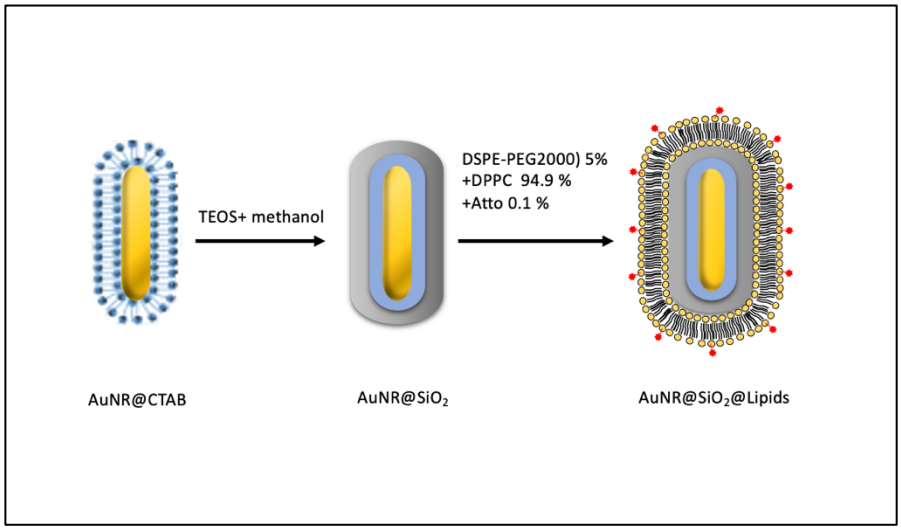

Figure 2.6 . Schematic illustration of Synthesis of Atto488 Lipids-Coated AuNRs@SiO_2. Using lipid film hydration method protocol.

The supernatant solution of the Atto488 Lipids-Coated AuNRs@SiO_2 showed high emission peak at 570 nm after the first centrifugation at 9,000 g for 8 min, this refers to the excess lipids in solution. To remove the excess lipids and leave enough lipids on AuNRs@SiO_2, the samples went through couples of washing cycles and their fluorescence emission spectra were taken after each cycle.

2.1.7 *In vitro* Cell Viability Assays

Every tissue culture experiment was carried out in a biosafety cabinet using sterile procedures and all supplies used were either sterile or autoclaved for 30 min at 131 °C.

2.1.7.1 SW620 Cells

The colorectal cancer cells SW620 were seeded in 96 well plates at a concentration of 5 $X10^3$ cells per well in 100 µl media. The plates were left for 24 h incubation at 37 °C in 5 % CO_2. Following 24 hours, the media was exchanged for new media with a known concentration of AuNRs that were washed twice with PBS buffer and filtered with (syringe filter 0.2 um) to remove any bacteria and the plate incubated for 24 hours. The media was not replaced after AuNRs@SiO_2 treatment, to avoid losing cells since a high percentage of the cells because were

detached after incubation. Post-incubation, the media was exchanged with a new media containing 10% of CCK-8 solution and left for 4 hours incubation. Following by taken the absorbance at 450 nm for all required wells using a microplate reader (Mithras LB 940).

2.1.7.2 CCK-8 Viability Assay

The cytotoxicity of AuNRs and AuNRs@SiO_2 to the SW620 cell line was analyzed using the CCK-8 cell viability assay. The Cell Counting Kit-8 (CCK-8) is ideal for sensitive colorimetric assays to determine the viability of different cell lines. WST-8 water-soluble tetrazolium salt in Kit-8 (CCK-8) allows dehydrogenase activities in cells creating a yellow formazan dye. The amount of the formazan dye produced by the dehydrogenase activities in cells is corresponding to the number of living cells.

2.1.7.3 HT29 Cells

HT29 is human colorectal adenocarcinoma cell line were seeded in 96 well plates at a concentration of 2 $X10^4$ cells per well in 100 µl media of a mixture of RPMI 1640 + 10% FBS. The cells used in this study are of passage number of 93. Then, the plates were left for 24 h incubation at 37 °C in 5 % CO_2. Following 24 hours, the media was exchanged for new media with a known concentration of AuNRs@SiO_2 and lipid-coated AuNRs@SiO_2, then the plates were incubated for 24h and 48h. Following incubation, the media was exchanged with a new media containing with 50 µl of 1 mg/ml working MTT solution (stock solution is diluted using the media cells are cultured in). Plates were incubated in the dark for a further 3 hours. Followed by removing the MTT solution. The dye formed (dark blue formazan) is dissolved in 100µl of propan-1-ol and left on Microplate Mixer for 30 min. Following by taken the absorbance at 570 nm for all required wells using a microplate reader (Opsys MR^{TM}, Dynex technologies ltd, UK). The schematic illustration of Atto 488 Lipids coated AuNRs@SiO_2 for Cytotoxicity assay in Figure 2.7.

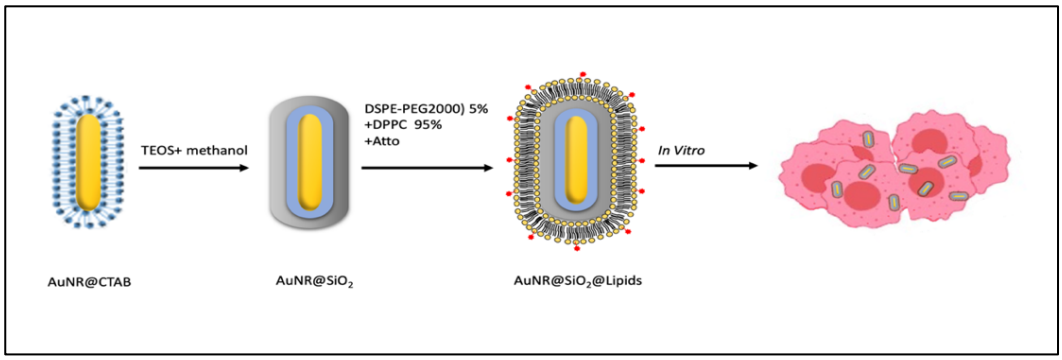

Figure 2.7. Schematic illustration of Atto 488 Lipids coated AuNRs@SiO_2 for Cytotoxicity assay.

2.1.7.4 MTT Viability Assay

The MTT tetrazolium salt is reduced into a blue formazan dye via the mitochondria of the cells. If the mitochondria are not viable or have reduced activity, then there will be none or very little precipitate formed. 5 mg/ml stock solution of MTT was prepared in PBS, it was made in a day before the assay and wrapped in foil to protect it from light.

The cell viability measurements were background corrected by subtracting the absorbance of wells containing AuNRs and media without cells. The absorbance was collected from at least three wells to obtain the average. The expressions of the cell viability and the percentage of the viability increase are as follow:

$$\Theta \text{ Viability } \% = \frac{A450\ sample - A\ 450\ bkgd - A450\ AuNRs}{A\ 450\ control - A\ 450\ bkgd} \times 100 \qquad (1)$$

$$\text{Viability increase } \% = = \frac{\text{IC 50 SiO2/AuNRs} - \text{IC 50 CTAB/AuNRs}}{\text{IC 50 SiO2/AuNRs}} \times 100 \qquad (2)$$

2.2. Characterisation methods

2.2.1. UV-Vis Spectroscopy

UV-vis spectroscopy is a beneficial technique used to study the optical properties of metal NPs. The technique is based on the intensity of light passing through the specimen and comparing this intensity when the specimen is not present. A UV-Vis instrument comprises of a light source, a sample holder, a monochromator, a detector(s), and a computer to record and calculate the output. The output is normally represented as absorbance versus wavelength, significantly, the 'absorbance' measured is the extinction which is the sum of the absorbance and scattering. The scattering of nanoparticles scales with size to power of six, and inversely to the power of four, for wavelength; and thus, the latter can be significant particularly in the UV to blue region of the spectrum (for larger particles). The absorbance is fundamentally a measure of photon absorption leading to electron excitation (or even emission). As one measures the absorbance as a function of wavelength peaks can be observed which correspond to, for example, electron transitions such as π to π* or σ to σ* in molecules, band gap transitions in semiconductors, and plasmonic oscillations in metals. Molecules containing many π bonds can absorb into the visible (e.g. Texas red) and even into the near infrared (e.g. ICG). The absorbance is measured by recording the light intensity without the specimen, I_0, and the intensity with the specimen and I is the intensity with the specimen present [1, 2].

$$A = log \frac{I_0}{I} \qquad (3)$$

If the absorption is known for an analyte i.e. the molar extinction coefficient, ϵ, is known, then the absorption can rapidly determine the analyte concentration using the Beer–Lambert law,

$$A=\epsilon cl \qquad (4)$$

Where, c is the concentration and l is path length of the light passing through the solution (Figure 2.8).

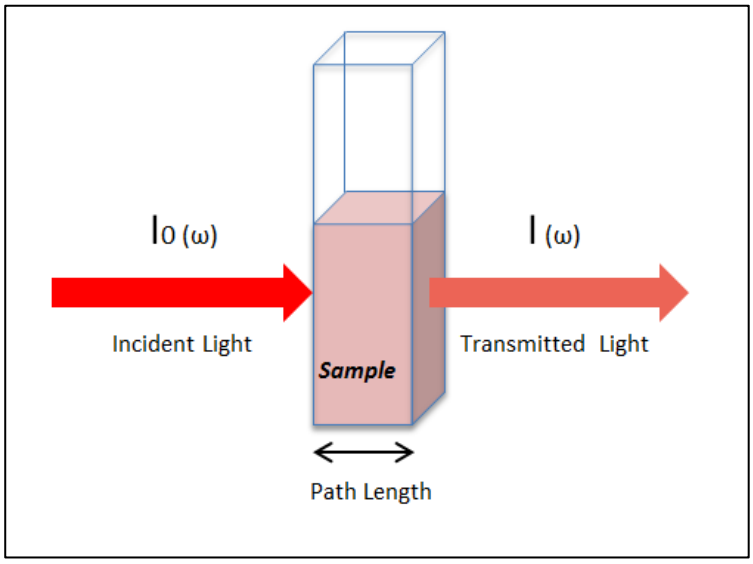

Figure 2.8 A schematic representation for Beer-Lambert law for the measurement of UV–vis absorption spectra.

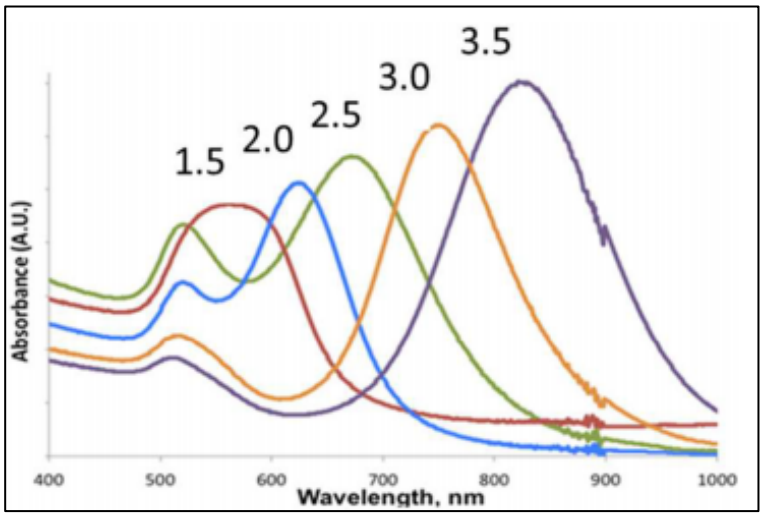

Figure 2.9 UV-vis spectra of AuNRs with various aspect ratios.

Showing AR from 1.5 to 3.5. (Adapted from Ref [19]).

The plasmonic properties of metal nanoparticles are sensitive to their size, shape, composition, and aggregation state. The transverse mode is located between 520 and 525 nm, while for the longitudinal mode, it is dependent on the AR of the AuNRs ranges from 600 nm to longer wavelengths, as presented in Figure 2.9 [19]. UV-vis therefore offers a rapid method of determining the properties of gold nanoparticle dispersions, e.g., the transverse

and longitudinal surface plasmon resonance wavelength positions, intensity, and width can be used to characterise the ensemble.

2.2.1.1. Practical details

The UV–vis absorbance spectra in this thesis were recorded using an Agilent Cary 5000 UV–vis-NIR. Quartz crystal cuvettes were used for all solution-based samples (standard path length of 1 cm). Typically, all samples were diluted by a factor of 20 before measurements. Followed by collecting the extinction spectrum of AuNRs from 400 to 900 nm. The spectra after these measurements were multiplied through by the dilution factor to return to the true extinction value. It was found that the absorbance A_{400} at = 400 nm can be used to calculate the total concentration of Au atoms C_{Au} [244]. The AuNRs concentrations were determined by plotting a calibration curve of AuNRs concentration of three different dilutions using atomic absorbance spectrometer (AAS) versus the absorbance of AuNRs solutions at 400 nm. As shown in Figure 2.10. The gold concentration using atomic absorbance spectrometer (AAS) and the absorbance A_{400nm} for three samples of different concentrations are showing a significant linear correlation between the two variables. This only gives the concentration of gold atoms. A combined with TEM images that gives sizes data, the AuNRs concentrations were estimated throughout the experiments.

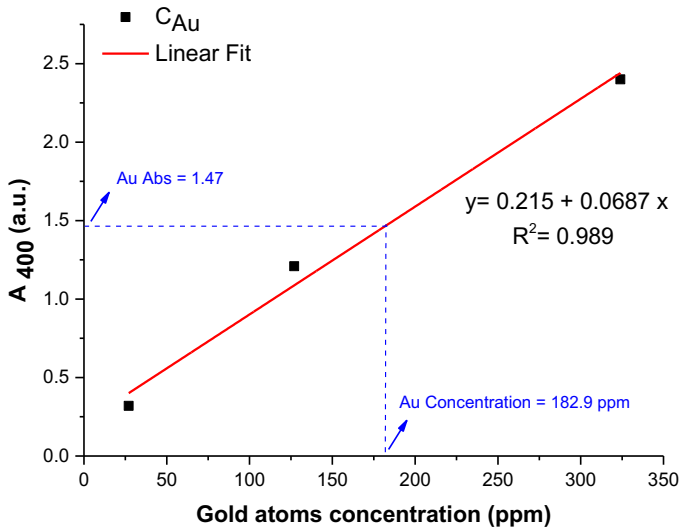

Figure 2.10 The gold atoms concentration using the calibration curve.

Showing the absorbance vs. concentration gold atoms as a function of A400nm. The red line is a linear fit.

2.2.2. Fluorescence Spectroscopy

The main focus of Fluorescence Spectroscopy is on electronic and vibrational states of molecules. The sample being analysed typically has a low energy (ground state) and a high energy (electronic level). There are different vibrational states in these electric level [245]. During fluorescence, a photon is absorbed by the sample to illuminate it; then it is elevated from its ground state to one of the vibrational states in the excited electronic level. Then, the excited molecule is assisted by collisions with other molecules in losing vibrational energy until it achieves the lowest vibrational state. [245]. This process is often explained with a Jablonski diagram [246], as shown in Figure 2.11.

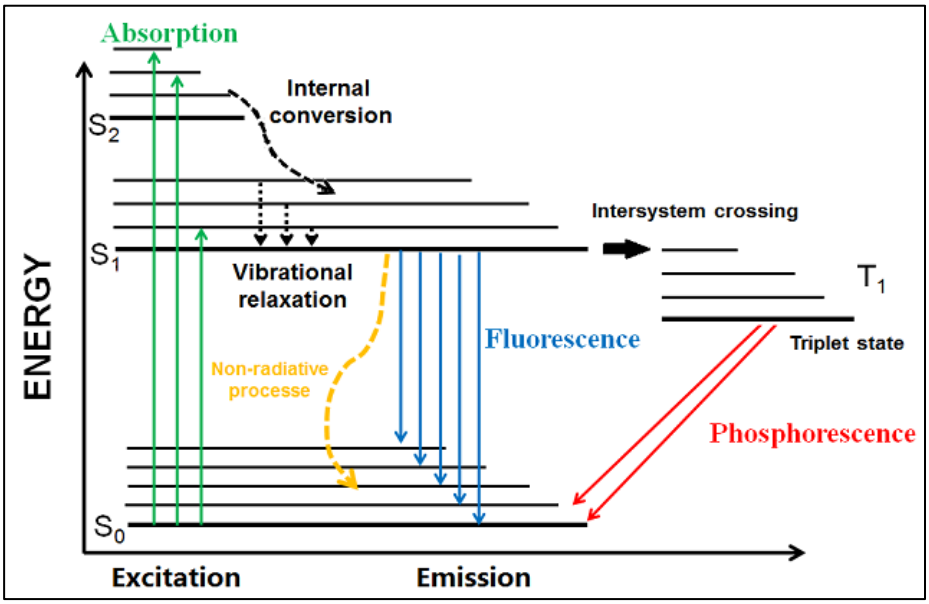

Figure 2.11 The schematic diagram explains the fluorescence process.

Proposed by Alexandre Jablonski in 1935. (Adapted from ref [246]).

The green arrows represent the light absorption. The vibrational relaxation from singlet excited state S_2 to S_1 are represented by the black arrows. When the excitation energy is lost as heat to the solution or vibrations, this called a non-radiative relaxation and shown as the yellow arrow. The fluorescence is emitted when after molecule relaxation back to one of the different vibrational levels of the ground electronic state S_o as represented in blue arrows in Figure 2.11 [246, 247]. Subsequently, fluorescent spectroscopy can analyse these different frequencies of emitted light and their intensities. Consequently, it is possible to determine the structure of different vibrational levels. [245]. At the end, the molecule releases a photon

when it relaxes back to one of the several vibrational states of the ground state. [245]. The molecule or atom has an impact on the precise frequencies of excitation and emission.

$$S_0 + h\nu_{ex} = S_1 \qquad (5)$$

Where $h\nu$ is an energy of the photon, h is Planck's constant, ν is the frequency of electromagnetic radiation, S_0 and S_1 are the ground state and is its first excited state of the fluorophore. The energy and wavelength of the light emitted are determined by the energy gap between the singlet excited state and the ground state (S_0) and (S_1) respectively. As shown in the following expression, the energy of the emitted light (E_{Fluor}) equals the absorbed energy from the absorbed light E_{Abs}, subtracted the vibrational energy that the molecules lost during the vibrational relaxation (E_{Vib})[248]:

$$E_{fluor} = E_{Abs} - E_{vib} - E_{solv.relax} \qquad (6)$$

Where $E_{solv.relax}$ refers to the energy of the cage effect of the molecules to reorient itself during excitation and relaxation in the excited state to ground state, respectively. The proportion of photons released to photons received is known as the fluorescence quantum yield and given by the following expression:

$$\Phi = \text{emitted photons} / \text{absorbed photons} \qquad (7)$$

The Figure 2.12 [248], shows the schematic illustration of the basic of fluorescence spectrometer. The basic a fluorescence spectrometer contains a light source, a detector, an adjustable monochromator and sample holder. The monochromator's function is not just for selecting the excitation and emission wavelengths, but also for monitoring and correcting the light intensity fluctuations. The reference beam is reflected to the reference photomultiplier tube after those beams travel through the primary filter. A couple of lenses utilized to focus the sample beam on the sample, generating fluorescence emission. The excitation monochromator is stationary while the emission monochromator changes to produce an

emission spectrum. However, to produce an excitation spectrum, the excitation monochromator fluctuates while the emission monochromator remains constant.

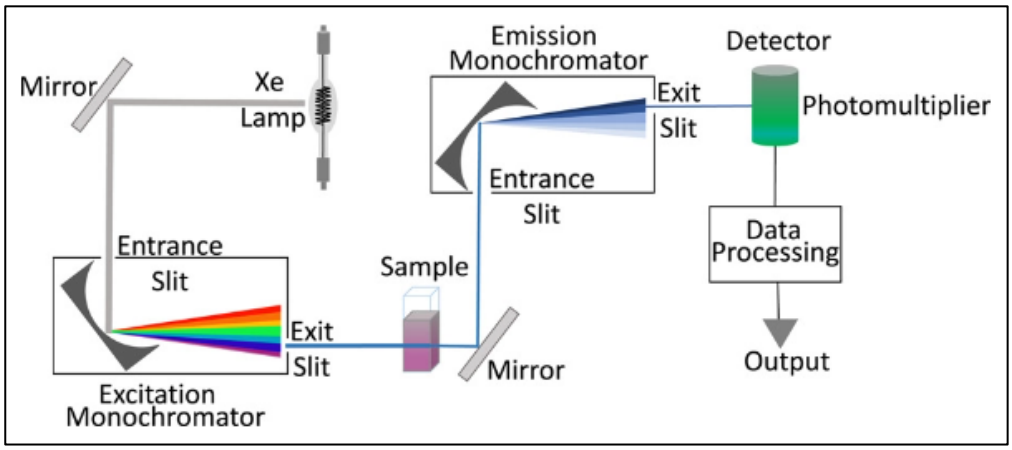

Figure 2.12 Schematic representation of a fluorescence spectrometer. (Adapted from Ref (250)).

2.2.2.1. Practical details

The fluorescence spectroscopy was used to characterize and observe photoluminescence properties of Atto488 lipids coated-AuNRs@mSiO_2. The emission peak of Atto488 is at 520 nm, thus the scanning range from 500 nm to 600 nm was collected. A quartz crystal cuvette of 10mm path length was used.

2.2.3. Fluorescence Microscopy

Fluorescence microscopy operates mainly using the principle of fluorescence. When a substance absorbs energy from shorter wavelength invisible radiation (like UV light) and produces longer wavelength of visible light, this is referred to as being fluorescent (such as green or red light). This is frequently employed in therapeutic and diagnostic contexts to rapidly detect bacteria, antibodies, and a variety of other chemicals. Some cells naturally emit fluorescence when they are exposed to ultraviolet light, because they consist of a fluorescent substance such as chlorophyll [249]. However, if they are not naturally fluoresced, fluorescent dyes known as fluorochromes can be used to stain the cells. DAPI (49,6-diamidino-2-phenylindole), Alexa Fluors, or DyLight 488 are examples of fluorescent dyes that are frequently used [249].

As shown in schematic illustration of fluorescence microscopy in Figure 2.13 [250], the photons of shorter wavelength and higher intensity produced by mercury vapour arc lamps pass through the excitation filter. The excitation filter is used to remove non-specific wavelengths and only light with a short wavelength are allowed to pass through. The fluorophore-labelled sample is illuminated by the filtered light after it has been reflected by the dichroic filter. Shorter wavelength light is absorbed by the fluorochrome, which then emits longer wavelength light of lower energy that sent to the emission filter. Then, the emission filter sends the desired longer emission wavelengths to the detector while blocking any remaining excitation light. As a result, the fluorochrome-labelled stain objects appear bright (fluoresce) luminous contrary to the dark background in the microscope.

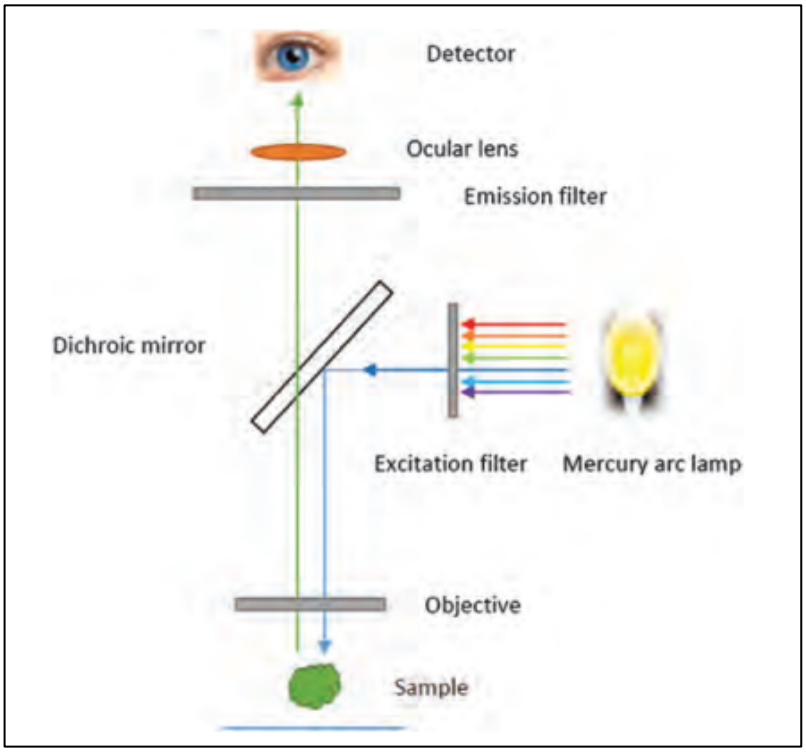

Figure 2.13. Schematic representation of a fluorescence microscopy. (Adapted from Ref [250]).

2.2.3.1. Practical details

1 µl of Hoechst was added to all wells to stain nuclei of HT29 cells, then left for 30 min. Then, the solution was removed, and then washed by adding 100 µl of DPBS. 100 µl of RPMI medium was added to all wells. They were tested using fluorescence microscopy.

2.2.4. Zeta Potential

Zeta potential was used to measure the effective electric charge on the AuNRs surface before and after the silica coating and to check the stability of colloidal solution as shown in figure 2.14 [251]. The degree of electrostatic repulsion between these colloidal dispersions can be determined by zeta potential. The higher the zeta potential magnitude the more stable the colloids as illustrated in Table 2.3 [252]

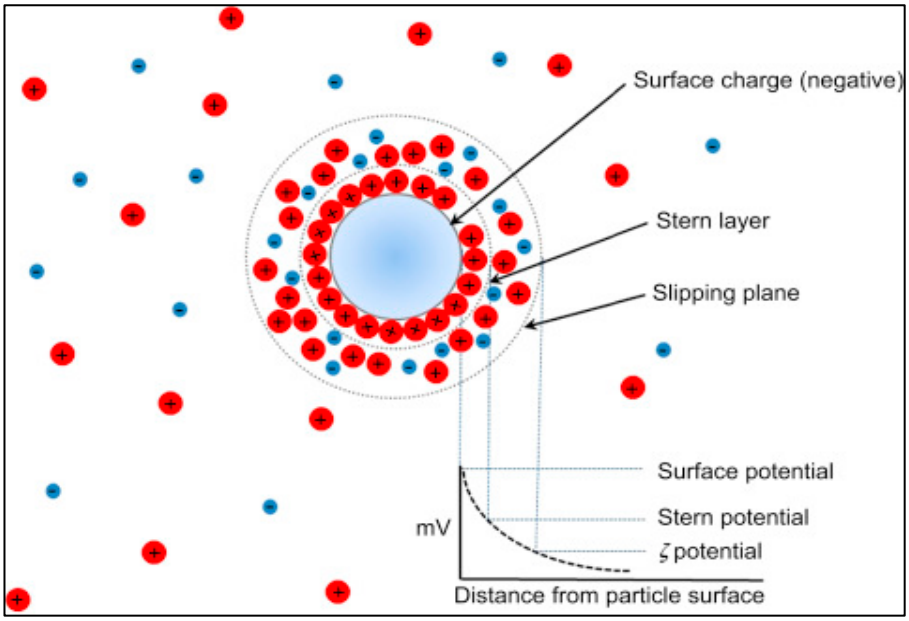

Figure 2.14. Diagram shows potential difference and the ionic concentration of the charged particle in a medium. (Adapted from Ref (253)).

Table 2.3 Stability behavior of a colloid depending on zeta potential. (The data in this table were adapted from Ref (252)).

Zeta potential (mV)	Stability behaviour
0 to ±5	Rapid coagulation or flocculation
±10 to ±30	Incipient instability
±30 to ±40	Moderate stability
±40 to ±60	Good stability
>61	Excellent stability

The z-potential measurements in this work were taken using a Malvern Zetasizer Nano ZSP. By applying DC voltage to the particles in solution, the z–potential can be measured. The z-

potentials can be determined by using the Smoluchiwski theory when the Debye length is lower than the particle's diameter [253]. When the Debye length is greater than the particle's diameter, then the Debye- Huckel assumption is applied. The following equation is Henry equation that can be used to determine the z–potential [15]:

$$U_E = \frac{2\varepsilon\zeta f(Ka)}{3\eta} \qquad (8)$$

Where U_E is the electrophoretic mobility, ε is the dielectric constant of the solvent., ζ is the zeta potential, f (ka) is Henry's function 1, k is the Debye length and a is the particle's diameter and η is the viscosity of a solvent. In this work, since the particle's diameter < 100 nm, according to the Debye-Hückel assumption , the f (ka) value is assumed to be 1 [254].

2.2.4.1. Practical details

10 µl of the sample were dispersed in 10 mM of sodium chloride solution of pH= 6 in Zeta potential sample cell disposable folding capillary cuvette (DTS0012). The measurement was taken 3 times at room temperature.

2.2.5. Dynamic Light Scattering (DLS)

In proportion to the sixth power of their radii, dispersed NPs scatter incident photons[255]. When NPs are smaller than one-tenth of the wavelength of the incident light, Elastic scattering occurs, thus the scattered light carrying as the same energy as the input light (Rayleigh scattering) [256]. However, when the NP's size reaches this limit, the anisotropic, Mie, scattering must be used in the place of Rayleigh scattering [257]. Figure 2.15. shows the schematic diagram of the fundamental components of DLS [258]. The following Stokes-Einstein equation can be used to determine the hydrodynamic radius R_h:

$$R_h = \frac{\mathrm{kT}}{6\,\pi\,\eta\,\mathrm{D}_t} \qquad (9)$$

Where k is Boltzmann's constant, T is the temperature in (Kelvin), η is the viscosity of the solvent, and D_t is the translational diffusion coefficient of the analyte.

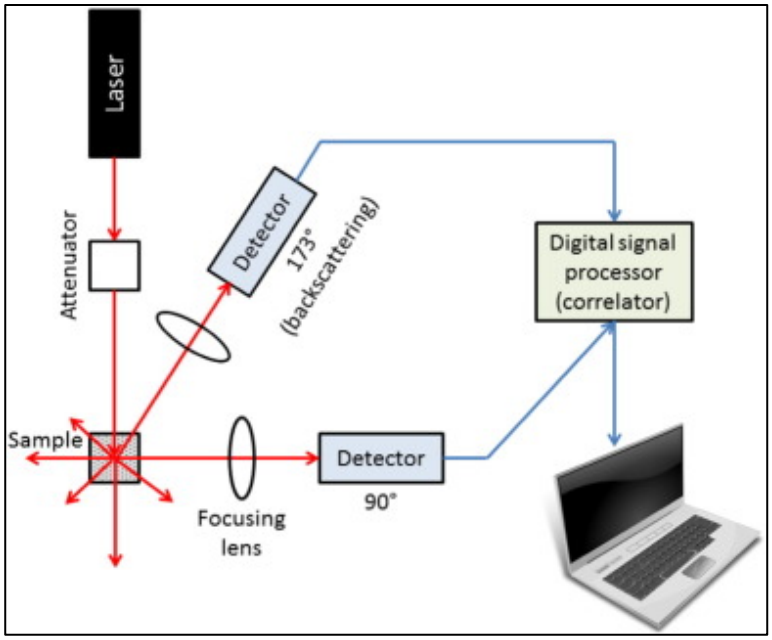

Figure 2.15. Schematic diagram illustrates the fundamental components of DLS. (Adapted from Ref [258]).

2.2.5.1. Practical details

Approximately 2 ml of sample should be prepared to obtain good quality data. Disposable plastic (10 × 10 mm) cuvettes were used. The sample should be clean, homogeneous and transparent without any precipitation.

2.2.6. Transmission Electron Microscopy (TEM)

A high voltage electron beam is used by the TEM to produce an image. A TEM's electron gun at the top produces electrons that move through the vacuum tube of the microscope. Then, the electromagnetic lens is used to concentrate the electrons into a very narrow beam. The electrons from this beam then pass through the extremely thin material and either scatter or strike a fluorescent screen at the microscope's base.

The specimen's images are displayed on the screen with each of its various components in various shades differently depending on density. Then, this picture can be either immediately examined in the TEM or captured on camera. A TEM's fundamental components are shown in

Figure 2.16 [259]. According to Louis-Victor de Broglie's theory, electrons contain both wave and particle qualities, and due to their wave-like characteristics, an electron beam can be directed and diffracted in a similar way to how light can. The following de Broglie equation states that the wavelength is inversely proportional to the momentum. Considering that the electron's velocity c in a TEM is a fundamental fraction of the speed of light. Thus, the wavelength is:

$$\lambda_e = \frac{h}{\sqrt{2\, m_0 \mathrm{E}\, (1+\frac{E}{2\, m_0\, c^2})}} \qquad (10)$$

Where m_0 is an electron's rest mass, *h* is Planck's constant, and E is the kinetic energy of a n accelerated electron. Typically, a filament usually tungsten produces electrons using a process known as thermionic emission [260].The electrons are then focused onto the sample using electrostatic and electromagnetic lenses after being accelerated by an electric potential measured in volts [260]. An example of TEM images are shown in Figure 2.17 [261].

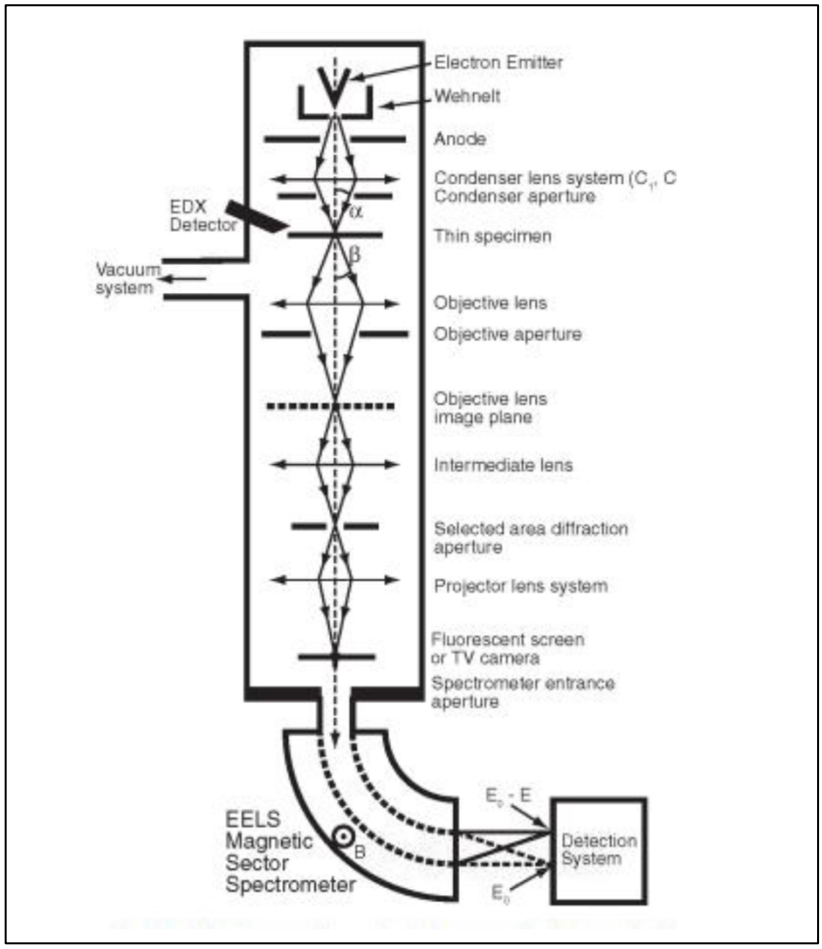

Figure 2.16. Schematic diagram illustrates the fundamental components of a conventional TEM. (Adapted from Ref [259]).

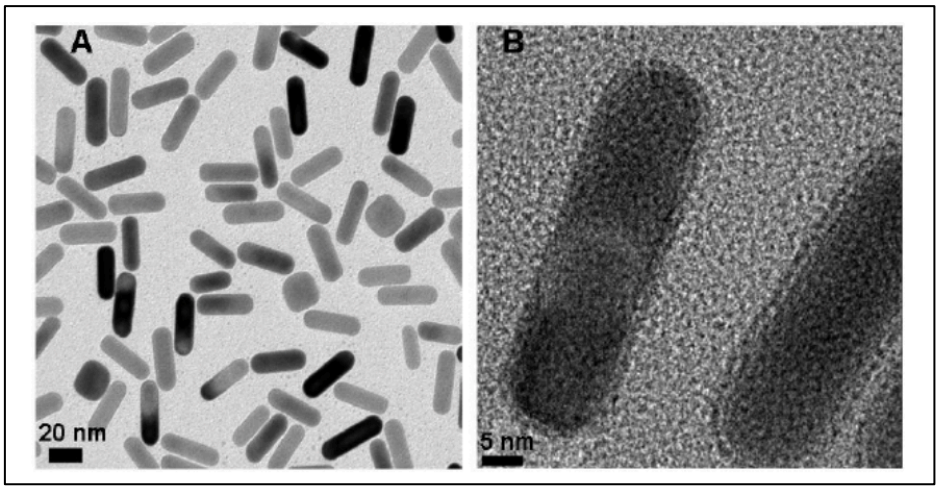

Figure 2.17 An example of TEM images of AuNRs of two magnification. (Adapted from Ref (261)).

2.2.6.1. Practical details

Transmission electron microscopy (TEM) was used to study the morphology and size of AuNRs. The TEM images of the synthesized AuNRs were obtained at a significantly high resolution (FEI Tecnai TF20 TEM) with an acceleration voltage of 120 kV. This microscopy provides fine detail about size, shape, aspect ratio, and silica coating. The samples were prepared by carefully depositing 2 µL of nanoparticle dispersion in Milli-Q water on a carbon coated copper grid 400 mesh (Agar Scientific) and left to dry. The size of the AuNRs and the silica shell thickness were measured using ImageJ.

2.2.7. Energy Dispersive X-Ray Analysis

Energy-dispersive X-ray spectroscopy (EDX) is used to study the elemental and chemical composition of materials and their surfaces. It is based mainly on an excitation the specimen by a source of X-ray. Due to the unique atomic structure of each element, EDX can study the elemental composition of the specimen [262]. When the electron beam is exerted on the sample, then the electron excitation and ionization occur. Then, this gives rise to excitation of an inner shell electron followed by ejection and leaving a hole in the inner shell. Then, de-excitation process occurs when after the relaxation of the ejected electron to the ground level. This process gives fingerprints of all elements in the samples, by illustrating X-ray peaks of each element [263]. The Figure 2.18. shows an example of EDX mapping images of Au@Ag core@shell was taken from [264]. Additionally, the EDX mapping images are combined with EDX spectra which normally shows peaks of the energies at which the greatest number of X-rays have been received as shown in Figure 2.19 [265]. Each one of these peaks is unique to a particular atom, they each stand for a different element. More concentration of the element is in the specimen results in a higher peak in the spectrum.

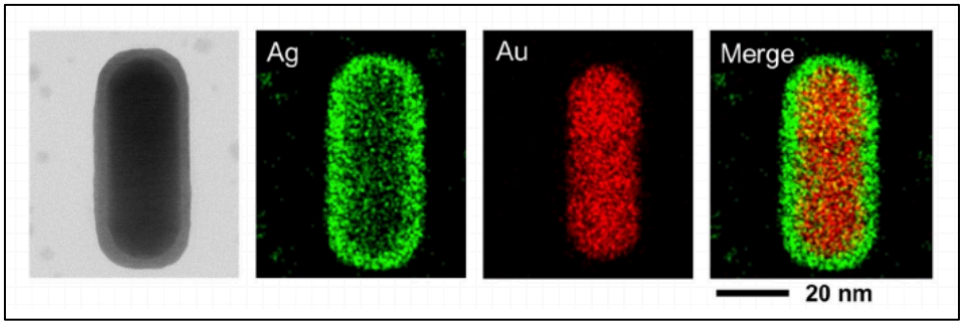

Figure 2.18. TEM images of an individual Au@Ag NR combined with the EDX element maps of maps of Au and Ag elements and the overlay maps image. (Adapted from Ref [264]).

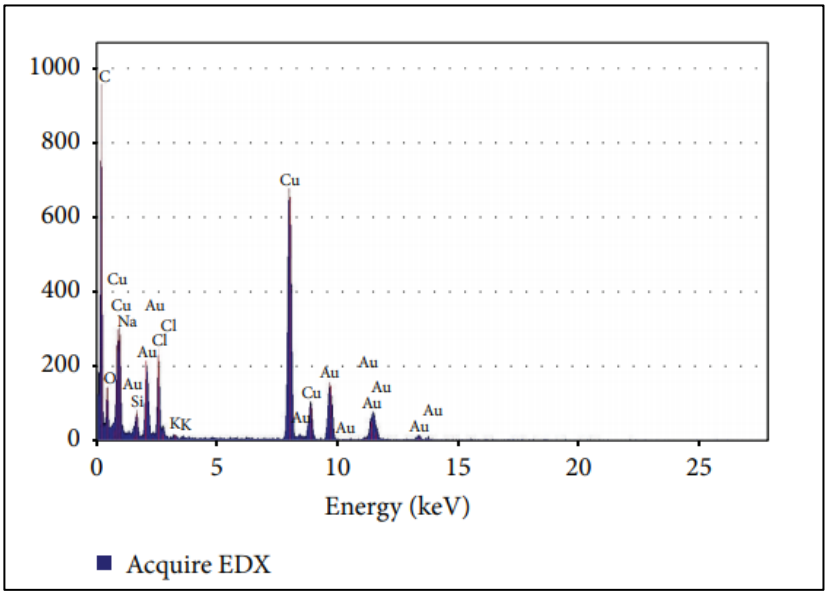

Figure 2.19. EDX energy spectra of prepared gold nanoparticles. (Adapted from Ref [265]).

2.2.7.1. Practical details

FEI Tecnai G2 TEM/STEM of 200 kV accelerating voltage and fitted with a Gatan Orius 600C camera. The samples were prepared by carefully depositing 2 µL of nanoparticle dispersion in Milli-Q water on a carbon coated copper grid 400 mesh (Agar Scientific) and left to dry. EDX spectroscopy was operated using an EDX detector (Oxford Instruments) and analyzed using digital micrograph software (Gatan). In this Thesis, I was interested to map Au, Si, Br, and N, because I assume that the synthesized gold nanorods consist of gold (Au), silica shell of SiO_2, and CTAB. The following table 2.4. illustrates the chemical structure of CTAB showing its chemical structure.

Table 2.4 The chemical structure of Cetyltrimetylammonium bromide (CTAB).

Chemical name	Structure	MW (g/mol)
Cetyltrimetylammonium bromide (CTAB)	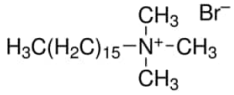	364.45

2.2.8. In situ heating transmission electron microscopy (TEM)

The thermal stability of AuNRs and AuNRs@SiO_2 were studied via in-situ TEM heating experiments. This microscopy is used to understand the morphology and behaviour of the material while heating. It uses a TEM microscope to make "in-situ heating" observations directly during heating by inserting a heating probe. The samples are dried on Si_3N_4 heating chip. Then, the chip is placed into the in-situ DENS heating holder. The specimen holder with an attached filament heater is inserted into the TEM. The filament is heated by applying an electric current.

2.2.8.1. Practical details

To prepare in situ heating TEM sample, the 2 µl of the samples were dried on Si_3N_4 heating chip. Two samples were tested, CTAB@AuNRs and AuNRs@mSiO_2. The samples were heated starting from room temperature to 1100 °C, by increasing the temperature 50 °C every 5 minutes. High-resolution TEM images were taken after 5 min dwell time at the target temperatures to observe the thermal stability of the two samples during heating.

2.2.9. Multispectral Optoacoustic Tomography (MSOT)

Optoacoustic phenomena have been used for decades in biomedical applications like spectroscopy and imaging, providing functional tissue data non-invasively [266, 267]. The foundation of optoacoustic imaging is the creation of acoustic waves after the absorption of pulses. By using the currently available nanosecond-range pulsed laser combined with acoustics detectors of high sensitivity. When laser pulses illuminate the phantom, causing local

heat after light absorption that generates pressure waves resulting from the contraction and expansion of the molecules as a response to the fast absorption of pulses [266-268]. Consequently, the mechanical waves at ultrasonic frequencies are generated. Then, acoustic detectors located near to the exposed tissue can collect these waves. The digital converters are used to sample the waves at the same time. Eventually, the post-processing algorithms is used to convert the obtained signals into an optoacoustic image by using post-processing algorithms. The optical absorption characteristics of the absorbers determine the amplitude of the broadband ultrasonic waves that are created. MSOT has a good tissue penetration compared to other optical methods, extending up to a few centimetres [269, 270] and allowing imaging in the clinical context. Figure 2.20 [271], it shows the MSOT set up and the operation principle.

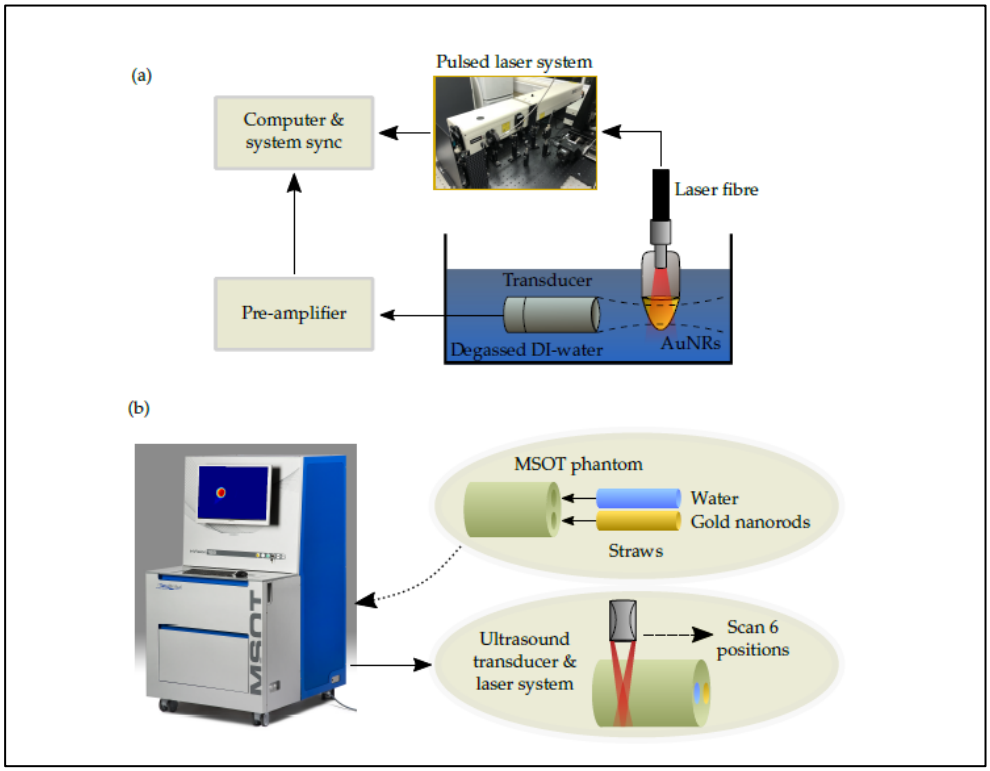

Figure 2.20. Schematic illustration of the experimental setup of the multispectral optoacoustic tomography (MSOT).

(a) The MSOT experimental setup a pulsed laser as an excitation source, agar tissue-mimicking phantom, transducer, and micro-objects. (b) The straws holding AuNRs and water as a baseline were put within a standard turbid, agar tissue-mimicking phantom. (Adapted from Ref [271]).

2.2.9.1. Practical details

By adjusting the laser wavelength to match a specific SPR peak of each AuNRs, a tuneable pulsed laser system (SureliteTM OPO Plus, Continuum®, San Jose, CA, USA) was utilized to produce a photoacoustic signal from the AuNRs. The laser's fluence ranges from 1 to 40 mJ/cm^2 with keeping the pulse width and the pulse repetition frequency fixed at 7 ns and 10 Hz, respectively. The pulsed laser spot size equals 5 mm. The AuNRs@$mSiO_2$ went through sequential dilution from their stock solutions of 1×10^8 NP/mL concentration to 1×10^{10} NP/mL. Then, the samples were sonicated in an ultrasound bath for 15 min. All samples AuNRs@$mSiO_2$ were prepared in a small plastic straw, closed at both ends, and diluted to a concentration of 1×10^{10} NP/mL. The straws holding AuNRs@$mSiO_2$ and a straw holding water as a baseline were put within a standard turbid, agar tissue-mimicking phantom. Each sample was scanned by multispectral scan from 680 nm to 980 nm from 6 different places along the straws to ensure reproducibility and in steps of 5 nm. The preclinical multispectral optoacoustic tomography (MSOT) system was used to determine the photoacoustic amplitude of the AuNRs@$mSiO_2$, the MSOT used is (inVision 128, iThera). Then, the viewMSOT software (viewMSOT 3.8, iThera) was used to analyse the MSOT images. Additionally, the PA values of AuNRs@$mSiO_2$were estimated at the SPR peaks.

2.2.10. Photothermal Reshaping of AuNRs@$mSiO_2$ Under Pulsed laser irradiation

During pulsed laser irradiation, the nanoparticle exposed to structural changes that could occur within 30 ps if their lattice temperature reach to values higher than its melting point [147]. Following that, phonon-phonon interactions disperse the stored energy to the environment (solvent) within 100 ps [187]. Consequently, the duration of a ns pulse exceeds the cooling period, causing a lower maximum particle temperature than that of a fs pulse of the same pulse energy [185]. Assuming that the thermalization that occur due to electron–phonon interaction is faster than external heat diffusion. The initial maximum temperature rise of the single irradiated NR with a single fs pulse can be estimated using the following expression [272]:

$$\Delta T^0 NP = \frac{\boldsymbol{\sigma}\mathrm{abs}\,\boldsymbol{F}}{V\,p\mathrm{Au}\,\mathrm{CAu}} \qquad (11)$$

Where σ_{abs} is the absorption cross section of gold nanorods. F is the fluence of the used laser, *V* is the volume of the single AuNR, p_{Au} is gold density, and C_{Au} is the gold specific heat capacity (129 J kg-1 K-1).

2.2.10.1. Practical details

In this section, the thermal reshaping of CTAB@AuNRs and AuNRs@mSiO$_2$ of (porosity degree of 43 %) of concentration of 50 µg/ml dispersed in were studied under NIR laser irradiation. The used pulsed laser was generated by a tuneable OPO laser system (Vibrant, OPOTEK, Inc.) of wavelength at 850 nm to match the LSPR peak of both CTAB@AuNRs and AuNRs@mSiO$_2$. The laser's output energy was raised to two fluences 10 and 20 mJ/cm^2, the pulse width is 7 ns, pulse repetition frequency is 10 Hz and the eliminated area is 6 mm. The aqueous solution of AuNRs@mSiO$_2$ was poured into a disposal cuvette and irradiated for different exposure time (0 s, 30 s, 1 min, 3 min, 5 min, 6 min, 7 min, and 10 min) under constant stirring with a magnetic bar. The pulsed laser illuminated the centre of the cuvette as shown in Figure 2.21. The extinction spectra before and after laser exposure were collected from a 100 µL AuNRs suspension in a 96-well microliter plate reader at room temperature using plate reader. The shape and morphology changes of the irradiated samples were monitored by TEM imaging. The ImageJ software was used to analyse the obtained TEM images.

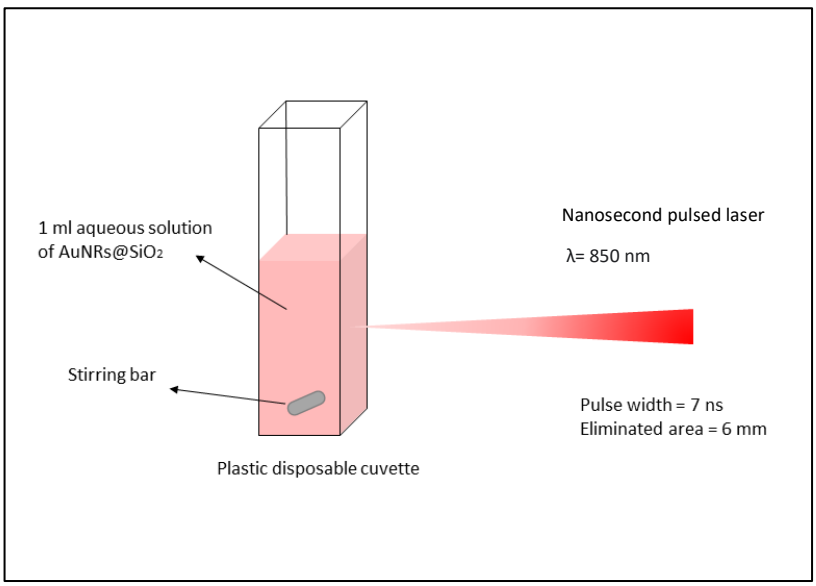

Figure 2.21. Schematic illustration of the experimental setup of photothermal reshaping of AuNRs@mSiO$_2$ under nanosecond pulsed laser irradiation.

2.2.11. Photothermal Reshaping of AuNRs@$mSiO_2$ of a Higher Porosity Under Pulsed laser irradiation

The thermal reshaping of AuNRs@$mSiO_2$ of porosity degree of 81% and concentration of 50 µg/ml dispersed in Milli-Q water were studied under NIR laser irradiation. All parameters (such as the laser's output energy, the pulse width, pulse repetition frequency, and the eliminated area) in this study were maintained as in the study in (Section 2.3.10), the only difference between these two study in the porosity degree of the silica shell of AuNRs@$mSiO_2$, the silica shell in this study is higher than the porosity degree of AuNRs@$mSiO_2$ studied in (Section 2.3.10 , porosity degree = 43 %). The aqueous solution of AuNRs@$mSiO_2$ was poured into a disposal cuvette and irradiated for only 1 min exposure time under constant stirring with a magnetic bar. The extinction spectra before and after laser exposure were collected from a 100 µL AuNRs suspension in a 96-well microliter plate reader at room temperature using plate reader.

2.2.12. Photothermal Reshaping of AuNRs@$mSiO_2$ Under Heating

AuNRs@$mSiO_2$ solution dispersed in Milli-Q water of porosity degree of 43 % of concentration of 50 µg/ml was poured into a glass vial and sealed. The solution was heated under stirring using dry heating bath at 50 °C for 33 days to study their thermal reshaping over time of heating. The extinction spectra before and after heating at different time points were collected from a 100 µL AuNRs@$mSiO_2$ suspension in a 96-well microliter plate reader at room temperature using plate reader.

2.2.13.Modelling of AuNRs@SiO_2 After Pulsed Laser Irradiation Using COMSOL

The COMSOL Multiphysics software was used to implement finite element analysis for AuNR and AuNR@SiO_2 before and after thermal reshaping. The use of COMSOL was made possible by its ability to produce correct solutions to the physical problem without the need for much previous modelling technique knowledge. Both AuNRs were embedded in water as surrounding medium to conduct this simulation. All values for length, diameter, aspect ratio,

and silica shell thickness were taken from the data obtained from TEM images of both AuNR and AuNR@SiO_2 before and after pulsed laser irradiation. Additionally, the COMSOL Multiphysics Material Library provides values of the refractive index of the surrounding medium. the COMSOL has the capacity to resolve intricate issues involving numerous physical phenomena, such as the electric-field enhancement and the temperature variation caused by the nanocomposite structure to an excitation light.

2.3. Materials

All solutions were prepared using Milli-Q water (18 M.cm).

- Synthesis

Reagent Name	Product No.	Supplier
Gold (III) chloride trihydrate	520918	Sigma–Aldrich
Hexadecylammonium bromide (CTAB)	H6269	Sigma–Aldrich
Sodium oleate	233978	Sigma–Aldrich
Sodium borohydride	452882	Sigma–Aldrich
Ascorbic acid	A15613	Alfa Aesar
Silver nitrate	11414	Fisher Scientific

- Surface Coating Experiments

Reagent Name	Product No.	Supplier
Tetraethyl orthosilicate (TEOS)	78-10-4	Sigma-Aldrich
DSPE-PEG_{2000} 1,2-distearoyl-sn-glycero-3-phosphoethanolamine-N-[methoxy(polyethylene glycol)-2000]	474922-26-4	Sigma-Aldrich
DPPC 1,2-dipalmitoyl-sn-glycero-3-phosphocholine	63-89-8	Sigma-Aldrich
Atto 488 DOPE 1,2-Dioleoyl-sn-glycero-3-phosphoethanolamine labeled with Atto 488	67335	Sigma-Aldrich

- Tissue Culture

Reagent Name	Product No.	Supplier
Dulbecco's phosphate–buffered saline	14190-136	ThermoFisher
Foetal bovine serum	A3160801	Fisher Scientific
RPMI 1640 + GlutaMAX media	11875-093	Gibco Life Sciences
DMEM + GlutaMAX media	11574486	Gibco Life Sciences
TrypLE express	12604013	Fisher Scientific
MTT	M-2128	Sigma,Cat.
Cell Counting Kit-8 (CCK-8)	96992	Sigma-Aldrich

- Consumable

Reagent Name	Product No.	Supplier
0.22 µm–pore syringe filters	SLGP033RS	Millipore
96 well plates, clear	3599	Corning
Quartz cuvettes (10x2 mm Light Path)	HL115-F-10-40	Hellma Analytics
TEM grids	S147-4	Agar Scientific

- Other Buffers, Acids, Solvents... etc

Reagent Name	Product No.	Supplier
Phosphate Buffered Saline PBS, pH 7.4	10010023	
Methanol	20847	VWR
Ethanol	E/0650DF/17	Fisher Scientific
Chloroform	22711	VWR
Hydrochloric acid (12.1 M)	UN1789	Fisher Scientific

3. Synthesis and Characterisation of Gold Nanorods Before and After Silica Coating

3.1. Motivation

Gold nanorods (AuNRs) possess unique optical and photothermal properties that enable them to be used for photothermal therapy [271]. For clinical photothermal therapy applications the AuNRs must be (i) able to absorb strongly in the biological window (i.e., the so-called first biological window with wavelengths ranging from 700 nm to 950 nm (NIR-I)) [189], (ii) colloidally stable so that they have a long-shelf, (iii) highly efficient at converting photon energy to heat to minimise healthy tissue from being exposed to laser light [146], (iv) photothermal stability for sufficiently long enough to perform a treatment, and (v) safe for the patient (e.g., no toxicity).

As-prepared AuNRs are capped typically by a cationic cetyltrimethylammonium bromide (CTAB) bilayer, which plays a significant role as stabilizing agent in AuNRs synthesis [273, 274]. Despite CTAB's unique properties as a surfactant and a detergent; the CTAB coating of AuNRs is not ideal for biological applications because studies have shown they have toxicity even at low concentrations. This is partly due to the electrostatic interaction between the highly positively charged and the negatively charged nanoparticles and cell membranes, respectively [275]. Generally, surfactant molecules have a striking similarity that cause disruption to the architecture of membrane lipid bilayer when they interfere with membrane lipid bilayer of cells [276]. CTAB was found to be a very effective surfactant to disrupt the cells [277]. Ray et al. [275] reported that CTAB left in solution must to be <1 μM to be not toxic for cells. Additionally, during the photothermal therapy, CTAB fails to prevent this heat induced reshaping of CTAB@AuNRs [278]. Consequently, the heat induced reshaping effect causes the NIR optical absorption peak to shift and the absorption at the laser wavelength is decrease [279].

To overcome these drawbacks, the CTAB layer can be passivated, or displaced, from the surface of the AuNRs by another post-synthesis procedure. The materials used to achieve this should be highly chemically and thermally stable, nontoxic, effortlessly functional by chemical

groups for further coating or targeting, and optically transparent at the desired photothermal therapy wavelength; to minimise the absorption and scattering potential of these coating material at LSPR peak of AuNR after coating, this leads to the desired efficiency and selectivity of the energy-to-heat transduction [280]. Coatings such as layer-by-layer (LbL) polyelectrolyte films, PEG derivatives, omega-alkanethiol, or lipids have been applied to AuNRs [55, 281] and do satisfy some of the requirements, but they all have some weaknesses. The LbL polyelectrolyte coating has shown only an improvement in AuNRs dispersion [282], as well as being slow to add and difficult to manage [283]. The polymer layers showed good colloidal stability of AuNRs; however, after the laser irradiation they only slowed the rate of reshaping. [158, 284]. On the other hand, Akiyama et al. [285] and Chen et al. [286] reported that PEG-coated AuNRs slowed the shape change under pulsed laser irradiation resulting in either a spherical or ellipsoidal shape. Self-assembled monolayers (SAMs) on gold that were prepared by adsorbing alkanethiols showed moderate stability at room temperature, but rapidly undergo desorption at elevated temperatures [287]. Phospholipids exhibited excellent stability in different biological medium in comparison to other surface modification with high biocompatibility [288]. However, they fail to prevent thermal reshaping and obtained shape changes were consistent with the thermal reshaping seen in other heated CTAB AuNRs [288].

Several researchers have investigated the replacement of the CTAB with a stable inorganic protective layer such as a silica shell [82, 286]. Silica's photothermal stability, chemical stability, and easy fabrication have made it a promising coating for AuNRs to overcome the challenges of using CTAB capped-AuNRs for photothermal therapy applications. With all these considerations in mind, in this Chapter, I discuss the preparation, characterization, optical properties, colloidal and thermal stability of AuNRs before and after silica coating. Additionally, here I provide a detailed study of the stability of the silica shell in photoacoustic imaging under high-energy nanosecond pulsed laser.

3.2. Gold Nanorod Characterisation

The AuNRs were fabricated using a binary–surfactant seedless synthesis (described in Chapter 2, section 2.1.1). The seedless synthesis approach is not widely adopted but the most advantageous aspect is the combining of the nucleation and growth into a single, simple, and fast step in one pot procedure, resulting in an anisotropic growth [36, 289]. This protocol demonstrated good reproducibility and uniformity as confirmed by the features seen in UV–Vis spectra, e.g. narrow symmetric absorption bands. Figure 3.1a shows the variation in LSPR position as function of the several concentrations of both CTAB and NaOL. The UV-Vis absorption spectra show the impact of the CTAB and oleate concentration on LSPR position, with all other components held constant.

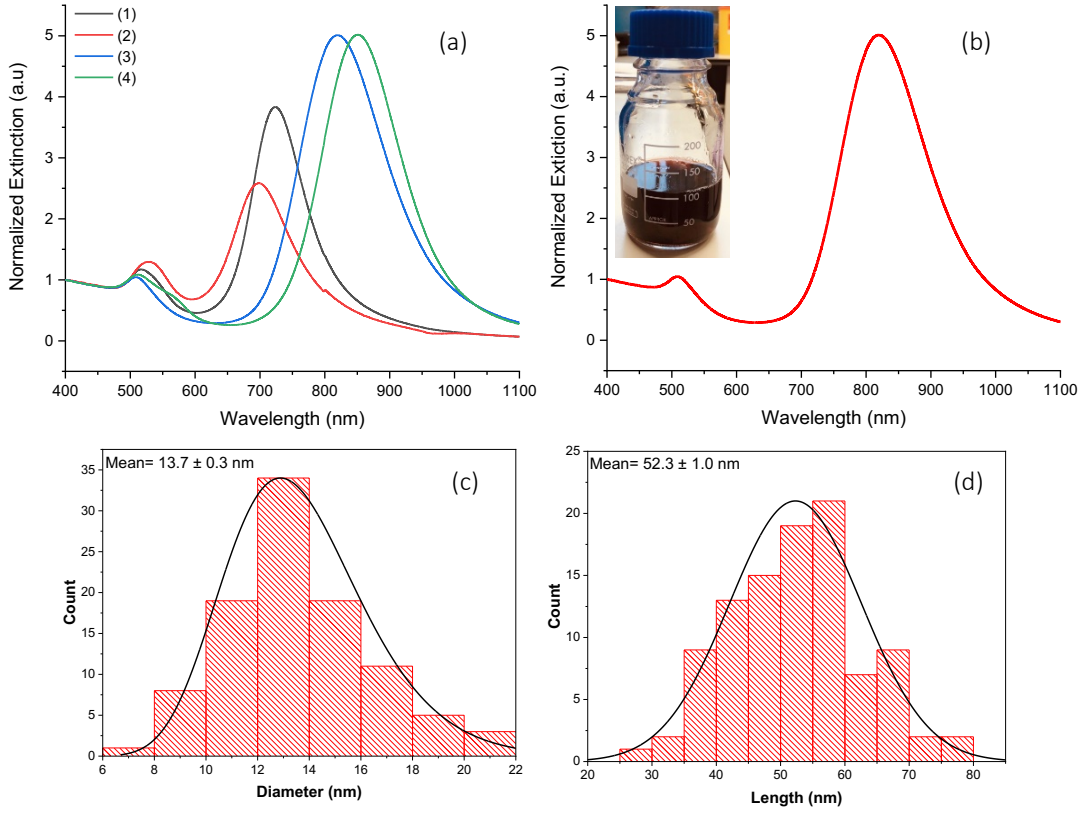

Figure 3.1. Gold Nanorod characterisation.

(a) UV–vis spectra of four solutions showing the impact of CTAB and oleate concentration on LSPR position. Spectra are 1) 60mM CTAB_12.5mM NaOL, 2) 60mM CTAB_20mM NaOL, 3) 40mM CTAB_12.5mM NaOL, 4) 40mM CTAB_20mM NaOL. All Spectra have been normalized at 400 nm. (b) UV–vis spectrum of synthesized AuNR of surfactant concentration of 40mM CTAB_12.5mM NaOL. (Inset: Photo of a 100 mL of synthesized AuNR). (c, d) Length and diameter histograms, respectively of batch in plot b derived from TEM imaging; the average length and diameter are indicated in the plots.

Different concentrations of CTAB and NaOL were added to the growth solution of AuNRs as listed in Table 3.1. Over these ranges 40 mM CTAB and 12.5 mM NaOL to 40 mM CTAB 20 mM NaOL, a narrow LSPR peak was found in the NIR region. Additionally, the TSPR peaks show different width as a result of adding different concentrations of CTAB and NaOL.

Table 3.1 The concentration ratio of CTAB and NaOL of the reaction mixture used in the seedless synthesis of the AuNR.

Batch	CTAB concentration (mM)	NaOL concentration (mM)	LSPR wavelength (nm)
1	60	12.5	725.9 ± 0.1
2	60	20.0	699.6 ± 0.2
3	40	12.5	821.4 ± 0.1
4	40	20.0	852.5 ± 0.1

The appearance of a shoulder at 550 nm in spectrum 4 (Figure 3.1a) is due to the presence of Au nanospheres resulting in a decrease in the shape yield. It was found that the addition of 40 mM CTAB and 12.5 mM NaOL (batch 3) provided the best results in NIR region, making them well suited for use as plasmonic photothermal therapies, their absorption spectra are shown separately in Figure 3.1 (b), with the inset photo showing the reddish-brown colour of a 100 mL of synthesised AuNRs. It displayed transverse and longitudinal plasmonic peaks at 508 ± 1 nm and 821 ± 1 nm, respectively. The corresponding full width at half-maximum (FWHM) of LSPR peak that was calculated from the UV-Vis spectra was found to be 158 nm. The TSPR peak of (batch 3) shows the narrowest peak comparing to other concentrations corresponding to high yields of AuNRs. Additionally, it has been demonstrated that the quality of NR samples related to the ratio between the longitudinal and transverse resonance absorption maxima is A2/A1 = A∥/A⊥. The higher the ratio the higher the quality of NR in the sample. [290] In our sample, the ratio A∥/A⊥ has a value of about 5, which corresponds to excellent quality.

The size and morphology of AuNRs were studied by using TEM. The length and diameter distribution histograms are shown in Fig 3.1c &d (n=100) have means of 52±1 nm and 13.7 ±0.3 nm, respectively with hemispherical caps on both sides, correspond to an aspect ratio of

~ 3.8. The synthesised AuNRs by using this protocol showed a good degree of monodispersity as illustrated in the wide–field TEM image (Figure 3.2).

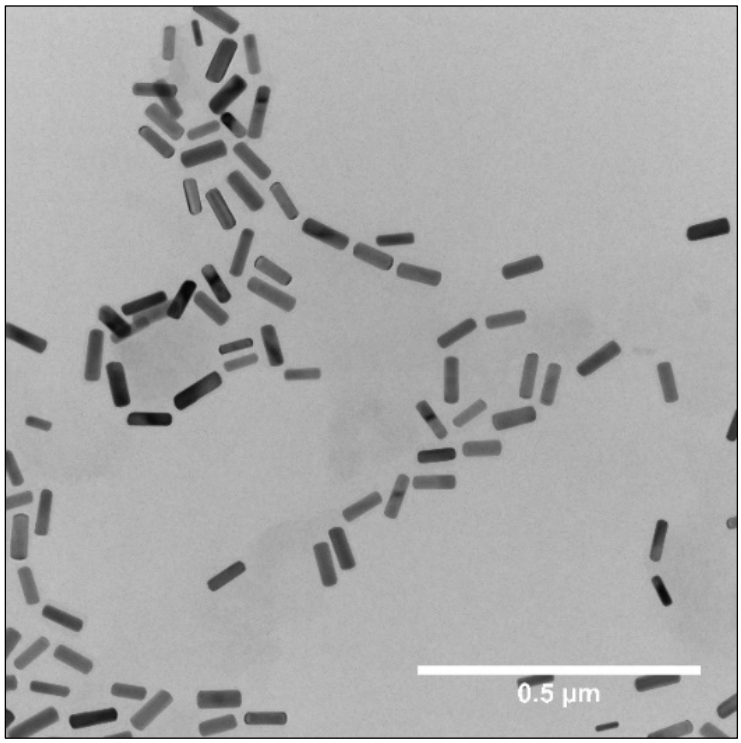

Figure 3.2. TEM image of AuNR.

Wide–field TEM image of AuNR batch in (figure 3.1, b) synthesized using a 40 mM CTAB and 12.5mM NaOL showing good monodispersity and good uniformity. (Scale bar: 0.5 µm).

3.3. CTAB Bilayer Thickness on Au Nanorods

Using CTAB is essential in in almost all AuNRs synthesis, due to its ability not just to direct the growth of AuNRs but also to stabilize them after synthesis. In literature, the thickness of surfactant CTAB bilayer was measured by a small angle x-ray (SAXS), neutron scattering [291] and TEM to be 2 nm [292]. The possible bilayer structure of CTAB on the AuNR surface and their molecular structure was detailed in Chapter 1. To measure the CTAB bilayer thickness of our synthesized AuNRs, several TEM images were taken. The TEM images of closely packed AuNRs were recorded. Figure 3.3 shows AuNRs almost touching each other. The gap between the AuNRs is likely to be due to the CTAB layer between them. By analysing the mean gap size one can estimate the CTAB thickness. The thickness of the CTAB bilayer was estimated by calculating the distance from the surface of one AuNR to the closest neighbour AuNR as shown in Figure 3.3. It was observed that the neighbouring AuNRs were by a consistent distance. The

histogram of an average of 100 NRs pairs, shows that the average gap between AuNRs is 2.4 nm, given that each AuNR will have a CTAB bilayer this would suggest the CTAB layer thickness on a AuNR is approximately 1.2 nm. This estimated thickness value of CTAB bilayer is thinner than the values in literature which suggested the CTAB bilayer thickness range between 3.0 and 3.9 nm [293]. CTAB has a molecular length of around 1.5 to 2 nm. The thinner than expected layer of CTAB is likely to be due to the partial removal of CTAB in the cleaning process, along with vacuum/drying effects causing the CTAB to be compressed (compared to when dispersed in water) [294].

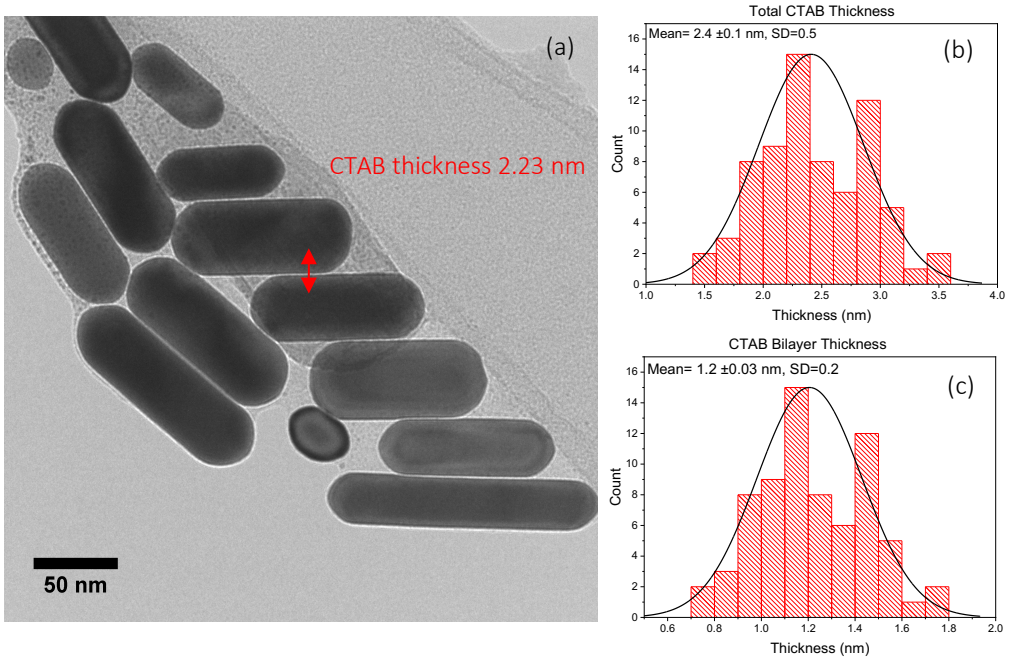

Figure 3.3. CTAB bilayer thickness.

(a) TEM image of synthesized AuNRs showing CTAB bilayer thickness. (b, c) Total CTAB thickness between two AuNRs and CTAB single bilayer thickness histograms, respectively derived from TEM image; (Scale bar: 50 nm).

3.4. Characterisation of Silica Coated-Gold Nanorods

In the second synthetic stage, the surfaces of CTAB-capped AuNRs were coated with silica shell via the base catalysed condensation of silane using precursor tetraethylethoxysilane (TEOS) that hydrolysed in methanol. The encapsulation of CTAB-stabilized AuNRs with silica shells was accomplished in a single step, and with no need to use any coupling agents as the primer. Before the silica coating stage, the excess CTAB was removed from the solution leaving

some CTAB in solution stabilized the AuNRs throughout coating stage and provide a CTAB template for the TEOS to hydrolyse, leading silica condensation.

To analyse the silica coating AuNR, both UV–vis absorption spectra and TEM images were taken. (Figure 3.4 a) shows the CTAB coated AuNRs had a strong absorption peak at 823 ± 1 nm. After the silica shell growth, the LSPR peak of AuNRs shows a redshift to 849 ± 1 nm, i.e., a red-shift of 26 nm. A shift in the LSPR peak was expected because it is dependent on the shape, size of AuNR and the refractive index of the medium [295]. Additionally, it was reported that TSPR of AuNR is insensitive to the changes in their aspect ratio and the refractive index of surrounding medium [296]. However, their LSPR is highly sensitive to any change of the refractive index and shows red-shift with the increase of aspect ratio [128, 297-299]. Thus, in this work, the LSPR band shows red shift to longer wavelength as the refractive index of the surrounding medium increases, whereas the TSPR band remains the unchanged. The refractive index of silica is higher than that of CTAB and water (the refractive index of CTAB, water, silica are n=1.44, n=1.33, and n=1.45, respectively) [300, 301]. These observations are consistent with what has been reported in literature and can be used as an indicator of the successful silica coating on AuNRs [302, 303].

To confirm that silica was formed on the AuNR surfaces, TEM analysis was performed before (Figure 3.4 b) and after (Figure 3.4 c) silica shell growth. Figure 3.4c shows a shell, which is much less electron dense than the Au, around each AuNR, which was not present before the TEOS reaction. This suggests that CTAB-capped AuNRs were successfully coated by silica. The AuNRs were uniformly and completely coated by a smooth silica shell and there were no silica nanoparticles without the Au core or uncoated AuNRs observed in TEM images. It is important to note that CTAB micelles van serve as a template for silica deposition. The growth of silica layer on the nanoparticle surface passed through stages: firstly silica oligomerization, following by formation of silica/CTAB particles, and finally and aggregation of the silica/CTAB particles [304]. Because the AuNRs are mostly coated by CTAB bilayer, the silica/CTAB particles have a tendency to aggregate on the nanorod surface, preventing any free silica nanoparticles formation [70, 304].

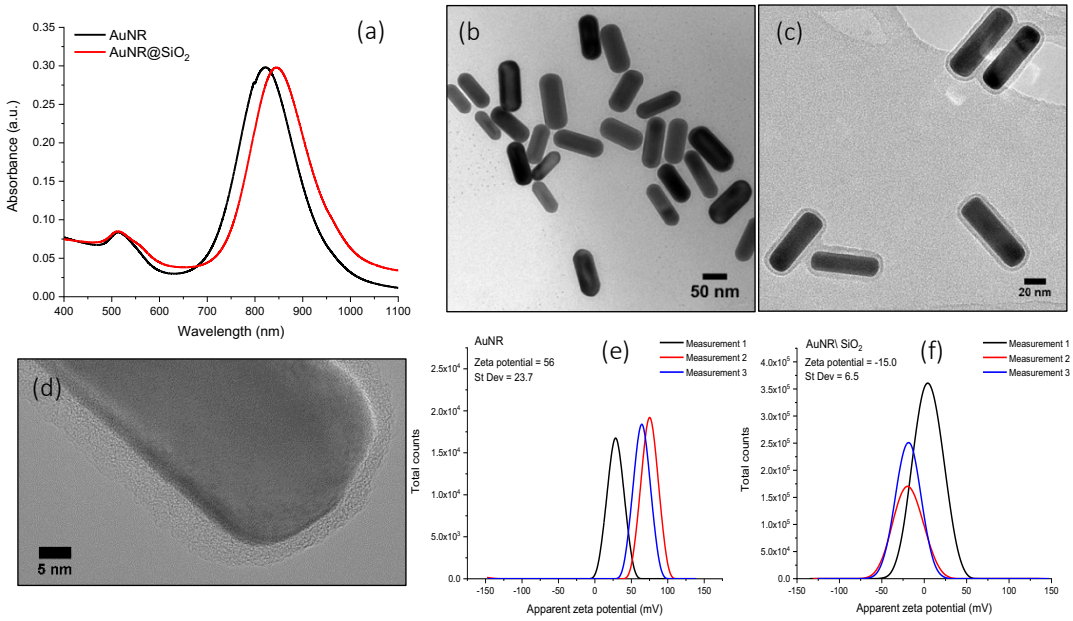

Figure 3.4. UV–vis absorption spectra, TEM images and Zeta potential of AuNRs and AuNRs@SiO_2.

(a) UV–vis absorption spectra of AuNRs and AuNRs@SiO_2. (b) TEM images of AuNRs synthesized by the seedless synthesis AuNRs/CTAB before silica coating; (Scale bar: 50 nm). (c) after silica coating; (Scale bar: 20 nm). (d) High magnified TEM image of silica coated AuNRs showing the silica shell; (Scale bar: 5 nm). (e, f) Zeta potential value of AuNRs and AuNRs@SiO_2 dispersed in Sodium chloride NaCl of pH 6.

Surface zeta potential of AuNRs coated with CTAB and SiO_2 were taken to determine the surface charge as presented in Figure 3.4 (e, f). Present results show that AuNRs that functionalized with CTAB are highly cationic +56 mV. After silica coating, CTAB layer was coated by SiO_2 shell which changed the polarity of the charge to become negatively charged with a zeta potential of -15 mV. The surface modification of AuNRs with a silica shell was successfully achieved, by the injection of (TEOS) in a mixture of mixture of methanol and water to the CTAB-capped AuNRs solution as shown in TEM image in Figure 3.5 (a).

The silane coupling agents on the silica shell enables the AuNRs for further surface modification. The silica shell thickness was measured to have a homogeneous thickness of 6.8 ± 0.2 nm (as shown in Figure 3.5b). One of the advantages of SiO_2 detailed in Chapter 1 is the transparency to electromagnetic radiation in the visible and NIR from 300 to 800 nm, which asserts that the optical properties of AuNRs are slightly modified after silica coated. However, the high extinction coefficient is maintained.

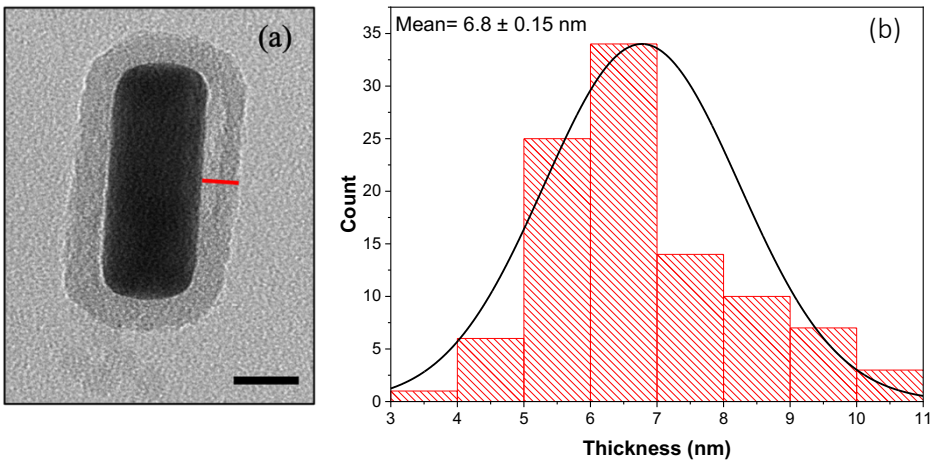

Figure 3.5. TEM image of a single silica coated AuNR.

(a) An enlarged TEM image of a single silica coated AuNR showing a silica layer coating uniformly the AuNR. The red line denotes to the silica shell thickness. (b) Silica shell thickness histogram showing the thickness distribution of 100 AuNRs@SiO2 were determined using ImageJ. (Scale bar: 10 nm).

3.5. Dispersive X-Ray Analysis (EDX)

Energy Dispersive X-ray analysis mapping was utilised to determine the elemental composition of AuNR as well as their distribution. The synthesized hybrid nanomaterial should consist of core of AuNR stabilized with a thin layer of CTAB coated with silicon dioxide (SiO_2) shell. Therefore, Au, Si, N, and Br elements were specifically mapped. The EDX elemental mapping images in Figure 3.6 (a) clearly reveals the presence of Au surrounded Br, N, and Si elements. Br molecules have been detected covering the core Au surface confirming that the remaining CTAB layer served as an organic template during silica coating process. Both Br and N elements are assumed to be associated with the CTAB present.

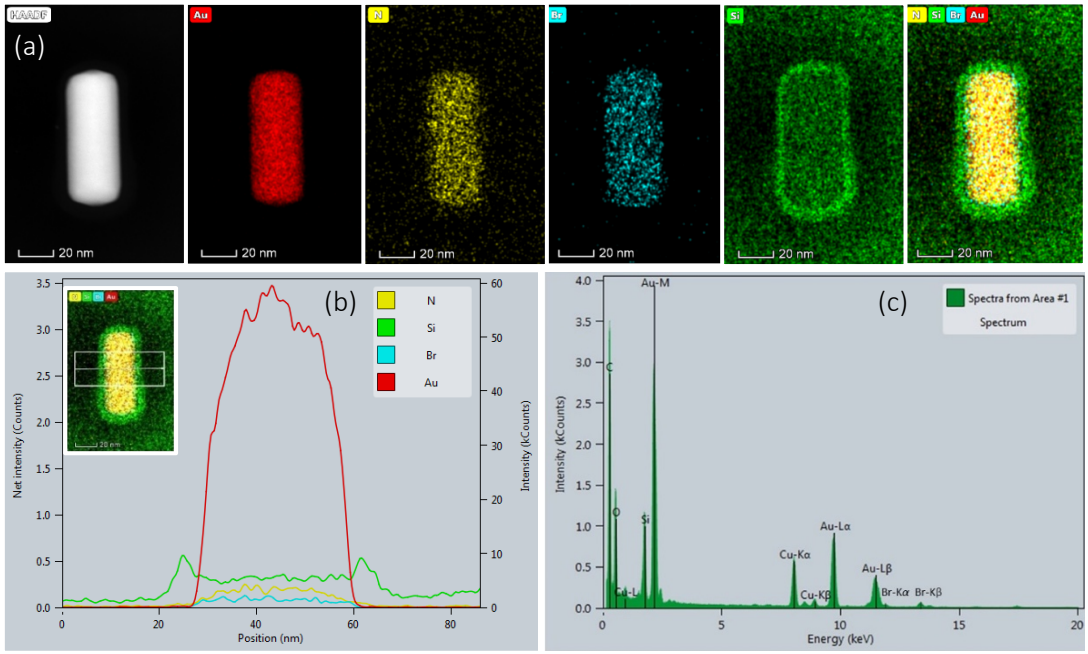

Figure 3.6. EDX elemental mapping of AuNR shows the core-shell elemental composition of AuNR@SiO_2.

(a) STEM-HAADF, Au, N, Br, Si, and their overlaid image respectively. The scale bar represents 20 nm. (b) EDX line scanning of AuNR@SiO_2 (Inset: EDX line scanning profile of cross section of AuNR@SiO_2). The inset image indicates the area of AuNR@SiO_2 that were used to measure the signal intensity of Au, Si, N, and Br. (c) Corresponding EDX spectra of AuNR@SiO_2 supported on a copper grid. SiO_2 shell thickness about 7.0 ± 0.2 nm. (Scale bar: 20 nm).

The overlaid image shows that AuNR is coated by two-layers consist of an inner thin CTAB bilayer (blue + yellow) and an outer SiO_2 layer (green). This observation is supported by EDX line scanning profile of cross section of AuNR@SiO_2 to measure the elements quantitative analysis as shown in the inset image in Figure (3.6 b). The measured profile line-scan analysis shows that the Si is mainly on the surface of the Au core and uniformly distributed overall the AuNR with a silica shell thickness of 7.0 ± 0.2 nm. EDX Energy dispersive X-ray (EDX) spectrum reveals the characteristic peak positions of each element corresponding to the possible electron transmissions in its shell. In the EDX spectrum in (Figure 3.6 c), the presence of Au is indicated by a strong Mα peak at 2.12, Lα peak at 9.7 keV and Lβ 11.4 keV. Br was detected by two weak peaks at 11.9 and 13.3 keV, which provides evidence of the presence of CTAB on the surface of AuNR. Moreover, the presence of silica coating on the surface of AuNR was confirmed by the presence of the Si EDX peak at 1.7 keV. The Cu signal is an artifact of the Cu coated TEM grid and is identified by two K (α & β) peaks and one Lβ peak at 8.0 and 8.9 keV and at 0.94 keV, respectively. The sample has excess Si element in the background as shown in Figure 3.6 (a) image Si. Therefore, further cycles of centrifugation were needed to remove excess silica left in the solution.

3.6. Thermal Stability of AuNR and AuNR@SiO2 Using In-situ TEM Heating

This experiment aims to study the effects of silica coating on the thermal stability of the AuNRs from low temperature up to their melting point. A comparison between the thermal stability of CTAB-capped AuNRs and AuNR@SiO_2 was made. It is worth mentioning that many studies have addressed that CTAB-capped AuNRs are thermally unstable [305]. CTAB-capped AuNRs started deforming and losing their anisotropic character at many hundreds of degrees below the bulk melting temperature of Au (1064°C) [306, 307]. The surface area to volume ratio of a nanoparticle is larger than the bulk material, thus this means the surface energy will be increased resulting in a reduction in melting point of nanoscale material. However, this decrease in melting point is only really observed in small metal nanoparticles (e.g., <10 nm). More important is the mobility of the surface atoms of metal nanoparticles [308]. Simulations and experimental evidence have shown that the surface atoms are liquid-like, even below the melting point, allowing them to flow. Through thermodynamic arguments such as Gibb's free energy, it is clear that there is an energy cost to being non-spherical, and therefore, just like a droplet of molecules in a liquid droplet, the surface atoms can rearrange to minimise the surface area and become spherical. However, for Au there is an energy barrier to achieving that lower energy state. Generally, heating of any organic compound (180 up to 320 °C) temperature leads to its decomposition [309]. To overcome this reshaping problem, coating the AuNRs with inorganic shell of higher melting temperature, such as silica, should enhance the thermal stability of AuNRs. Researchers have found that using silica shell prevents the diffusion of Au surface atoms [310-313]. In this study, to understand the kinetics of reshaping and the thermally induced deformations of AuNRs and AuNR@SiO_2 through in situ heating transmission electron microscopy, the shape and phase transition behaviours of both AuNRs and AuNRs@SiO_2 was monitored by taken TEM images with increasing temperature. Firstly, both AuNRs and AuNRs@SiO_2 were dried on a TEM Si_3N_4 heating chip. High-resolution TEM images of AuNRs were taken after 5 min of heating at temperatures of 20°C, 200°C, 400°C, 800°C, 1000°C, and 1200°C.

The reshaping and melting point decrease of nanoparticles have previously been observed and characterised for several types of nanoparticles [314-318]. Because of the high surface-to-volume ratio of nanoparticles, their melting point is lower in comparison to the bulk

material. As a result, the surface free energy of the particles increases [314]. For bulk gold the melting point is at 1064 °C [319], in the case of gold nanoparticles, the melting point was observed at lower value than this. However, studies have reported that large AuNRs less resistant to thermal reshaping under laser irradiation compared to small AuNRs (widths < 25 nm) [238], due to their ability of heat dissipation to the surroundings medium at a faster rate more than large AuNRs. Thus, the optical absorption of the particles will also decrease as their size decreases [320]. This could explain why AuNRs in our study are thermally resistant to relatively high temperature.

In anisotropic growth of AuNRs, CTAB is likely bound strongly to the sides Au(1 0 0) and Au(1 1 0) facets than on Au(1 1 1) to the tips, which consequently contributes to anisotropic growth [321]. Therefore, this suggests that the lower packing density of CTAB bilayer on Au (1 1 1) facet induced higher volatility and lower stability at this facet. As the temperature was increased from RT to 100°C, the aspect ratio of CTAB-caped-AuNR started slightly decreasing. The melting temperatures of CTAB is relatively low at 237 to 243 °C [45]. At this melting point temperature, CTAB bilayer starts to decompose when the surface temperature of CTAB-capped AuNRs exceeds 200°C. The TEM images in Figure 3.7 show shape defects were observed when the AuNR reached 200°C. The CTAB-stabilized AuNRs showed that the surface reconstructions at the tips were ongoing. The observed effect that could be explained by mobility and migrating of the surface atoms of the rod tip into a more spherical shape. This has been reported by G Opletal et al, [150], their simulation of the heating process of AuNR after 9 ns heating confirms that the least stable facet of the AuNR is (111), atoms were observed migrating from the considerably lower energy (111) surface to the higher energy (100) surface.

Based on the above findings, deformation of AuNRs would take place during in-situ TEM if the CTAB layer were removed. Increasing the temperature of CTAB-stabilized AuNRs would leads to CTAB decomposition and a slight diffusion of the Au surface atoms of the AuNRs was observed at 200°C along with a decrease in aspect ratio of AuNR. Horiguchi et el, [284] reported that after excess CTAB removal using centrifugation, the remaining CTAB bilayers on the surfaces of AuNRs would be most likely unstable. The outermost part CTAB molecules were regularly exchanged by unbound CTAB molecules from the bulk water phase. Leading to thin CTAB bilayers on the centrifuged AuNRs to be dynamic and unstable showing

photothermal reshaping during rapid heat diffusion [189]. At 1000 °C the CTAB-stabilized AuNRs significantly deformed losing their anisotropy property, leading to indeterminable AR. Studies have shown that AuNRs undergo shape change through stacking faults and twinning even below the melting temperature [155]. It was found that CTAB-capped AuNRs with an average AR = 2.6 ± 0.02 (78 ± 0.2 nm x 29.6 ± 0.1 nm) were completely reshaped after heating below (1064 °C) the Au melting point, see Figure 3.7, TEM image of 1200°C, with a reduced size due to evaporation.

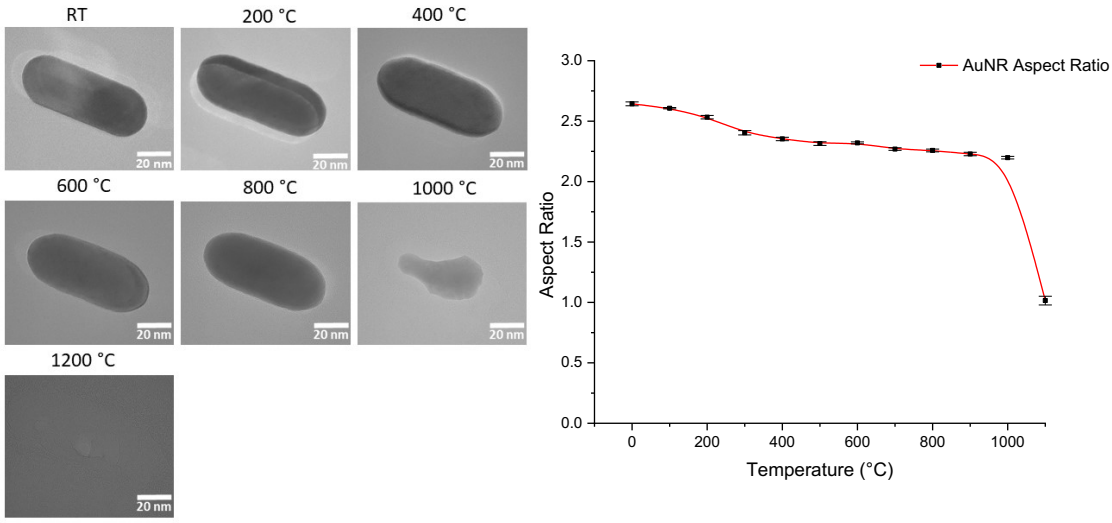

Figure 3.7. TEM images of AuNR in-situ heat from room temperature to 1200°C.

Images were taken after 5 min dwell time at the given temperature (Left). Aspect ratio of AuNR versus heating temperature calculated from TEM images after 5 min of heating (Right). The red line is a guide to the eye.

AuNR@SiO_2 samples were heated using the same in-situ heating system from room temperature to 1200 °C under vacuum. TEM images were taken after 0-, 5-, 10-, and 15-minutes dwell time at the given temperature as shown in (Figure 3.8). The TEM image of AuNR@SiO_2 at RT shows a 6.7 nm thick silica layer around the AuNR. The aspect ratio of AuNR@SiO_2 decreased from 3 to 2.7 when the temperature increased from room temperature to 200 °C. Then, the aspect ratio slightly decreased to 2.6 at 900 °C and no more decrease was detected (Figure 3.9c). However, at 800 °C the silica layer thickness started to decrease with diffusion of structural defects and become thinner even that it did not reach the silica melting point as shown in (Figure 3.9a). The silica shell thickness at room temperature was ~ 6.7 nm and after heating is 3.4 nm. That means the SiO_2 shell thickness

was reduced by the half after heating. Presumably, the semi-porous silica shell may have a structure and shape change as an effect of thermal annealing mechanism. The results showed the SiO_2 layer largely helps maintain an aspect ratio > 2.6 and appears to prevent the nanorods from becoming excessively distorted. The shape of the AuNR does however become more ellipsoidal after the heating.

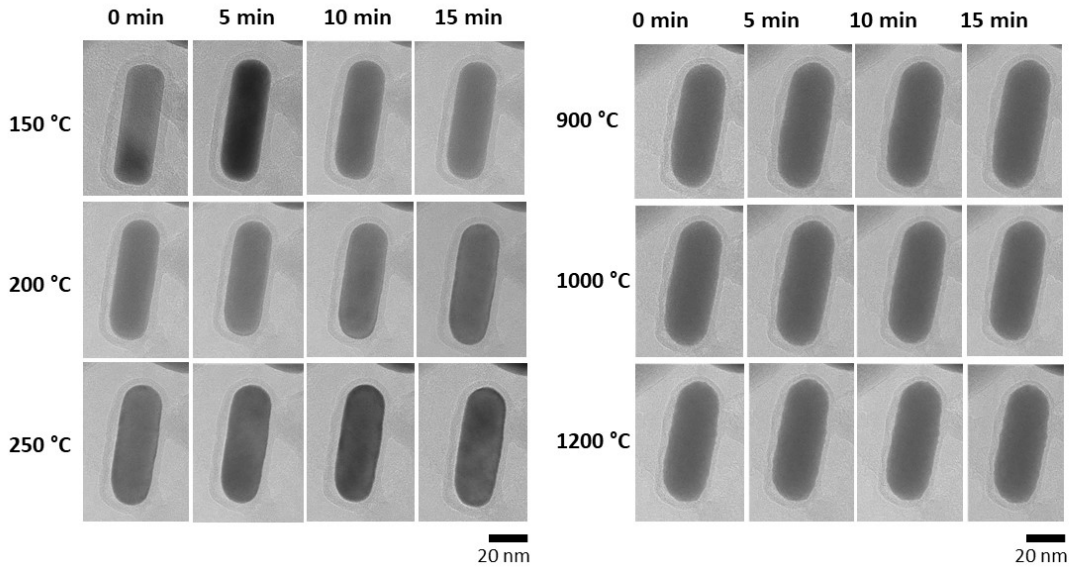

Figure 3.8. TEM images of AuNR@SiO_2 in-situ heat from room temperature to 1200°C under vacuum.

Images were taken after 0, 5, 10 and 15min dwell time at the given temperature. TEM image of AuNR@SiO_2 at RT indicating the presence of 6.7 nm thick silica layer around the gold nanorod.

As discussed earlier in EDX mapping and the CTAB bilayer thickness on AuNR section, the AuNRs is coated firstly by a thin layer of CTAB and a thicker shell of SiO_2 about at 1.2 nm (but up to 4 nm in water). During heating, CTAB bilayer beyond a certain temperature is exposed to decomposition. Wang et al. reported that during the continuous heating, the surface atoms that are initially located in the caps of AuNR move toward the centre, whereas the surface atoms in the centre move away from the rod axis radially [322].Therefore, after heating our AuNR@SiO_2; its diameter increased from 19 ±0.04 nm to 21 ± 0.3 nm, by roughly the same value of the decomposed CTAB bilayer thickness. Subsequently, this has attributed in a decrease in the AR. To understand the behaviour of the silica shell formation between 800°C to 1100 °C, we should mention the transformation mechanism of the crystal phase of SiO_2. In general, the silica particles at nanoscale have an amorphous structured [323]. The transformation mechanism of the crystal phase of SiO_2 is controlled by the temperature and

pressure [324]. The crystal phase of SiO_2 polymorphs at normal pressure to the phase transformation of α-quartz to β-quartz occurs at 573°C, the phase transformation of β-quarts to β-Tridymite occurs 870 °C and phase transformation [325]. Two phases transformation occur during this experiment at 573°C and 870 °C. During the transition from α to β (First transition), the atoms in the crystal lattice are softly displaced, without any change in their places inside the lattice [326].

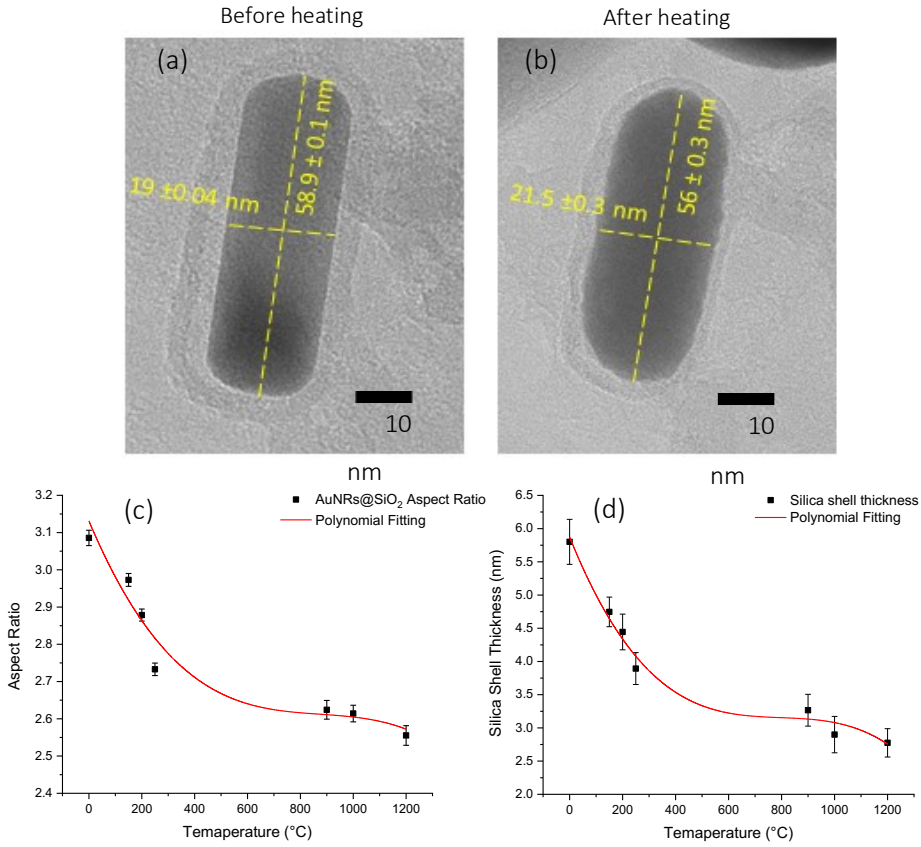

Figure 3.9. Comparison of AuNR@SiO_2 before and after in-situ TEM heating.

(a, b) TEM images of Silica coated-AuNRs before and after in-situ TEM heating at different. (c) Aspect ratio of silica coated-AuNRs versus heating temperature calculated from TEM images after 15 min of heating. (d) Silica shell thickness versus heating temperature calculated from TEM images. (Scale bar: 20 nm).

For a direct comparison of the thermal stability of AuNR and AuNR@SiO_2 and understanding the effect of silica shell on AuNR, the reduction percentage of their AR were compared using the same heat treatment for both as shown in Figure 3.10. The AR of both CTAB-capped-AuNR and silica coated-AuNRs slightly decreased with increasing temperature up to 900 °C. However, the uncoated AuNR showed a shape transformation to spherical shape as the temperature increased from 900 °C to 1000 °C. Further increase in temperature above

1000 °C has shown rapid melting for CTAB-coated AuNR as shown in (Figure 3.10) at 1200 °C. The melting point of bulk gold is 1,064 °C. However, melting point begins to decrease in particle size (typically the effects is seen most strongly when at a few nanometres in size) [327].

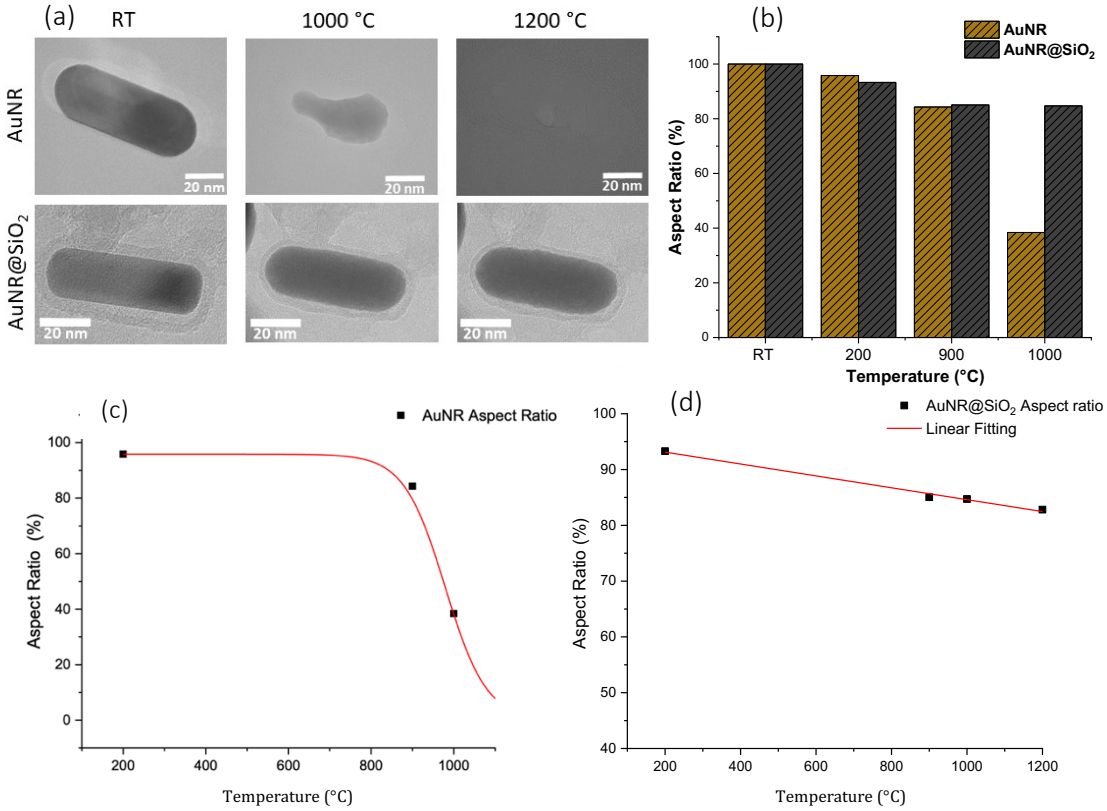

Figure 3.10. Comparison between AuNR and AuNR@SiO_2 before and after in-situ TEM heating.

(a) TEM images of AuNR and AuNR@SiO_2 before and after in-situ TEM heating at RT, 1000°C, 1200°C, (Scale bar: 20 nm). (b) Aspect ratio of AuNR and AuNR@SiO_2 versus heating temperature calculated from TEM images after 5 min of heating. (c) The change rate of AR for uncoated AuNR with heating temperature. The red line is to guide the eye. (d) The linear regression of the change rate of AR for AuNR@SiO_2 with heating temperature.

The silica shell with a higher melting point than the Au melting point (silica melting point is 1710 °C) has successfully prevented the Au nanorod shape change at high temperature ranges. The silica coated AuNR showed a slight change in AR from 200 °C to 800 °C. This could be due to presence of the CTAB bilayer on the Au allowing for greater mobility and diffusion of the Au surface atoms leads to a change in AR. Beyond 800 °C, the silica-coated AuNRs showed negligible change in AR even at the temperatures greater than the melting point of bulk gold (1064 °C). Maintaining rod-shaped morphology throughout the in-situ TEM heating as shown in Figure 3.10 (a, bottom). A structural rearrangement within the silica shell was

detected during the heat treatment. This happens due to the silica rearrangement that occurs amorphous silica reaches its glass transition temperature [328, 329]. Therefore, causing a small drop in AR. Gold atoms on surface of the AuNR tip showed higher mobility, diffusion, and rearrangement towards the centre of the rod. As the temperature was increased, the smooth surface with uniform thickness of AuNR@SiO_2 was observed to be rough as shown in (Figure 3.10a). Wang et al. [322] investigated the morphological and structural behaviour of AuNRs during continuous heating using molecular dynamic simulations. They found that during heating, the AuNR was slightly shortened at 241 °C. Then the AuNR showed further reduction in the length and became wider at 791 °C. Finally, the AuNR melted and transformed into a liquid sphere at 1195 °C [322].

The rate of change of AR of AuNR with heating temperature was higher when the silica coating is absent (Figure 3.9c). The change rate of AR for AuNR@SiO_2 with heating temperature showed a linear regression of (slope= - 0.012 ± 6.9 and intercept = 95.3 ± 0.6). Overall, at high temperatures, the rate of change of the morphology accelerates, leading to faster deformation at temperatures beyond 800°C. The findings are in good agreement with previous research [163, 330, 331]. These findings indicate surface melting and surface diffusion at temperatures substantially that are far below the melting point of bulk gold, as a result of the enhanced surface energy for a curved surface [163, 330, 331]. Taylor et al. have reported that rod AR and length affect the curvature at the nanorod tip [182]. The results show the silica shell effectively maintained the rod shape of the nanorod and protected it from turning into nanospheres even up to 1100 °C.

3.7. Photoacoustic Imaging

Photoacoustic (AP) imaging is beneficial during drug delivery to the target location biological application and to potentially generate temperature mapping during photothermal therapy [231]. AuNRs can be used as promising agents for use in photoacoustics, this is due to their unique optical and photothermal properties such as their large absorbance cross-sections which are controllable and their exceptionally high efficiency of photothermal conversion [332]. However, their wide absorption cross-sections and high heat production efficiencies lead to temperatures that are high enough to induce thermal reshaping for AuNRs

[271, 333]. Chen et al. [286] studied the stability of photoacoustic response of AuNRs@PEG and AuNR@SiO_2 of silica shell thickness of 20 nm by determining the PA amplitudes produced during pulsed of fluencies of 4 and 18 mJ/cm^2. Their results showed that AuNR@SiO_2 is more stable with higher photoacoustic signal compared to the AuNRs@PEG. The AuNRs concentration used to generate a PA signal has a significant effect on PA amplitude. The PA signal amplitude is dependent on the concentration of the AuNRs [334]. For clinical purposes, the concentration of AuNRs needs to be non-toxic to the healthy tissues as well as being able to produce detectable PA signals. Therefore, it is necessary to study the concentration dependence of the photoacoustic response of our AuNR@SiO_2, aiming to produce detectable PA signals without requiring many AuNR@SiO_2 in the region of interest. With all these considerations in mind, I discuss in this work the PA of AuNRs@SiO_2 with plasmon resonance in the near infrared (NIR) at a series of concentrations from 0 to 180 µg/ml. The intense irradiation with nanosecond laser pulses of wavelength range (680-950 nm) was applied and PA response were determined as a function of concentrations. The samples were assessed using a pre-clinical MSOT imaging system after being placed in an agar phantom to imitate the predicted irradiation environment *in vivo*. To obtain the mean value, the measurements were performed 5 times for each concentration. PA intensity values were calculated by calculating the mean pixel intensity (MSOT a.u.) of averaged the mean pixels intensity in the region of interest. PA response of the water was subtracted from that of the AuNR solutions to correct the spectra. As shown in figure 3.11 (a), the averaged maximum pixel intensity of PA signal of highest concentration of 180 µg/ml in Figure 3.11 (a) is shows good qualitative similarity to the UV–vis spectrum with blue shift. It has been reported that the absorption of small nanoparticles dominates their scattering (considering aspect ratio importance). However, the absorption of large nanoparticles is dominated by scattering [335]. The UV–vis spectrum is a total extinction (absorption + scattering), while the PA response is an absorption only. Thus, the blue shift of averaged maximum pixel intensity of photoacoustic signal was expected. The spectra over 850 nm become increasingly inaccurate, due to the increasing absorbance of water (the surrounding water) that limits the intensity of light to reach the sample, then restrain the PA signal as shown in Figure 3.11 (a).

In addition, the concentration dependence of the photoacoustic response of AuNR@SiO_2 was studied. As more particles are irradiated in a given unit volume, the higher PA response is deducted [336]. Thus, not surprisingly, PA response was found to be roughly linear below ~ 70 µg/ml with concentration as demonstrated in Figure 3.11 (b).

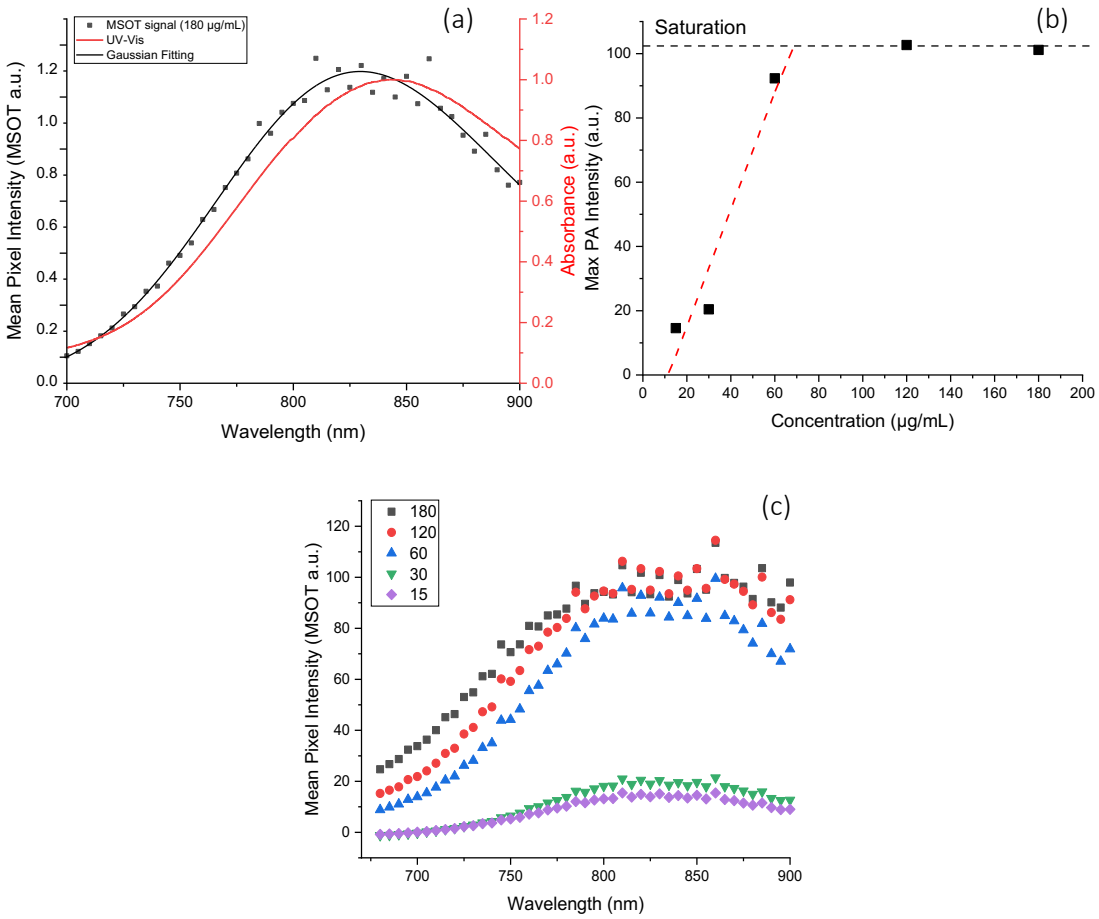

Figure 3.11. PA signal amplitude measured by the MSOT.

(a) The comparison the averaged maximum pixel intensity of PA signal amplitude measured by the MSOT of highest concentration of 180 µg/ml of AuNRs@SiO_2 and the UV-vis of the same sample before laser exposure. (b) The mean values of maximum pixel intensity measured by the MSOT versus AuNRs@SiO_2 concentration with a linear function below ~70 µg/ml. (c) Photoacoustic spectra as obtained from MSOT images (obtain from back projection algorithm). The data presented here are those determined from MSOT intensity maps during the first of the five runs show in fig. 3.12.

The strength of the PA response has started to become increasingly saturated, which has caused the peak of the particle response's spectral response to flatten out, as shown in the spectra 120 and 180 µg/ml samples. It is possible that this saturation results from the sample completely absorbing all incident light or from the system's transducers reaching their maximum negative pressure.

Based on the MSOT intensity maps in Figure 3.12, the former appears to be more likely, which show that small fraction of PA signal was produced inside the phantom, confirming that complete absorption of the incident light at the surface of the phantom resembling a ring shape. It was observed that the PA signal intensity of AuNR@SiO_2 decreased significantly after the fifth spectral scan for concentrations 60 µg/ml. As mentioned earlier, at higher concentrations the incident light is absorbed on the surface leading to the creating a narrow shell around the outside of the sample as shown in scans of 120 µg/ml and 180 µg/ml samples in Figure 3.12.

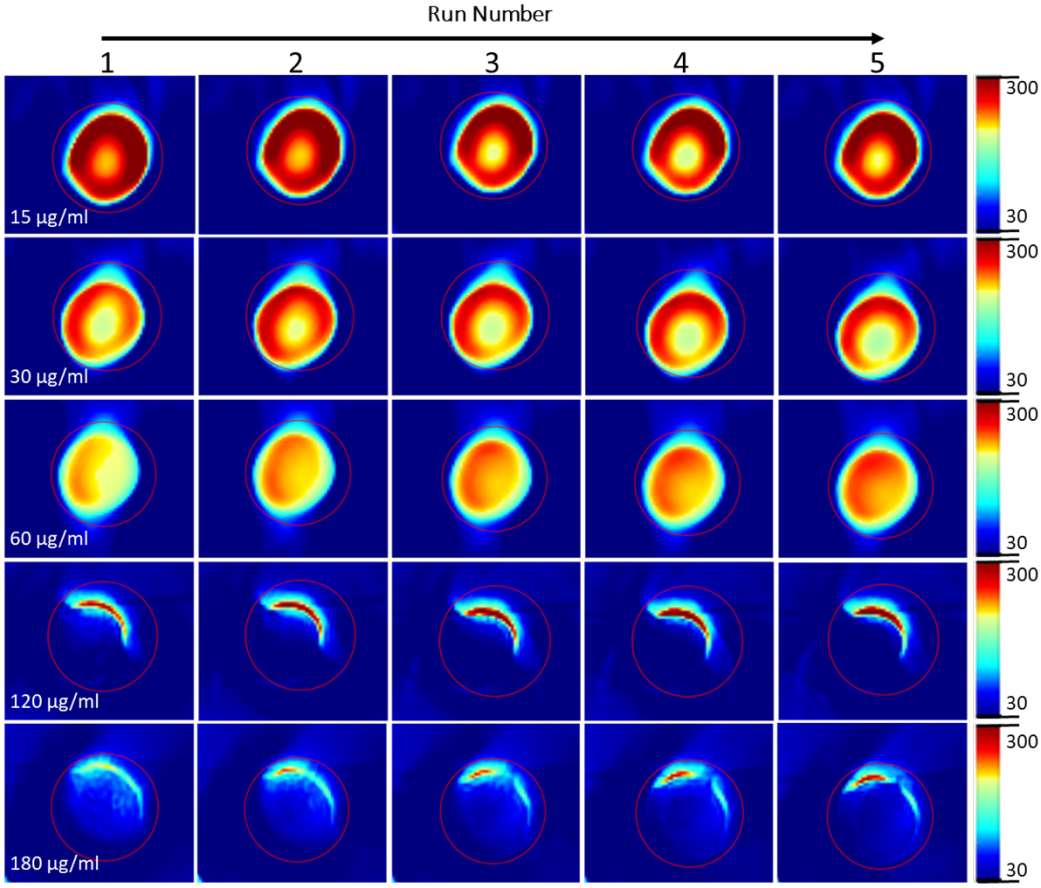

Figure 3.12 MSOT intensity maps of a single plane passing through an agar phantom with different AuNRs concentrations.

A linear reconstruction approach was used to compute the distribution pattern of the AuNR solution using data obtained from UV-vis spectra. The reconstructions have been limited to the region of interest surrounding the AuNR solution; each row is made up of a single measurement, with 5 repeat collected in sequence (displayed left to right). At 120 µg/ml, the incident light is absorbed on the surface leading to the creating a narrow shell around the surface particles.

It can be observed that with increasing concentration, the width of this ring decreases as due to the reduction in the penetration depth of incident light. It was also planned that this study will be supported by additional measurements such as UV-Vis spectrum and TEM images

of the particles after pulsed laser irradiation, but these are remained unaddressed in this thesis due to time restraints. However, the reshaping behaviour of AuNR@SiO_2 under pulsed illumination will be addressed separately in detail in Chapter 5.

3.8. Increasing the Porosity Degree of the m-SiO_2 Shell of AuNR@SiO_2

Mercadal, P.A. *et al* [241], published a method to determine the porosity degree of the silica shell of AuNRs@m-SiO_2. Their method is based on the use of the extinction spectra of AuNRs@m-SiO_2 combined with modelling the optical properties to measure the degree of porosity of the SiO_2 shell. It is well known that the pores in SiO_2 can be templated by CTAB micelles, therefore by forming the shell at a CTAB concentration above the critical micelle concentration (CMC) (reportedly, 0.0009 mol/L and 0.24 mol/L in water and ethanol, respectively) results in a shell with higher porosity [337]. The principle behind determining the porosity involves placing the AuNR@m-SiO_2 particles in medium with increasing dielectric constant. The solvent can diffuse through silica shell pores and therefore the effective dielectric constant (ε_{ef}) of the shell is given by.

$$\varepsilon_{ef} = (1 - f)\varepsilon_{SiO_2} + f\varepsilon_m \,, \qquad \text{(Eq. 1)}$$

Where, f is the fraction of porosity, ε_{SiO_2} is the dielectric constant of silica, and $\varepsilon_m$is the medium. Any change in the effective dielectric constant (ε_{ef}) of the surrounding medium causes a change in the peak position of the longitudinal LSPR band to shift. It is shown that the LSPR is sensitive to the refractive index of the first few nanometres surrounding the AuNR [295]. Thus, we applied this modelling to the optical properties of the optical properties of the AuNRs@m-SiO_2 used in these studies. The core shape and size of AuNRs@m-SiO_2 were kept the same during this study.

3.8.1. CTAB Extraction Refluxing

To determine the porosity of the silica shells, it was necessary to extract the CTAB from the fabricated silica shells after synthesis, else it is possible that the CTAB 'template' could remain in the pores and prevent the medium from entering the pores. The AuNRs@m-SiO_2 with different of porosity were formed by adding various concentrations of CTAB of 5 $\times 10^{-3}$ and10 $\times 10^{-3}$ M to the AuNRs solution during silica coating growth. The CTAB was extracted from the pores by refluxing in an ethanol and hydrochloric acid solution. The reflux technique used in this study was selected to be at a low temperature, to prevent any structural reshaping to the AuNRs. Therefore, the AuNR@SiO_2 were dispersed in ethanol HCl solution and refluxed at 70 °C for 2 hours. The samples were cooled and washed before their extinction spectra were taken using UV-Vis spectroscopy. The extinction spectra of CTAB@AuNRs and AuNRs@mSiO_2 after adding various concentrations of CTAB during silica coating synthesis and dispersed in water after CTAB extraction are shown in Figure 3.13.

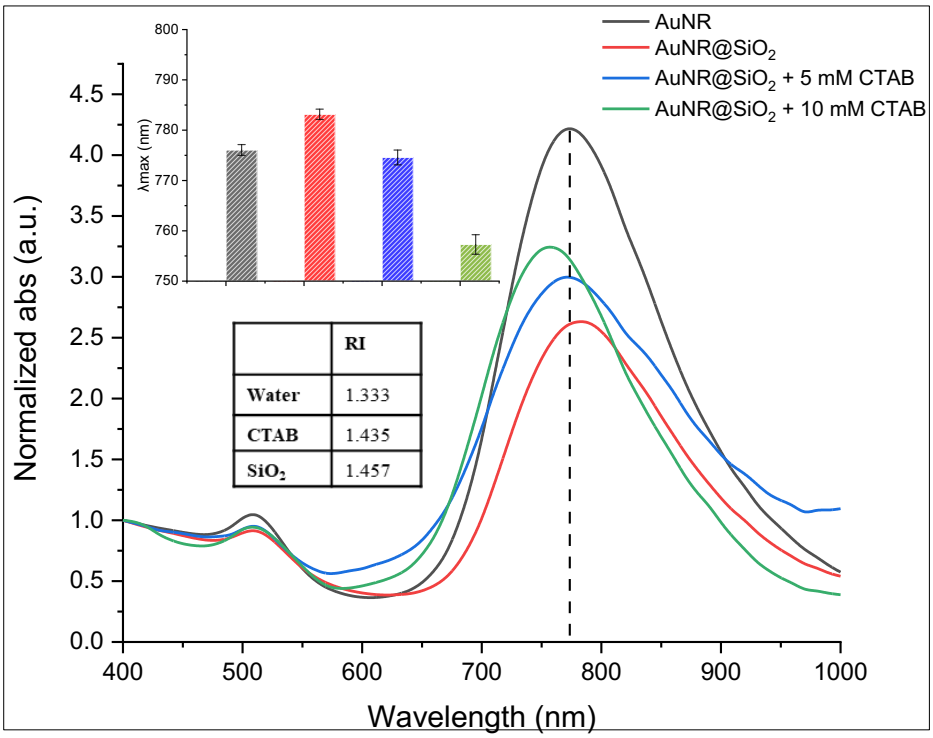

Figure 3.13 UV–vis absorption spectra of AuNRs, AuNRs@mSiO_2, and AuNRs@mSiO_2 after adding various concentrations of CTAB.

The CTAB concentrations of 5 X10^{-3} and 10 X10^{-3} M were added to the AuNRs solution during silica coating synthesis. (Inset) The LSPR peak shifts of AuNRs before and after silica coating and adding different concentrations of CTAB. The samples were dispersed in MQ water. The table is showing the RI of the water, CTAB, and SiO_2.

The LSPR peak of CTAB@AuNRs dispersed in water is at 776 ± 1 nm these AuNRs are coated with a thin layer of CTAB. However, after silica coating with no additional CTAB added to the solution, the LSPR peak redshifted to 783 ± 1 nm due to the higher RI of SiO_2, which has been discussed in detail earlier in this Chapter. However, the AuNR@mSiO_2 of 5 x10^{-3} M of CTAB and after extracted the CTAB show blue shift to 774.5 ± 1.5 nm, which is a shorter wavelength than AuNR@mSiO_2 with no CTAB added, and slightly similar to the peak position of CTAB@AuNRs. This confirms the reduction in the refractive index surrounding the AuNRs. Moreover, the successful extraction of CTAB and having more water (lower RI) in pores of silica shell causing the LSPR peak position to blue shift. Further increase in CTAB of 10 x10^{-3} M concertation during silica shell growth showed a higher blue shift of LSPR peak indicating higher porosity. These observations were in good agreement with what was reported by Mercadal, P.A. *et al* [241]. The red and blue shifts of AuNRs before and after silica coating of two different concentrations of CTAB are shown in inset in Figure 3.13.

3.8.2. Measuring the Porosity of Silica Shell

After CTAB extraction using a refluxing method, the AuNR@mSiO_2 of different degree of porosity were centrifuged to form pellets, then they were dispersed into different concentrations of a mixture of glycerine/water of range of 20-70% v/v. Therefore, they were left for 30 min under stirring at room temperature.

The UV-Vis absorption spectra were taken for the AuNRs to define their LSPR peaks position. It was observed that the LSPR peak of AuNR@mSiO_2 of different degree of porosity showed red shifts with increasing the amount of glycerine of the mixture as shown in Figure 3.14.

This result was explained by Mercadal, P.A. *et al* [241], their assumption is that the formed volume fraction of silica pores are loaded with the different mixtures of the medium surrounding of different refractive indexes (RIs) that cause redshifts due the change in their viscosity. Therefore, the degree of uptake was analysed by plotting the relation of the LSPR peak position of AuNRs versus the effective dielectric constant (ε_{ef}) of the corresponding medium. The dielectric constant of SiO_2 is represented in the equation 1 with ε_{SiO2} = 2.1 and ε_m =1.77 for water, respectively. By fractionally mixing glycerine and water it is possible to adjust the medium's refractive index. Note that, $\varepsilon_m = RI^2$ is the dielectric constant of the respective

solvent mixtures, determined as the average of water and glycerine dielectric constants of each mixture.

The extinction spectra in Figure 3.14 show that the LSPR peak position of all three different AuNRs@mSiO$_2$ show red shifts with increasing the effective dielectric constant (ε_{ef}) of the mixture. This is in agreement with what was published by Mercadal, P.A. *et al* [241]. They assumed that the pores of the silica shell are filled with a mixture whose their ε_{ef} is linearly fitted with their LSPR peak positions of AuNRs.

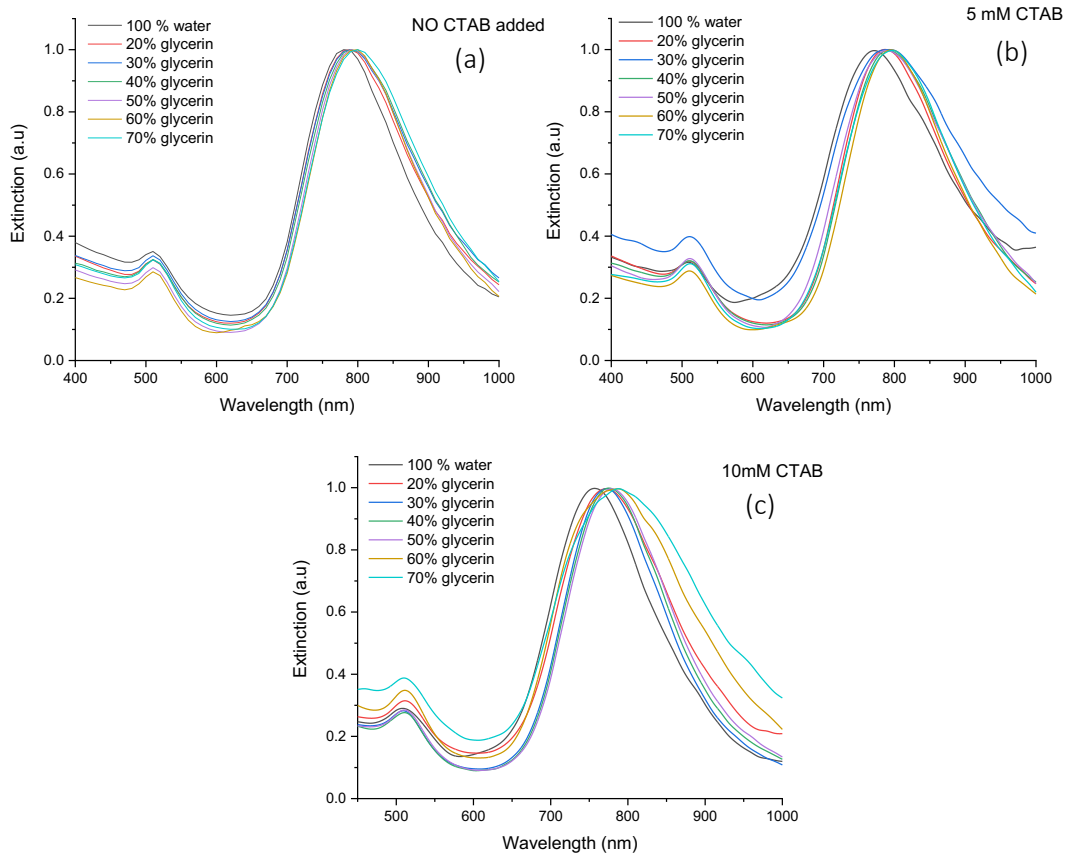

Figure 3.14 UV–vis absorption spectra of AuNRs@mSiO$_2$ after adding various concentrations of CTAB.

(a) No CTAB added (b) 5 X10^{-3} and (c) 10 X10^{-3} M to the AuNRs solution during silica coating synthesis. All spectra were normalized to λ_{max}.

Mercadal showed that the resonance condition of the AuNR can be approximated to,

$$-Re(\varepsilon_{Au}) = \left(\frac{1-L_3}{L_3}\right)\varepsilon_{ef}\,, \qquad \text{(Eq. 2)}$$

Where the term on the left is the real part of the dielectric constant of the gold (at the LSPR frequency), ε_{ef} is the dielectric constant of the shell, and L_3 is the so called depolarisation shape factor which is dependent on the aspect ratio of the AuNR. This shape factor is given by,

$$L_3 = (1 + AR)^{-1.6}, \qquad \text{(Eq. 3)}$$

Where AR is the aspect ratio of the AuNR core inside the shell. These approximations hold for when L_3<0.135, and the AR of the both the AuNR core and AuNR@SiO_2 are greater than 2.5. These conditions are true for the samples in this study. Therefore, for a given AR and shell dielectric constant we can calculate the required real part of the complex dielectric constant of gold. The LSPR wavelength position is then found by looking up the wavelength of gold which gives the real part of the refractive index. The dielectric properties over the UV to NIR range are well-known. In other words, if the AR of the AuNR is known and the LSPR band has been experimentally determined, the dielectric of the shell ε_{ef} can be determined using Eq.2 and Eq3. Eq 1. gives an expression for the dielectric constant of the shell and if the medium and SiO_2 dielectric constants are known then the porosity factor, f, can be calculated. To achieve this, a range of dielectric medium was prepared by mixing glycerine with water by well-defined volume fractions, to give a range of ε_m from 1.768 to 2.047. The position of the LSPR band of the AuNR@SiO_2 sample collected for the full range of ε_m. The LSPR peak wavelengths can used to find the dielectric constants of gold, i.e. $Re(\varepsilon_{Au})$ can be found from the dielectric properties of bulk gold [338]. Eq 4 can be found by substituting Eq. 1 and Eq. 3 into Eq. 2.

$$-Re(\varepsilon_{Au}) = \left(\frac{1-(1+AR)^{-1.6}}{(1+AR)^{-1.6}}\right)\left((1-f)\varepsilon_{SiO_2} + f\varepsilon_m\right) \qquad \text{(Eq.4)}$$

Eq. 4 can then be fitted to experimentally determined $Re(\varepsilon_{Au})$ versus ε_m values to find f and AR. This fitting was achieved using a python 3 script, with $Re(\varepsilon_{Au})$ converted into wavelength by approximating the relationship to be linear (fitted over the range used),

$$. \qquad Re(\varepsilon_{Au}) = -0.0847\lambda + 43.718 \qquad \text{(Eq. 5)}$$

where, λ, is given in units of nanometres. The results are presented in Figure 3.13 and the values obtained from the fits are given in Table 3.2. Our results show that for 10 mM of CTAB the porosity fraction *f* was 0.81. This indicates 81 % of the shell corresponds to the medium. The lower CTAB concentration of 5 mM caused a lower porosity of 0.64. Additionally, the results of AuNR@SiO_2 that were fabricated without adding additional CTAB to the solution during the silica shell growth had a porosity of 0.43, i.e. the silica has a lower porosity. In our study, the (ε_m) for each glycerine/water mixture was adopted from Mercadal, P.A. *et al.* [241]. While the AR of the AuNRs were different from Mercadal and the thickness of the shell was much thinner, our resultant porosity values were consistent with their report.

*Table 3.2 CTAB concentrations for the AuNRs@m-SiO_2, their AR, and F values correspond to the porosity degrees at each CTAB concertation. * We assume this samples contain excess CTAB left in the solution after cleaning. The F values are measured with considering that all the silica pores are filled with surrounding mixtures.*

Sample	CTAB (mM)	Slope	Error (±)	AR	Error (±)	f	Error (±)
AuNR@$mSiO_2$	*	59.4	3.6	3.9	0.01	0.43	0.03
AuNR@$mSiO_2$	5	90.3	19.6	3.9	0.04	0.64	0.1
AuNR@$mSiO_2$	10	110	11.7	3.8	0.02	0.81	0.1

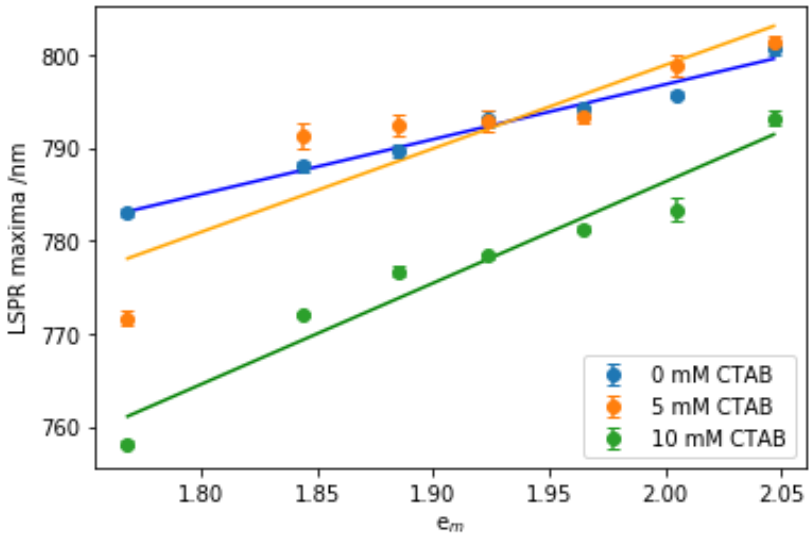

Figure 3.15 The relationship between the positions of LSPR peaks and ε_m the dielectric constant of the solvent mixtures of the surrounding medium.

The (bule) line is the AuNRs@$mSiO_2$ that were fabricated without adding CTAB, we assume the pores were made due to the excess CTAB in the solution. The (orange) line is the AuNRs@$mSiO_2$ fabricated after adding 5 mM of CTAB. The (green) line is the AuNRs@$mSiO_2$ produced after adding 10 mM of CTAB.

3.9. Conclusion

The AuNRs were synthesised using a binary–surfactant seedless protocol. Direct coating of AuNRs with silica by a seeded growth technique has been demonstrated to prepare the core–shell particles containing single gold cores. The silica coating was accomplished by one single step of the addition of TEOS/ethanol to the gold colloid dispersed in water. The method required no silane coupling agents or aqueous silicate. The EDX mapping confirmed that the synthesized AuNR@SiO_2 consists of core of AuNR stabilized with a thin layer of CTAB coated with (SiO_2) shell. In-situ TEM heating experiments of both CTAB-AuNR and silica coated AuNR investigated the morphology changes of individual Au nanorod during the heating. Surface modification used in this work has significantly enhanced thermal stability of AuNR at high temperature. The silica shell of thickness 7 nm has enhanced the photoacoustic signal of AuNRs and effectively maintained the rod shape of the nanorod and protected it from turning into nanospheres even up to 1200 °C. The results of our study suggest that silica coated AuNRs are promising candidate with high thermal stabilities for photothermal therapy. Additionally, AuNRs@SiO_2 provided a stable photoacoustic signal. Therefore, these findings suggest AuNRs@SiO_2 can potentially be used efficiently for photoacoustic imaging without altering the optical absorption. In this chapter, I have increased the porosity degree of the silica shell by varying the CTAB concentrations higher and lower than its (CMC) during the silica shell growth. I have determined the porosity degree of AuNRs@mSiO_2 from the LSPR peak positions and their respective volume percentage of water f in the m-SiO_2.

4. Surface Modification of Silica Coated Gold Nanorods with Phospholipids

4.1. Motivation

In Chapter 3, AuNR@SiO_2 were synthesized by the modified Stöber's process to coat the AuNR to provide more thermal stability and replace the toxic CTAB from the surface. However, further coating on the inorganic shell will help to reduce their toxicity, enhance their compatibility with biological cells, prevent agglomeration, and enable targeting [339]. Surface coating and modification of nanoparticles is commonly used to also improve the cell internalization rate and control drug release [340]. However, Zhu, X.M., et al [217] studied the cytotoxicity of AuNRs@mSiO_2 in human glioblastoma U-87 MG cells and mouse macrophage RAW 264.7 cells; both cells lines were incubated with various concentrations of AuNRs@mSiO_2 (5 –150 µg Au.mL^{-1}) for 24 h. Their results showed moderate cytotoxicity at 150 µg Au mL^{-1} (55 % and 65 % of viability) of U-87 MG and RAW 264.7 cells, respectively [217]. In addition, other studies claimed that due to the stability of SiO_2, it consequently results in poor degradation and are therefore accumulated in some living organs (e.g., kidneys) [341, 342]. Another potential issue of using AuNRs@mSiO_2 for biological applications, is the possible cytotoxicity of the CTAB molecules that are present in the mSiO_2 shell. To overcome such drawbacks, it has been reported that coating the silica shell with organic layers is an effective way to extend their use in a wide range of biomedical applications [93, 94, 101, 343]. For instance, Mueller, E.N, *et al* have coated the silica shell of AuNRs@SiO_2 with dodecyltrichlorosilane and then coated them with lipid monolayer [336]. However, Song, Z., *et al* have used an inorganic component hydroxyapatite for drug delivery purposes due its biocompability and biodegradability [67]. Hence, they found these nanocomposites are compatible for MCF-7 cells. Overall, the phospholipid modification offers potential benefits, but they still need to be utilized accompanied with other surface functionalisation techniques. A limited number of studies on cytotoxicity of lipid-capped AuNR@SiO_2 have been reported to date [243].

In this chapter, I will discuss lipid-modified AuNR@SiO_2 of silica shell thickness ~ 7 nm, their functionalization, and their plasmonic properties. In addition, I will present the cytotoxicity and cellular uptake of synthesized lipids coated AuNR@SiO_2 by human colorectal cell lines

SW620 and HT29. Understanding such modifications on silica shells could reduce the toxicity of AuNRs in biological systems.

4.2. Surface Modification of Silica Coated Gold Nanorods with Phospholipid

The synthesised AuNRs, with LSPR peaks near-infrared region, were coated with a silica shell, as detailed in Chapter 2. Following that, phospholipid functionalised silica-coated gold nanorod composites were prepared by modification of the AuNR@SiO_2 surface with a lipid mixture of 1,2-distearoyl-sn-glycero-3-phosphoethanolamine-N- [methoxy (polyethylene glycol)-2000] (DSPE-PEG2000) and dipalmitoylphosphatidylcholine (DPPC) of volume ratio DPPC: DSPE-PEG-2000 of 95:5. Phospholipid coated–AuNR@SiO_2 were prepared by the spontaneous deposition of lipid vesicles via lipid film hydration method.

The AuNRs@CTAB sample has an LSPR peak at a wavelength of 847.0 ± 0.3 nm before any surface modification as shown in Figure 4.1. After the successful silica coating, the AuNRs LSPR peak redshifted to 853.0 ± 0.3 nm with FWHM of 208.4 ± 5.0 nm. This shift is due to a change in the effective dielectric constant of the medium surrounding the AuNRs. After lipid modification on AuNRs@SiO_2, the LSPR maxima decreased slightly to 852.7 ± 0.3 nm but remained within the experimental uncertainty. The refractive index of the lipids is expected to be in the range of 1.42 to 1.45, which is similar to the SiO_2 shell and therefore the 'effective' dielectric constant surrounding the gold is not altered by the addition of the lipids [344]. Overall, no tailing or broadening was observed in the absorption spectra, indicating excellent colloidal stability of the synthesized AuNRs@SiO_2 after the lipid coating.

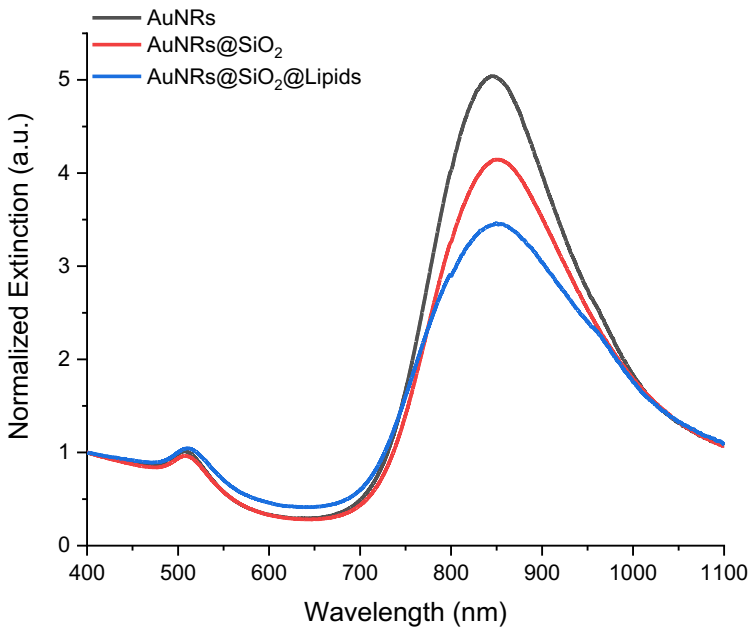

Figure 4.1. UV-Vis absorbance spectra of AuNR, AuNRs@SiO_2, AuNRs@SiO_2 stabilized DPPC + DSPE-PEG2000 lipid.

4.3. Dynamic Light Scattering

Dynamic Light Scattering (DLS) is useful to determine nanoparticle size. Since a complete lipid layer is ~4 nm thick the overall diameter would be expected to increase by ~8 nm after coating. Figure 4.2 shows the DLS size distribution of the AuNRs before and after coating with silica and lipids. It is important to remember that these sizes are the hydrodynamic sizes. The small peak does not measure the actual dimension of the nanorods, it is attributed to the rotational diffusion of the nanorods and it has been shown that the small peak in size distribution increases with aspect ratio [345].

The homogeneous colloidal size of both AuNR and AuNRs@SiO_2@Lipids was confirmed by size distribution diagrams as demonstrated in figure 4.2. The uncoated AuNRs show two size distribution peaks, the first one with an average hydrodynamic diameter at 16 ± 0.1 nm, and the second one at 38 ± 0.3 nm. However, AuNRs@SiO_2@Lipids reveal a weak size peak at 26 ± 0.2 nm and another strong peak at 41 ± 0.4 nm. Both samples exhibit very weak peaks at ~ 65 nm, suggesting that some level of agglomeration may also have occurred (albeit a very small proportion of the sample due to the enhanced sensitivity of larger particles). From the

comparison of the two samples, we noticed that the small size peak increased after both silica coating and lipids functionalization by roughly 10 nm. The thicknesses of lipid bilayers is estimated to be approximately 5.4 ± 0.2 nm [346].

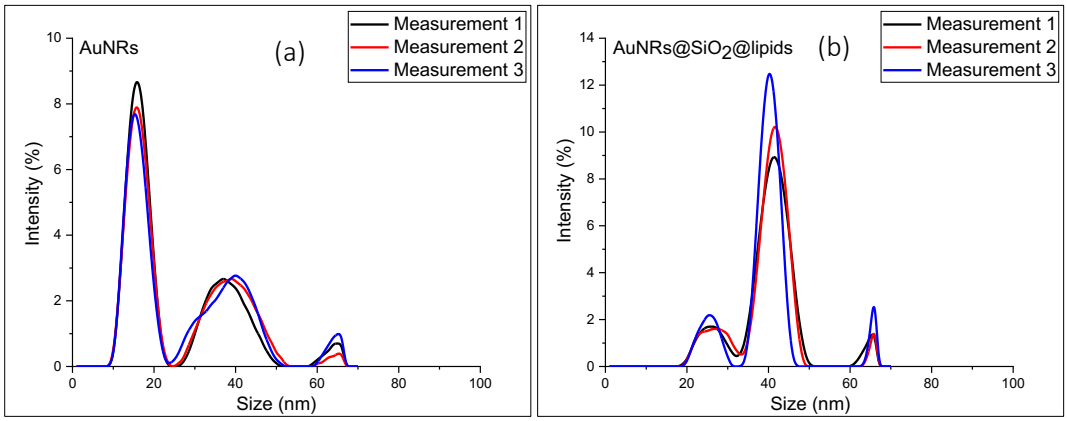

Figure 4.2. Dynamic Light Scattering DLS intensity size distribution.

(a) AuNRs (b) AuNRs@SiO_2@Lipids-Atto 488 in Milli-Q water after repeated 5 cycles of centrifugation.

4.4. Zeta Potential

To complement the characterization of the lipids coated- AuNR@SiO_2, ζ-potential was taken before and after the surface modification of the silica shell with phospholipid. As demonstrated in Figure 4.3, uncoated silica shell shows a zeta potential of highly negatively charge - 44±2 mV, this is consistent with what has been reported in literature previously [347]. However, after being functionalized by lipids their zeta potential reduced to -16.7 ±0.2 mV, as shown.

The zeta potential is measured by net charge accumulated on the liposome surface. In our study, the mixture of lipids used consists of DPPC: DSPE-PEG-2000 (95:5). The phospholipid DPPC is zwitterionic, according to Makino et al. [348]. Moreover, DSPE is normally zwitterionic, when it is bound covalently to PEG is converted to be anionic [349]. As a reason of the presence of the zwitterionic lipid DPPC of 95 % of lipids mixture, the reduction of any positive charge on our AuNR@SiO_2 confirms that phospholipid coating is present. This is in excellent agreement with the expectations, the reduction in the surface charge of SiO_2 shell was observed due to charge shielding by the zwitterionic lipid bilayer.

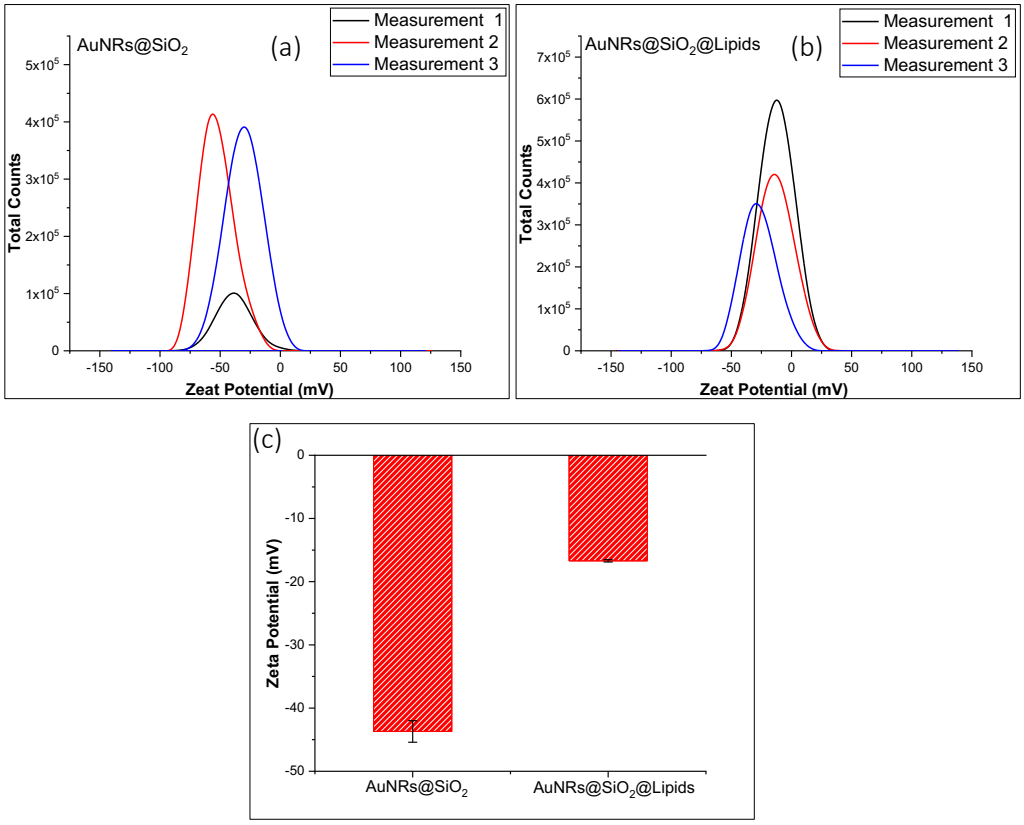

Figure 4.3 Zeta potential.

(a) AuNRs@SiO_2. (b) AuNRs@SiO_2@Lipids in Milli-Q water. (c) The reduction in the surface charge of SiO2 shell was observed due to charge shielding by the zwitterionic lipid bilayer.

4.5. Stability of phospholipids functionalised AuNR@SiO_2 in PBS buffer

In this section, the aim is to demonstrate high stability of AuNRs in colloidal and biocompatible applications. To do so, the stability of AuNRs in phosphate-buffered saline (PBS) was investigated. PBS was particularly used in this study because it is a buffer solution that is commonly used in biological research. Maintaining colloidal properties is necessary due their impact on the plasmon peaks position that plays an essential role in photothermal therapy applications.

AuNRs@CTAB, AuNR@SiO_2 and lipids coated- AuNR@SiO_2 were dispersed in PBS buffer and left for 1 h before taking the UV-Vis absorption. As shown in Figure 4.4, the uncoated AuNRs@CTAB aggregated immediately in PBS and showed a broad peak at higher wavelengths due to the formation of massive aggregation. The obtained aggregation in PBS buffer is due to the screen produced by high salt concentration that cause a reduction in the repulsive

interactions between individual AuNRs. However, the silica coated-AuNRs were noticeably stable, and they showed a strong LSPR peak. Moreover, after coating AuNR@SiO_2 with the bilayer lipids showing excellent stability at pH 7.4 with no aggregation observed. The absorption spectrum remained the same as for the AuNRs in pure water. To compare the AuNR@SiO_2 with the lipids modified-AuNRs AuNR@SiO_2, the LSPR peak of lipids coated AuNR@SiO_2 is slightly sharper than the peak of AuNR@SiO_2. It indicated that the lipid bilayer coated-AuNR@SiO_2 can greatly improve the dispersing stability of AuNR@SiO_2 and making them promising candidates for photothermal experiments. Furthermore, this was used as a simple method to confirm the coating of either silica coating or lipid coating.

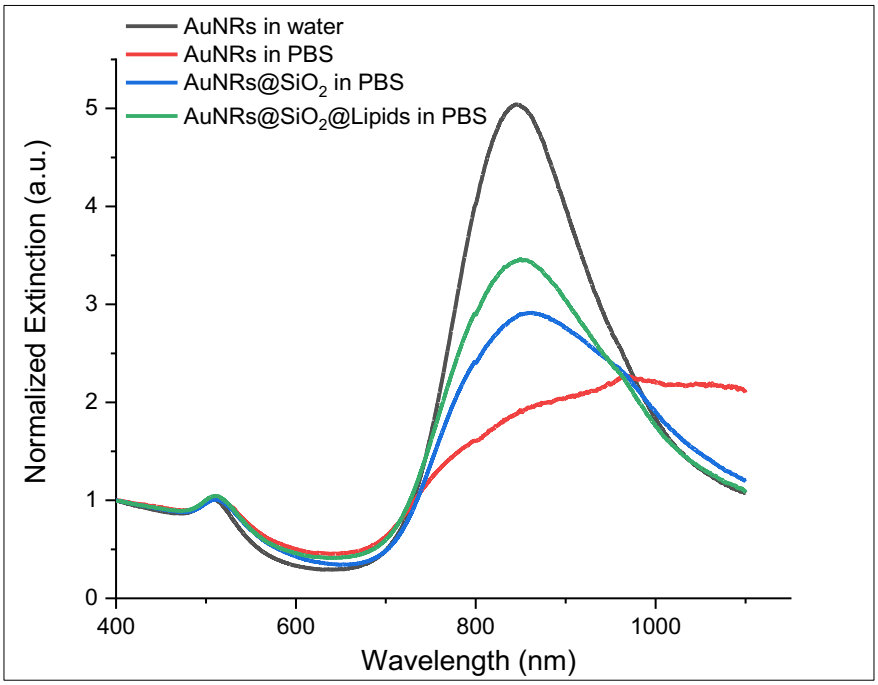

Figure 4.4 UV-Vis absorbance spectra.

of AuNRs, Silica coated AuNRs and lipid coated silica coated AuNRs of two concentration 5 and 10 mg/ml dispersed in PBS buffer of pH 7.4 for 1h.

4.6. Surface Modification of Silica Coated Gold Nanorods using fluorescently labelled lipid-Atto488

The lipid mixture was mixed with fluorescently tagged lipids of volume ratio of DPPC:DSPE-PEG2,000:Atto-488-DPPE (95:4:1). Atto-488-DPPE used in this work is a bright fluorescent label. Thus, it can be utilized to visually identify existence of any excess or free lipids in the

system. Moreover, due to their unique optical properties, they will not only help to optimize the *in-vitro* imaging, but also confirming the cellular uptake using fluorescent microscopy. Therefore, it is ideal for detection studies and help to produce high fluorescent microscopy images.

To identify the presence of the excess and free lipids in the solution, repeated cycles of centrifugations were conducted to separate the excess lipids from the solution. Then, the fluorescent emission of both the supernatants and the pellets of AuNR@SiO_2@lipids-Atto488 were measured after every cycle of centrifugation. Samples were excited at 488 nm and the emission intensity was recorded from 500 to 600 nm. AuNR@SiO_2@lipids-Atto488 dispersed in Milli-Q water were centrifuged to form pellets at 9000g for 8 min for 5 cycles. The pellets were resuspended in Milli-Q water after every cycle of centrifugation. The fluorescence (FL) emission was taken for both sample and supernatant after every cycle. Supernatant and Atto488-lipids sample showed high emission peak at 527 ± 0.07 nm after the first centrifugation as shown in Figure 4.5 (a and b). More cycles of washing were needed to ensure that no excess of lipids left in the solution. As shown in Figure 4.5 (c), the fluorescence emission intensity of AuNR@SiO_2@Lipids-Atto 488 pellets dispersed in Milli-Q gradually decreased with number of cycles. It was found that three cycles repetition of centrifugation were necessary for successful removal of the excess and free lipids. The percentage of lipids-Atto488 left on the silica shell was calculated by using this formula ((FL intensity of Atto488 sample cycle 5/Total FL intensity of Atto488)*100). Since the total FL intensity of Atto488 = 3.4×10^6. Therefore, the percentage of lipids-Atto488 left on the silica after cycle 5 is 2.0 %.

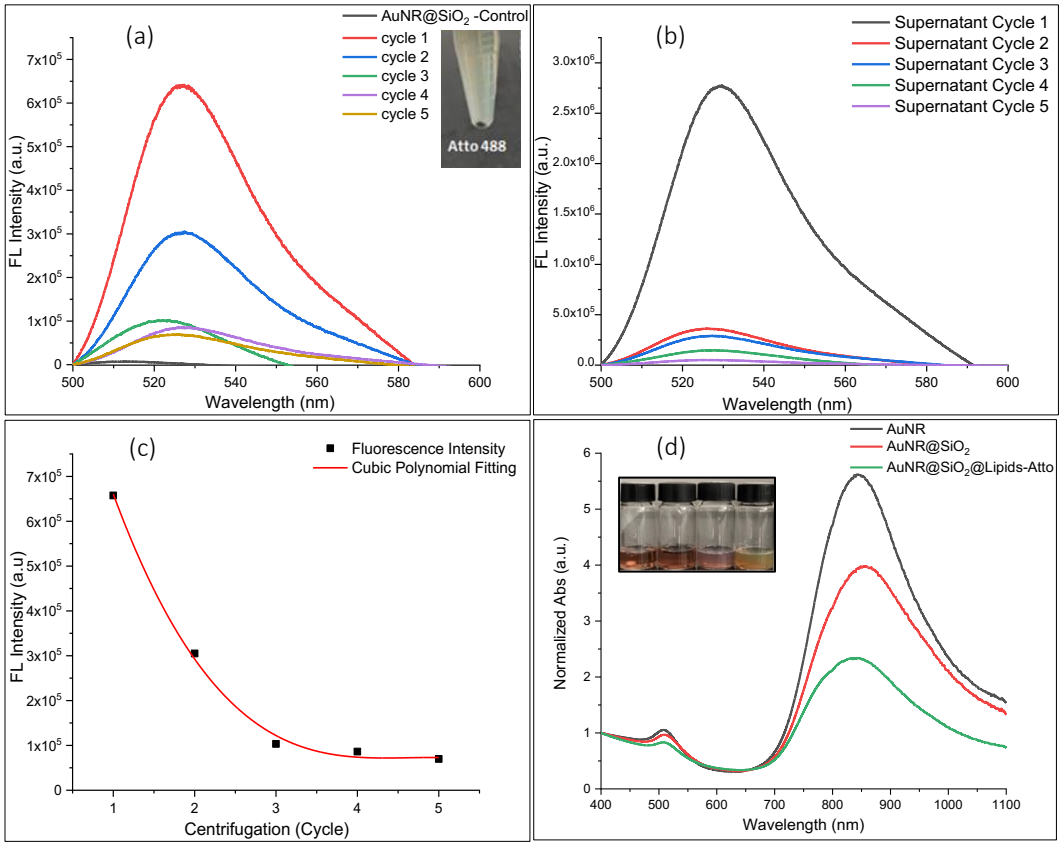

Figure 4.5 Fluorescence emission spectra and UV-vis absorbance spectra.

(a) Fluorescence emission spectra of AuNR@SiO_2 (control no lipids), AuNR@SiO_2@Lipids-Atto 488 pellets dispersed in Milli-Q water after repeated 5 cycles of centrifugation. (Inset: AuNR@SiO_2@Lipids-Atto 488 pellets after centrifugation at 9,000 ×g for 8 min) .(b) Fluorescence emission spectra of Atto488-lipid coated silica coated AuNRs supernatant dispersed in Milli-Q water after five cycles of centrifugation. (c) Fluorescence emission intensity of AuNR@SiO2@Lipids-Atto 488 pellets dispersed in Milli-Q water after repeated 5 cycles of centrifugation. (d) UV-vis absorbance spectra of AuNRs, Silica coated AuNRs, lipid coated silica coated AuNRs and Atto488-lipid coated silica coated AuNRs dispersed in Milli-Q water. Inset: solutions of AuNR, AuNR@SiO_2, AuNR@SiO_2@Lipids, and AuNR@SiO_2@Lipids-Atto 488 (in order from left to right).

4.7. Stability of fluorescence intensity of AuNR@SiO_2@Lipids-Atto 488 over time

The stability of fluorescence emission of AuNR@SiO_2@Lipids-Atto 488 dispersed in Milli-Q water after repeated 5 cycles of centrifugation was checked. At each time interval the fluorescence emission was taken using the fluorescence spectroscopy starting from first day up to 48 days. As shown in the Figure 4.6 (b), The decay rate was described by a biexponential decay with a sharp initial decay followed by a much slower fluorescence loss with the decay rate of 8.9. The observed reduction is caused by the fluorophores continuing to degrade

naturally as a result of spontaneous emission [350]. However, the fluorescence emission obtained from AuNR@SiO_2@Lipids-Atto488 sample in this measurement is fluorescently strong enough to be used as tagged lipids for fluorescence microscopy imaging.

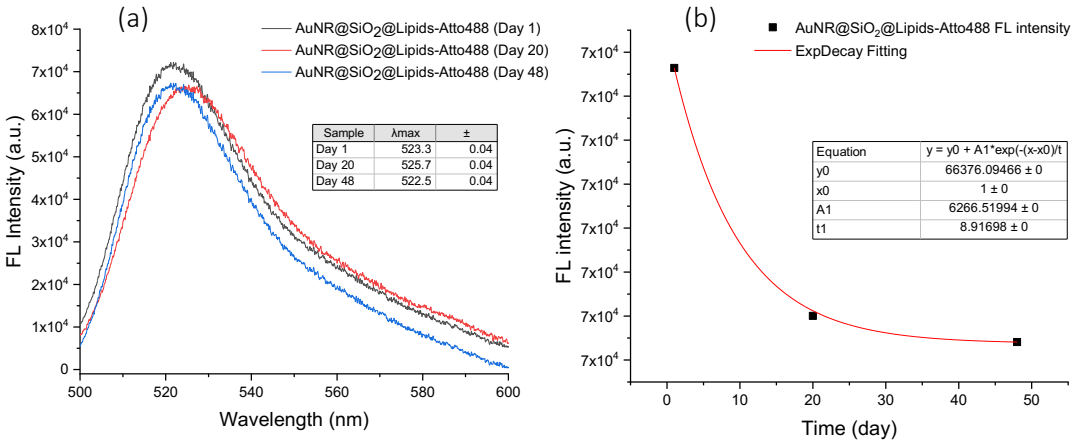

Figure 4.6 Fluorescence emission spectra of AuNR@SiO_2@Lipids-Atto 488.

(a) Fluorescence emission spectra of AuNR@SiO_2@Lipids-Atto 488 pellets dispersed in Milli-Q water after repeated 5 cycles of centrifugation after 1, 20 and 48 days. (b) The stability of fluorescence emission of AuNR@SiO_2@Lipids-Atto 488 dispersed in Milli-Q water after repeated 5 cycles of centrifugation over days.

4.8. *In Vitro* Studies

4.8.1. CCK-8 Cell Viability Assay for AuNR and AuNR@SiO_2

To measure efficiency of synthesized AuNRs@SiO_2 for potential non-invasive photothermal treatment, it is necessary first to study the cytotoxicity of these nanoparticles in biological context. In this section, the cytotoxicity of AuNRs@SiO_2 is studied in a human colorectal cell line SW620 (Passage 40) was assessed using the CCK-8 cell viability assay. Cells were seeded in 96 well plates at a density of 5 $\times 10^3$ cells per well in 100 µl media of DMEM medium containing 10% FBS. The plates were then incubated at 37°C in 5% CO_2 for 24 hours. Two groups of SW620 cells were treated with different concentrations of AuNRs@CTAB and AuNR@SiO_2 for 24 hours, to study the dependency of viability on doses of both AuNRs@CTAB and AuNRs@SiO_2. Concentrations of 0, 0.11, 0.44, 1.09, 2.4, 20.3, 74.4 and 179 µg/mL were incubated for 24 h with SW620 cells.

In Figure 4.7, the microscopy images of the SW620 treated cells with AuNRs@SiO_2 (2.4 µg. mL^{-1}) for 24 h and after washing to remove the nanoparticles that were not taken up by the cells, the images show an evidence of particles internalization in cells and not on the cell surface. The cells incubated with AuNRs@CTAB showed high toxicity, reaching 50 % viability at (16 µg/mL). As shown in Figure 4.8, more concentration showed high cytotoxicity; only 20 % viabilities were observed at 179 µg/mL. In contrast, more than 90 % cells viabilities of cells incubated with AuNRs@SiO_2 were observed in increasing concentrations. (i.e., from 0.11 to 20.3 µg/mL). When the concertation was increased to 179 µg/mL, the cell viability remained above 55 %. The observed results suggested that AuNRs@CTAB at above 20 µg/mL is considered to have significant toxicity. Hence, it can be suggested that the formation of silica shell on AuNRs has successfully reduced the toxicity of CTAB by 84.4 % after silica coating. The low cytotoxicity that was observed from AuNRs@SiO_2 at high doses originates from the residual CTAB molecules that were either left in the solution or present in the mSiO_2 shell of the AuNRs@SiO_2.

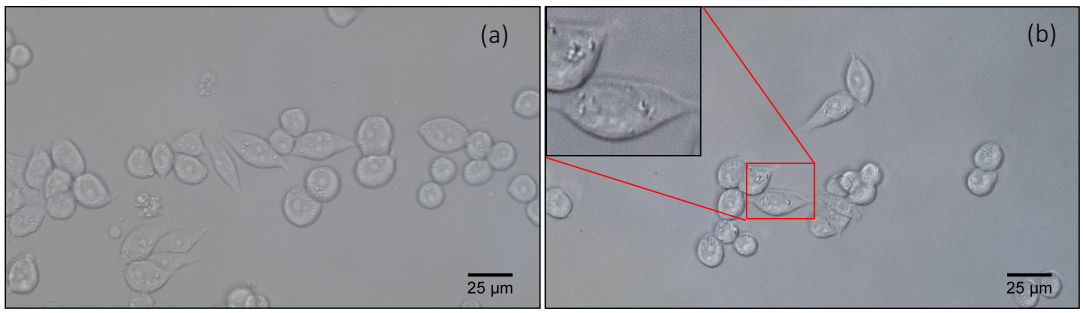

Figure 4.7 Microscopy images of the SW620 cells.

(a) Untreated cells. (b) Treated cells with AuNRs@SiO_2 (2.4 µg. mL^{-1}) for 24 h. Scale bars are 25 µm.

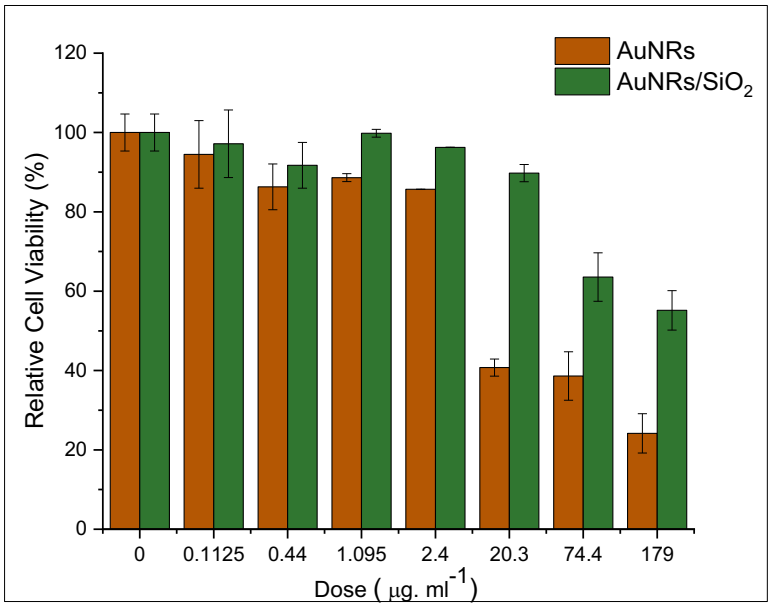

Figure 4.8 Results of CCK-8 cell viability assay of SW620 cells.

After 24 hours incubation with AuNRs@CTAB and AuNRs@SiO_2 of different concentrations (0.11, 0.44, 1.0, 2.4, 20.3, 74.4 and 179 μg/mL). The control (untreated cells) are shown as 100% of viable cells. Data are presented as the mean ± standard error. Error bars indicate the s.d. (n = 5 independent samples).

4.8.2. A MTT Cell Viability Assay for AuNR@SiO_2 and AuNR@SiO_2@lipids@Atto488

To examine the impact of lipid functionalisation on the synthesized AuNRs@SiO_2 viability, the cytotoxicity profile of both AuNRs@SiO_2 and AuNR@SiO2@lipids-Atto488 were studied in a human colorectal adenocarcinoma cell line HT29 (Passage 90) was assessed using the MTT cell viability assay. Cells were seeded in 96 well plates at a density of 5×10^3 cells per well in 100 µl media of RPMI 1640 + 10% FBS. The plates were then incubated at 37°C in 5% CO_2 for 24 and 48 hours. Two groups of HT29 cells were treated with different concentrations of AuNRs@SiO_2 and AuNR@SiO_2@lipids-Atto488 from 0, 0.2, 2.0, 20.0 and 200 µg/mL were incubated for 24 and 48 h.

As shown in Figure 4.9, 99 % and 85 % cells viabilities of cells incubated with AuNR@SiO_2 for 24 and 48 h respectively, the viabilities were observed in a variety of concentrations. (i.e.,

from 0.2 to 20. µg/mL). However, when the AuNR@SiO_2 doses were increased to 200 µg/mL, the cells viability decreased to 49.5 % and 27.4 % after 24 h and 48 h incubation respectively. On the other hand, after lipids functionalisation, high cells viabilities of cells above 98 % at a wide range of concentrations were observed after 24 h incubation. Moreover, after 48 h; the cell viability remained above 82 % with no significant cell death was detected. The observed results suggested that low viability of AuNR@SiO_2 comparably with lipids functionalized AuNR@SiO_2 could be a result of the abundant silanol groups on the surface of silica shell, that eventually causing structural damage to the building blocks of the cells membrane such as lipids and proteins [351]. Therefore, based on the above results, the lipids functionalisation on synthesised AuNR@SiO_2 has successfully optimised their biocompatibility due to the concealing of the silica shell silanol groups and increased their viability by approximately 53 %.

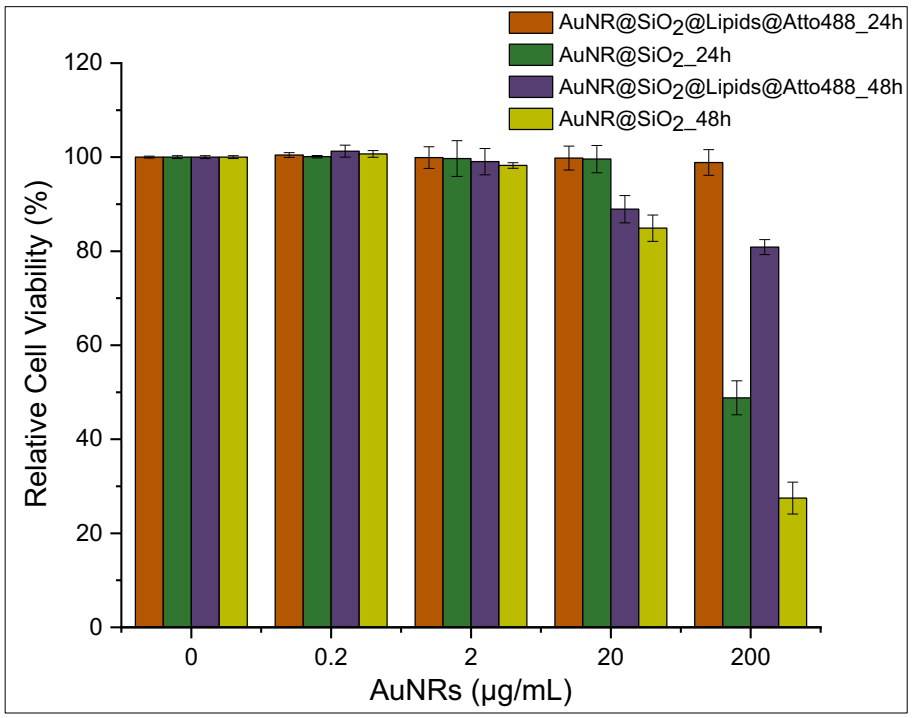

Figure 4.9 Results of MTT cell viability assay of HT29 cells.

treated by various concentrations (0, 0.2, 2, 20, 200 µg/mL) of AuNR@SiO_2@Lipids-Atto 488, they were incubated for 24 h and 48 h. the control (untreated) group is referred as 100 % of viable cells. Data are presented as the mean ± standard deviation. Error bars indicate the s.d. (n = 5 independent samples).

4.8.3. Cellular Uptake of Lipids Coated AuNR@SiO_2 *In-vitro* Imaging

One possible concern that I had following the viability experiments was that the greater viabilities may be due to a lack of absorption by the cells. Higher viabilities would be expected if the particles did not interact with the cells at all and remained in the surrounding medium.

To answer this question, the cellular uptake was studied using fluorescence microscopy of HT29 cells treated by various concentrations of AuNRs@SiO_2@Lipids-Atto 488 after 24 h and 48 h incubation. As shown earlier in this chapter that AuNRs@SiO_2 were labelled with the fluorescent lipid Atto488 for labelling lipids bilayer purpose in *In Vitro* study. Using these labelled lipids will enable us to detect lipid coated AuNR@SiO_2 within the HT29 cells and examine the influence of the lipid bilayer on the cellular uptake efficiency using fluorescence microscopy. Considering that the cellular uptake is both time and dose dependent, the fluorescence images were taken for cells incubated with AuNRs@SiO_2@Lipids-Atto488 for 24 and 48 hours with different concentration (0, 0.2, 2.0, 20 and 200 µg/mL). The cells nuclei were stained with Hoechst (DAPI, blue fluorescence) and the incubated Atto488 labelled lipids-coated AuNR@SiO_2 shown as (FITC, green fluorescence). All fluorescence images were taken under the identical conditions. Note that the cells were then rinsed before imaging to remove any free nanoparticles. The successful cellular uptake of the cells treated with AuNRs@SiO_2@Lipids-Atto 488 was observed by the green emission in comparison with control cells as shown in fluorescence images in Figure 4.10 and 4.11 of both cells after 24 h and 48 h incubation, respectively. Overall, there were no visible evidence of cytotoxicity following incubation. However, the fluorescence images of 200 µg/mL for 48 h sample in Figure 4.11. shows very low fluorescence intensity; indicating that cells exposed to infection after viability study.

In this study, the aim was not to precisely locate the synthesized AuNRs@SiO_2 whether they are in the nucleus or the cytoplasm, it was sufficient to measure the average of their maximum intensity of labelled AuNRs@SiO_2@Lipids that uptaking by the cells and located in a ring-shaped region around the nucleus. The average of corrected total cell fluorescence (CTCF) and integrated density were collected of untreated and treated HT29 cells after incubation for both 24 and 48 h by. Cells were randomly selected (n= 6). The stained cells were observed under fluorescent microscope and their average fluorescence was collected using

ImageJ software. Both groups of data the 24 and 48 hours of incubation samples are presented as corrected total cell fluorescence [CTCF = Integrated density - (Area of total cell x mean fluorescence of background)] normalized to vector control cells. The Corrected total cell fluorescence (CTCF) and integrated density histogram of both groups of data the 24 and 48 hours of incubation are shown in Figures 4.12 and 4.13.

From the comparison of average integrated density of (FITC, green fluorescence) and their average corrected total cell fluorescence (CTCF) of 24 h incubation of different concentration of Atto488 labelled lipids-coated AuNR@SiO_2 in Figure 4.12, Un-treated HT29 cells showed very low fluorescence signals due to the cellular autofluorescence. After incubation for 24 h, it can be seen the maximum intensity of HT29 cells treated with 0.2 µg/mL is 1.9-fold larger than the control cells. However, when the cells were treated with 200 µg/mL, fluorescence intensity was significantly enhanced demonstrating 14-fold compared to control cells. After 48-h incubation, the maximum intensity of cells treated with 0.2 µg/mL and incubated for 48 h is 1.2-fold higher than untreated cells as demonstrated in Figure 4.13. In addition, these cells showed fluorescence intensity of 1.3-fold larger than the CTCF of cells of the same doses (0.2 µg/mL) of AuNRs@SiO_2@Lipids-Atto 488 after 24 h incubation. However, the cells treated by a higher dose of 20 µg/mL showed fluorescence intensity 2-fold higher than control cells. Overall, with increasing incubation time, much stronger fluorescence signals were observed, confirming that more AuNRs@SiO_2@Lipids-Atto 488 were up taken by HT29 cells. Moreover, the results obtained from this study indicate that the lipids functionalisation can greatly promote the cellular uptake of silica coated-AuNRs. This is in excellent agreement with the expectations, confirming the neutrally charged lipid bilayer has helped the AuNRs@SiO_2 to reach the cell surface more easily and taken up by cancer cells through their membrane since they have the similar structure.

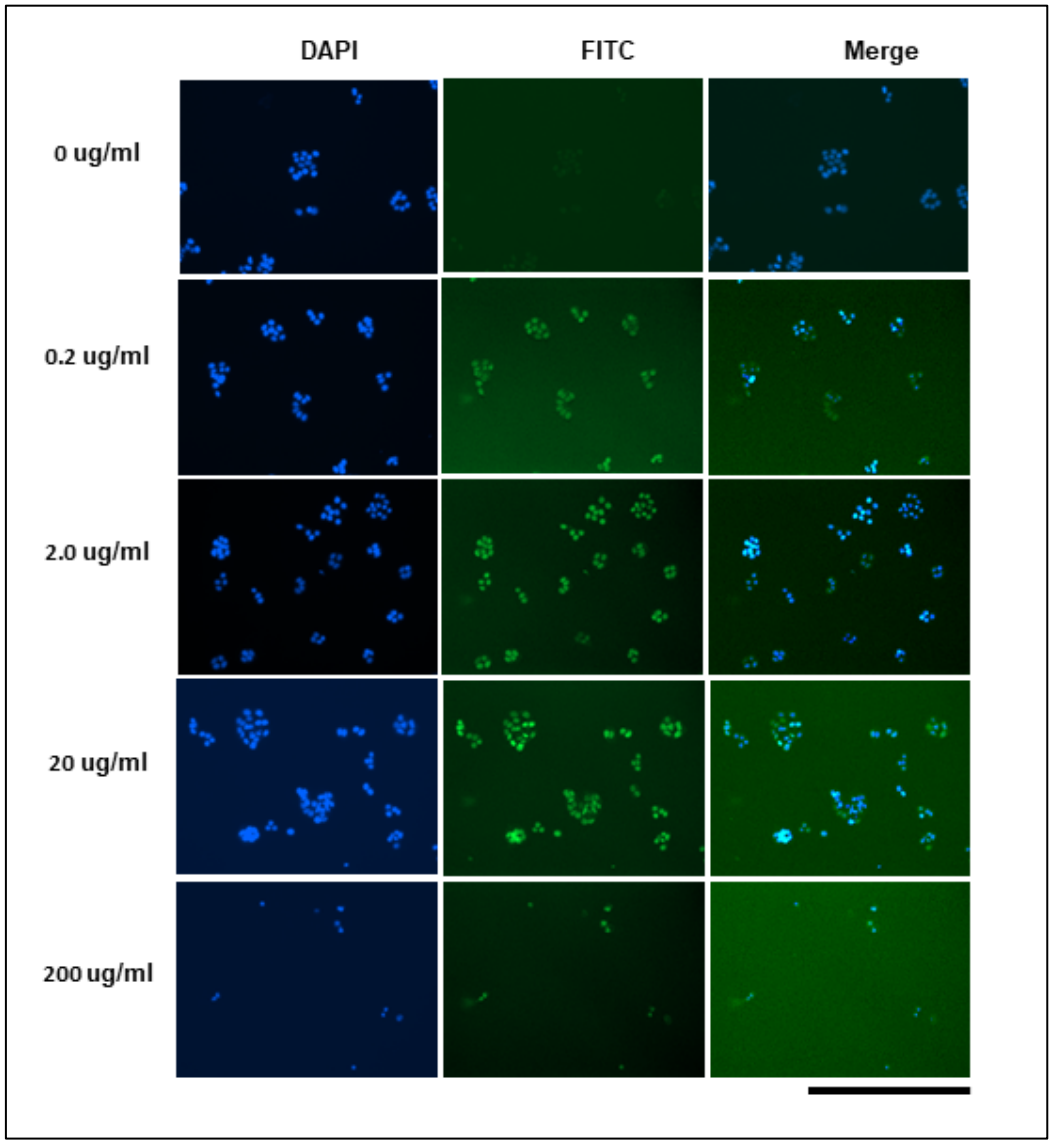

Figure 4.10 Fluorescence microscopy images.

Showing the uptake of different concentration by different concentration of Atto488 labelled lipids-coated AuNR@SiO_2 (0.2, 2.0, 20 and 200 µg/mL) by HT29 cells after 24 h incubation. The cells nuclei were stained with Hoechst (DAPI, blue fluorescence) and the incubated Atto488 labelled lipids-coated AuNR@SiO_2 shown as (FITC, green fluorescence). Scale bar equals 200 µm.

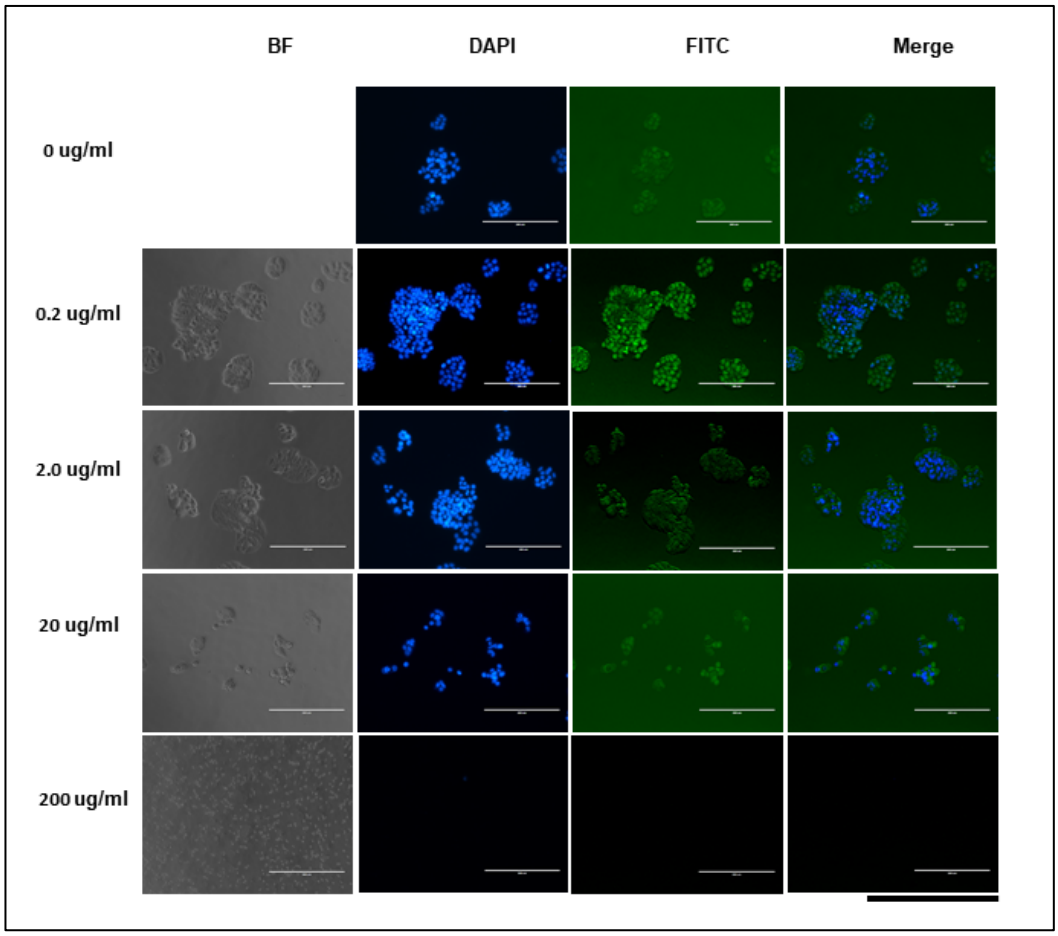

Figure 4.11 Fluorescence microscopy images.

Showing the uptake of different concentration by different concentration of Atto488 labelled lipids-coated AuNR@SiO_2 (0.2, 2.0, 20 and 200 µg/mL) by HT29 cells after 48 h incubation. The cells nuclei were stained with Hoechst (DAPI, blue fluorescence) and the incubated Atto488 labelled lipids-coated AuNR@SiO_2 shown as (FITC, green fluorescence). Scale bar equals 200 µm.

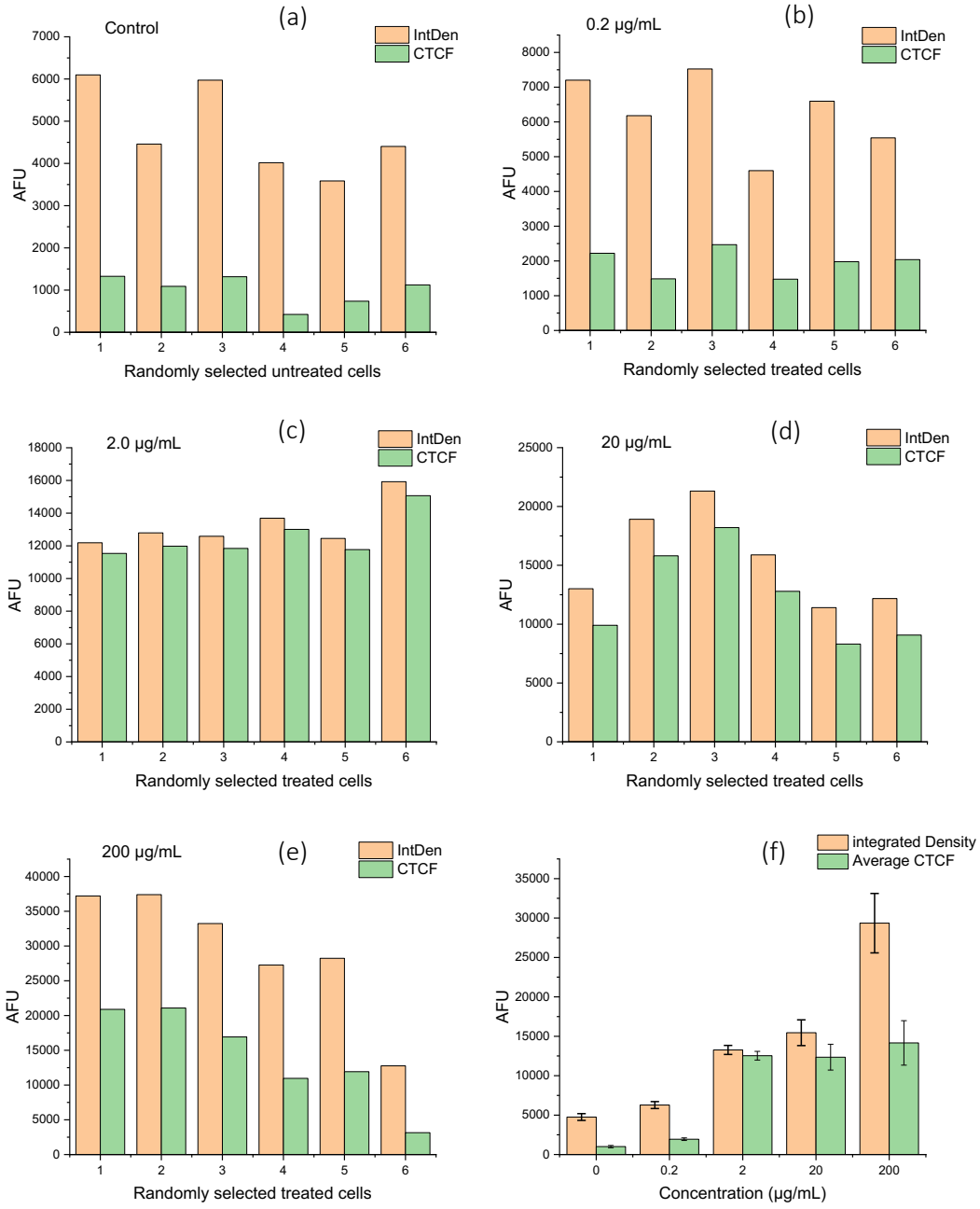

Figure 4.12 Corrected total cell fluorescence (CTCF) and integrated density histogram.

(a) Untreated HT29 cells and (b-e) Treated HT29 cells after incubation for 24 h by different concentration of Atto488 labelled lipids-coated AuNR@SiO_2 (0.2, 2.0, 20 and 200 µg/mL). Cells were randomly selected (n= 6). (f) Comparison of average integrated density of (FITC, green fluorescence) and their average corrected total cell fluorescence (CTCF). The areas without fluorescence adjacent to fluorescent cells was collected as background. ImageJ software was used to determine the level of cellular fluorescence from fluorescence microscopy images. The fluorescent signal intensity is expressed in arbitrary fluorescent units (AFU).

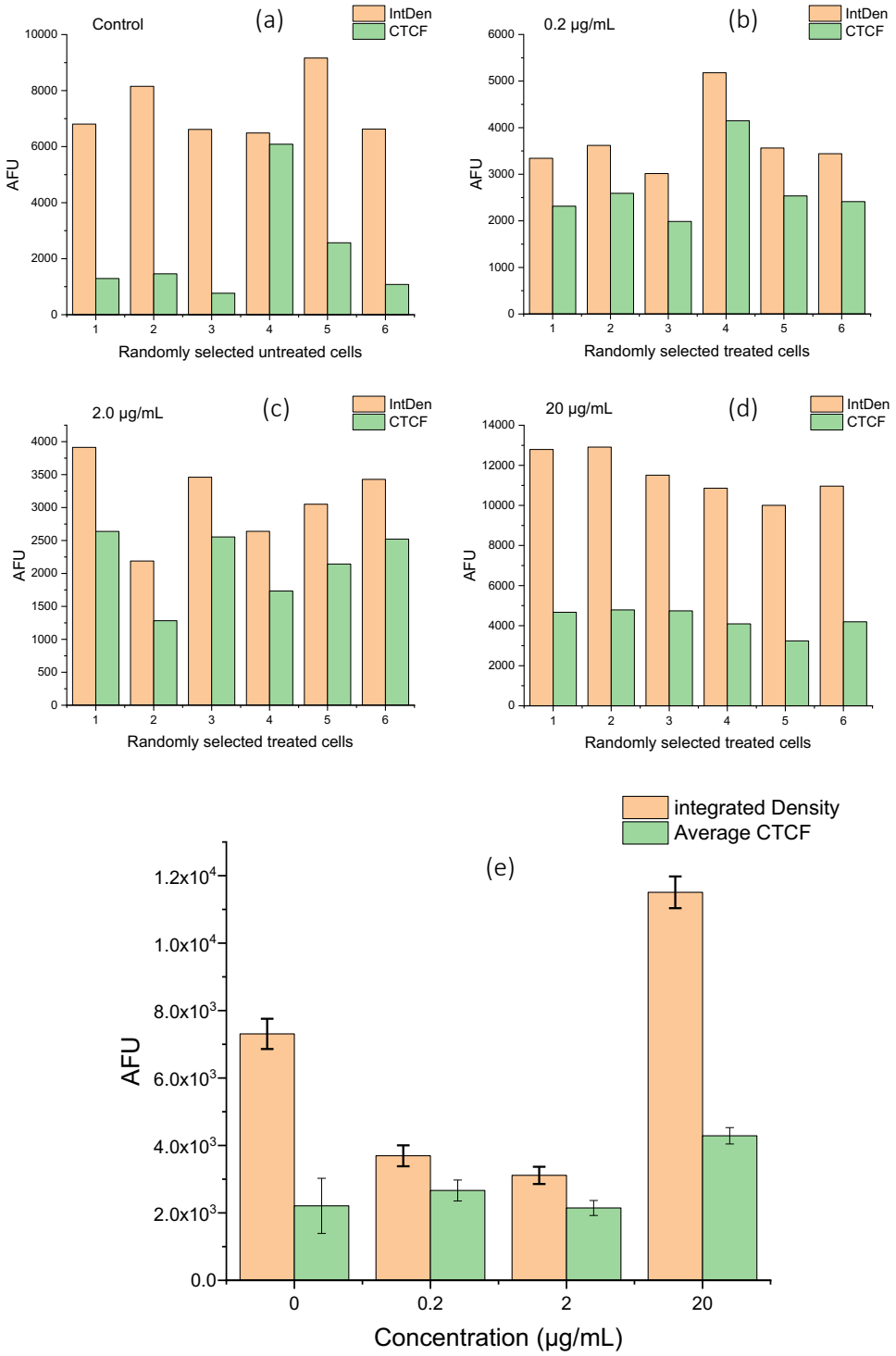

Figure 4.13 Corrected total cell fluorescence (CTCF) and integrated density histogram.

(a) Untreated HT29 cells and (b-d) Treated HT29 cells after incubation for 48 h by different concentration of Atto488 labelled lipids-coated AuNR@SiO_2 (0.2, 2.0, and 20 µg/mL). Cells were randomly selected (n= 6). (e) Comparison of average integrated density of (FITC, green fluorescence) and their average corrected total cell fluorescence (CTCF). The areas without fluorescence adjacent to fluorescent cells was collected as background. ImageJ software was used to determine the level of cellular fluorescence from fluorescence microscopy images. The fluorescent signal intensity is expressed in arbitrary fluorescent units (AFU).

4.9. Conclusion

In summary, the findings suggest a way of improving biocompatibility of AuNR@SiO_2 by modification their surface with lipids. The obtained results confirmed that lipids modified AuNR@SiO_2 were colloidally stable in PBS compared to uncoated AuNRs. Additionally, the SW620 cells incubated AuNRs@SiO_2 for 24 h have survived reasonably well remained above 55 % even at the highest doses used in this study. Confirming that the successful silica coating has reduced the CTAB toxicity. However, HT29 cells incubated with lipids modified AuNR@SiO_2 showed excellent viability after incubation for 24 and 48 h compared to AuNR@SiO_2. Moreover, the lipids functionalisation has greatly promoted the cellular uptake of silica coated-AuNRs. The fluorescence microscopy images showed the nanocomposites were internalized and not on the cell surface. This is in excellent agreement with the expectations, confirming the neutrally charged lipid bilayer has helped the AuNRs@SiO_2 to reach the cell surface more easily and taken up by cancer cells through their membrane since they have the similar structure.

5. Gold Nanorods Reshaping Under Nanosecond Pulsed Laser Irradiation

5.1. Motivation

Gold nanorods (AuNRs) are widely studied for photothermal therapy technologies, due to their longitudinal surface plasmon resonance (SPR) in the near-infrared region [128, 352]. The strong SPR bands in the NIR region make AuNRs highly effective materials for analytical [353, 354], photofunctional [49, 291], biochemical [297, 355], photoacoustics applications [332]. The AuNRs are rapidly heated when they are irradiated using a pulsed laser at a wavelength matching the surface plasmon resonance band [356]. It is well-known the AuNRs can rapidly change shape during the laser irradiation. However, their reshaping behaviour is not fully understood due to studies being performed with different conditions such as aspect ratio, volume, surfactant type (and concentration), other coatings, laser conditions (femtosecond, nanosecond, or continuous), and in solvent (water or organic) or under dry conditions (air or vacuum). All these factors influence the reshaping, and it can be difficult to rationalise the key parameters.

In general, melting can occur when the nanoparticle lattice is heated in a rate faster than it is cooled [147]. Thus, the type of excitation source used plays a crucial role in the photothermal reshaping. By comparing the two different excitation pulsed lasers (femtosecond vs nanosecond), Link, S., et al., reported that employing nanosecond laser pulses can rapidly, and effectively, heat nanorod lattices, which resulted in a complete melting of the nanorods into nanospheres that is roughly 2 orders of magnitude greater than femtosecond laser pulses [147]. Moreover, it was found that femtosecond laser pulses of wavelength 800 nm on resonance caused the AuNRs to melt and fragment, with an energy threshold about 0.01 J cm^{-2}, while using the nanosecond pulses for the same AuNRs is around 1 J cm^{-2} energy threshold.

Earlier studies of the laser induced AuNR shape change was carried out by Link et al [155]. Their study demonstrated the AuNRs shape transition at low fluence of 1 mJ cm^{-2} using femtosecond laser pulses. In addition, they reported the new structures were either spherical

nanoparticles or ϕ-shaped nanorods [103, 154, 186]. Shape change causes the longitudinal SPR peak of the AuNRs to blue-shift, and the extinction coefficient to decrease – importantly, the combined effects limit their effectiveness for photothermal therapy applications [103, 357]. In all these studies the AuNR coating was CTAB. It would therefore seem logical to attempt to coat the AuNR with a solid shell (e.g. silica) to control the extent of the reshaping.

A method for post-synthesis control over the AR of the AuNR within a silica shell was recently demonstrated by the selective oxidization of the AuNR inside AuNR@SiO_2. Choi *et al*. reported Rattle-structured a AuNR core in a silica shell obtained by a further selective etching for Ag of AuNR@Ag@SiO_2 by the addition of hydrogen peroxide [358]. In addition, Wu *et al.* introduced a new approach for selective oxidations of the ends (or tips) for the AuNR of AuNR@SiO_2 using chloroauric acid as weak oxidant. However, Zhiwei *et al*, reported a unique surface concavity method creating a new concavity sensitive plasmonic AuNRs by using two templates Fe_3O_4 rods and silica shells of 35 nm diameter and ∼ 5 nm respectively [359].

In this work, I introduce a novel method for the fabrication of AuNR@Cavity@mSiO_2 nanomaterials that could be fabricated by nanosecond laser pulse illumination at 850 nm. This study focuses on the effect of the silica coating on AuNRs reshaping behaviour as a function of irradiation time, fluence, and porosity degree. To our knowledge nanosecond pulsed laser reshaping of AuNR@SiO_2 has not been reported. In this Chapter, I describe the results and discuss the observed behaviour.

5.2. Synthesis of AuNR and AuNR@SiO_2

The cleaned CTAB-capped AuNRs were first characterised by UV–Vis-NIR absorption spectroscopy. The UV–Vis–NIR spectra Figure 5.1 shows that the AuNRs display two absorption bands: a transverse (TSPR) and a longitudinal surface plasmon resonances (LSPR) bands at 520 ± 2 nm and 830 ± 1 nm, respectively. Any change in the AR, or distribution of AR, can be determined from plasmon peak maxima position and full-width-half-maximum (FWHM) [244].

The absorption spectra in Figure 5.1 shows that LSPR peak position as well as the FWHM exhibited a certain amount of variation after silica coating. The FWHM of the LSPR before silica coating was found to be 174 ± 1 nm. However, after silica coating the LSPR peak of the AuNR was red-shifted by ~ 5.5 nm to be 836 ± 1 nm with the FWHM of 204 nm. The redshift of LSPR peak is understood by the effective change in the refractive index of the medium surrounding AuNRs after the silica coating, this has been discussed in detail in Chapter 3. Furthermore, it was observed that the FWHM of LSPR peak, after silica coating is 30 nm wider than the LSPR peak before coating. The TSPR band was found unchanged after silica coating at 502 ± 2 nm. The TEM images in Figure 5.2 (a, b) show that the mean AuNRs length and diameter were 46.9 ± 1 nm and 12.0 ± 0.2 nm, respectively, giving an AR of 3.9 ± 0.1. They were successfully and uniformly coated by silica shells; with a mean thickness of 6.8 ± 0.2 nm. The size distribution histograms of AuNRs and AuNR@SiO_2 shown in Figure (5.2 c-e) were derived from TEM images by analysing 100 AuNRs using ImageJ.

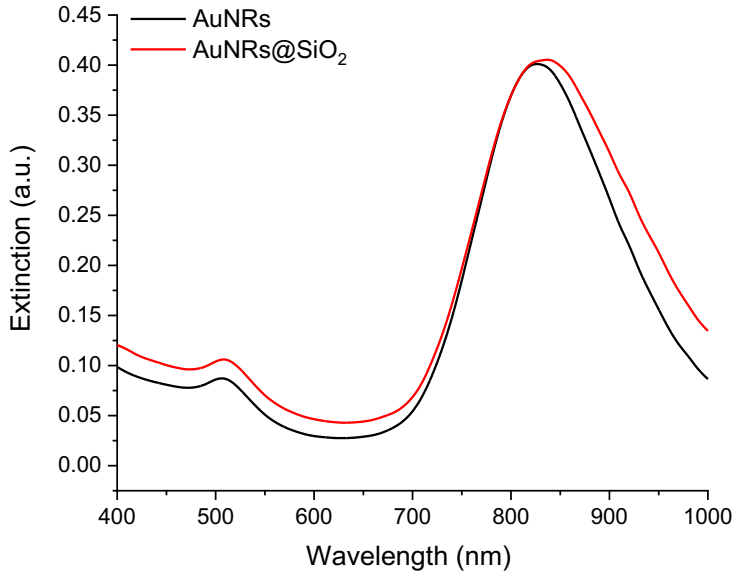

Figure 5.1. The UV–Vis–NIR spectra of AuNRs and AuNRs@mSiO_2.

The black and red lines representing before and after silica coating, respectively.

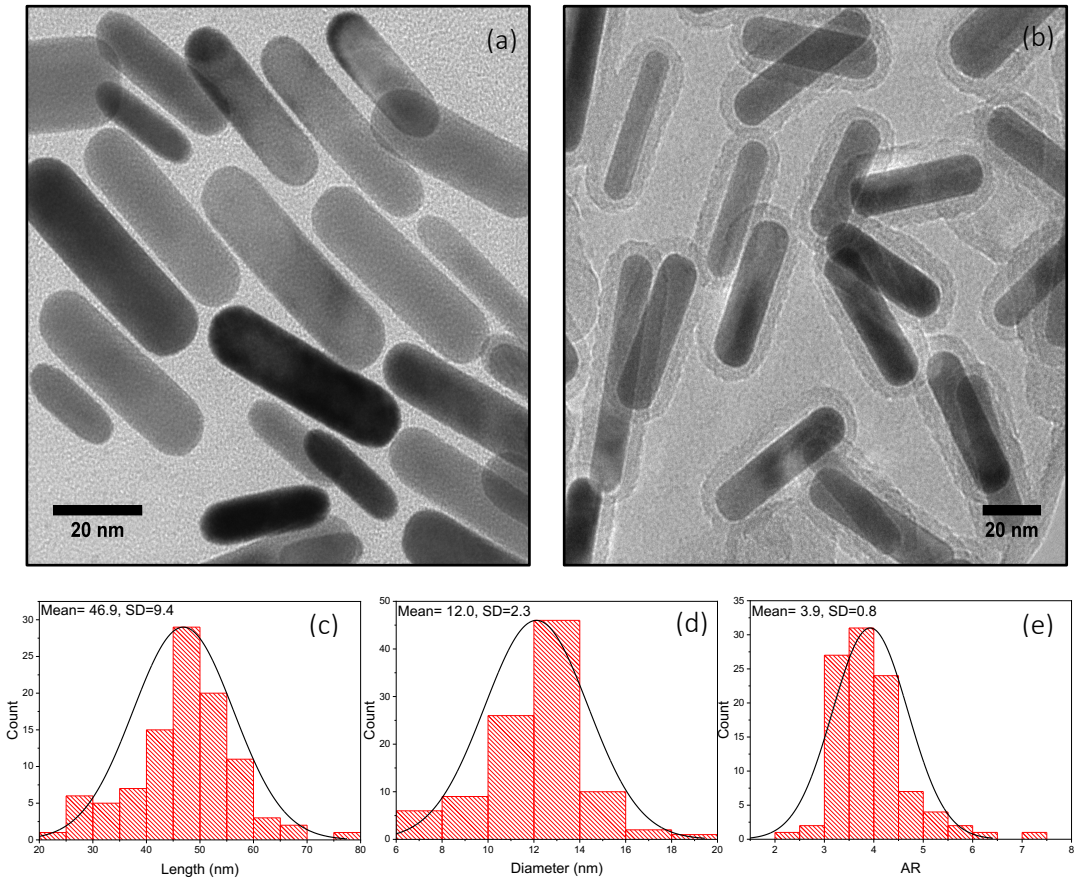

Figure 5.2. Transmission electron microscopy (TEM) images.

(a) uncoated AuNRs (b) AuNR@mSiO$_2$. (c-e) Length, diameter, and AR distribution histograms of AuNRs, respectively derived from TEM analysis. These data were obtained from 100 AuNRs.

5.3. Pulsed laser irradiation

The photothermal reshaping study of the CTAB-capped AuNRs and AuNR@mSiO$_2$ was carried out using high and low pulsed laser of wavelength of 850 nm of fluences 10 and 20 mJ/cm^2. The colloidal solutions of concentration of 50 µg/ml were irradiated for set periods of time (30 s, 1 min, 3 min, 5 min, 6 min, and 7 min). The pulse width of the laser used in this work is 7 ns at 10 Hz repetition rate with 6-mm beam width.

The shape transformations of the AuNRs and AuNR@mSiO$_2$ were monitored using two techniques: (1) UV-Vis spectroscopy to monitor change in plasmon bands position; because the LSPR band position is largely dependent on the aspect ratio, this can be used as an indicator of AuNRs shape change [360-362] and (2) transmission electron microscopy (TEM)

to measure the size distribution, to confirm the reshaping behaviour and to define the final shape of the final products. The study was carried out for two main cases: (1) when the solution were not stirred; (2) when the solution were stirred during the pulsed laser irradiation.

5.3.1. Pulsed laser irradiation (without stirring)

5.3.1.1. UV-Vis Spectroscopy

The corresponding UV-Vis spectra of both exposed CTAB-capped AuNRs and AuNR@$mSiO_2$ are shown in Figure 5.3. The LSPR peak of CTAB-capped AuNRs irradiated with 20 mJ/cm^2 is slightly blue shifted and their absorption intensity strongly decreased with increasing irradiation time. In addition, the band at 520 nm associated with the TSPR did not show any shift after the laser irradiation. However, they were gradually increased in amplitude as presented in the corresponding extinction spectra in Figure 5.3 a. Figure 5.4, shows how the intensity of TSPR band increases, with time, resulting in a single absorption peak observed in its absorbance spectrum at 520 ± 2 nm. The 520 nm band is associated with the SPR of spherical Au NPs and the TSPR band of Au NRs. If the TSPR peak increases and the LSPR band decrease, it indicates the conversion of a fraction of the AuNRs into spherical AuNPs [363]. At lower power laser of fluence of 10 mJ/cm^2, the CTAB-capped AuNRs showed the same spectral trends as the higher power with a slower apparent conversion from AuNR to spherical NP conversion rate as shown in Figure 5.3 c.

In contrast, the effect of pulsed laser irradiation on silica-coated AuNRs yielded different behaviour from the CTAB-coated AuNRs. The variations of the LSPR peak position for AuNR@$mSiO_2$ as function of the irradiation time are plotted in (Figure 5.3). The irradiation causes an initial decrease in the LSPR band at 820 nm, along with the growth of a band (or shoulder) at 624 ± 1 nm. After 5 minutes of exposure, the plasmon band at 820 nm has been dramatically reduced, and the band of 624 nm has increased (albeit a much smaller peak size) and has a FWHM of ~ 160 ± 1 nm. Notably, even after longer exposure times the new LSPR band remains stable. The TSPR band increased slightly with irradiation time, but the change is small in contrast with the bare AuNRs. These results suggests that the pulsed irradiation causes the AuNR AR to decrease to a new, smaller, AR, and that few AuNRs are converted into

spherical AuNPs. In other words, it appears that the silica shell does not prevent reshaping of the AuNR but prevents the AR of the AuNRs from reducing below a certain value. The same effect is seen in both the high and lower power studies (Figure 5.3), with the lower power (10 mJ/cm^2) showing evidence of a more gradual transition from the starting AR to a stable final AR. In fact, between 3 and 5 minutes there appears to be an intermediate band between the 820 and 620 nm, but this blue-shifts to the 'stable' 620 nm band position after longer exposure. Importantly, in both cases the new AR has very low absorbance at the laser wavelength, i.e., the LSPR has blue-shifted laser wavelength and therefore the light is no longer strongly absorbed and therefore it is likely that the AuNRs are heated to a much lower temperature and thus the energy threshold needed to reshape may no longer be reached. Furthermore, the silica template may serve to enhance the heat transfer (which would slow the reshaping), physically template the Au such that it prevents a spherical shape forming, or both.

The irradiated solutions (Fig 5.3 e & f) show the progression of the solution colours compared to the control sample. The AuNR@$mSiO_2$ solutions show different colour progression compared to the CTAB-AuNR sample. This colour difference is due to the shifting and reduction of the LSPR bands from near-infrared region to the visible region. The change in colour of the aqueous solutions of AuNRs@$mSiO_2$ from red to blue as shown in Figure 5.3 (e-f) varies with irradiation time which is indicating to change in aspect ratios of AuNRs from higher to lower AR, respectively. The change of solution colour is accompanied by the change of AR of NPs, since different size of NPs absorb certain wavelength and reflect different colours [364, 365]. However, the uncoated-AuNRs solutions after irradiation turned from brownish red to red as shown in Figure 5.3 (e), whereas the red colour of the solution indicating the formation of gold nanoparticles [365, 366]. In all cases the resultant nanoparticle dispersion remains stable after application of the laser.

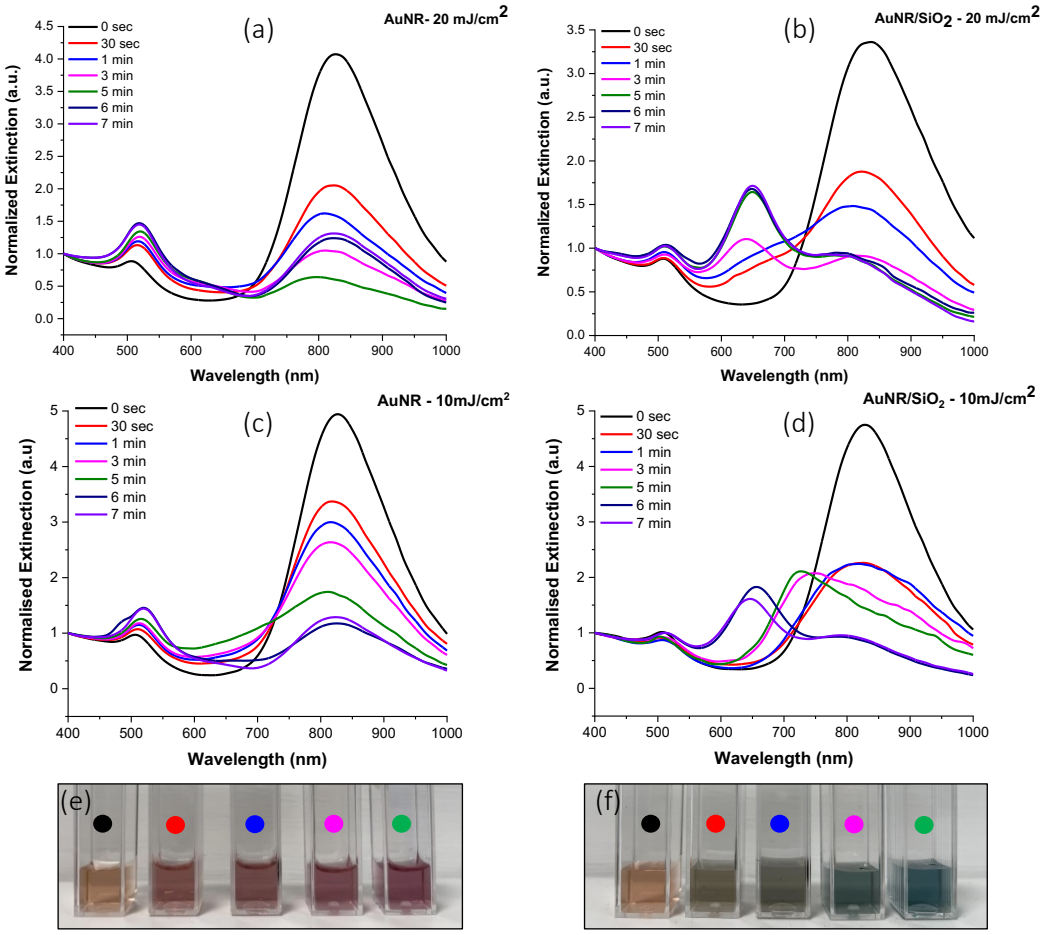

Figure 5.3. Normalized UV–Vis–NIR spectra.

(a & b) AuNR and AuNR@mSiO$_2$ after 20 mJ/cm^2 pulsed laser irradiation of different times respectively. (c & d) AuNR and AuNR@mSiO$_2$ after 10 mJ/cm^2 pulsed laser irradiation of different times respectively. All samples were irradiated for (0, 30 s, 1 min, 3 min, 5 min, 6 min and 7 min). (e & f) Photograph of aqueous solutions of AuNRs and AuNRs@SiO$_2$ respectively, showing different colours after pulsed laser irradiation of fluence 20 mJ/cm^2 (The colour of each label in the solution images corresponds to the line colour in a & b plots).

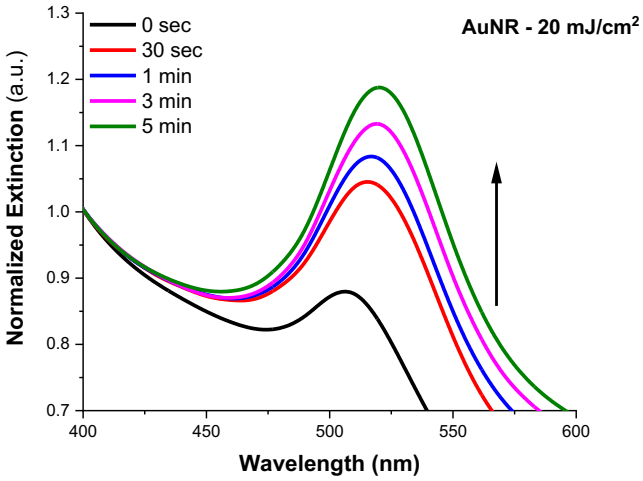

Figure 5.4 Normalized UV-vis spectra of the transverse plasmon bands region. of the AuNRs after exposure to 20 mJ/cm^2 pulsed laser irradiation.

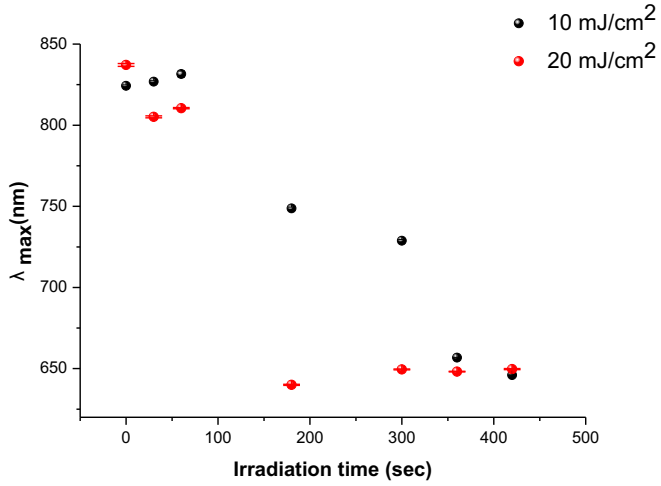

Figure 5.5. LSPR peak position of AuNRs@mSiO$_2$ before and after laser irradiation. of 20 and 10 mJ/cm^2 fluence at five time point 0, 30, 60, 180, and 300 sec.

5.3.1.2. Transmission electron microscopy (TEM)

The shape and morphology changes of AuNR and AuNR@$mSiO_2$ after 1 min and 5 min of pulsed laser irradiation (20 mJ/cm^2) were analysed by TEM. The TEM images of CTAB-capped AuNRs (of starting mean length of 47 ± 1 nm, diameter of 12 ± 1 nm, and an aspect ratio of 3.9 ± 0.3; (Fig. 5.6a) show a pronounced morphological change after 1 min of pulsed laser irradiation to spherical, ellipsoidal, or "ϕ" shape (Fig. 5.6b). The most frequently detected particles were spherical and ϕ-shaped AuNRs with a yield of 35 % and 32 % respectively (100 particles were counted). The same ϕ-shaped AuNRs have been previously reported elsewhere [148, 154, 155]. However, 18 % of the AuNRs whose original shapes were maintained even after pulsed laser irradiation. The remaining 14 % were found to be shorter AuNRs. However, after 5 min of 20 mJ/cm^2 of laser irradiation, the CTAB-capped AuNRs were completely reshaped into spherical-like particles of diameter 24 ± 1 nm (Fig 5.6c).

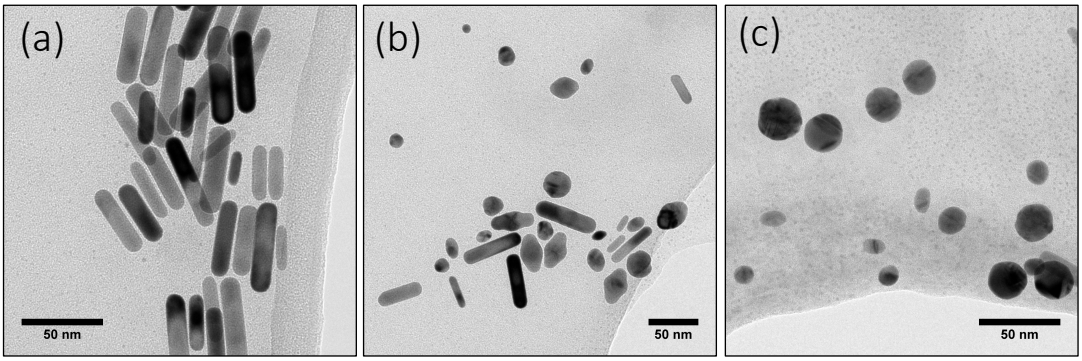

Figure 5.6. Transmission electron microscopy (TEM) images of uncoated AuNRs.

(a) before pulsed laser irradiation. (b) After pulsed laser irradiation of fluence of 20 mJ/cm^2 for 1 min showing different shapes (ϕ-shaped gold nanorods, spherical particles and shortened gold nanorods). (c) For 5 min.

The AuNR@$mSiO_2$ sample before pulsed laser exposure is shown in Figure 5.7a. The AuNR core had a similar mean length, width, and aspect ratio of 52 ± 1 nm, 13 ± 1 nm, and 4.0 ± 0.3, respectively. After they were irradiated for 1 min at a fluence of 20 mJ/cm^2, the TEM images in Figure 5.7b show that the long axis of the AuNR@$mSiO_2$ core was shortened with no measurable change in diameter over the distribution measured (within the uncertainty of measurement). The silica shell appears to be unaffected, thereby leaving behind an apparent sealed cavity, typically at one end. In contrast to the CTAB capped AuNR, the 5 min irradiation (Fig 5.7b) shows similar result to the 1 min irradiation. We observed after 1 and 5 min of

irradiation that the AuNR core length significantly decreased to 35.8 ± 1 nm and 35.2 ± 0.7 nm, respectively, and their new diameter mean are 13.7 ± 0.4 nm and 16.0 ± 0.3 nm, respectively. Consequently, yielding AR of 2.7 ± 0.3 and 2.2 ± 0.3, respectively as shown in (Figure 5.9). After irradiation with pulsed laser of fluence of 10 mJ/cm^2 for 1 and 5 min, the TEM images AuNR@mSiO_2 in Figure 5.8 show that the length decreased to 45.2 ± 0.8 nm with no noticeable change in diameter with AR of 3.7 ± 0.1 and 3.2 ± 0.1, respectively. The observation suggests that the silica shell remains intact during the pulsed laser irradiation making rod-shaped of AuNR@mSiO_2 to more stable compared to CTAB-capped AuNR. In addition, 91.9 % of AuNR@mSiO_2 show a reduction in the length where one end of the rod was found to detach from the silica shell than the other end that remained attached to the silica shell. Moreover, we found that 8.1 % of AuNR@mSiO_2 have reduction in the length of the core from both ends resulting in cavities at both ends. Overall, as the solutions were irradiated with pulsed laser, the Au atoms from the ends of AuNRs migrated to form shorter NRs, subsequently this caused reduction in their AR and significant shift from 820 to ~ 624 nm. The obtained results confirmed the work of Wang *et al.* [322], who simulated the structural transition of bare AuNRs during pulsed laser irradiation using molecular dynamics. Their findings show that above a transition temperature, T_s, the surface atoms of the AuNR caps can migrate toward the middle of the Au NR. They predicted this happens at temperatures of around T_S= 515 K , e.g. much lower temperatures than the melting point of Au. The simulation was performed over a time scale of nanoseconds. The simulation predicts that the AuNRs should become shorter and wider. Interestingly, this is in good agreement with our observation, however, no measurable change in width over the distribution measured. At higher temperatures they observed results consisted with the formation of Φ shaped nanorods (and ultimately at higher temperatures, spheres). However, in our pulsed laser irradiated AuNRs, the silica shell has limited the migration of the capped atoms even after extended exposure. The Au core shapes are either symmetric rods or monkey-nut shaped.

Furthermore, I found that their final irradiation shapes are highly dependent on the laser fluences as well as on its irradiation duration. The TEM images confirming that the spectral changes seen were due to the ends-selective reduction and the silica coating of 6.8 nm has successfully maintained the rod-shaped nanoparticles. The silica shell showed excellent thermal stability as listed in the table 5.1. with negligible reduction in its thickness by ~ 1.2 nm. All histogram figures of size distribution of AuNR, AuNR@mSiO_2, and silica shell

thicknesses are shown in appendix. The table 5.1. summarising the main parameters of AuNR@mSiO$_2$ before and after pulsed laser irradiation.

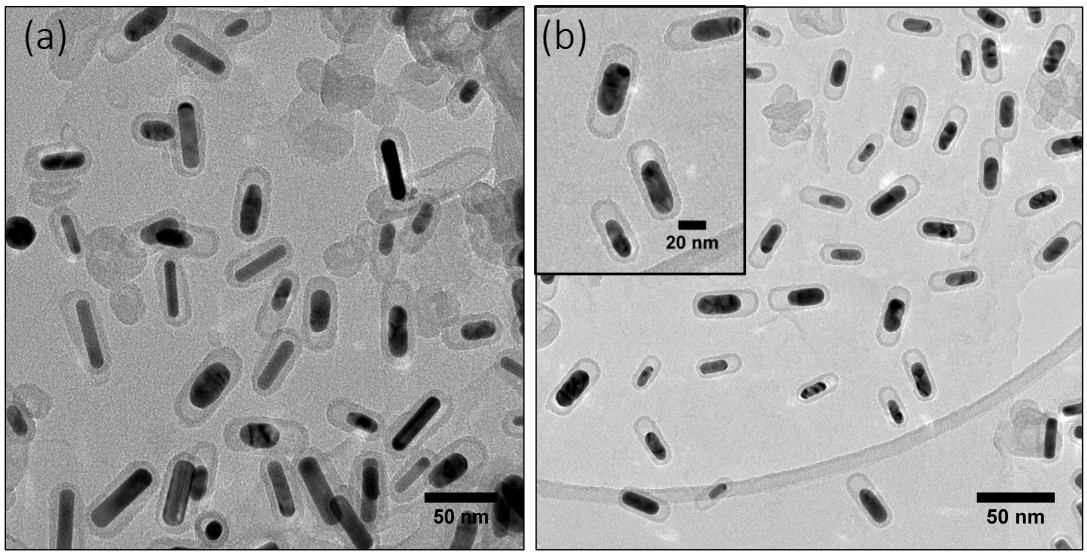

Figure 5.7. Transmission electron microscopy (TEM) images of AuNR@mSiO$_2$ after pulsed laser irradiation of energy of 20 mJ/cm^2

(a) 1 min and (b) 5 min. (Inset: High-magnification TEM image exhibiting the two types of cavities formed after 5 min of pulsed laser irradiation of 20 mJ/cm^2). (Scale bar: 50 nm).

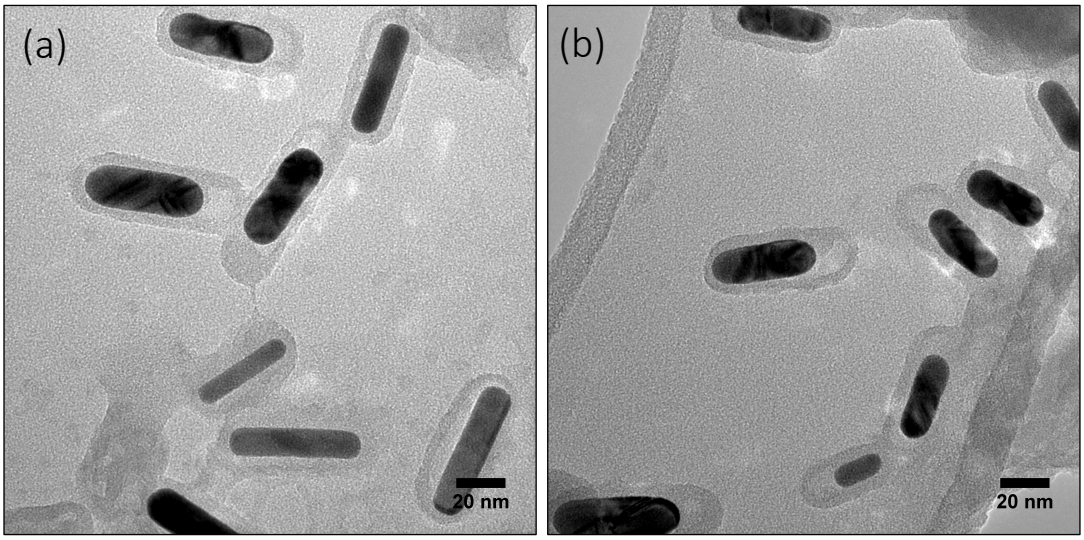

Figure 5.8. Transmission electron microscopy (TEM) images of AuNR@mSiO$_2$ after pulsed laser irradiation of energy of 10 mJ/cm^2.

(a) 1 min and (b) 5 min. (Scale bar: 20 nm).

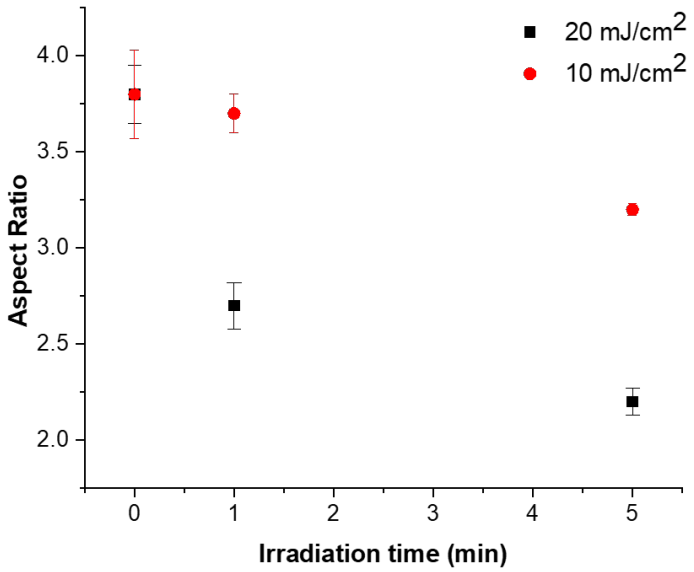

Figure 5.9. Aspect Ratio of AuNRs@mSiO$_2$ versus irradiation time of pulsed laser. of 20 and 10 mJ/cm^2 fluences at (0, 1, and 5 min) obtained from TEM images.

Table 5.1 Summary of the mean lengths, diameters, AR and silica shell thicknesses as measured manually from TEM images of AuNR@mSiO$_2$ control (no laser), AuNR@mSiO$_2$ irradiated by pulsed laser of fluence of 10 mJ for 1 min and 5 min and AuNR@SiO$_2$ irradiated by pulsed laser of fluence of 20 mJ for 1 min and 5 min.

Sample	Fluence (mJ/cm^2)	Time (min)	Length (nm)	Diameter (nm)	AR	Silica shell thickness (nm)
AuNRs@SiO$_2$,Control	0	0	52.3	13.7	3.8	6.8
AuNRs@ SiO$_2$	10	1	45.2	12.3	3.7	5.5
AuNRs@ SiO$_2$	10	5	40.3	13.0	3.2	5.6
AuNRs@ SiO$_2$	20	1	35.8	13.7	2.7	5.6
AuNRs@ SiO$_2$	20	5	35.0	16.0	2.2	5.5

5.3.1.3. EDX mapping after laser irradiation

In Chapter 3 (Section 3.5), the Energy Dispersive X-ray analysis mapping was conducted for the AuNR@mSiO$_2$ to study their elemental distribution. It was proved that the CTAB layer served as an organic template during silica coating process. Both Br and N elements were observed due to CTAB composition and EDX mapping confirmed that the AuNR is coated by two-layers consist of an inner thin CTAB bilayer and an outer SiO$_2$ layer. In this chapter, I used

EDX mapping after irradiated AuNR@mSiO_2 for 5 min of 20 mJ/cm^2 to study the influence of irradiation on the inner thin CTAB bilayer and an outer SiO_2 layer and compare it to their elemental distribution before laser irradiation.

The EDX elemental mapping images of the irradiated AuNR@mSiO_2 in Figure 5.10 (a) clearly reveals the presence and location of Au (green), Br (blue), N (yellow), and Si (red). The hybrid nanoparticle consists of a core of AuNR of length and diameter of 30.5 nm and 12.6 nm respectively, coated with a silica shell of thickness of 5.7 ± 0.2 nm. Firstly, no Au fragmentation is observed in the sample, i.e. the Au signal is confined to the core and therefore we conclude that the laser power was too low to induce fragmentation of the Au within the shell as has been reported in other Au NPs systems. Secondly, a constituent part of CTAB is Br^- and while the formation of AuNRs and the precise role of CTAB, Ag and Br are debated, it is widely known that the Br^- ions provide the CTAB with a strong affinity to gold (as compared to Cl^-). Therefore, mapping the Br should indicate where the CTAB is present (but not its density). The Br is detected over the Au core and appears largely not in the shell. Therefore, I suggest that a CTAB layer (albeit low density) is present on the gold after laser treatment. There is some evidence of a low concentration of CTAB being present cavity region (and the cavity end of the shell), but this is viewed with caution given the low intensity. It is also noted that the CTAB layer is less uniform compared to EDX mapping images of AuNR@mSiO_2 before any laser irradiation see (Fig 3.6) in Chapter 3; however, unless the experimental conditions for collection a direct comparison could be misleading. It appears that CTAB is detached from the AuNR cap (Fig. 5.10a). Furthermore, the EDX mapping images confirm the formation of cavity gap of 10 ± 1 nm between the silica shell and the AuNR core.

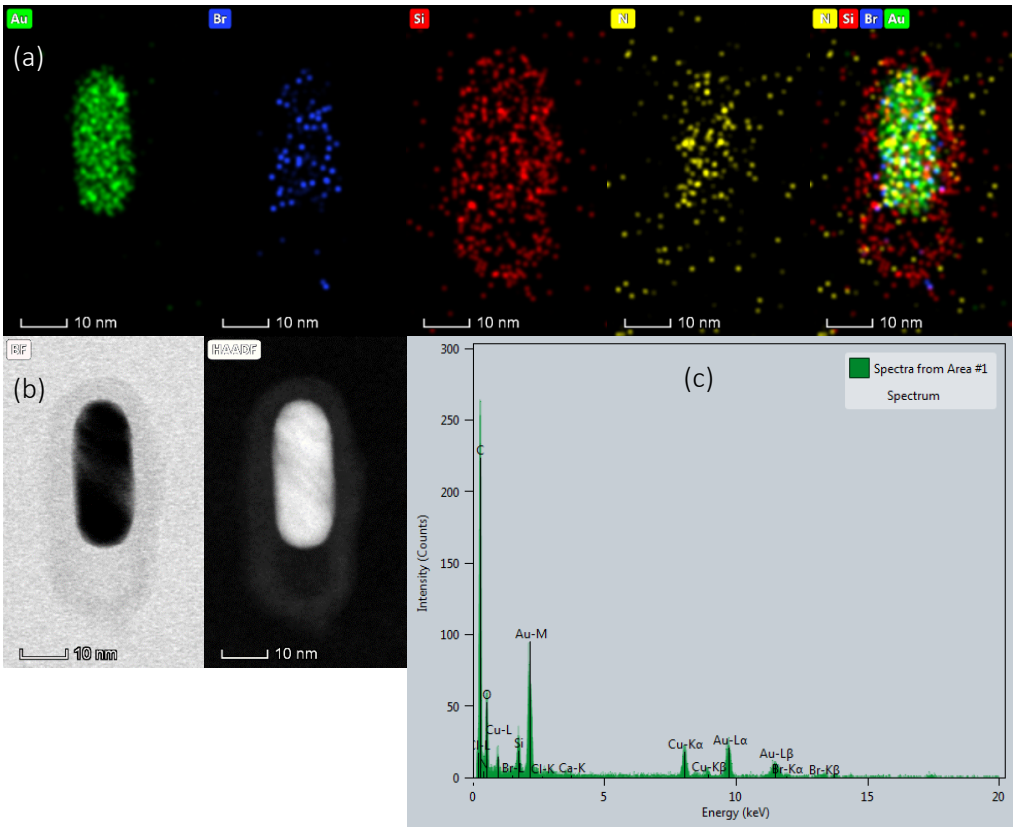

Figure 5.10 EDX elemental mapping.

showing the core-shell elemental composition of AuNR@mSiO$_2$ post irradiation by pulsed laser of fluence of 20 mJ for 5 min. (a) Upper row Au (green), Br (blue), Si (red), N (yellow) and their overlaid image. (b) BF and STEM-HAADF images. (Scale bar: 10 nm). (c) Corresponding EDX spectra of AuNR@mSiO$_2$ supported on a copper grid.

In the EDX spectrum in (Figure 5.10 c), the presence of Au is confirmed by a strong Mα peak at 2.12, Lα peak at 9.7 keV and Lβ 11.4 keV. The Br element was detected by two weak peaks at 11.9 and 13.3 keV, which provides evidence of the presence of CTAB on the surface of AuNR. Moreover, the presence of silica coating on the surface of AuNR was confirmed by the presence of Si element at 1.7 keV. The Cu signal is an artefact of the presence of Cu in the used TEM grid in this measurement.

5.3.2. Pulsed laser irradiation (with stirring)

5.3.2.1. UV-Vis Spectroscopy

The AuNR were exposed to the same laser source, but due to the fact that the laser diameter was not large enough to expose the entire solution at once. This could mean that

some AuNRs outside the beam were not exposed and therefore complicate the post treatment analysis. To overcome this problem and test whether it was something that needed consideration, it was decided that stirring the sample during exposure would ensure more even exposure over the time ranges used. The AuNRs and AuNRs@$mSiO_2$ were irradiated by pulsed laser of wavelength of 850 nm of two fluences 10 and 20 mJ/cm^2 for the same duration.

The result of stirring CTAB-capped AuNRs (Figure 5.11a) shows that the LSPR band of CTAB-capped AuNRs dramatically decreases compared to the non-stirred study. Resulting in a single absorption peak observed in its absorbance spectrum at 530 nm. The same observed for the 10 mJ cm^{-2} laser power (Figure 5.11c). This suggests that almost all of the CTAB coated AuNRs are converted into spheres within 30 s of the laser exposure. This also suggests that not stirring the sample results in AuNRs solutions with a wide distribution of exposures within the ensemble.

The AuNRs@$mSiO_2$ were also exposed during stirring (Figure 5.11b). The first observation is that the LSPR band decreases rapidly but in contrast to the CTAB-coated AuNR a band at 850 nm is persistent even at longer exposure times. Secondly, a new band emerges at around 620 nm, the position of which blue-shifts to a stable position and magnitude. Thirdly, the TSPR peak position remains approximately constant with only marginal increase as compared to the CTAB coated AuNRs. The shortest exposure time (30 s) shows an intermediate sample state with a LSPR peak at 650 nm. A similar observation is made for the 10 mJ cm^{-2} laser power (Figure 5.11d), where the 30 s intermediate is even more pronounced. For both laser powers, a 1 min exposure was sufficient to produce a AuNR@Cavity@$mSiO_2$ material. It is apparent that time is not a good parameter for fine-tuning the AR of the AuNR core, but on the other hand the end result is relatively consistent for times >1 minute.

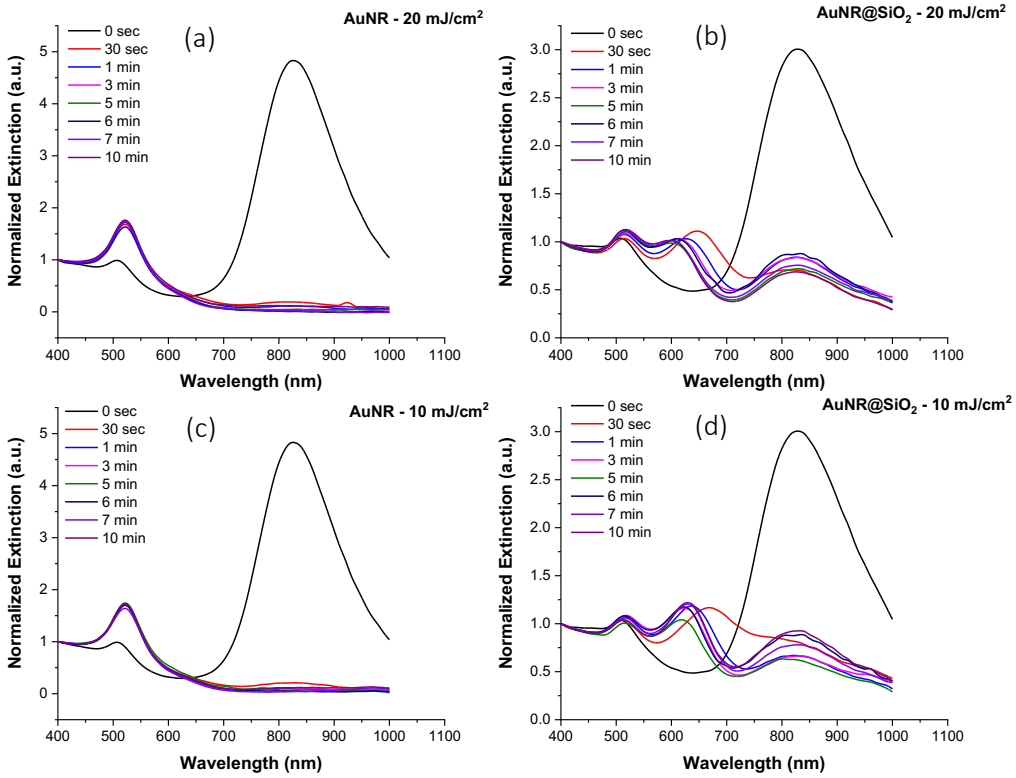

Figure 5.11 Normalized UV–Vis–NIR spectra.

(a & b) AuNR and AuNR@mSiO₂ after 20 mJ/cm² pulsed laser irradiation of different times respectively. (c & d) AuNR and AuNR@mSiO₂ after 10 mJ/cm² pulsed laser irradiation of different times respectively. All samples were irradiated for (0, 30 s, 1 min, 3 min, 5 min, 6 min, 7 min and 10 min). The sample were irradiated during stirring.

5.4. Modelling of AuNRs@SiO_2 After Pulsed Laser Irradiation Using COMSOL

The electric-field enhancement caused by the nanocomposite structure before and after pulsed laser irradiation was stimulated in this section, to understand the silica coating influence on electric-field enhancement. Here, we discuss the simulated results obtained using COMSOL in comparison with experimental results. The software COMSOL's radio frequency module was used to model the electric-field enhancement of plasmonic AuNRs and AuNRs@mSiO_2 before and after thermal reshaping.

The parameters of AuNR and AuNR@mSiO_2 such as length, width, and aspect ratio were obtained from the TEM images that were shown earlier in this Chapter in (Section 5.3). As shown in Figure 5.12 (a, b), the length and diameter of the original AuNRs is 52.31 and 13.7 nm, respectively. On the other hand, the AuNRs@mSiO_2 of a length of 52.31 nm, diameter of 13.7 nm, and silica shell thickness of 6.8 nm. The electric-field enhancement is shown from *y*–*z* view. As shown in Figure 5.12 (a, b), It is observed that the electric field is noticeably inhomogeneous along the long axis AuNR. Moreover, the highest electric field enhancement for the bare AuNR is located between the tips of the AuNR and the surrounding medium. It is obvious that an electric-field enhancement occurred at the corners of both AuNRs and the AuNRs@mSiO_2 with value of electric-field enhancement of ~ 70 near the tips of both NRs. The electric field enhancement of AuNRs@mSiO_2 was observed close to the ends between the silica shell and the AuNR core.

The corresponding scattering, extinction and absorption cross section spectra for of both AuNRs and AuNRs@mSiO_2 were simulated and are presented in Figure 5.12 (c-f). The simulated spectra of AuNRs show mainly two SPR peaks strong and weak plasmon peaks, a weak plasmon peaks at 520 nm associated to the transverse plasmon peak and a strong peak at 807 nm associated to the longitudinal plasmon peak as shown in Figure 5.12 (c-d). However, it can be clearly observed in Figure 5.12 (e-f) that after coating the AuNR with a silica shell, their LSPR red-shifted to 836 nm, whereas the TSPR peak remained the same at 520 nm. These observations demonstrate a similar trend as the experimental results shown earlier in this chapter.

The electric-field enhancement of both bare AuNRs and AuNRs@mSiO_2 are similar, no influence on the electric-field enhancement of AuNRs@mSiO_2 after silica coating was observed. However, the shortened core nanorod of AuNRs@mSiO_2 Figure 5.13 (b) shows non-uniform electric field distribution around AuNRs@mSiO_2 after reshaping, its electric field generated at the shortened tip (in the formed gap) is higher than the other tip nearly 30 (V/m).

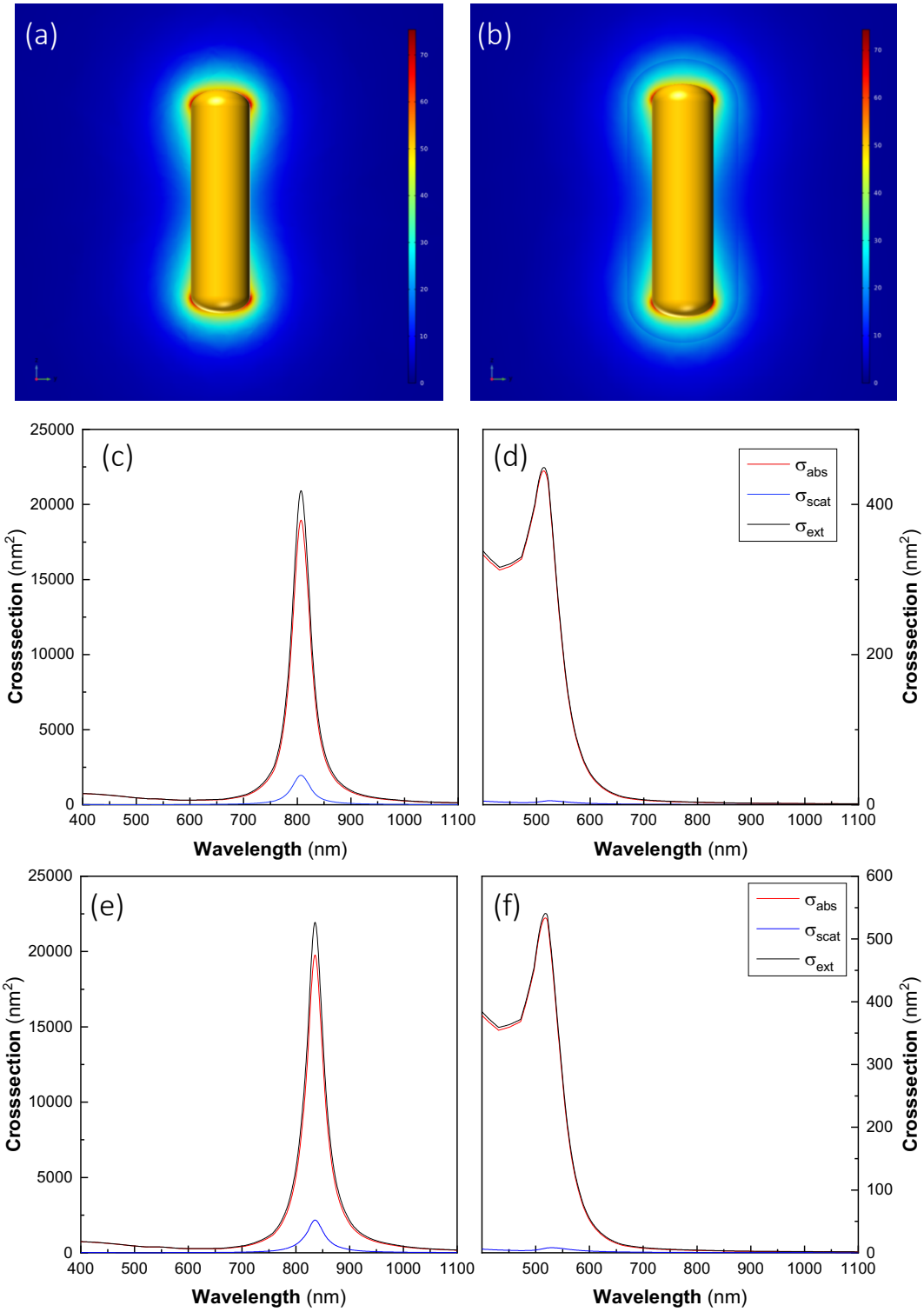

Figure 5.12 Modelling of AuNRs@SiO_2 After Pulsed Laser Irradiation Using COMSOL.

(a, b) The simulated near-field electromagnetic enhancement maps and distributions around the individual gold nanorod for the transverse and longitudinal plasmon modes for original AuNR and AuNR with mesoporous SiO_2 shell of length of 52.3 nm and diameter of 13.7 nm in water irradiated by an 850 nm laser polarized linearly along its great axis. (c, d) Simulated absorption spectra of the original AuNRs, (e, f) Simulated absorption spectra of the original AuNR with mesoporous SiO_2 shell.

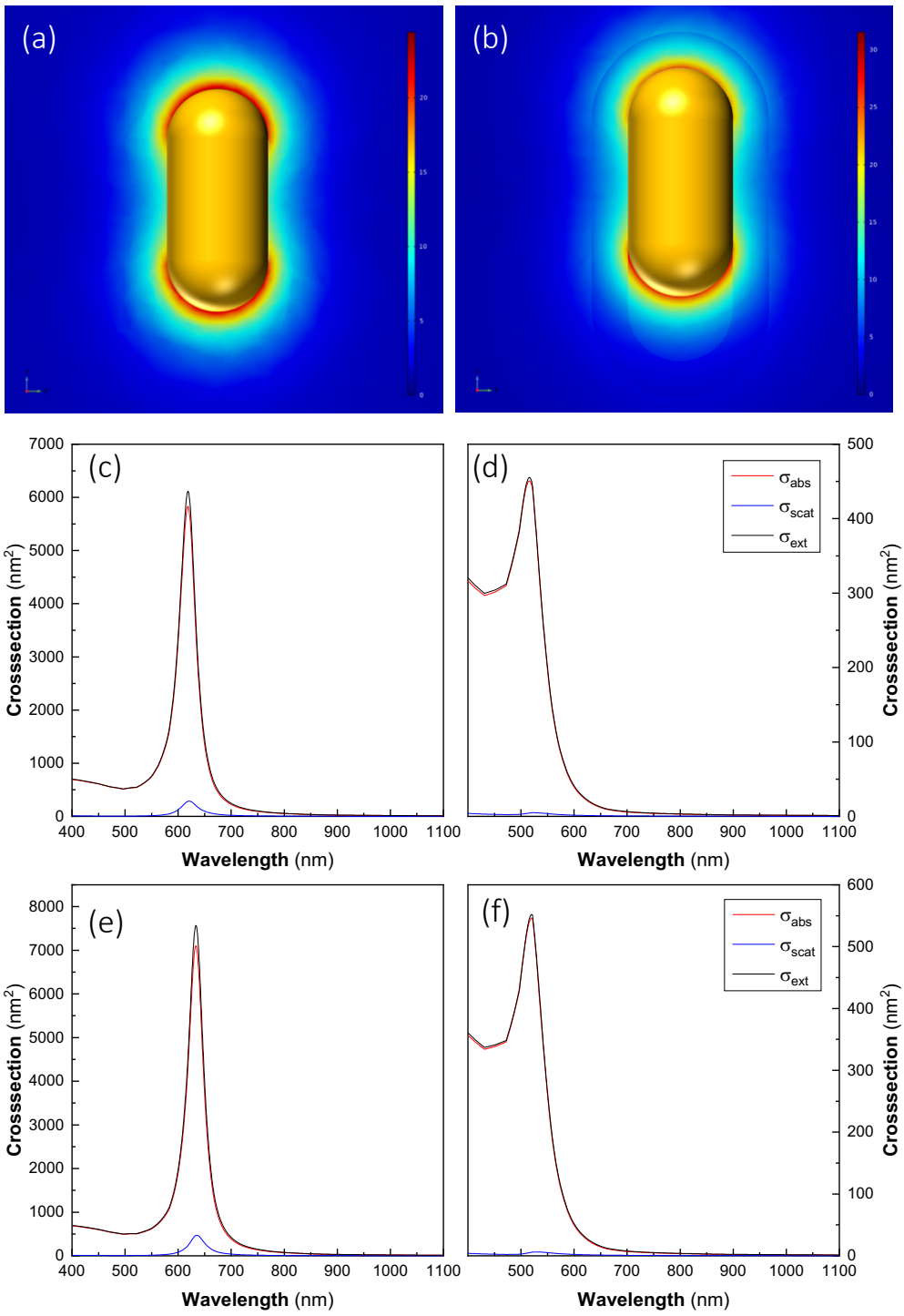

Figure 5.13 Modelling of AuNRs@SiO_2 After Pulsed Laser Irradiation Using COMSOL.

(a, b) The simulated near-field electromagnetic enhancement maps and distributions around the individual gold nanorod for the transverse and longitudinal plasmon modes for reshaped AuNR and AuNR with mesopores SiO_2 shell of length of 35.15 nm and diameter of 16.12 nm in water irradiated by an 850 nm laser polarized linearly along its great axis. (c, d) Simulated absorption spectra of the irradiated AuNRs, (e, f) Simulated absorption spectra of the irradiated AuNR@mSiO_2.

Generally, when AuNPs are illuminated by pulsed laser, their free electrons become high-energy electrons due to the absorption of the photons energy, causing rise in their temperature [171]. Subsequently the heat would be transferred to the surrounding medium [367]. Here, we investigate the photothermal response of AuNR@mSiO_2 before and after reshaping as a function of distance. We simulated the lattice temperature of AuNR of length of 52.3 nm, diameter of 13.7 nm, and silica shell thickness of 6.8 nm in water after 7 ns pulse, 13 mJ·cm^2 and the pulse of 10 ns of 850 nm single laser pulse. The temperature increase was studied as a function of the distance from the surface of AuNR of both nanorods under the same irradiation conditions.

The heating curve across the original water–AuNR@mSiO_2 interface of length of 52.3 nm, diameter of 13.7 nm, and silica shell thickness of 6.8 nm was simulated. As shown in Figure 5.14 (a), the temperature of Au rod (core) of AuNR@mSiO_2 gradually increased with time, reached a maximum temperature increase of about 110°C in 11.5 ns under the irradiation. The temperature of Au rod (core) of reshaped AuNR@mSiO_2 gradually increased with time and reached a maximum increase of about 122 °C in 11.5 ns, as shown in Figure 5.15 (a). The maximum temperature change at water Au/SiO_2 interface is lower than the core reaching ~ 95°C.

The simulated cooling curve of the original water–AuNR@mSiO_2 interface and reshaped water–AuNR@mSiO_2 interface show the cooling (Figure 5.14 b & 5.15 b). The temperature curves dropped from the maximum temperature of 110°C and 122°C, back to the starting temperature (e.g. room temperature) within 50 ns. This suggests that the AuNR heat is completely dissipated between laser pulses.

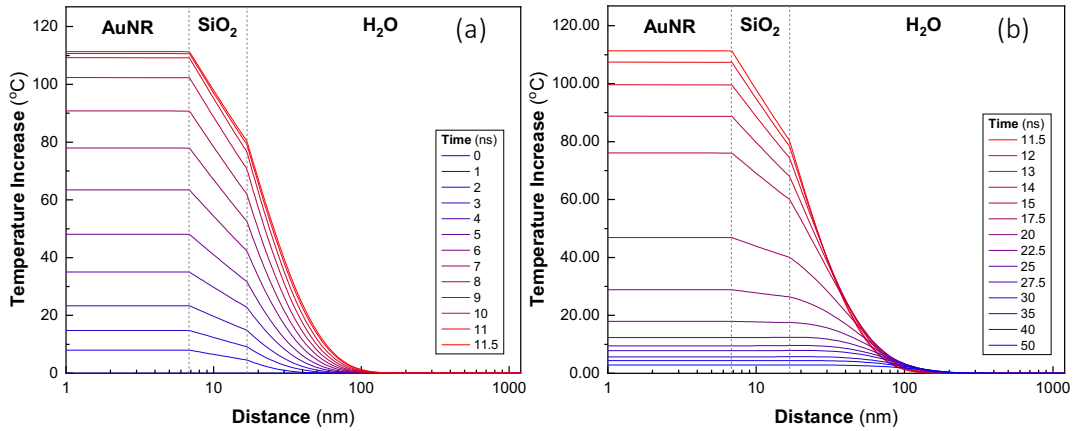

Figure 5.14 The calculated temperature profiles across the water–AuNR@mSiO$_2$ interface of the original AuNR@mSiO$_2$.

(a) The simulated temperature increases of the original AuNR@mSiO$_2$ of length of 52.3 nm, diameter of 13.7 nm, and silica shell thickness of 6.8 nm in water as a function of the distance from the surface of the particle. Irradiated by 850 nm laser of 7 ns pulse, fluence =13 mJ·cm^2, pulse centre = 10 ns. (b) The simulated temperature distribution (cooling) of the same original AuNR@mSiO$_2$ (after peak AuNR temp, cooling).

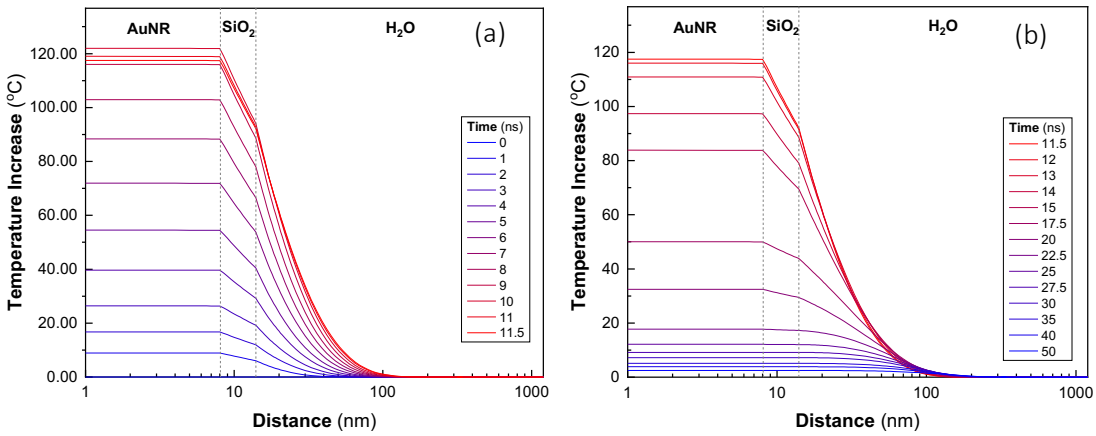

Figure 5.15 The calculated temperature profiles across the water–AuNR@mSiO$_2$ interface the reshaped AuNR@mSiO$_2$.

(a) The simulated temperature increases of the reshaped AuNR@mSiO$_2$ of length of 52.3 nm, diameter of 13.7 nm, and silica shell thickness of 6.8 nm in water as a function of the distance from the surface of the particle. Irradiated by 850 nm laser of 7 ns pulse, fluence =13 mJ·cm^2, pulse centre = 10 ns. (b) The simulated temperature distribution (cooling) of the same original AuNR@mSiO$_2$ (after peak AuNR temp, cooling).

In summary, the goal of these simulations is to understand the silica coating influence on electric-field enhancement and investigate the photothermal response of AuNR@mSiO$_2$ before and after reshaping as a function of distance. These simulations provided predictions of electric-field enhancement of both bare AuNRs and AuNRs@mSiO$_2$. The electric-field enhancement of both bare AuNRs and AuNRs@mSiO$_2$ are similar with no influence on the electric-field enhancement of AuNRs@mSiO$_2$ after silica coating was observed. Moreover, the temperature of Au rod (core) of AuNR@mSiO$_2$ gradually increased with time, reached a maximum temperature increase of about 110°C in 11.5 ns under the irradiation. However, the temperature of Au rod (core) of reshaped AuNR@mSiO$_2$ gradually increased with time and reached a maximum increase of about 122°C in 11.5 ns. The temperature would drop from the maximum temperature to room temperature within 50 ns due to the heat dissipation of AuNR between laser pulses.

5.5. Pulsed Laser Rrradiation Using 900 nm Laser (with stirring)

It was hypothesized that the laser wavelength could be a useful parameter for controlling the reshaping behaviour. If the laser wavelength is on the red-side of the AuNR LSPR band, then the optical cross-sectional absorption per nanorod will be reduced. If the light absorbed is reduced, then the maximum temperature of the AuNR should also be lower. Assuming that a transition temperature is required for reshaping e.g. T_s, then the expected result would be slower reshaping or even no reshaping at all. Moreover, as the AR decreases the LSPR band

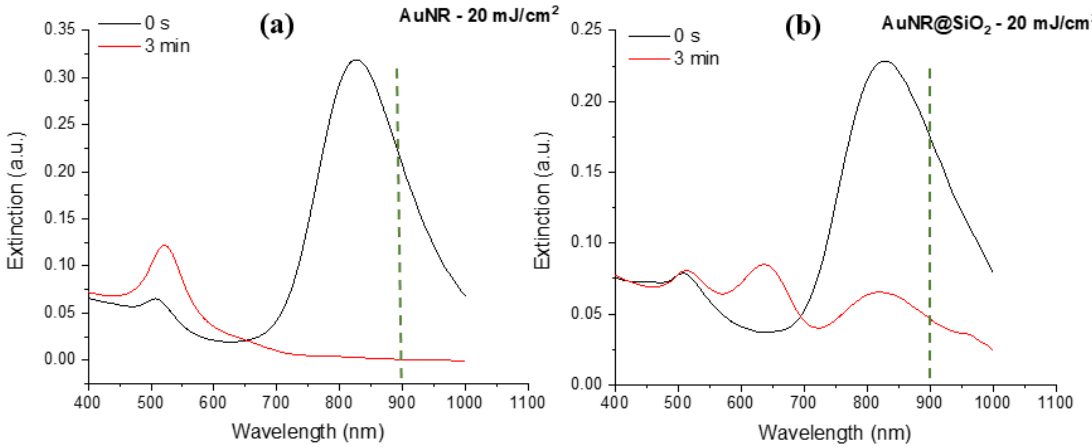

Figure 5.16 UV–Vis–NIR spectra of AuNR and AuNR@mSiO$_2$.

after 3 min of irradiation of a longer laser wavelength of 900 nm of 20 mJ/cm^2 fluence (with stirring). (a) AuNRs. (b) AuNR@mSiO$_2$.

will blue-shift further away from the laser wavelength causing even less heating and therefore any further AR change. The photothermal reshaping behaviour of the CTAB-capped AuNRs and AuNRs@$mSiO_2$ were therefore studied using longer laser wavelength of 900 nm. A fixed time of 3 minutes, with a power of 20 mJ cm^{-2}, was set as this provided consistent results for the 850 nm wavelength.

Figure 5.16 shows the UV-vis results from CTAB-capped AuNRs and AuNRs@SiO_2. Firstly, the CTAB-capped sample (Figure 5.16a) behaved in an almost identical manner to the 850 nm laser irradiation see (Figure 5.11a) ends with the formation of spheres. The AuNRs@$mSiO_2$ sample (Figure 5.16b) also behaved in the same manner as the 850 nm experiment (Figure 5.11b). Specifically, a new LSPR band appears, there is some persistence of the original 850 nm LSPR peak and the TSPR peak remained unchanged. This suggests that the absorbed energy per AuNR was still above reshaping threshold and that the reshaping is rapid e.g., sufficiently rapid so that the shape change is not controlled by the use of a longer wavelength. This is presumably because the spectral overlap remains high enough to reshape to an AR corresponding to a LSPR peak at ~ 620 nm.

5.6. Thermal Reshaping of AuNR@$mSiO_2$ of Higher Porosity Under Pulsed Laser Irradiation

In section 5.2, both laser powers 10 and 20 mJ cm^{-2} were sufficient to produce a AuNR@Cavity@$mSiO_2$ material after 1 min exposure, which confirmed that time was not a good parameter for fine-tuning the AR of the AuNR core, producing a final product which is relatively consistent for times >1 minute.

Therefore, in this section, our aim was to study the influence of the porosity degree on the thermal reshaping of AuNRs@$mSiO_2$ of two different porosity degrees of 81% and 43 %. The porosity degree of 81% of AuNRs@$mSiO_2$ was increased by adding 10 $X10^{-3}$ M of CTAB to the silica shell growth solution and the 43% porosity was obtained as a result of the CTAB presence in the solution after cycles of centrifugation before the silica shell growth, as discussed in (Chapter 3 section 3.8). After the formation of the AuNRs@$mSiO_2$ of two porosity degrees, the two samples of concentration of 50 µg/ml dispersed in Milli-Q water were irradiated by

pulsed laser irradiation of laser wavelength of 850 under stirring for 1 min with all other parameters constant with study in **section 5.2** (laser fluence = 10 mJ/cm^2, the eliminated area = 6 mm, laser pulse = 7 ns, repetition rate = 10 Hz, and with stirring).

5.6.1. UV-Vis Spectroscopy

The corresponding UV-Vis spectra of both exposed AuNR@mSiO$_2$ of the two porosity degrees are shown in Figure 5.17. The LSPR peak of AuNR@mSiO$_2$ of 43 % porosity and irradiated with 10 mJ/cm^2 blue shifted from 796 ± 2 nm to 716 ± 2 nm and Δλ ~ 80 ± 3.4 nm. The relative extinction peak shifts were calculated by $\Delta\lambda = \lambda_{initial} - \lambda_{final}$, where Δλ is defined as the peak shift upon thermal reshaping induced by pulsed laser irradiation, $\lambda_{initial}$ is the LSPR peak position before irradiation and λ_{final} is the LSPR band position after irradiation. The absorption intensity of the LSPR was observed to be maintained as before irradiation. In addition, the band at 520 nm, associated with the TSPR did not change after the laser irradiation. However, the FWHM decreased from 161.3 to 112.7 as shown in (Figure 5.17a). The reduction in in FWHM suggesting that the AR distribution decreases as a result of irradiating AuNR@mSiO$_2$ by laser which is off-resonance wavelength.

On the other hand, the AuNR@mSiO$_2$ of porosity to 81%, the LSPR peak shows a blue shift from 771 ± 1 nm to 706 ± 1 nm (Δλ ~ 65 ± 1 nm) as shown in (Figure 5.17b). The absorption intensity decreased and the TSPR peak increase, this could be associated to the conversion of

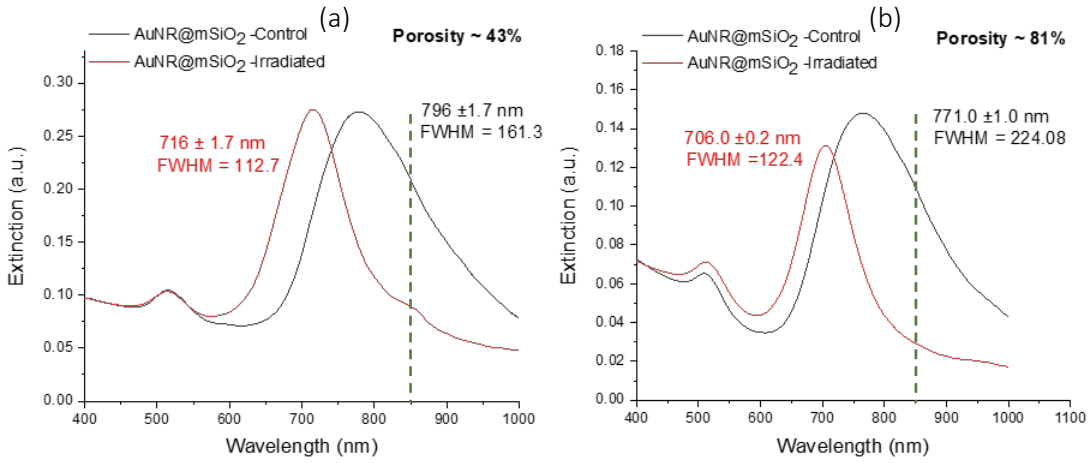

Figure 5.17 UV–Vis–NIR spectra of AuNR@mSiO$_2$.

after 1 min of irradiation of wavelength of 850 nm of 10 mJ/cm^2 fluence (with stirring). (a) Porosity 43%. (b) Porosity 81%. The vertical dashed line at 850 nm corresponding to overlapping between the laser wavelength and the absorption spectra of AuNR@mSiO$_2$.

a fraction of the AuNRs into spherical AuNPs. The FWHM decreased from 224 nm to 122 nm. We assume that AuNR@mSiO$_2$ thermal reshaping behaviour is influenced by how much energy absorbed during pulsed laser irradiation. When the laser is off resonance, only a fraction of the energy is absorbed and mainly the larger AuNRs are affected.

5.6.2. Transmission Electron Microscopy (TEM)

The shape and morphology changes of AuNR@mSiO$_2$ of porosity of 81% after 1 min of pulsed laser irradiation at fluence of 10 mJ cm^{-2} were analysed by TEM. The TEM images show

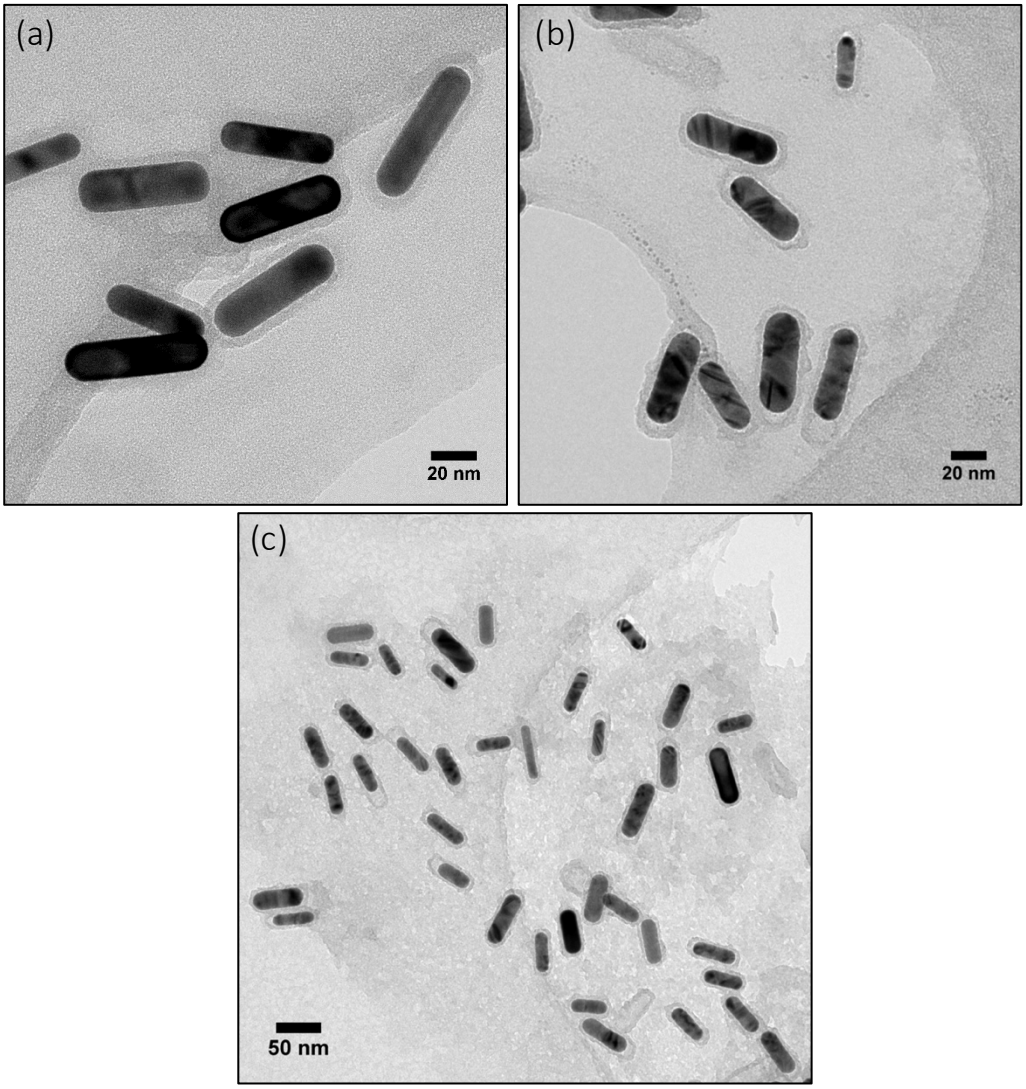

Figure 5.18 TEM images of AuNR@mSiO$_2$ of porosity of 81 %.

(a) Before laser irradiation (b) After pulsed laser irradiation of energy of 10 mJ cm^{-2} for 1 min. (Scale bar: 20 nm). (c) Wide-field TEM image of AuNR@mSiO$_2$ after pulsed laser irradiation. (Scale bar: 50 nm).

that the starting mean length of AuNR@mSiO$_2$ is 52 ± 1 nm, diameter of 13 ± 0.3 nm, silica shell thickness of 6.8 ± 0.2 nm and an aspect ratio of 3.8 ± 0.6.(Figure 5.18a)

After they were irradiated for 1 min at a fluence of 10 mJ/cm^2, the TEM images in (Figure 5.18 b & c) show variety of products from the photothermal reshaping. The most frequently detected particles were AuNR@mSiO$_2$ with a lower core AR, i.e. the long axis of the AuNR core was shortened to 45.2 ± 0.8 nm with a yield of 60 %, but the rod shape was maintained with the diameter being approximately the same as before irradiation (within the uncertainty of measurement).

The observed reduction in the core AuNRs is less than the reduction observed in (**section 5.2),** consequently creating a smaller sealed cavity ~ 5.4 ± 0.4 nm, typically at one end. The second most detected particles are stable AuNR@mSiO$_2$ with unchanged length and diameter with a yield of 30 %. Small portion of spheres were observed after the pulsed laser irradiation with yield of 10 %. The silica shell appears to be remained unaffected as shown in size distributions in (Figure 5.19d).

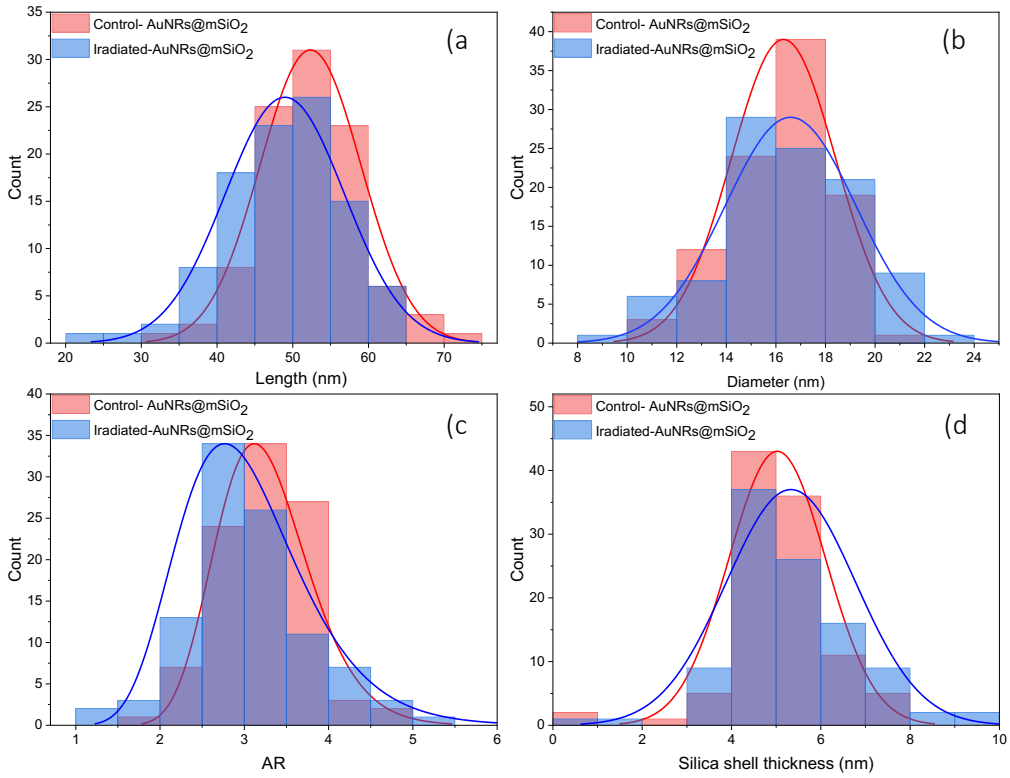

Figure 5.19 Size distributions of AuNR@mSiO$_2$ of porosity of 81 %.

before (red) and after (blue) pulsed laser irradiation of wavelength of 850 nm and 10 mJ/cm^2 fluence for 1 min. (a) Length. (b) Diameter. (c) Aspect ratio. (d) Silica shell thickness. (These data were derived from TEM analysis from 100 AuNRs).

5.6.3. EDX mapping after laser irradiation

The Energy Dispersive X-ray analysis mapping of the AuNR@mSiO$_2$ (of 81% porosity) after irradiation for 1 min of 10 mJ cm^{-2} was conducted to quantify atomic-scale chemical compositions of AuNR@mSiO$_2$ of higher porosity after CTAB extraction and the influence of irradiation on the inner thin CTAB bilayer and an outer SiO$_2$ layer and compare it to their elemental distribution to the EDX mapping of AuNR@SiO$_2$ of lower porosity in (Figure 5.20).

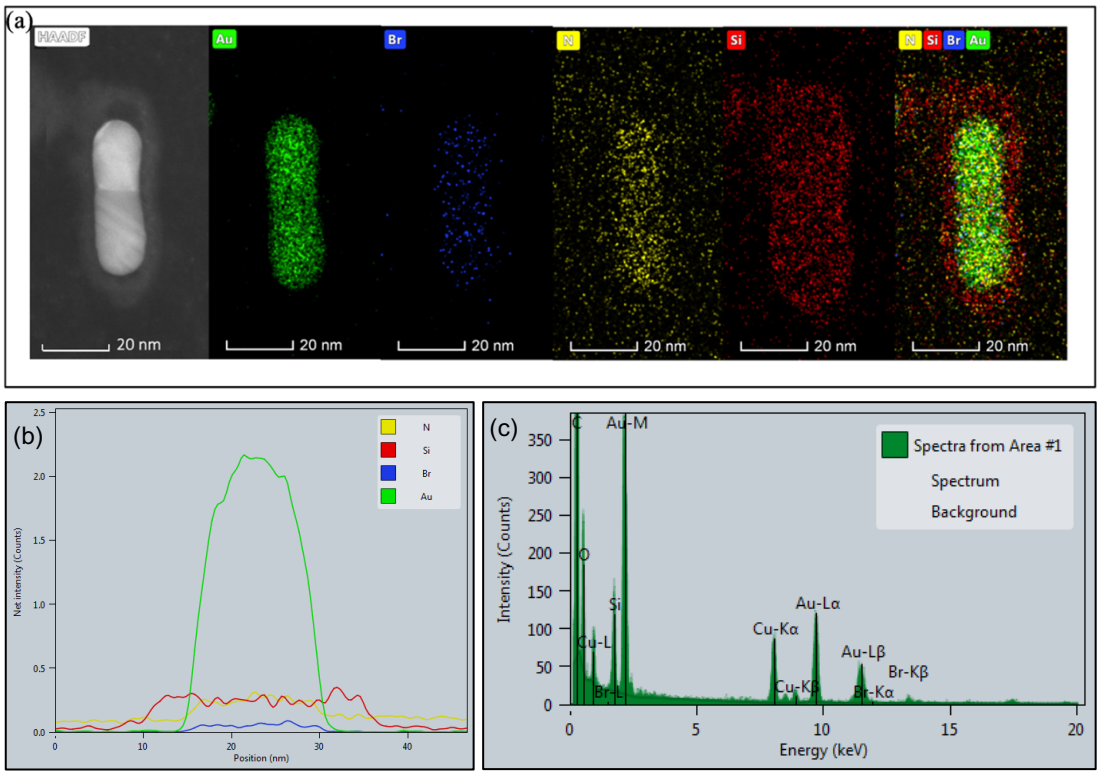

Figure 5.20 EDX elemental mapping of AuNR@mSiO$_2$ post irradiation.

Showing the core-shell elemental composition of AuNR@mSiO$_2$ post irradiation by pulsed laser of fluence of 20 mJ for 5 min. (a) STEM-HAADF image and color-map images of Au (green), Br (blue), N (yellow), Si (red), and their overlaid image (Scale bar: 20 nm). (b) EDX line scanning profile of cross section of AuNR@mSiO$_2$). (c) Corresponding EDX spectra of AuNR@mSiO$_2$ supported on a copper grid.

The color-map images in (Figure 5.20 a) clearly reveal the presence of Au (green) surrounded by Br (bule), N (yellow), and Si (red) elements. The obtained EDX mapping images confirmed that the AuNR core is coated by two-layers consist of an inner thin CTAB bilayer and an outer SiO$_2$ layer similar to the AuNR@mSiO$_2$ of lower porosity 43 % in (Figure 5.20a).

No Au fragmentation was observed in EDX mapping images. The presence of CTAB was confirmed by detecting Br and N elements on the surface of AuNR core. The Br is detected over the Au core and appears largely not in the shell, confirming the successful CTAB extraction the silica pores. Moreover, it was noted that the CTAB layer was detached from the AuNR cap, and more uniform compared to AuNR@mSiO_2 of lower porosity of 43 % in (Figure 5.10). The Si is uniformly distributed on the surface of the CTAB@AuNRs core with a silica shell thickness estimated ~ 5.4 ± 0.4 nm as estimated from EDX line scanning profile of cross section of AuNR@mSiO_2 (Figure 5.20 b). It was observed that there was no CTAB being present in the cavity region (the cavity at the two caps of AuNR core, as shown in (Figure 5.20 a, the overlap image).

Furthermore, in the EDX spectrum, the different elements show their presence through energy peaks in (Figure 5.20 c), the presence of Au is confirmed by a strong Mα peak at 2.12, Lα peak at 9.7 keV and Lβ 11.4 keV. The Br element was detected by two weak peaks at 11.9 and 13.3 keV, which provides extra evidence of the presence of CTAB on the surface of AuNR. Moreover, the presence of silica coating on the surface of AuNR was confirmed by the presence of Si element at 1.7 keV. The Cu signal is an artefact of the presence of Cu in the used TEM grid in this measurement. The data obtained from the EDX spectrum of AuNR@mSiO_2 (81 % porosity) is reasonably similar to the EDX spectrum of AuNR@mSiO_2 of a lower porosity (43 % porosity) in Figure 5.10, with considering the net intensity difference between the two samples.

In summary, several factors can affect the thermal stability of AuNR@mSiO_2 such as (exposure time, LSPR band position with laser wavelength, AR, surface area, and heat relaxation time of AuNRs). I found that 1 min exposure is sufficient to produce a AuNR@Cavity@mSiO_2 material using both laser powers 10 and 20 mJ cm^{-2}. The cavity gap size can be controlled by choosing the starting LSPR peak position of AuNRs@mSiO_2. The gap size of AuNRs@mSiO_2 of LSPR band at 830 ± 1 nm (on resonance) is ~ 10 nm after 20 mJ/cm^2 irradiation (see Figure 5.21 c). However, when LSPR band of AuNR@SiO_2 was at 771 ± 1 nm (off resonance), a cavity gap of size ~ 5.4 nm was formed after 10 mJ/cm^2 irradiation (see Figure 5.21 d). The sizes of the formed cavity at each blue shifts of LSPR band are shown in Figure 5.22.

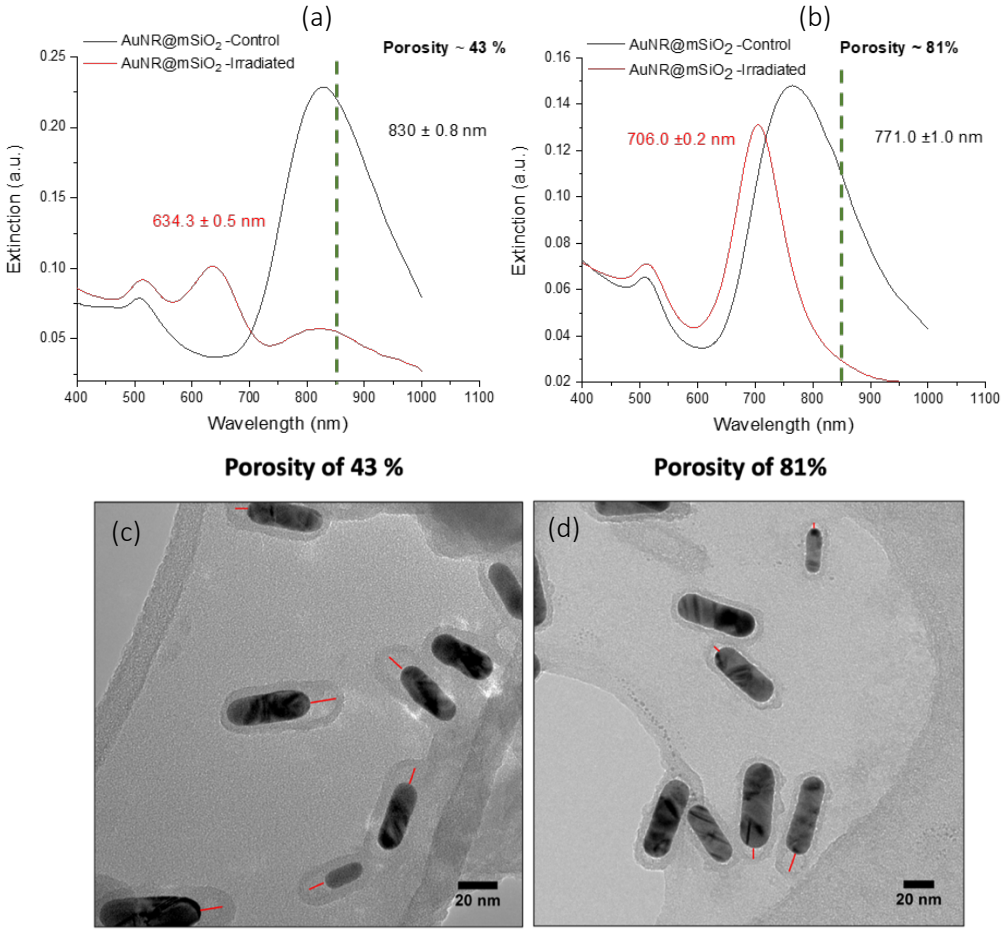

Figure 5.21 Extinction spectra and TEM images of AuNR@mSiO₂ of porosity 43% and 81 %.

(a) Extinction spectra of AuNR@mSiO₂ of porosity 43 % after 5 min irradiation of pulsed laser irradiation at fluence of 20 mJ cm^{-2}. (b) Extinction spectra of AuNR@mSiO₂ of porosity 81 % after 1 min of irradiation of pulsed laser irradiation at fluence of 10 mJ cm^{-2}. The wavelength of pulsed laser used for both irradiation is 850 nm. The vertical dashed line at 850 nm corresponding to overlapping between the laser wavelength and the absorption spectra of AuNR@mSiO₂. (c) TEM image of irradiated AuNR@mSiO₂ of porosity of 43 % showing the formation of a cavity gap of size 10 ± 0.2 nm after 20 mJ/cm^2 of (sample shown in plot a). (d) TEM image of irradiated AuNR@mSiO₂ porosity of 81 % showing the formation of a cavity gap of size 5.4 ± 0.4 nm after 10 mJ/cm^2 of (sample shown in plot b). The red lines denote the formation of gaps after pulsed laser irradiation. (Scale bar: 20 nm).

The heat relaxation time of AuNR was found to be depended on the size, surface area and the surrounding medium [284]. The thermal relaxation time of gold nanorods in silica shells was estimated by Chon et al. to be 20 ps [368, 369]. However, when the AuNR is passivated by CTAB bilayer, the heat relaxation time was found to be ~ 150 ps. The efficient thermal reshaping of the AuNRs was found to occur at slow heat relaxation time [368, 369]. Therefore, the fragmentation and reshaping of the AuNRs into spherical particles will be inhibited by rapid heat diffusion [284]. Our core AuNR of our AuNRs@mSiO₂ of both porosity degrees were found

to be coated by an inner thin CTAB bilayer and an outer SiO_2 layer. We assume that the CTAB bilayers' low heat diffusion constant effectively accelerated the photothermal reshaping of AuNRs.

Table 5.2 Summary of the mean lengths, diameters, AR and silica shell thicknesses, and gap size (as measured manually from TEM images) of two different AuNR@$mSiO_2$ of two different porosity 43 % and 81 %. AuNR@$mSiO_2$ 81 % were irradiated by pulsed laser of fluence of 10 mJ $cm^{-2}$and AuNR@$mSiO_2$ 81 % were irradiated by pulsed laser of fluence of 20 mJ cm^{-2}. Both samples were irradiated by pulsed laser irradiation of wavelength of 850 nm 1 min.

Sample	SiO_2 Porosity %	Length (nm)	Diameter (nm)	AR	SiO_2 shell thickness (nm)	λ_{max}	Δ L = Gap size (nm)
AuNRs@$mSiO_2$ – Control	43	52.6 ± 0.8	16.3 ± 0.3	3.3 ± 0.1	5.1 ± 0.1	830 ± 0.8	
AuNRs@$mSiO_2$ – Laser irradiated	43	48.9 ± 0.8	16.6 ± 0.3	3.0 ± 0.1	5.4 ± 0.1	634.3 ± 0.5	10 ± 0.2
AuNRs@SiO_2 – Control	81	52.3 ± 1	13.7 ± 0.3	3.8 ± 0.6	6.8 ± 0.2	771 ± 1.0	
AuNRs@SiO_2 – Laser irradiated	81	45.2 ± 0.8	12.3 ± 0.2	3.7 ± 0.1	5.5 ± 0.1	706 ± 0.2	5.4 ± 0.4

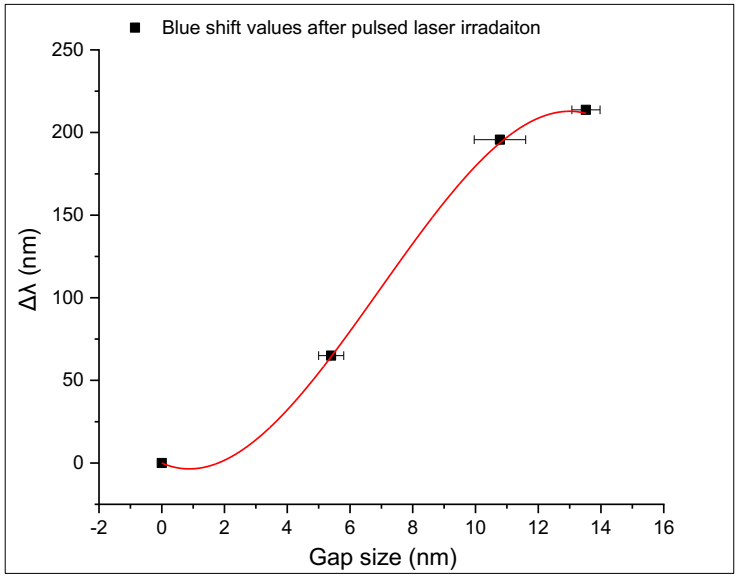

Figure 5.22 The plasmon peak blue shifts of AuNRs@$mSiO_2$ as a function of cavity gap size.

(The red line is to guide the eye).

5.7. Controlling Thermal Reshaping of AuNR@mSiO$_2$ By Dry Bath Heating

In previous sections, we observed the sensitivity of LSPR band to the absorbed energy of pulsed laser irradiation. Irradiating AuNRs@mSiO$_2$ by pulsed laser of 10 mJ cm^{-2} caused rapid end-selective shortening of AuNR core creating a cavity within seconds. The reshaping can be monitored from the bule shifts of LSPR bands. Here, we study the thermal reshaping of AuNRs@mSiO$_2$ under dry bath heating. The AuNRs@mSiO$_2$ of porosity degree of 43% of concentration of 50 µg/ml were dispersed in water and heated at 50°C for different periods. To monitor the thermal reshaping, the extinction spectra before and after heating were collected from a 100 µL AuNRs@mSiO$_2$ suspension at different time intervals.

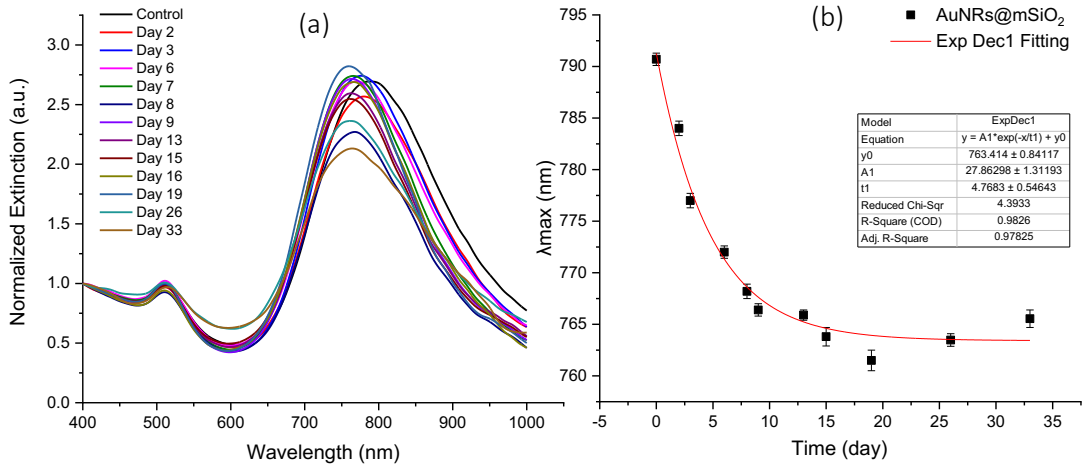

Figure 5.23 Extinction spectra of AuNR@mSiO$_2$ of porosity degree of 41 % after dry bath heating at 50 °C.

under stirring at different time point during 33 days of constant heating. (b) AuNR/SiO$_2$. The exponential decay curve of LSPR peak positions of AuNRs@mSiO$_2$ obtained from UV–Vis–NIR spectra in plot (a) versus heating time, with t1= 4.7 ± 0.5.

The variations of the LSPR peak positions for AuNR@mSiO$_2$ as function of heating time are plotted in (Figure 5.23). The heating caused the LSPR band to gradually blue-shift with time. In fact, between 1-9 days the LSPR band positions decreased exponentially from 802.0 ± 1.6 nm (FWHM ~ 223 ± 1) to 766.4 ± 0.6 nm (FWHM ~ 224 ± 1), with a half-life of approximately 4.7 days. The blue-shift appeared to stabilise to around 765 nm after 13 days. The reduction in the LSPR band intensity is most likely due the loss of AuNRs caused by aggregation. However, the TSPR band appears to be unchanged with heating time, that confirms that no spherical AuNPs are obtained during heating. Notably, even after longer heating times, no new

LSPR band appears in the extinction spectra. It appears that the silica shell does not prevent reshaping of the AuNR but prevents the AR of the AuNRs from reducing below a certain value. The same effect is seen in both the high and lower power of pulsed laser studies discussed earlier in this section. The observed extinction peak shifts were, $\Delta\lambda \sim 37 \pm 2$ nm, which is relatively small compared to the extinction peak shifts obtained by nanosecond pulsed laser irradiation of both fluences. We assume that the dry heating resulted in a smaller cavity than the cavities obtained by nanosecond pulsed laser irradiation. There remain open questions about the efficiency of using dry heating to control the cavity formation employed here. The suggested studies for further investigations on using dry heating are intended to be addressed and discussed in future work section.

5.8. Conclusion

To improve the colloidal and thermal stability of the AuNRs, they were successfully coated with silica shell. The coating was confirmed by UV-Vis spectroscopy, Zeta potential, TEM, and EDX elemental mapping. In this work, TEM images revealed that the silica shell thickness on AuNR@mSiO_2 has shown excellent photothermal stability of AuNR@SiO_2 under laser irradiation of fluences 10 mJ/cm^2 at 30, 60, and 180 sec, making the LSPR within the NIR region after nanosecond pulsed laser exposure. In contrast, CTAB@AuNRs show shape transformation process rod-to-sphere shape. However, the silica layer helps the particles to maintain the rod-like morphology during irradiation of high energy laser, and their UV-Vis spectrum still has two absorption peaks compared to uncoated AuNR.

When the AuNR@mSiO_2 are off resonance of the nanosecond pulsed laser, the thermal reshaping is more controllable for AuNR@mSiO_2. The slight blue shift helped to form sealed cavities, the gap size of AuNRs@mSiO_2 of LSPR band at (on resonance) is ~ 10 nm after 20 mJ/cm^2 irradiation and when LSPR band of AuNR@mSiO_2 is at (off resonance), a cavity gap of size ~ 5.4 nm was formed after 10 mJ/cm^2 nanosecond pulsed laser irradiation of wavelength of 850 nm 1 min. The silica layer helps both AuNRs@mSiO_2 of 81% and 43% to maintain the rod-like morphology during pulsed laser irradiation. In addition, increasing the porosity degrees of the silica shell did not influence their absorption spectra.

The strategy in this work has several advantages compared to others selectively oxidization strategies. First, this strategy provides easy and reproducible control of the cavity. Second, washing steps are not needed after laser irradiation. Third, the cavity can be created in nanoseconds that making this as simple, rapid end-selective shortening of AuNRs with no additional chemicals needed. This introduces a new route for fabrication an advantageous dual AuNR@Cavity@mSiO_2 of fine-tune cavity and high efficiency for photothermal therapy in the near-infrared biological window (700-800 nm) with high porosity for potential drug uploading without influencing the absorption spectra.

6. Conclusion and Future Work

The aim of this project was to engineer and modify the AuNRs to make them able to satisfy the conditions required for the ideal plasmonic photothermal agents for the clinical photothermal therapy of cancer treatment.; (i) able to absorb lasers strongly in the biological window (i.e., the so-called first biological window with wavelengths ranging from 700 nm to 950 nm (NIR-I)), (ii) colloidally stable (iii), (iv) photothermal stability and efficiency at converting photon energy to heat in treatment, and (v) no toxicity. This chapter provides a summary of the findings of each chapter and discuss the potential future study that can contribute to improving the findings obtained in this thesis.

In Chapter 3, AuNRs were fabricated using a binary–surfactant seedless protocol followed by a direct coating with silica. A silica shell of thickness 7 nm was formed on the CTAB@AuNR creating Core–shell nanoparticles to coat toxic CTAB bilayer. Single gold core was achieved by adjusting the gold and aqueous silicate concentrations. The silica coating was confirmed by different techniques, such as UV-Vis spectroscopy, Zeta potential, TEM, and EDX elemental mapping. The absorption spectra using UV-Vis spectroscopy showed redshift of the LSPR band upon silica coating due to the change in the refractive index of the surrounding medium of AuNR. The silica coated-AuNRs morphology were investigated using Transmission electron microscopic (TEM). Moreover, the element composition of the synthesized AuNR@SiO_2 was investigated by EDX, it was observed that the single AuNR core was stabilized with a thin layer of CTAB coated with SiO_2 shell.

Initial experiments were performed looking at the thermal stability of AuNRs@SiO_2 compared to CTAB@AuNRs using In-situ TEM heating. The morphology change during the heating of both were investigated at different temperatures. Surface modification using silica shells of thickness 7 nm has significantly enhanced thermal stability of AuNRs, effectively maintained their rod shape and protected them from turning into nanospheres even up to 1200°C. Additionally, the silica shell enhanced the photoacoustic signal AuNRs@SiO_2 by preventing the AuNRs from melting and shape transformation into nanospheres. Therefore, these findings suggest AuNRs@SiO_2 can potentially be used efficiently for photoacoustic imaging without altering the optical absorption.

In Chapter 4, the development of biocompatibility of AuNR@SiO_2 by surface modification with of 1,2-distearoyl-sn-glycero-3-phosphoethanolamine-N- [methoxy (polyethylene glycol)-2000] (DSPE-PEG2000) and dipalmitoylphosphatidylcholine (DPPC) phospholipids was explored. First, the colloidally stability the lipids modified AuNRs@SiO_2 were investigated in PBS before *in vitro* tests. The findings showed that the lipids modified AuNR@SiO_2 are colloidally stable compared to uncoated AuNRs. Then, the SW620 cells incubated by AuNRs@SiO_2 for 24 h survived reasonably well remained above 55 % even at the highest doses used in this study, confirming that the successful silica coating has reduced the CTAB toxicity. However, the cytotoxicity of lipids modified AuNR@SiO_2 was studied by incubating them with HT29 cells, the results showed that surface modification with lipids improved the cells viability after incubation for 24 and 48 h compared to unmodified AuNR@SiO_2.

Moreover, the cellular uptake of lipids coated-AuNR@SiO_2 was investigated by using fluorescently tagged lipids on the lipids coated-AuNR@SiO_2. The unique optical properties helped in optimizing the *in vitro* imaging and confirming the cellular uptake using fluorescent microscopy. The fluorescent images showed the nanocomposites were internalized and not on the cell surface. The findings confirmed the neutrally charged lipid bilayer improved biocompability of the AuNRs@SiO_2 and enhanced the cellular uptake of human colorectal cell lines.

In Chapter 5, the main focus was on the effect of the silica coating on AuNRs reshaping behaviour as a function of irradiation time and fluence of pulsed laser irradiation. The stability of these AuNR@mSiO_2 under pulsed laser irradiation of two fluences 10 mJ/cm^2 and 20 mJ/cm^2 for different periods was investigated and compared to uncoated CTAB@AuNRs. The obtained results showed that the silica shell helped the AuNR to maintain the rod-like morphology during irradiation of high energy laser, with maintaining the two plasmons bands in their absorption spectrum compared to uncoated AuNR. The LSPR within the NIR region after laser exposure, however, CTAB@AuNRs show shape transformation process rod-to-sphere shape.

I observed that when AuNR@mSiO_2 are off resonance of the pulsed laser, the thermal reshaping is more controllable. The slight blue shift helped to form sealed cavities, the gap size of AuNRs@mSiO_2 of LSPR band at (on resonance) is ~ 10 nm after 20 mJ/cm^2 irradiation

and when LSPR band of AuNR@$mSiO_2$ is at (off resonance), a cavity gap of size ~ 5.4 nm was formed after 10 mJ/cm^2 irradiation of wavelength of 850 nm 1 min. The silica layer helps both AuNRs@$mSiO_2$ to maintain the rod-like morphology during pulsed laser irradiation. In addition, increasing the porosity degrees of the silica shell did not influence their absorption spectra.

Finally, this introduced a novel method for fabrication an advantageous dual AuNR@Cavity@$mSiO_2$ of fine-tune cavity and high efficiency for photothermal therapy in first biological window with high porosity for potential drug uploading without influencing the absorption spectra. The rapid end-selective shortening of AuNRs with no additional chemicals needed was achieved in 1 min of nanosecond pulsed laser irradiation.

Combined this data indicates that uncoated nanoparticles are colloidally unstable and frequently toxic in biological solutions, making surface modification of nanoparticles essential for both in vitro and in vivo applications. The employed surface modifications for AuNRs@$mSiO_2$ improve their efficiency to be used as photothermal agents; due to their low toxicity, good heat generation, and strong photothermal stability under pulsed laser irradiation. When compared to other photothermal agents, the surface modifications used in this thesis (SiO_2 and phospholipid coating) overcame the current challenges associated to using AuNRs in photothermal application such as the CTAB toxicity, instability under pulsed laser irradiation. The obtained data in this thesis confirmed that the employed surface modifications were successful in reducing CTAB toxicity, enhancing cellular uptake, and controlling the photothermal reshaping and maintaining the rod-like shape of AuNRs and efficient in NIR absorption after pulsed laser irradiation of high energy. Moreover, the high porosity of AuNRs@$mSiO_2$ would be potential for drug uploading without influencing the absorption spectra and would induce cancer cells treatment. But there are still unanswered questions regarding the photothermal effectiveness of these AuNRs@$mSiO_2$ as photothermal agents. The following section discusses the methods that will be used to address them.

6.1. Future Work

Some of the work in Chapter 5 remains unfinished, the work performed was on the effect of the silica coating of thickness of = 7 nm on AuNRs reshaping behaviour as a function of irradiation time, fluence, and porosity degree. It would be beneficial to investigate the influence of silica shell of different thickness on the thermal stability of AuNRs. This would allow optimizing the thermal stability of AuNRs. Ideally this study need to be supported by TEM.

Further investigation on the heat dissipation from AuNRs@$mSiO_2$ to the surrounding environment need to be addressed. Ideally these measurements will allow good understanding and improve controlling the thermal reshaping of AuNRs under pulsed laser irradiation. This can be manged by using transient absorption spectroscopy that will provide quantitative dynamics and a good understanding on the influence of the surrounding medium (CTAB, silica, and water) on the heat dissipation.

In the dry heating study, more measurements are needed by varying the heating temperature high[370]er than 50°C. following by monitoring the bule shifts for the LSPR bands with time. This study could be supported by TEM to investigate the end-selective shortening of AuNRs. Moreover, it would be beneficial to upload the cavity and the silica shell of a high porosity degree of the fabricated dual AuNR@Cavity@$mSiO_2$ with drug. The drug-loaded AuNR@Cavity@$mSiO_2$ could enable combination of chemotherapeutic and photo-thermal effects in killing tumour cells upon light irradiation, thus improving the efficiency of killing. The drug uploading of AuNR@Cavity@$mSiO_2$ can be supported by Raman measurement. The Raman measurement can help to confirm the drug uploading onto AuNRs@Cavity@$mSiO_2$, by comparing the Raman signal of un-adsorbed drug and AuNRs@Cavity@$mSiO_2$@Drug.

In addition, it was always intended that the *in vitro and in vivo* work would be conducted to examine the photothermal efficiency of AuNRs@$mSiO_2$ as photothermal agents, unfortunately, shortage of time prevented this from happening. Therefore, it would be beneficial to investigate the AuNRs@$mSiO_2$ photothermal efficiency in localised tissue heating in the vicinity. To target cancer cells specifically and prevent nonspecific binding such as

electrostatic binding and endocytosis, this AuNRs@mSiO2@lipids can be conjugated with various antibodies and a blocker (PEG) [370].

When all of these ideas are considered together, they offer a better understanding of how these particles function both *in vitro* and *in vivo* and would also considerably increase their effectiveness as theranostic agents.

References

1. Ferlay, J., et al., *Cancer statistics for the year 2020: An overview.* International journal of cancer, 2021. **149**(4): p. 778-789.

2. Organization, W.H. *Home*. [online] Who.int. 2022; Available from: https://www.who.int..

3. Chua, C.Y.X., et al., *Emerging technologies for local cancer treatment.* Advanced therapeutics, 2020. **3**(9): p. 2000027.

4. Schirrmacher, V., *From chemotherapy to biological therapy: A review of novel concepts to reduce the side effects of systemic cancer treatment.* International journal of oncology, 2019. **54**(2): p. 407-419.

5. Das, S.K., et al., *Gene therapies for cancer: strategies, challenges and successes.* Journal of cellular physiology, 2015. **230**(2): p. 259-271.

6. Arruebo, M., et al., *Assessment of the evolution of cancer treatment therapies.* Cancers, 2011. **3**(3): p. 3279-3330.

7. Parish, C.R., *Cancer immunotherapy: the past, the present and the future.* Immunology and cell biology, 2003. **81**(2): p. 106-113.

8. Duan, X., C. Chan, and W. Lin, *Nanoparticle-mediated immunogenic cell death enables and potentiates cancer immunotherapy.* Angewandte Chemie International Edition, 2019. **58**(3): p. 670-680.

9. Urano, M. and E.B. Douple, *Thermal effects on cells and tissues*. Vol. 1. 1988: VSP.

10. Tsai, M.-F., et al., *Au nanorod design as light-absorber in the first and second biological near-infrared windows for in vivo photothermal therapy.* ACS nano, 2013. **7**(6): p. 5330-5342.

11. Espinosa, A., et al., *Intracellular biodegradation of Ag nanoparticles, storage in ferritin, and protection by a Au shell for enhanced photothermal therapy.* ACS nano, 2018. **12**(7): p. 6523-6535.

12. Zhou, F., et al., *Cancer photothermal therapy in the near-infrared region by using single-walled carbon nanotubes.* Journal of biomedical optics, 2009. **14**(2): p. 021009.

13. Robinson, J.T., et al., *Ultrasmall reduced graphene oxide with high near-infrared absorbance for photothermal therapy.* Journal of the American Chemical Society, 2011. **133**(17): p. 6825-6831.

14. Yang, W., et al., *Gold nanoparticle based photothermal therapy: Development and application for effective cancer treatment.* Sustainable Materials and Technologies, 2019. **22**: p. e00109.

15. Alkilany, A.M., et al., *Gold nanorods: their potential for photothermal therapeutics and drug delivery, tempered by the complexity of their biological interactions.* Advanced drug delivery reviews, 2012. **64**(2): p. 190-199.

16. Yang, W., et al., *Shape effects of gold nanoparticles in photothermal cancer therapy.* Materials Today Sustainability, 2021. **13**: p. 100078.

17. Shi, Z., Y. Xu, and A. Wu, *Gold nanorods for biomedical imaging and therapy in cancer*, in *Advances in nanotheranostics I*. 2016, Springer. p. 103-136.

18. Henderson, T.A. and L.D. Morries, *Near-infrared photonic energy penetration: can infrared phototherapy effectively reach the human brain?* Neuropsychiatric disease and treatment, 2015. **11**: p. 2191.

19. Lohse, S.E. and C.J. Murphy, *The quest for shape control: a history of gold nanorod synthesis.* Chemistry of Materials, 2013. **25**(8): p. 1250-1261.

20. Abadeer, N.S., et al., *Distance and plasmon wavelength dependent fluorescence of molecules bound to silica-coated gold nanorods.* ACS nano, 2014. **8**(8): p. 8392-8406.

21. Vigderman, L. and E.R. Zubarev, *High-yield synthesis of gold nanorods with longitudinal SPR peak greater than 1200 nm using hydroquinone as a reducing agent.* Chemistry of Materials, 2013. **25**(8): p. 1450-1457.

22. Chang, H.-H. and C.J. Murphy, *Mini gold nanorods with tunable plasmonic peaks beyond 1000 nm.* Chemistry of Materials, 2018. **30**(4): p. 1427-1435.

23. Hu, M., et al., *Gold nanostructures: engineering their plasmonic properties for biomedical applications.* Chemical Society Reviews, 2006. **35**(11): p. 1084-1094.

24. Von Maltzahn, G., et al., *Computationally guided photothermal tumor therapy using long-circulating gold nanorod antennas.* Cancer research, 2009. **69**(9): p. 3892-3900.

25. Esumi, K., K. Matsuhisa, and K. Torigoe, *Preparation of rodlike gold particles by UV irradiation using cationic micelles as a template.* Langmuir, 1995. **11**(9): p. 3285-3287.

26. Samal, A.K., T.S. Sreeprasad, and T. Pradeep, *Investigation of the role of NaBH4 in the chemical synthesis of gold nanorods.* Journal of Nanoparticle Research, 2010. **12**(5): p. 1777-1786.

27. Jiang, K. and A.O. Pinchuk, *Noble metal nanomaterials: synthetic routes, fundamental properties, and promising applications*, in *Solid State Physics*. 2015, Elsevier. p. 131-211.

28. Nikoobakht, B. and M.A. El-Sayed, *Preparation and growth mechanism of gold nanorods (NRs) using seed-mediated growth method.* Chemistry of Materials, 2003. **15**(10): p. 1957-1962.

29. Sau, T.K. and C.J. Murphy, *Seeded high yield synthesis of short Au nanorods in aqueous solution.* Langmuir, 2004. **20**(15): p. 6414-6420.

30. Guerrero-Martínez, A., et al., *Gemini-surfactant-directed self-assembly of monodisperse gold nanorods into standing superlattices.* Angewandte Chemie, 2009. **121**(50): p. 9648-9652.

31. Busbee, B.D., S.O. Obare, and C.J. Murphy, *An improved synthesis of high-aspect-ratio gold nanorods.* Advanced Materials, 2003. **15**(5): p. 414-416.

32. Xu, X., et al., *Seedless synthesis of high aspect ratio gold nanorods with high yield.* Journal of Materials Chemistry A, 2014. **2**(10): p. 3528-3535.

33. Zhang, J., et al., *High yield seedless synthesis of high-quality gold nanocrystals with various shapes.* Langmuir, 2014. **30**(9): p. 2480-2489.

34. Ali, M.R., B. Snyder, and M.A. El-Sayed, *Synthesis and optical properties of small Au nanorods using a seedless growth technique.* Langmuir, 2012. **28**(25): p. 9807-9815.

35. Jana, N.R., *Gram-scale synthesis of soluble, near-monodisperse gold nanorods and other anisotropic nanoparticles.* Small, 2005. **1**(8-9): p. 875-882.

36. Liu, K., et al., *Seedless synthesis of monodispersed gold nanorods with remarkably high yield: synergistic effect of template modification and growth kinetics regulation.* Chemistry–A European Journal, 2017. **23**(14): p. 3291-3299.

37. Roach, L., et al., *Morphological control of seedlessly-synthesized gold nanorods using binary surfactants.* 2018. **29**(13): p. 135601.

38. Ye, X., et al., *Using binary surfactant mixtures to simultaneously improve the dimensional tunability and monodispersity in the seeded growth of gold nanorods.* Nano letters, 2013. **13**(2): p. 765-771.

39. Lai, J., et al., *One-pot synthesis of gold nanorods using binary surfactant systems with improved monodispersity, dimensional tunability and plasmon resonance scattering properties.* Nanotechnology, 2014. **25**(12): p. 125601.

40. Walsh, M.J., et al., *A mechanism for symmetry breaking and shape control in single-crystal gold nanorods.* Accounts of Chemical Research, 2017. **50**(12): p. 2925-2935.

41. Jana, N.R., et al., *Liquid crystalline assemblies of ordered gold nanorods.* Journal of Materials Chemistry, 2002. **12**(10): p. 2909-2912.

42. Vigderman, L., B.P. Khanal, and E.R. Zubarev, *Functional gold nanorods: synthesis, self-assembly, and sensing applications.* Advanced materials, 2012. **24**(36): p. 4811-4841.

43. Elfeky, S.A., S.E. Mahmoud, and A.F. Youssef, *Applications of CTAB modified magnetic nanoparticles for removal of chromium (VI) from contaminated water.* Journal of advanced research, 2017. **8**(4): p. 435-443.

44. Imae, T. and S. Ikeda, *Characteristics of rodlike micelles of cetyltrimethylammonium chloride in aqueous NaCl solutions: their flexibility and the scaling laws in dilute and semidilute regimes.* Colloid and Polymer Science, 1987. **265**(12): p. 1090-1098.

45. Modaressi, A., et al., *CTAB aggregation in aqueous solutions of ammonium based ionic liquids; conductimetric studies.* Colloids and Surfaces A: Physicochemical and Engineering Aspects, 2007. **296**(1-3): p. 104-108.

46. Anachkov, S.E., et al., *Determination of the aggregation number and charge of ionic surfactant micelles from the stepwise thinning of foam films.* Advances in Colloid and Interface Science, 2012. **183**: p. 55-67.

47. Meena, S.K. and M. Sulpizi, *Understanding the microscopic origin of gold nanoparticle anisotropic growth from molecular dynamics simulations.* Langmuir, 2013. **29**(48): p. 14954-14961.

48. Goia, D. and E. Matijević, *Tailoring the particle size of monodispersed colloidal gold.* Colloids and Surfaces A: Physicochemical and Engineering Aspects, 1999. **146**(1-3): p. 139-152.

49. Pérez-Juste, J., et al., *Optical control and patterning of gold-nanorod–poly (vinyl alcohol) nanocomposite films.* Advanced Functional Materials, 2005. **15**(7): p. 1065-1071.

50. Chen, H., et al., *Gold nanorods and their plasmonic properties.* Chemical Society Reviews, 2013. **42**(7): p. 2679-2724.

51. Wei, M.-Z., et al., *Seed-mediated synthesis of gold nanorods at low concentrations of CTAB.* ACS omega, 2021. **6**(13): p. 9188-9195.

52. Fujimoto, J.G., et al., *Optical biopsy and imaging using optical coherence tomography.* Nature medicine, 1995. **1**(9): p. 970-972.

53. Zysk, A.M., et al., *Optical coherence tomography: a review of clinical development from bench to bedside.* Journal of biomedical optics, 2007. **12**(5): p. 051403.

54. Fujimoto, J.G., *Optical coherence tomography for ultrahigh resolution in vivo imaging.* Nature biotechnology, 2003. **21**(11): p. 1361-1367.

55. Alkilany, A.M., et al., *Cellular uptake and cytotoxicity of gold nanorods: molecular origin of cytotoxicity and surface effects.* 2009. **5**(6): p. 701-708.

56. Cortesi, R., et al., *Effect of cationic liposome composition on in vitro cytotoxicity and protective effect on carried DNA.* International Journal of Pharmaceutics, 1996. **139**(1-2): p. 69-78.

57. Huff, T.B., et al., *Controlling the cellular uptake of gold nanorods.* Langmuir, 2007. **23**(4): p. 1596-1599.

58. Ito, E., et al., *Potential use of cetrimonium bromide as an apoptosis-promoting anticancer agent for head and neck cancer.* Molecular pharmacology, 2009. **76**(5): p. 969-983.

59. Yasun, E., et al., *BSA modification to reduce CTAB induced nonspecificity and cytotoxicity of aptamer-conjugated gold nanorods.* Nanoscale, 2015. **7**(22): p. 10240-10248.

60. Schulz, F., et al., *Effective PEGylation of gold nanorods.* Nanoscale, 2016. **8**(13): p. 7296-7308.

61. Santhosh, P.B., et al., *Phospholipid stabilized gold nanorods: towards improved colloidal stability and biocompatibility.* Physical Chemistry Chemical Physics, 2017. **19**(28): p. 18494-18504.

62. Pan, B., et al., *Controlled self-assembly of thiol-terminated poly (amidoamine) dendrimer and gold nanoparticles.* Colloids and Surfaces A: Physicochemical and Engineering Aspects, 2005. **259**(1-3): p. 89-94.

63. Novak, J.P. and D.L. Feldheim, *Assembly of phenylacetylene-bridged silver and gold nanoparticle arrays.* Journal of the American Chemical Society, 2000. **122**(16): p. 3979-3980.

64. Sun, Y. and Y. Xia, *Shape-controlled synthesis of gold and silver nanoparticles.* science, 2002. **298**(5601): p. 2176-2179.

65. Zhang, Z., et al., *Mesoporous silica-coated gold nanorods as a light-mediated multifunctional theranostic platform for cancer treatment.* 2012. **24**(11): p. 1418-1423.

66. Baek, S., et al., *Triple hit with drug carriers: pH-and temperature-responsive theranostics for multimodal chemo-and photothermal therapy and diagnostic applications.* ACS applied materials & interfaces, 2016. **8**(14): p. 8967-8979.

67. Song, Z., et al., *Hydroxyapatite/mesoporous silica coated gold nanorods with improved degradability as a multi-responsive drug delivery platform.* Materials Science and Engineering: C, 2018. **83**: p. 90-98.

68. Pellas, V., et al., *Gold nanorods for LSPR biosensing: synthesis, coating by silica, and bioanalytical applications.* Biosensors, 2020. **10**(10): p. 146.

69. Graf, C., et al., *A general method to coat colloidal particles with silica.* Langmuir, 2003. **19**(17): p. 6693-6700.

70. Gorelikov, I. and N.J.N.l. Matsuura, *Single-step coating of mesoporous silica on cetyltrimethyl ammonium bromide-capped nanoparticles.* 2008. **8**(1): p. 369-373.

71. Wu, W.-C. and J.B. Tracy, *Large-scale silica overcoating of gold nanorods with tunable shell thicknesses.* Chemistry of Materials, 2015. **27**(8): p. 2888-2894.

72. Cong, H., et al., *Silica-coated gold nanorods with a gold overcoat: controlling optical properties by controlling the dimensions of a gold− silica− gold layered nanoparticle.* Langmuir, 2010. **26**(6): p. 4188-4195.

73. Stöber, W., A. Fink, and E. Bohn, *Controlled growth of monodisperse silica spheres in the micron size range.* Journal of colloid and interface science, 1968. **26**(1): p. 62-69.

74. Saha, K., et al., *Gold nanoparticles in chemical and biological sensing.* Chemical reviews, 2012. **112**(5): p. 2739-2779.

75. Sepúlveda, B., et al., *LSPR-based nanobiosensors.* Nano today, 2009. **4**(3): p. 244-251.

76. Zapelini, I.W., L.L. Silva, and D. Cardoso, *Effect of hydrothermal treatment on structural and catalytic properties of [CTA]-MCM-41 silica.* Materials, 2018. **11**(5): p. 860.

77. Wang, M., et al., *Dumbbell-Like Silica Coated Gold Nanorods and Their Plasmonic Properties.* Langmuir, 2019. **35**(51): p. 16886-16892.

78. Tian, X., et al., *Modulated fluorescence properties in fluorophore-containing gold nanorods@ mSiO 2.* RSC Advances, 2014. **4**(18): p. 9343-9348.

79. Wu, C. and Q.-H. Xu, *Stable and functionable mesoporous silica-coated gold nanorods as sensitive localized surface plasmon resonance (LSPR) nanosensors.* Langmuir, 2009. **25**(16): p. 9441-9446.

80. Zhang, R., et al., *Influence of SiO2 shell thickness on power conversion efficiency in plasmonic polymer solar cells with Au nanorod@ SiO2 core-shell structures.* Scientific reports, 2016. **6**(1): p. 1-9.

81. Mohanta, J., S. Satapathy, and S. Si, *Porous silica-coated gold nanorods: a highly active catalyst for the reduction of 4-nitrophenol.* ChemPhysChem, 2016. **17**(3): p. 364-368.

82. Vega, M.S., F. Brisset, and G. Laurent, *Optimized silica shell synthesis surrounding gold nanorods for enhanced spectroscopies.* Plasmonics, 2021. **16**(3): p. 635-642.

83. Heuer-Jungemann, A., et al., *The role of ligands in the chemical synthesis and applications of inorganic nanoparticles.* Chemical reviews, 2019. **119**(8): p. 4819-4880.

84. Senapati, S., et al., *Controlled drug delivery vehicles for cancer treatment and their performance.* Signal transduction and targeted therapy, 2018. **3**(1): p. 1-19.

85. Alberts, B., et al., *The lipid bilayer*, in *Molecular Biology of the Cell. 4th edition*. 2002, Garland Science.

86. Proteomics, C. *Phospholipids Analysis Service*. [online] Creative Proteomics. 2019; Available from: https://www.creative-proteomics.com/services/phospholipids-analysis-service.htm.

87. Zhang, Z., D. Yomo, and C. Gradinaru, *Choosing the right fluorophore for single-molecule fluorescence studies in a lipid environment.* Biochimica et Biophysica Acta (BBA)-Biomembranes, 2017. **1859**(7): p. 1242-1253.

88. Akbarzadeh, A., et al., *Liposome: classification, preparation, and applications.* Nanoscale research letters, 2013. **8**(1): p. 1-9.

89. Ha, Y., et al., *Fabrication of Remarkably Bright QD Densely-Embedded Silica Nanoparticle.* 2019. **40**(1): p. 9-13.

90. Cho, H.-M., et al., *Fabrication of protein-anchoring surface by modification of Sio2 with liposomal bilayer.* Colloids and Surfaces B: Biointerfaces, 2010. **75**(1): p. 209-213.

91. Bégu, S., et al., *Characterization of a phospholipid bilayer entrapped into non-porous silica nanospheres.* Journal of Materials Chemistry, 2004. **14**(8): p. 1316-1320.

92. Zhou, G., et al., *Layer-by-layer construction of lipid bilayer on mesoporous silica nanoparticle to improve its water suspensibility and hemocompatibility.* Journal of Sol-Gel Science and Technology, 2017. **82**: p. 490-499.

93. Durfee, P.N., et al., *Mesoporous silica nanoparticle-supported lipid bilayers (protocells) for active targeting and delivery to individual leukemia cells.* ACS nano, 2016. **10**(9): p. 8325-8345.

94. Butler, K.S., et al., *Protocells: modular mesoporous silica nanoparticle-supported lipid bilayers for drug delivery.* small, 2016. **12**(16): p. 2173-2185.

95. Teng, I.-T., et al., *Phospholipid-functionalized mesoporous silica nanocarriers for selective photodynamic therapy of cancer.* Biomaterials, 2013. **34**(30): p. 7462-7470.

96. Wang, L.-S., et al., *Biofunctionalized phospholipid-capped mesoporous silica nanoshuttles for targeted drug delivery: improved water suspensibility and decreased nonspecific protein binding.* ACS nano, 2010. **4**(8): p. 4371-4379.

97. Samad, A., Y. Sultana, and M. Aqil, *Liposomal drug delivery systems: an update review.* Current drug delivery, 2007. **4**(4): p. 297-305.

98. Puri, A., et al., *Lipid-based nanoparticles as pharmaceutical drug carriers: from concepts to clinic.* Critical Reviews™ in Therapeutic Drug Carrier Systems, 2009. **26**(6).

99. Van Schooneveld, M.M., et al., *Improved biocompatibility and pharmacokinetics of silica nanoparticles by means of a lipid coating: a multimodality investigation.* Nano letters, 2008. **8**(8): p. 2517-2525.

100. Yang, Y., et al., *Lipid coated mesoporous silica nanoparticles as photosensitive drug carriers.* Physical Chemistry Chemical Physics, 2010. **12**(17): p. 4418-4422.

101. Cauda, V., et al., *Colchicine-loaded lipid bilayer-coated 50 nm mesoporous nanoparticles efficiently induce microtubule depolymerization upon cell uptake.* Nano letters, 2010. **10**(7): p. 2484-2492.

102. Bimbo, L.M., et al., *Inhibition of influenza A virus infection in vitro by saliphenylhalamide-loaded porous silicon nanoparticles.* ACS nano, 2013. **7**(8): p. 6884-6893.

103. Willets, K.A. and R.P. Van Duyne, *Localized surface plasmon resonance spectroscopy and sensing.* Annu. Rev. Phys. Chem., 2007. **58**: p. 267-297.

104. Stewart, M.E., et al., *Nanostructured plasmonic sensors.* Chemical reviews, 2008. **108**(2): p. 494-521.

105. Homola, J., *Surface plasmon resonance sensors for detection of chemical and biological species.* Chemical reviews, 2008. **108**(2): p. 462-493.

106. Yu, Q., et al., *Detection of low-molecular-weight domoic acid using surface plasmon resonance sensor.* Sensors and Actuators B: Chemical, 2005. **107**(1): p. 193-201.

107. Cao, J., T. Sun, and K.T. Grattan, *Gold nanorod-based localized surface plasmon resonance biosensors: A review.* Sensors and actuators B: Chemical, 2014. **195**: p. 332-351.

108. Kreibig, U. and M. Vollmer, *Optical properties of metal clusters*. Vol. 25. 2013: Springer Science & Business Media.

109. Mie, G., *Beiträge zur Optik trüber Medien, speziell kolloidaler Metallösungen.* Annalen der physik, 1908. **330**(3): p. 377-445.

110. Taylor, M.L., et al., *Gold Nanorod-Assisted Photothermal Therapy and Improvement Strategies.* Bioengineering, 2022. **9**(5): p. 200.

111. Teranishi, T., et al., *Controlled localized surface plasmon resonance wavelength for conductive nanoparticles over the ultraviolet to near-infrared region.* Journal of Materials Chemistry, 2011. **21**(28): p. 10238-10242.

112. Orendorff, C.J., T.K. Sau, and C.J. Murphy, *Shape-dependent plasmon-resonant gold nanoparticles.* small, 2006. **2**(5): p. 636-639.

113. Yu, C. and J. Irudayaraj, *Multiplex biosensor using gold nanorods.* Analytical chemistry, 2007. **79**(2): p. 572-579.

114. Stone, J.W., et al., *Using gold nanorods to probe cell-induced collagen deformation.* Nano letters, 2007. **7**(1): p. 116-119.

115. Hauck, T. and W. CW Chan, *Nanostructure-mediated thermal therapy–the path from bench to clinic.* 2006.

116. Gans, R., *Über die form ultramikroskopischer goldteilchen.* Annalen der Physik, 1912. **342**(5): p. 881-900.

117. Jung, L.S., et al., *Quantitative interpretation of the response of surface plasmon resonance sensors to adsorbed films.* Langmuir, 1998. **14**(19): p. 5636-5648.

118. Willets, K.A. and R.P. Van Duyne, *Localized surface plasmon resonance spectroscopy and sensing.* Annual review of physical chemistry, 2007. **58**(1): p. 267-297.

119. Chen, Q., et al., *Visible laser-induced photosensitive effects in Tb3+-/Ce3+-doped heavy metal glasses for optical waveguide fabrication.* Applied Physics A, 2016. **122**(3): p. 1-7.

120. Jaque, D., et al., *Nanoparticles for photothermal therapies.* nanoscale, 2014. **6**(16): p. 9494-9530.

121. Mackey, M.A., et al., *The most effective gold nanorod size for plasmonic photothermal therapy: theory and in vitro experiments.* The Journal of Physical Chemistry B, 2014. **118**(5): p. 1319-1326.

122. Roper, D.K., W. Ahn, and M. Hoepfner, *Microscale heat transfer transduced by surface plasmon resonant gold nanoparticles.* The Journal of Physical Chemistry C, 2007. **111**(9): p. 3636-3641.

123. Tian, Q., et al., *Hydrophilic Cu9S5 nanocrystals: a photothermal agent with a 25.7% heat conversion efficiency for photothermal ablation of cancer cells in vivo.* ACS nano, 2011. **5**(12): p. 9761-9771.

124. Kim, H.S. and D.Y. Lee, *Near-infrared-responsive cancer photothermal and photodynamic therapy using gold nanoparticles.* Polymers, 2018. **10**(9): p. 961.

125. Breitenborn, H., et al., *Quantifying the photothermal conversion efficiency of plasmonic nanoparticles by means of terahertz radiation.* Apl Photonics, 2019. **4**(12): p. 126106.

126. Qin, Z., et al., *Quantitative comparison of photothermal heat generation between gold nanospheres and nanorods.* Scientific reports, 2016. **6**(1): p. 1-13.

127. Sherman, A.I. and M. Ter-Pogossian, *Lymph-node concentration of radioactive colloidal gold following interstitial injection.* Cancer, 1953. **6**(6): p. 1238-1240.

128. Link, S. and M.A. El-Sayed, *Shape and size dependence of radiative, non-radiative and photothermal properties of gold nanocrystals.* International reviews in physical chemistry, 2000. **19**(3): p. 409-453.

129. Jain, P.K., et al., *Noble metals on the nanoscale: optical and photothermal properties and some applications in imaging, sensing, biology, and medicine.* Accounts of chemical research, 2008. **41**(12): p. 1578-1586.

130. Hartland, G.V., *Optical studies of dynamics in noble metal nanostructures.* Chemical reviews, 2011. **111**(6): p. 3858-3887.

131. Tong, L., et al., *Gold nanorods as contrast agents for biological imaging: optical properties, surface conjugation and photothermal effects.* Photochemistry and photobiology, 2009. **85**(1): p. 21-32.

132. Schoenlein, R., et al., *Femtosecond studies of nonequilibrium electronic processes in metals.* Physical Review Letters, 1987. **58**(16): p. 1680.

133. Hwang, Y.-N., et al., *Femtosecond emission studies on gold nanoparticles.* The Journal of Physical Chemistry B, 2002. **106**(31): p. 7581-7584.

134. Link, S., et al., *Electron dynamics in gold and gold–silver alloy nanoparticles: The influence of a nonequilibrium electron distribution and the size dependence of the electron–phonon relaxation.* The Journal of chemical physics, 1999. **111**(3): p. 1255-1264.

135. Hartland, G.V., *Electron-phonon coupling and heat dissipation in metal nanoparticles.* International journal of nanotechnology, 2004. **1**(3): p. 307-327.

136. El-Sayed, I.H., X. Huang, and M.A. El-Sayed, *Selective laser photo-thermal therapy of epithelial carcinoma using anti-EGFR antibody conjugated gold nanoparticles.* Cancer letters, 2006. **239**(1): p. 129-135.

137. O'Neal, D.P., et al., *Photo-thermal tumor ablation in mice using near infrared-absorbing nanoparticles.* Cancer letters, 2004. **209**(2): p. 171-176.

138. Dickerson, E.B., et al., *Gold nanorod assisted near-infrared plasmonic photothermal therapy (PPTT) of squamous cell carcinoma in mice.* Cancer letters, 2008. **269**(1): p. 57-66.

139. Pitsillides, C.M., et al., *Selective cell targeting with light-absorbing microparticles and nanoparticles.* Biophysical journal, 2003. **84**(6): p. 4023-4032.

140. Weissleder, R., *A clearer vision for in vivo imaging.* Nature biotechnology, 2001. **19**(4): p. 316-317.

141. Burda, C., et al., *Chemistry and properties of nanocrystals of different shapes.* Chemical reviews, 2005. **105**(4): p. 1025-1102.

142. Jain, P.K., et al., *Calculated absorption and scattering properties of gold nanoparticles of different size, shape, and composition: applications in biological imaging and biomedicine.* The journal of physical chemistry B, 2006. **110**(14): p. 7238-7248.

143. Kelly, K.L., et al., *The optical properties of metal nanoparticles: the influence of size, shape, and dielectric environment*. 2003, ACS Publications.

144. Link, S., et al., *Femtosecond transient-absorption dynamics of colloidal gold nanorods: Shape independence of the electron-phonon relaxation time.* Physical Review B, 2000. **61**(9): p. 6086.

145. Chou, C.-H., C.-D. Chen, and C.C. Wang, *Highly efficient, wavelength-tunable, gold nanoparticle based optothermal nanoconvertors.* The journal of physical chemistry B, 2005. **109**(22): p. 11135-11138.

146. Huang, X., et al., *Determination of the minimum temperature required for selective photothermal destruction of cancer cells with the use of immunotargeted gold nanoparticles.* Photochemistry and photobiology, 2006. **82**(2): p. 412-417.

147. Link, S., et al., *Laser-induced shape changes of colloidal gold nanorods using femtosecond and nanosecond laser pulses.* The Journal of Physical Chemistry B, 2000. **104**(26): p. 6152-6163.

148. Link, S., et al., *Laser photothermal melting and fragmentation of gold nanorods: energy and laser pulse-width dependence.* The Journal of Physical Chemistry A, 1999. **103**(9): p. 1165-1170.

149. Wang, Y., S. Teitel, and C. Dellago, *Surface-driven bulk reorganization of gold nanorods.* Nano letters, 2005. **5**(11): p. 2174-2178.

150. Opletal, G., et al., *Stability and transformations of heated gold nanorods.* The Journal of Physical Chemistry C, 2011. **115**(11): p. 4375-4380.

151. Goswami, G.K. and K.K. Nanda, *Size-dependent melting of finite-length nanowires.* The Journal of Physical Chemistry C, 2010. **114**(34): p. 14327-14331.

152. Petrova, H., et al., *On the temperature stability of gold nanorods: comparison between thermal and ultrafast laser-induced heating.* Physical Chemistry Chemical Physics, 2006. **8**(7): p. 814-821.

153. Chen, L.-C., et al., *Enhanced photoacoustic stability of gold nanorods by silica matrix confinement.* Journal of Biomedical optics, 2010. **15**(1): p. 016010.

154. Chang, S.-S., et al., *The shape transition of gold nanorods.* Langmuir, 1999. **15**(3): p. 701-709.

155. Link, S., Z.L. Wang, and M.A. El-Sayed, *How does a gold nanorod melt?* The Journal of Physical Chemistry B, 2000. **104**(33): p. 7867-7870.

156. Horiguchi, Y., et al., *Photothermal reshaping of gold nanorods depends on the passivating layers of the nanorod surfaces.* 2008. **24**(20): p. 12026-12031.

157. Joy, N.A., et al., *Thermal stability of gold nanorods for high-temperature plasmonic sensing.* The Journal of Physical Chemistry C, 2013. **117**(22): p. 11718-11724.

158. Liu, Y., E.N. Mills, and R.J. Composto, *Tuning optical properties of gold nanorods in polymer films through thermal reshaping.* Journal of Materials Chemistry, 2009. **19**(18): p. 2704-2709.

159. Tollan, C.M., et al., *Irreversible thermochromic behavior in gold and silver nanorod/polymeric ionic liquid nanocomposite films.* ACS Applied Materials & Interfaces, 2009. **1**(2): p. 348-352.

160. Kennedy, W.J., et al., *High-resolution mapping of thermal history in polymer nanocomposites: gold nanorods as microscale temperature sensors.* ACS applied materials & interfaces, 2015. **7**(50): p. 27624-27631.

161. Jana, N.R., et al., *Anisotropic chemical reactivity of gold spheroids and nanorods.* Langmuir, 2002. **18**(3): p. 922-927.

162. Mohamed, M.B., et al., *Thermal reshaping of gold nanorods in micelles.* The Journal of Physical Chemistry B, 1998. **102**(47): p. 9370-9374.

163. Zou, R., et al., *Thermal stability of gold nanorods in an aqueous solution.* 2010. **372**(1-3): p. 177-181.

164. Takahashi, Y., N. Miyahara, and S. Yamada, *Gold nanorods embedded in titanium oxide film for sensing applications.* Analytical Sciences, 2013. **29**(1): p. 101-105.

165. Khalavka, Y., et al., *Enhanced thermal stability of gold and silver nanorods by thin surface layers.* The Journal of Physical Chemistry C, 2007. **111**(35): p. 12886-12889.

166. Antonello, A., et al., *Improved thermal stability of Au nanorods by use of photosensitive layered titanates for gas sensing applications.* Journal of Materials Chemistry, 2011. **21**(34): p. 13074-13078.

167. Albrecht, W., et al., *Single particle deformation and analysis of silica-coated gold nanorods before and after femtosecond laser pulse excitation.* Nano letters, 2016. **16**(3): p. 1818-1825.

168. Danielsen, S.P., J. Choi, and R.J. Composto, *Retardation of shape change of Au nanorods using photo-cross-linkable ligands.* Journal of Polymer Science Part B: Polymer Physics, 2016. **54**(2): p. 301-307.

169. Nguyen, S.C., et al., *Study of heat transfer dynamics from gold nanorods to the environment via time-resolved infrared spectroscopy.* Acs Nano, 2016. **10**(2): p. 2144-2151.

170. González-Rubio, G., A. Guerrero-Martínez, and L.M. Liz-Marzán, *Reshaping, fragmentation, and assembly of gold nanoparticles assisted by pulse lasers.* Accounts of chemical research, 2016. **49**(4): p. 678-686.

171. Ekici, O., et al., *Thermal analysis of gold nanorods heated with femtosecond laser pulses.* Journal of physics D: Applied physics, 2008. **41**(18): p. 185501.

172. Kaganov, M., E. Lifshitz, and L. Tanatarov, *Relaxation between electrons and the crystalline lattice.* Soviet Physics-JETP, 1957. **4**: p. 173-178.

173. Link, S., et al., *Hot electron relaxation dynamics of gold nanoparticles embedded in MgSO4 powder compared to solution: the effect of the surrounding medium.* The Journal of Physical Chemistry B, 2002. **106**(5): p. 945-955.

174. Mohamed, M.B., et al., *Hot electron and phonon dynamics of gold nanoparticles embedded in a gel matrix.* Chemical physics letters, 2001. **343**(1-2): p. 55-63.

175. Alper, J. and K. Hamad-Schifferli, *Effect of ligands on thermal dissipation from gold nanorods.* Langmuir, 2010. **26**(6): p. 3786-3789.

176. Stoll, T., et al., *Time-resolved investigations of the cooling dynamics of metal nanoparticles: impact of environment.* The Journal of Physical Chemistry C, 2015. **119**(22): p. 12757-12764.

177. Wu, X., et al., *Thermal transport across surfactant layers on gold nanorods in aqueous solution.* ACS applied materials & interfaces, 2016. **8**(16): p. 10581-10589.

178. Huang, J., et al., *Ultrafast thermal analysis of surface functionalized gold nanorods in aqueous solution.* ACS nano, 2013. **7**(1): p. 589-597.

179. Coquil, T., et al., *Thermal conductivity of cubic and hexagonal mesoporous silica thin films.* Journal of Applied Physics, 2009. **106**(3): p. 034910.

180. Hu, M., et al., *Heat dissipation in gold–silica core-shell nanoparticles.* Chemical Physics Letters, 2003. **372**(5-6): p. 767-772.

181. González-Rubio, G., et al., *Femtosecond laser reshaping yields gold nanorods with ultranarrow surface plasmon resonances.* Science, 2017. **358**(6363): p. 640-644.

182. Taylor, A.B., A.M. Siddiquee, and J.W.J.A.n. Chon, *Below melting point photothermal reshaping of single gold nanorods driven by surface diffusion.* 2014. **8**(12): p. 12071-12079.

183. Cai, Y.-Y., et al., *Anti-Stokes emission from hot carriers in gold nanorods.* Nano letters, 2019. **19**(2): p. 1067-1073.

184. Gergely-Fülöp, E., D. Zámbó, and A. Deák, *Thermal stability of mesoporous silica-coated gold nanorods with different aspect ratios.* Materials Chemistry and Physics, 2014. **148**(3): p. 909-913.

185. Gordel, M., et al., *Post-synthesis reshaping of gold nanorods using a femtosecond laser.* Physical Chemistry Chemical Physics, 2014. **16**(1): p. 71-78.

186. Link, S. and M.A. El-Sayed, *Spectral properties and relaxation dynamics of surface plasmon electronic oscillations in gold and silver nanodots and nanorods*. 1999, ACS Publications. p. 8410-8426.

187. Perner, M., et al., *Optically induced damping of the surface plasmon resonance in gold colloids.* Physical Review Letters, 1997. **78**(11): p. 2192.

188. Lombard, J., T. Biben, and S. Merabia, *Nanobubbles around plasmonic nanoparticles: Thermodynamic analysis.* Physical Review E, 2015. **91**(4): p. 043007.

189. Hemmer, E., et al., *Exploiting the biological windows: current perspectives on fluorescent bioprobes emitting above 1000 nm.* Nanoscale Horizons, 2016. **1**(3): p. 168-184.

190. Harm, W., *Biological effects of ultraviolet radiation.* 1980.

191. Huang, L.-Y., et al., *Noninvasive in vivo imaging in the second near-infrared window by inorganic nanoparticle-based fluorescent probes.* Analytical chemistry, 2019. **92**(1): p. 535-542.

192. Smith, A.M., M.C. Mancini, and S. Nie, *Second window for in vivo imaging.* Nature nanotechnology, 2009. **4**(11): p. 710-711.

193. Welsher, K., S.P. Sherlock, and H. Dai, *Deep-tissue anatomical imaging of mice using carbon nanotube fluorophores in the second near-infrared window.* Proceedings of the National Academy of Sciences, 2011. **108**(22): p. 8943-8948.

194. Hong, G., et al., *In vivo fluorescence imaging with Ag2S quantum dots in the second near-infrared region.* Angewandte Chemie International Edition, 2012. **51**(39): p. 9818-9821.

195. Alrahili, M., et al., *Absorption cross section of gold nanoparticles based on NIR laser heating and thermodynamic calculations.* Scientific reports, 2020. **10**(1): p. 1-9.

196. Garcia, J., et al., *The combined use of gold nanoparticles and infrared radiation enables cytosolic protein delivery.* Chemistry–A European Journal, 2021. **27**(14): p. 4670-4675.

197. Dreaden, E.C., et al., *The golden age: gold nanoparticles for biomedicine.* Chemical Society Reviews, 2012. **41**(7): p. 2740-2779.

198. Huang, X., et al., *Plasmonic photothermal therapy (PPTT) using gold nanoparticles.* Lasers in medical science, 2008. **23**(3): p. 217.

199. Wang, Y., et al., *Photoacoustic tomography of a nanoshell contrast agent in the in vivo rat brain.* Nano letters, 2004. **4**(9): p. 1689-1692.

200. Jain, P.K., I.H. El-Sayed, and M.A. El-Sayed, *Au nanoparticles target cancer.* nano today, 2007. **2**(1): p. 18-29.

201. Bao, Z., et al., *Near-infrared light-responsive inorganic nanomaterials for photothermal therapy.* asian journal of pharmaceutical sciences, 2016. **11**(3): p. 349-364.

202. Zhao, T., et al., *Gold nanorods as dual photo-sensitizing and imaging agents for two-photon photodynamic therapy.* Nanoscale, 2012. **4**(24): p. 7712-7719.

203. Luo, G.F., et al., *A triple-collaborative strategy for high-performance tumor therapy by multifunctional mesoporous silica-coated gold nanorods.* Advanced Functional Materials, 2016. **26**(24): p. 4339-4350.

204. Hauck, T.S., A.A. Ghazani, and W.C. Chan, *Assessing the effect of surface chemistry on gold nanorod uptake, toxicity, and gene expression in mammalian cells.* Small, 2008. **4**(1): p. 153-159.

205. Shukla, R., et al., *Biocompatibility of gold nanoparticles and their endocytotic fate inside the cellular compartment: a microscopic overview.* Langmuir, 2005. **21**(23): p. 10644-10654.

206. Chithrani, B.D. and W.C. Chan, *Elucidating the mechanism of cellular uptake and removal of protein-coated gold nanoparticles of different sizes and shapes.* Nano letters, 2007. **7**(6): p. 1542-1550.

207. Baskar, R. and K. Itahana, *Radiation therapy and cancer control in developing countries: Can we save more lives?* International journal of medical sciences, 2017. **14**(1): p. 13.

208. Yang, H., et al., *Mechanism for the cellular uptake of targeted gold nanorods of defined aspect ratios.* Small, 2016. **12**(37): p. 5178-5189.

209. Xie, L., et al., *Preparation, toxicity reduction and radiation therapy application of gold nanorods.* Journal of Nanobiotechnology, 2021. **19**(1): p. 1-17.

210. Chithrani, B.D., A.A. Ghazani, and W.C. Chan, *Determining the size and shape dependence of gold nanoparticle uptake into mammalian cells.* Nano letters, 2006. **6**(4): p. 662-668.

211. Gratton, S.E., et al., *The effect of particle design on cellular internalization pathways.* Proceedings of the National Academy of Sciences, 2008. **105**(33): p. 11613-11618.

212. Nan, A., et al., *Cellular uptake and cytotoxicity of silica nanotubes.* Nano letters, 2008. **8**(8): p. 2150-2154.

213. Wang, L., et al., *Selective targeting of gold nanorods at the mitochondria of cancer cells: implications for cancer therapy.* Nano letters, 2011. **11**(2): p. 772-780.

214. Jiang, W., et al., *Nanoparticle-mediated cellular response is size-dependent.* Nature nanotechnology, 2008. **3**(3): p. 145-150.

215. Bandyopadhyay, S., et al., *Growing gold nanostructures for shape-selective cellular uptake.* Nanoscale research letters, 2018. **13**(1): p. 1-12.

216. Mahmoud, N.N., et al., *Interaction of gold nanorods with human dermal fibroblasts: cytotoxicity, cellular uptake, and wound healing.* Nanomaterials, 2019. **9**(8): p. 1131.

217. Zhu, X.-M., et al., *Cellular uptake behaviour, photothermal therapy performance, and cytotoxicity of gold nanorods with various coatings.* Nanoscale, 2014. **6**(19): p. 11462-11472.

218. Liao, S., et al., *Improvement of gold nanorods in photothermal therapy: Recent progress and perspective.* Frontiers in Pharmacology, 2021: p. 781.

219. Alkilany, A.M., et al., *Toxicity and cellular uptake of gold nanorods in vascular endothelium and smooth muscles of isolated rat blood vessel: importance of surface modification.* Small, 2012. **8**(8): p. 1270-1278.

220. Goodrich, G.P., et al., *Photothermal therapy in a murine colon cancer model using near-infrared absorbing gold nanorods.* Journal of Biomedical Optics, 2010. **15**(1): p. 018001.

221. Huang, X., et al., *Cancer cell imaging and photothermal therapy in the near-infrared region by using gold nanorods.* Journal of the American Chemical Society, 2006. **128**(6): p. 2115-2120.

222. Huang, X., et al., *The potential use of the enhanced nonlinear properties of gold nanospheres in photothermal cancer therapy.* Lasers in Surgery and Medicine: The Official Journal of the American Society for Laser Medicine and Surgery, 2007. **39**(9): p. 747-753.

223. Pattani, V.P., et al., *Role of apoptosis and necrosis in cell death induced by nanoparticle-mediated photothermal therapy.* Journal of Nanoparticle Research, 2015. **17**(1): p. 1-11.

224. Bonfil, R.D., et al., *Tumor necrosis can facilitate the appearance of metastases.* Clinical & experimental metastasis, 1988. **6**(2): p. 121-129.

225. Hanahan, D. and R.A. Weinberg, *Hallmarks of cancer: the next generation.* cell, 2011. **144**(5): p. 646-674.

226. Danial, N.N. and S.J. Korsmeyer, *Cell death: critical control points.* Cell, 2004. **116**(2): p. 205-219.

227. Ali, M.R., et al., *Treatment of natural mammary gland tumors in canines and felines using gold nanorods-assisted plasmonic photothermal therapy to induce tumor apoptosis.* International journal of nanomedicine, 2016. **11**: p. 4849.

228. Ali, M.R., et al., *Targeting heat shock protein 70 using gold nanorods enhances cancer cell apoptosis in low dose plasmonic photothermal therapy.* Biomaterials, 2016. **102**: p. 1-8.

229. Pérez-Hernández, M., et al., *Dissecting the molecular mechanism of apoptosis during photothermal therapy using gold nanoprisms.* ACS nano, 2015. **9**(1): p. 52-61.

230. Lim, Z.-Z.J., et al., *Gold nanoparticles in cancer therapy.* Acta Pharmacologica Sinica, 2011. **32**(8): p. 983-990.

231. Shah, J., et al., *Photoacoustic imaging and temperature measurement for photothermal cancer therapy.* Journal of biomedical optics, 2008. **13**(3): p. 034024.

232. West, J.L. and N.J. Halas, *Engineered nanomaterials for biophotonics applications: improving sensing, imaging, and therapeutics.* Annual review of biomedical engineering, 2003. **5**(1): p. 285-292.

233. Zhong, J., et al., *Imaging-guided high-efficient photoacoustic tumor therapy with targeting gold nanorods.* Nanomedicine: Nanotechnology, Biology and Medicine, 2015. **11**(6): p. 1499-1509.

234. Brix, G., et al., *Tracer kinetic modelling of tumour angiogenesis based on dynamic contrast-enhanced CT and MRI measurements.* European journal of nuclear medicine and molecular imaging, 2010. **37**(1): p. 30-51.

235. Sivasubramanian, M. and L.-W. Lo, *Assessment of Nanoparticle-Mediated Tumor Oxygen Modulation by Photoacoustic Imaging.* Biosensors, 2022. **12**(5): p. 336.

236. Taruttis, A., et al., *Real-time imaging of cardiovascular dynamics and circulating gold nanorods with multispectral optoacoustic tomography.* Optics express, 2010. **18**(19): p. 19592-19602.

237. Moon, H., et al., *Amplified photoacoustic performance and enhanced photothermal stability of reduced graphene oxide coated gold nanorods for sensitive photoacoustic imaging.* ACS nano, 2015. **9**(3): p. 2711-2719.

238. Knights, O.B., et al., *Optimising gold nanorods for photoacoustic imaging in vitro.* Nanoscale Advances, 2019. **1**(4): p. 1472-1481.

239. Ungureanu, C., et al., *Light interactions with gold nanorods and cells: implications for photothermal nanotherapeutics.* Nano letters, 2011. **11**(5): p. 1887-1894.

240. Ashrafi, S.J., et al., *Thermal Distribution of Silica Coated Gold Nano Rods in Tissue-Like Phantom as In Vitro Model for Plasmonic Photo Thermal Therapy.* Biomedical and Pharmacology Journal, 2016. **9**(3): p. 1189-1201.

241. Mercadal, P.A., L.A. Perez, and E.A. Coronado, *Optical Properties of Silica-Coated Au Nanorods: Correlating Theory and Experiments for Determining the Shell Porosity.* The Journal of Physical Chemistry C, 2021. **125**(28): p. 15516-15526.

242. Kobayashi, T., et al., *Spatial distribution of organic functional groups supported on mesoporous silica nanoparticles: A study by conventional and DNP-enhanced 29 Si solid-state NMR.* Physical Chemistry Chemical Physics, 2017. **19**(3): p. 1781-1789.

243. Cui, X., W. Cheng, and X. Han, *Lipid bilayer modified gold nanorod@ mesoporous silica nanoparticles for controlled drug delivery triggered by near-infrared light.* Journal of Materials Chemistry B, 2018. **6**(48): p. 8078-8084.

244. Hu, Z., et al., *Fast characterization of gold nanorods ensemble by correlating its structure with optical extinction spectral features.* 2014. **4**(11): p. 117137.

245. Lakowicz, J., *Principles of fluorescence spectroscopy (ed. Lakowicz, JR) 1–14*. 2013, Springer science & business media.

246. Jabłoński, A., *Über den mechanismus der photolumineszenz von farbstoffphosphoren.* Zeitschrift für Physik, 1935. **94**(1): p. 38-46.

247. Valeur, B. and J.-C. Brochon, *New trends in fluorescence spectroscopy: applications to chemical and life sciences*. Vol. 1. 2012: Springer Science & Business Media.

248. Gomes, A.J., et al., *Experimental methods in chemical engineering: Fluorescence emission spectroscopy.* The Canadian Journal of Chemical Engineering, 2019. **97**(8): p. 2168-2175.

249. Lichtman, J.W. and J.-A. Conchello, *Fluorescence microscopy.* Nature methods, 2005. **2**(12): p. 910-919.

250. Zhang, R. and B.D. Ulery, *Synthetic vaccine characterization and design.* Journal of Bionanoscience, 2018. **12**(1): p. 1-11.

251. Newcombe, G. and D. Dixon, *Interface science in drinking water treatment: theory and applications*. 2006: Academic Press.

252. Mahajan, A. and E. V Ramana, *Patents on magnetoelectric multiferroics and their processing by electrophoretic deposition.* Recent Patents on Materials Science, 2014. **7**(2): p. 109-130.

253. Lionberger, R. and W. Russel, *A Smoluchowski theory with simple approximations for hydrodynamic interactions in concentrated dispersions.* Journal of Rheology, 1997. **41**(2): p. 399-425.

254. Debye, P. and E. Huckel, *The theory of the electrolyte II-The border law for electrical conductivity.* Physikalische Zeitschrift, 1923. **24**: p. 305-325.

255. Rademeyer, P., et al., *Microfluidic system for high throughput characterisation of echogenic particles.* Lab on a Chip, 2015. **15**(2): p. 417-428.

256. Fan, X., W. Zheng, and D.J. Singh, *Light scattering and surface plasmons on small spherical particles.* Light: Science & Applications, 2014. **3**(6): p. e179-e179.

257. Ross, D.J. and R. Sigel, *Mie scattering by soft core-shell particles and its applications to ellipsometric light scattering.* Physical Review E, 2012. **85**(5): p. 056710.

258. Bhattacharjee, S., *DLS and zeta potential–what they are and what they are not?* Journal of controlled release, 2016. **235**: p. 337-351.

259. Brydson, R., et al., *Analytical transmission electron microscopy.* Reviews in Mineralogy and Geochemistry, 2014. **78**(1): p. 219-269.

260. Hubbard, A.T., *The Handbook of surface imaging and visualization*. 2022: CRC press.

261. Cai, X., et al., *Tailored Au nanorods: optimizing functionality, controlling the aspect ratio and increasing biocompatibility.* Nanotechnology, 2010. **21**(33): p. 335604.

262. Henry, D., *The cataphoresis of suspended particles. Part I.—The equation of cataphoresis.* Proceedings of the Royal Society of London. Series A, Containing Papers of a Mathematical and Physical Character, 1931. **133**(821): p. 106-129.

263. Carlson, T., *Photoelectron and Auger spectroscopy*. 2013: Springer Science & Business Media.

264. Li, H., et al., *In vivo metabolic response upon exposure to gold nanorod core/silver shell nanostructures: modulation of inflammation and upregulation of dopamine.* International journal of molecular sciences, 2020. **21**(2): p. 384.

265. Jeong, J.-S., et al., *ZnO-coated TiO2 nanotube arrays for a photoelectrode in dye-sensitized solar cells.* Journal of electronic materials, 2014. **43**(2): p. 375-380.

266. Liu, J.-n., W. Bu, and J. Shi, *Chemical design and synthesis of functionalized probes for imaging and treating tumor hypoxia.* Chemical reviews, 2017. **117**(9): p. 6160-6224.

267. Yin, C., et al., *Amphiphilic semiconducting oligomer for near-infrared photoacoustic and fluorescence imaging.* Acs Applied Materials & Interfaces, 2017. **9**(14): p. 12332-12339.

268. Xu, G., et al., *New generation cadmium-free quantum dots for biophotonics and nanomedicine.* Chemical reviews, 2016. **116**(19): p. 12234-12327.

269. Buehler, A., et al., *Real-time handheld multispectral optoacoustic imaging.* Optics letters, 2013. **38**(9): p. 1404-1406.

270. Dima, A. and V. Ntziachristos, *In-vivo handheld optoacoustic tomography of the human thyroid.* Photoacoustics, 2016. **4**(2): p. 65-69.

271. Knights, O.B. and J.R. McLaughlan, *Gold nanorods for light-based lung cancer theranostics.* International Journal of Molecular Sciences, 2018. **19**(11): p. 3318.

272. Baffou, G. and H. Rigneault, *Femtosecond-pulsed optical heating of gold nanoparticles.* Physical Review B, 2011. **84**(3): p. 035415.

273. Niidome, T., et al., *PEG-modified gold nanorods with a stealth character for in vivo applications.* 2006. **114**(3): p. 343-347.

274. Smith, D.K. and B.A. Korgel, *The importance of the CTAB surfactant on the colloidal seed-mediated synthesis of gold nanorods.* Langmuir, 2008. **24**(3): p. 644-649.

275. Ray, P.C., H. Yu, and P.P. Fu, *Toxicity and environmental risks of nanomaterials: challenges and future needs.* Journal of Environmental Science and Health Part C, 2009. **27**(1): p. 1-35.

276. Parsi, K., *Interaction of detergent sclerosants with cell membranes.* Phlebology, 2015. **30**(5): p. 306-315.

277. Lai, Y.S., et al., *Cell disruption by cationic surfactants affects bioproduct recovery from Synechocystis sp. PCC 6803.* Algal Research, 2018. **34**: p. 250-255.

278. Taylor, A.B., A.M. Siddiquee, and J.W. Chon, *Below melting point photothermal reshaping of single gold nanorods driven by surface diffusion.* ACS nano, 2014. **8**(12): p. 12071-12079.

279. Harris-Birtill, D., et al., *Gold nanorod reshaping in vitro and in vivo using a continuous wave laser.* PLoS One, 2017. **12**(10): p. e0185990.

280. Estelrich, J. and M.A. Busquets, *Iron oxide nanoparticles in photothermal therapy.* Molecules, 2018. **23**(7): p. 1567.

281. Kato, N., et al., *Thin multilayer films of weak polyelectrolytes on colloid particles.* 2002. **35**(26): p. 9780-9787.

282. Omura, N., I. Uechi, and S.J.A.S. Yamada, *Comparison of plasmonic sensing between polymer-and silica-coated gold nanorods.* 2009. **25**(2): p. 255-259.

283. Li, X., et al., *Fluorescence quenching of quantum dots by gold nanorods and its application to DNA detection.* 2009. **94**(6): p. 063111.

284. Horiguchi, Y., et al., *Photothermal reshaping of gold nanorods depends on the passivating layers of the nanorod surfaces.* Langmuir, 2008. **24**(20): p. 12026-12031.

285. Akiyama, Y., et al., *Conversion of rod-shaped gold nanoparticles to spherical forms and their effect on biodistribution in tumor-bearing mice.* Nanoscale research letters, 2012. **7**(1): p. 1-6.

286. Chen, Y.-S., et al., *Enhanced thermal stability of silica-coated gold nanorods for photoacoustic imaging and image-guided therapy.* Optics express, 2010. **18**(9): p. 8867-8878.

287. Srisombat, L.-o., S. Zhang, and T.R. Lee, *Thermal stability of mono-, bis-, and tris-chelating alkanethiol films assembled on gold nanoparticles and evaporated "flat" gold.* Langmuir, 2010. **26**(1): p. 41-46.

288. Roach, L., et al., *Evaluating Phospholipid-Functionalized Gold Nanorods for In Vivo Applications.* Small, 2021. **17**(13): p. 2006797.

289. Lebepe, T.C., S. Parani, and O.S. Oluwafemi, *Graphene oxide-coated gold nanorods: synthesis and applications.* Nanomaterials, 2020. **10**(11): p. 2149.

290. Khlebtsov, B.N., et al., *Overgrowth of gold nanorods by using a binary surfactant mixture.* 2014. **30**(6): p. 1696-1703.

291. Das, M., et al., *Microgels loaded with gold nanorods: photothermally triggered volume transitions under physiological conditions.* Langmuir, 2007. **23**(1): p. 196-201.

292. Jun, P. and H.Z. HU, *Simulation of CTAB bilayer adsorbed on Au (100), Au (110), and Au (111) surfaces: structure stability and dynamic properties.* 2017.

293. Abate, Y., et al., *Nanometer-scale size dependent imaging of cetyl trimethyl ammonium bromide (CTAB) capped and uncapped gold nanoparticles by apertureless near-field optical microscopy.* 2009. **474**(1-3): p. 146-152.

294. Ahmad, I., et al., *Self-assembly and wetting properties of gold nanorod–CTAB molecules on HOPG.* Beilstein journal of nanotechnology, 2019. **10**(1): p. 696-705.

295. Truong, P.L., et al., *A new method for non-labeling attomolar detection of diseases based on an individual gold nanorod immunosensor.* 2011. **11**(15): p. 2591-2597.

296. Link, S., M.B. Mohamed, and M. El-Sayed, *Simulation of the optical absorption spectra of gold nanorods as a function of their aspect ratio and the effect of the medium dielectric constant.* The Journal of Physical Chemistry B, 1999. **103**(16): p. 3073-3077.

297. Huang, X., S. Neretina, and M.A. El-Sayed, *Gold nanorods: from synthesis and properties to biological and biomedical applications.* Advanced materials, 2009. **21**(48): p. 4880-4910.

298. Sharma, V., K. Park, and M. Srinivasarao, *Colloidal dispersion of gold nanorods: Historical background, optical properties, seed-mediated synthesis, shape separation and self-assembly.* Materials Science and Engineering: R: Reports, 2009. **65**(1-3): p. 1-38.

299. Hutter, E. and J.H. Fendler, *Exploitation of localized surface plasmon resonance.* Advanced materials, 2004. **16**(19): p. 1685-1706.

300. Yu, C. and J.J.B.j. Irudayaraj, *Quantitative evaluation of sensitivity and selectivity of multiplex nanoSPR biosensor assays.* 2007. **93**(10): p. 3684-3692.

301. Liz-Marzán, L.M., M. Giersig, and P. Mulvaney, *Synthesis of nanosized gold− silica core− shell particles.* Langmuir, 1996. **12**(18): p. 4329-4335.

302. Kinnear, C., et al., *Gold nanorods: controlling their surface chemistry and complete detoxification by a two-step place exchange.* Angewandte Chemie International Edition, 2013. **52**(7): p. 1934-1938.

303. Mehtala, J.G., et al., *Citrate-stabilized gold nanorods.* Langmuir, 2014. **30**(46): p. 13727-13730.

304. Nooney, R.I., et al., *Self-assembly of mesoporous nanoscale silica/gold composites.* 2003. **19**(18): p. 7628-7637.

305. Pallares, R.M., et al., *Fine-tuning of gold nanorod dimensions and plasmonic properties using the Hofmeister effects.* 2016. **4**(1): p. 53-61.

306. Van Der Spoel, D., et al., *GROMACS: fast, flexible, and free.* 2005. **26**(16): p. 1701-1718.

307. Lindahl, E., B. Hess, and D.J.M.m.a. Van Der Spoel, *GROMACS 3.0: a package for molecular simulation and trajectory analysis.* 2001. **7**(8): p. 306-317.

308. Jose-Yacaman, M., et al., *Surface diffusion and coalescence of mobile metal nanoparticles.* The Journal of Physical Chemistry B, 2005. **109**(19): p. 9703-9711.

309. Flores, E.M.M., *Microwave-assisted sample preparation for trace element determination*. 2014: Newnes.

310. Orendorff, C.J. and C.J.J.T.J.o.P.C.B. Murphy, *Quantitation of metal content in the silver-assisted growth of gold nanorods.* 2006. **110**(9): p. 3990-3994.

311. Chen, Y., et al., *Shape controlled growth of gold nanoparticles by a solution synthesis.* 2005(33): p. 4181-4183.

312. Kolb, D., et al., *Underpotential deposition of metals and work function differences.* 1974. **54**(1): p. 25-38.

313. Herrero, E., L.J. Buller, and H.D.J.C.R. Abruña, *Underpotential deposition at single crystal surfaces of Au, Pt, Ag and other materials.* 2001. **101**(7): p. 1897-1930.

314. Nanda, K.J.P., *Size-dependent melting of nanoparticles: Hundred years of thermodynamic model.* 2009. **72**(4): p. 617-628.

315. Gülseren, O., F. Ercolessi, and E.J.P.R.B. Tosatti, *Premelting of thin wires.* 1995. **51**(11): p. 7377.

316. Allen, G., et al., *Small particle melting of pure metals.* 1986. **144**(2): p. 297-308.

317. Little, S., et al., *Optical detection of melting point depression for silver nanoparticles via in situ real time spectroscopic ellipsometry.* 2012. **100**(5): p. 051107.

318. Borel, J.-P.J.S.S., *Thermodynamical size effect and the structure of metallic clusters.* 1981. **106**(1-3): p. 1-9.

319. Radtke, G., et al., *Structure and chemistry of the Si (111)/AlN interface.* 2012. **100**(1): p. 011910.

320. Al-Sherbini, E.-S.A., *UV–visible light reshaping of gold nanorods.* Materials chemistry and physics, 2010. **121**(1-2): p. 349-353.

321. Grochola, G., I.K. Snook, and S.P.J.T.J.o.c.p. Russo, *Computational modeling of nanorod growth.* 2007. **127**(19): p. 194707.

322. Wang, Y. and C. Dellago, *Structural and morphological transitions in gold nanorods: A computer simulation study.* The Journal of Physical Chemistry B, 2003. **107**(35): p. 9214-9219.

323. Zainuri, M., *Synthesis of sio nanopowders containing quartz and cristobalite phases from silica sands.* Materials Science-Poland, 2015. **33**(1): p. 47-55.

324. Supardi, Z.A.I., et al. *Phase transition of SiO2 nanoparticles prepared from natural sand: the calcination temperature effect*. in *Journal of Physics: Conference Series*. 2018. IOP Publishing.

325. Reka, A.A., et al., *Phase transformations of amorphous SiO2 in diatomite at temperature range of 1000–1200 C.* Geologica Macedonica, 2015. **29**(1): p. 87-92.

326. Meneses, D.D.S., et al., *Phase transformations of crystalline SiO2 versus dynamic disorder between room temperature and liquid state.* Journal of Physics: Condensed Matter, 2014. **26**(25): p. 255402.

327. Schmid, G. and B.J.E.J.o.I.C. Corain, *Nanoparticulated gold: syntheses, structures, electronics, and reactivities.* 2003. **2003**(17): p. 3081-3098.

328. Baur, E., K. Ruhrberg, and W. Woishnis, *Chemical resistance of commodity thermoplastics*. 2016: William Andrew.

329. Ojovan, M.I.J.A.i.C.M.P., *Viscosity and glass transition in amorphous oxides.* 2008. **2008**.

330. Inasawa, S., M. Sugiyama, and Y.J.T.J.o.P.C.B. Yamaguchi, *Laser-induced shape transformation of gold nanoparticles below the melting point: the effect of surface melting.* 2005. **109**(8): p. 3104-3111.

331. Vanrompay, H., et al., *3D characterization of heat-induced morphological changes of Au nanostars by fast in situ electron tomography.* 2018. **10**(48): p. 22792-22801.

332. Xu, C., et al., *Bacteria-like mesoporous silica-coated gold nanorods for positron emission tomography and photoacoustic imaging-guided chemo-photothermal combined therapy.* Biomaterials, 2018. **165**: p. 56-65.

333. Cavigli, L., et al., *Size affects the stability of the photoacoustic conversion of gold nanorods.* The Journal of Physical Chemistry C, 2014. **118**(29): p. 16140-16146.

334. Ferrauto, G., et al., *Large photoacoustic effect enhancement for ICG confined inside MCM-41 mesoporous silica nanoparticles.* Nanoscale, 2017. **9**(1): p. 99-103.

335. Sambou, A., et al., *Control of the surface plasmon resonance of two configurations of nanoparticles: simple gold nanorod and gold/silica core/shell.* Nanoscience and Nanotechnology Research, 2017. **4**(1): p. 1-6.

336. Mueller, E.N., et al., *Hydrophobically Modified Silica-Coated Gold Nanorods for Generating Nonlinear Photoacoustic Signals.* ACS Applied Nano Materials, 2021. **4**(11): p. 12073-12082.

337. Li, W., et al., *Self-assembly of cetyl trimethylammonium bromide in ethanol-water mixtures.* Frontiers of Chemistry in China, 2006. **1**(4): p. 438-442.

338. Johnson, P.B. and R.-W. Christy, *Optical constants of the noble metals.* Physical review B, 1972. **6**(12): p. 4370.

339. Mudakavi, R.J., A.M. Raichur, and D. Chakravortty, *Lipid coated mesoporous silica nanoparticles as an oral delivery system for targeting and treatment of intravacuolar Salmonella infections.* RSC advances, 2014. **4**(105): p. 61160-61166.

340. Han, N., et al., *Facile synthesis of the lipid bilayer coated mesoporous silica nanocomposites and their application in drug delivery.* Microporous and mesoporous materials, 2016. **219**: p. 209-218.

341. Croissant, J., et al., *Biodegradable ethylene-bis (Propyl) disulfide-based periodic mesoporous organosilica nanorods and nanospheres for efficient in-vitro drug delivery.* Advanced Materials, 2014. **26**(35): p. 6174-6180.

342. Lu, J., et al., *Biocompatibility, biodistribution, and drug-delivery efficiency of mesoporous silica nanoparticles for cancer therapy in animals.* Small, 2010. **6**(16): p. 1794-1805.

343. Noureddine, A., et al., *Emerging lipid-coated silica nanoparticles for cancer therapy*, in *Cancer nanotheranostics*. 2021, Springer. p. 335-361.

344. Ardhammar, M., P. Lincoln, and B. Nordén, *Invisible liposomes: refractive index matching with sucrose enables flow dichroism assessment of peptide orientation in lipid vesicle membrane.* Proceedings of the National Academy of Sciences, 2002. **99**(24): p. 15313-15317.

345. Liu, H., N. Pierre-Pierre, and Q. Huo, *Dynamic light scattering for gold nanorod size characterization and study of nanorod–protein interactions.* Gold bulletin, 2012. **45**(4): p. 187-195.

346. Regan, D., et al., *Lipid bilayer thickness measured by quantitative DIC reveals phase transitions and effects of substrate hydrophilicity.* Langmuir, 2019. **35**(43): p. 13805-13814.

347. Kim, J.-K. and D.F. Lawler, *Characteristics of zeta potential distribution in silica particles.* Bulletin of the Korean Chemical Society, 2005. **26**(7): p. 1083-1089.

348. Makino, K., et al., *Temperature-and ionic strength-induced conformational changes in the lipid head group region of liposomes as suggested by zeta potential data.* Biophysical chemistry, 1991. **41**(2): p. 175-183.

349. Zhu, G., et al., *Secretory phospholipase A2 responsive liposomes.* Journal of pharmaceutical sciences, 2011. **100**(8): p. 3146-3159.

350. Gryczynski, I., J. Kusba, and J.R. Lakowicz, *Light quenching of fluorescence using time-delayed laser pulses as observed by frequency-domain fluorometry.* The Journal of physical chemistry, 1994. **98**(36): p. 8886-8895.

351. Pavan, C., et al., *Nearly free surface silanols are the critical molecular moieties that initiate the toxicity of silica particles.* Proceedings of the National Academy of Sciences, 2020. **117**(45): p. 27836-27846.

352. Yu, Y.-Y., et al., *Gold nanorods: electrochemical synthesis and optical properties.* The Journal of Physical Chemistry B, 1997. **101**(34): p. 6661-6664.

353. Nikoobakht, B., J. Wang, and M.A. El-Sayed, *Surface-enhanced Raman scattering of molecules adsorbed on gold nanorods: off-surface plasmon resonance condition.* Chemical Physics Letters, 2002. **366**(1-2): p. 17-23.

354. Ueno, K., et al., *Spectral sensitivity of uniform arrays of gold nanorods to dielectric environment.* The Journal of Physical Chemistry C, 2007. **111**(11): p. 4180-4184.

355. Takahashi, H., et al., *Gold nanorod-sensitized cell death: microscopic observation of single living cells irradiated by pulsed near-infrared laser light in the presence of gold nanorods.* Chemistry letters, 2006. **35**(5): p. 500-501.

356. Huang, X. and M.A. El-Sayed, *Gold nanoparticles: Optical properties and implementations in cancer diagnosis and photothermal therapy.* Journal of advanced research, 2010. **1**(1): p. 13-28.

357. Grzelczak, M. and L.M. Liz-Marzán, *The relevance of light in the formation of colloidal metal nanoparticles.* Chemical Society Reviews, 2014. **43**(7): p. 2089-2097.

358. Choi, E., et al., *Highly monodisperse rattle-structured nanomaterials with gold nanorod core–mesoporous silica shell as drug delivery vehicles and nanoreactors.* Nanoscale, 2013. **5**(1): p. 151-154.

359. Li, Z., et al., *Creation and reconstruction of thermochromic Au nanorods with surface concavity.* Journal of the American Chemical Society, 2021. **143**(38): p. 15791-15799.

360. Zhang, Q., et al., *Reconstruction of silver nanoplates by UV irradiation: tailored optical properties and enhanced stability.* Angewandte Chemie, 2009. **121**(19): p. 3568-3571.

361. An, J., et al., *Sculpturing effect of chloride ions in shape transformation from triangular to discal silver nanoplates.* The Journal of Physical Chemistry C, 2008. **112**(39): p. 15176-15182.

362. Lee, K.-S. and M.A. El-Sayed, *Gold and silver nanoparticles in sensing and imaging: sensitivity of plasmon response to size, shape, and metal composition.* The Journal of Physical Chemistry B, 2006. **110**(39): p. 19220-19225.

363. Awan, U.A., et al., *Stable and reproducible synthesis of gold nanorods for biomedical applications: a comprehensive study.* Iet Nanobiotechnology, 2018. **12**(2): p. 182-190.

364. Fan, J., Y. Cheng, and M. Sun, *Functionalized gold nanoparticles: Synthesis, properties and biomedical applications.* The Chemical Record, 2020. **20**(12): p. 1474-1504.

365. Jenkins, J.A., T.J. Wax, and J. Zhao, *Seed-mediated synthesis of gold nanoparticles of controlled sizes to demonstrate the impact of size on optical properties.* Journal of Chemical Education, 2017. **94**(8): p. 1090-1093.

366. Eustis, S. and M.A. El-Sayed, *Why gold nanoparticles are more precious than pretty gold: noble metal surface plasmon resonance and its enhancement of the radiative and nonradiative properties of nanocrystals of different shapes.* Chemical society reviews, 2006. **35**(3): p. 209-217.

367. Gan, R., et al., *Photothermal response of hollow gold nanorods under femtosecond laser irradiation.* Nanomaterials, 2019. **9**(5): p. 711.

368. Chon, J.W., et al., *Spectral encoding on Gold nanorods doped in a silica sol–gel matrix and its application to high-density optical data storage.* Advanced Functional Materials, 2007. **17**(6): p. 875-880.

369. Zijlstra, P., J.W. Chon, and M. Gu, *Effect of heat accumulation on the dynamic range of a gold nanorod doped polymer nanocomposite for optical laser writing and patterning.* Optics express, 2007. **15**(19): p. 12151-12160.

370. Li, P.-C., et al., *In vivo photoacoustic molecular imaging with simultaneous multiple selective targeting using antibody-conjugated gold nanorods.* Optics Express, 2008. **16**(23): p. 18605-18615.

Appendix

Particle Sizes

a) Size (length, diameter, AR) of AuNRs@$mSiO_2$ after laser irradiation.

AuNRs@$mSiO_2$-Control

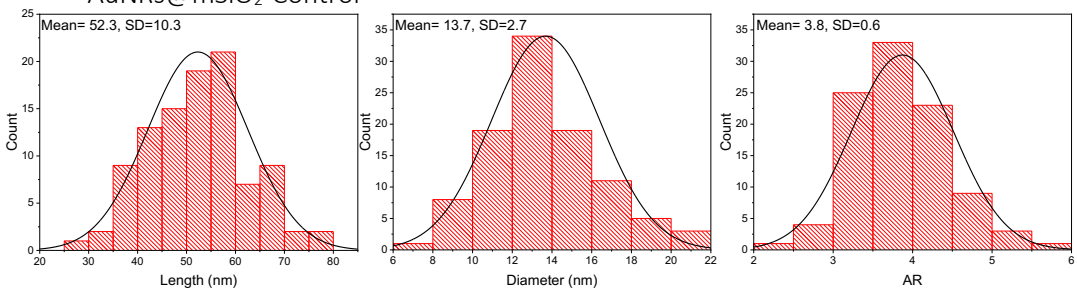

AuNRs@$mSiO_2$ 10 mJ -1 min

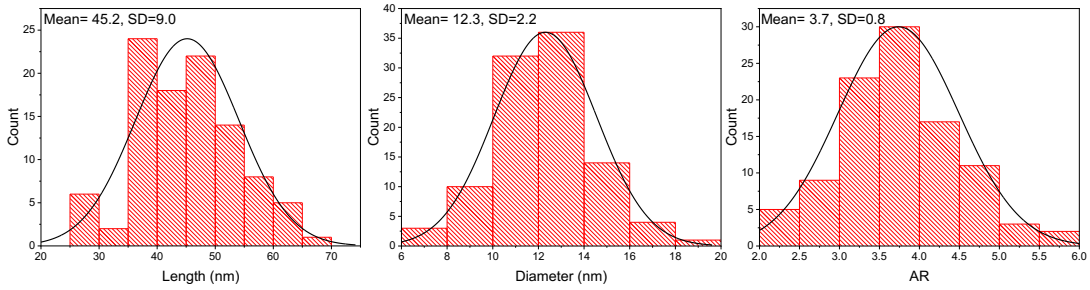

AuNRs@$mSiO_2$ 10 mJ- 5min

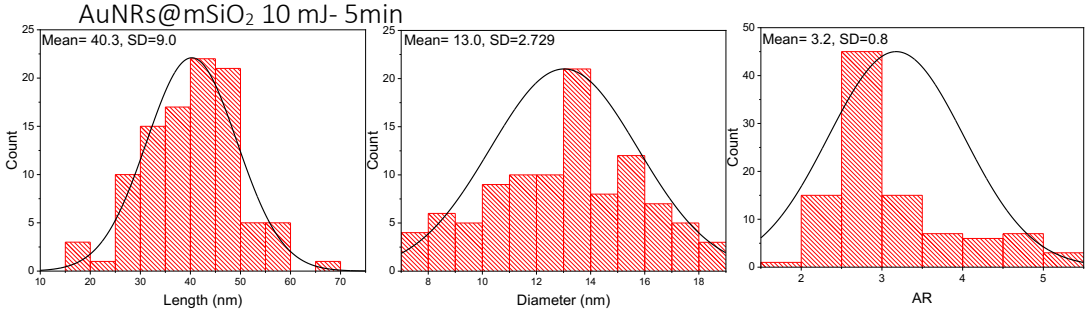

AuNRs@$mSiO_2$ 20 mJ-1min

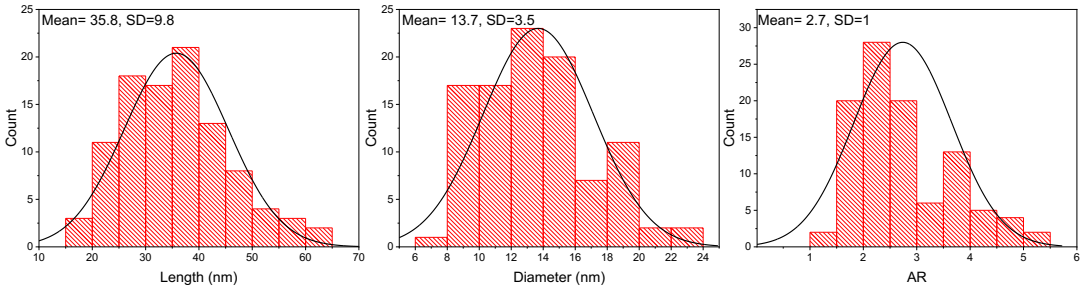

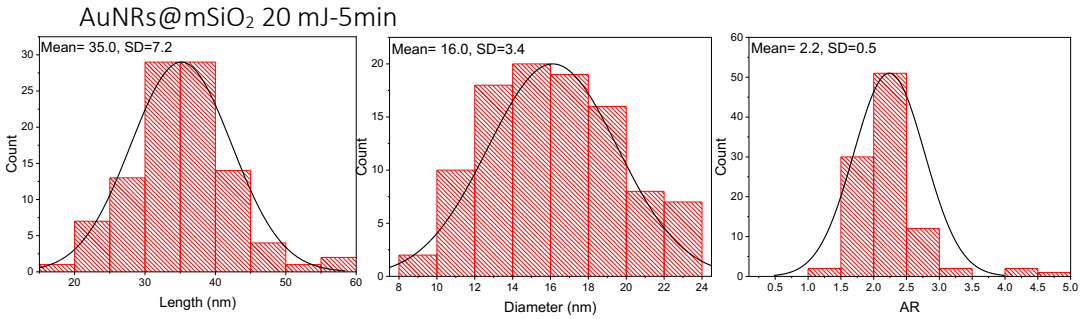

b) Mesoporous silica shell thicknesses

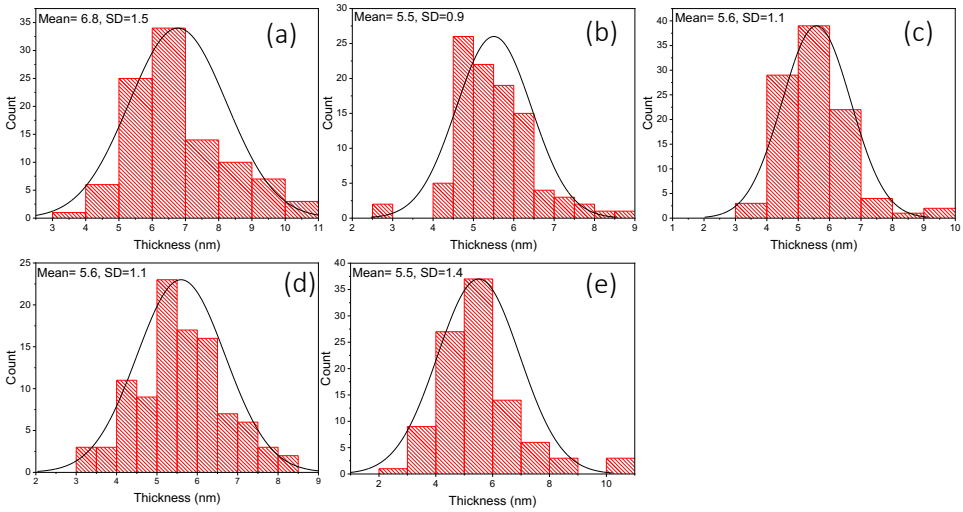

Figure. Mesoporous silica shell thicknesses of (a) AuNR@$mSiO_2$ control (no laser), (b &c) AuNR@$mSiO_2$ irradiated by pulsed laser of fluence of 10 mJ for 1 min and 5 min respectively. (d & e) AuNR@$mSiO_2$ irradiated by pulsed laser of fluence of 20 mJ for 1 min and 5 min respectively.